

**The mechanics of an accretionary wedge affected by
a layer with varying rheology, viscosity, and thickness**

Dissertation

zur Erlangung des Doktorgrades der Naturwissenschaften am
Fachbereich Geowissenschaften der Universität Bremen

vorgelegt von

Linda Marie Wenk

Bremen,

November 2013

*Diese Dissertation widme ich
meinem Großvater Herbert Otto Hube
(*11.09.1921, †22.07.1997)
dessen Neugierde mich geprägt hat.*

Abstract

The mechanics of accretionary wedges is determined by the geometrical boundary conditions and the physical properties of the incoming material particularly the décollement. If the décollement is located in an extremely weak material such as a viscous evaporite the accretionary wedge evolves wide extended, flat and with a characteristic thrust system (e.g., large thrust spacing, symmetrical dip angles of fore- and backthrusts, dually or no-preferred thrust vergence) or folding. The deformation processes and the mass transfer of such wedges are highly complex. Previous studies have embedded different materials such as glass beads or silicon layers to test the effect of viscous evaporites. Nevertheless, until now the mechanics and kinematics of such accretionary wedges is not fully understood. Therefore, the aim of the first three studies is to gain a better understanding for accretionary wedges which are influenced by weak viscous layers. In the first three studies 2D numerical ‘sandbox’ experiments are developed in which an incoming ‘sediment’ sequence is accreted against a fixed vertical wall due to the movement of the box bottom acting as basal décollement. The experiments contain a brittle incoming ‘sediment’ sequence in which either a brittle layer (Mohr Coulomb rheology) or a viscoelastic-plastic layer (Burger’s rheology) is embedded. In all experiments we analyze and compare the thrusts, the thrust vergence, the thrust dip angles and the slope angles.

Previous studies have used different materials to simulate a viscous layer. Hence, the first study (Chapter III) is focused on the materials which can be used to simulate an embedded viscous layer. Therein, the aim is to analyze the differences which occur in the mechanics of two wedge experiments if either a weak viscoelastic-plastic or a weak low-friction brittle layer is embedded between two high friction brittle layers. This setting highlights the importance of using a viscous rheology if a natural viscous layer is simulated. Therefore, we analyze additionally the absolute offsets as well as the relative offsets along thrusts and the thrust spacing within the two evolved wedge structures. We show that although identical properties are used for the weak brittle and the weak viscoelastic-plastic material, the latter one is more suitable to simulate the mechanics of an accretionary wedge incorporating a weak viscous décollement.

To find out the viscosity under which the wedge deforms most likely as it would grow on top of an evaporite, the next study (Chapter IV) analyzes the effects of different viscous

materials on wedge mechanics. Therefore, we vary the viscosity and compare, besides the above mentioned factors, the mass transport pattern of the particles in the accretionary wedge. As a result, we show that the influence of the viscoelastic-plastic layer on the wedge mechanics depends highly on the viscosity values. A high viscous embedded layer has only a negligible effect, whereas a low viscosity value has a high impact on accretion modes (frontal or basal accretion), thrust system, mass transport and uplift patterns. In this case, the viscoelastic-plastic layer acts as a mid-level detachment and decouples the frontal wedge and the basal duplex. Furthermore, we show that a low viscous layer is most suitable to simulate an ‘evaporite’-like behavior. In this case, relative symmetrical thrusts, typical flat material paths in the frontal wedge and steep paths in the basal duplex structure occur.

Afterwards, the calibrated model is used to study the effects of different incoming sediment thicknesses on the thrust system and the accretion process (Chapter V). In this case, the layer thicknesses of the viscous material and the upper brittle layer are adapted from those at the Mediterranean Ridge. Besides the above mentioned factors, we analyze the internal stress values and ratios between the different layers. As a result, a thin upper brittle layer and a thin embedded layer supports rather the evolution of a brittle imbricated wedge, while in case of a thick formation the deformation style is more similar to that in a ‘salt’-based wedge. Additionally, the results show that the effect of an increasing embedded layer thickness stagnates after a certain thickness has reached. The upper brittle layer thickness seems to be an important factor for explaining the different accretion mechanisms occurring at the Mediterranean Ridge.

Summing up, the here presented numerical ‘sandbox’ experiments help to gain a better understanding for mechanisms in accretionary wedges growing on viscous décollements in general and, in particular, for the Mediterranean Ridge. The results confirm with previous studies and, additionally, give detailed new insight into mass transport, accretion mode, thrust system as well as internal stress values in accreted wedges.

Besides the above presented studies, a further study with a similar model approach is undertaken to analyze the effect of the décollement strength and the effect of deep seated geometries. This approach helps to investigate the relationship between deep seated lower crustal and upper crustal processes and to increase the understanding how deep crustal conditions can be inferred from the exhumation history of rocks. Therefore, pure brittle double-vergent wedges with different basal friction values and geometries are developed

in a group of numerical ‘sandbox’ experiments and the exhumation history of upper crustal rocks is reconstructed by an apatite fission track (AFT) analysis. Hence, we use a combined approach to couple numerical 'sandbox' experiments and AFT analysis. Synthetic AFT ages are calculated for selected and extracted particles of the numerical 'sandbox' by forward thermal history modeling of the time-temperature history. The AFT-patterns of the different experiments are compared to gain a better understanding which effect the underlying processes have on the exhumation. As a result, we show that depending on the décollement strength and on the geometrical conditions characteristic AFT-patterns evolve due to the different uplift rates along the wedge. Consequently, different exhumation patterns of the upper crust result from different deep seated geometries and conditions, and the combined approach presented in this study helps to examine these coherencies and can be used to develop conceptual models.

Zusammenfassung

Die Mechanik von Akkretionskeilen wird durch die geometrischen Randbedingungen und die physikalischen Eigenschaften des eingetragenen Materials, vor allem des Décollements, bestimmt. Wird dieses Décollement durch ein sehr schwaches Material wie zum Beispiel viskose Evaporite gebildet, entwickelt sich ein extrem weiter und flacher Akkretionskeil. Dieser zeigt ein charakteristisches Störungssystem (weite Störungsabstände, gleiche Einfallswinkel der synthetischen und antithetischen Störungen, keine bevorzugte oder eine beidseitige Vergenz) und Faltenbildung. Der Deformationsprozess und die Massenbewegungen innerhalb dieser Keile sind sehr komplex und es wurden unterschiedliche Studien durchgeführt, um den Einfluss von viskosen Evaporiten zu analysieren. Hierfür wurden unterschiedliche Materialien wie Glasskugeln oder Silikonlagen in analogen Modellen verwendet. Trotzdem ist die Mechanik und Kinematik solcher Akkretionskeile bis heute noch nicht vollkommen verstanden. Aus diesem Grund widmen sich die ersten drei Studien dem Verständnis von Akkretionskeilen, die durch schwache, viskose Lagen beeinflusst werden.

In den ersten drei Studien werden zwei-dimensionale numerische „Sandkisten“ entwickelt, in denen eine „Sedimentsequenz“ durch die Bewegung eines basalen Modelbodens gegen eine feste und vertikale Wand akkretiert wird. Dieser Boden verhält sich somit wie ein Décollement einer abtauchenden Platte. Die Experimente bestehen aus spröden „Sedimentsequenzen“ (Mohr Coulomb Rheologie), in die eine viskoelastisch-plastische Lage (Burger's Rheologie) eingebettet wurde. In allen Experimenten wurden das Störungssystem, die Störungsvergeng, die Abtauchwinkel der Störungen und der Hangneigungswinkel des Keiles analysiert.

Die erste Studie (Kapitel III) beschäftigt sich mit dem Material, das verwendet wurde, um die eingebettete, viskose Lage zu simulieren. Da in früheren Studien sowohl spröde als auch viskose Materialien verwendet wurden, liegt der Fokus dieser Studie auf den Unterschieden in der Mechanik zwischen einem Model mit einer eingelagerten viskoelastisch-plastischen Lage und einem Model, in das eine spröde Lage mit einer geringen Reibung eingelagert wurde. Dieser Aufbau zeigt die Notwendigkeit ein Material mit viskosen Eigenschaften zu nutzen, wenn ein natürliches Salzverhalten simuliert werden

soll. Für diese Studie wird, neben den bereits erwähnten Faktoren, der absolute und relative Versatz entlang der Störungen sowie der Abstand zwischen zwei Störungen analysiert. Das Ergebnis dieser Studie ist, dass auch bei gleichen physikalischen Eigenschaften das viskoelastisch-plastische Material eher geeignet ist ein viskoses Décollement zu simulieren als ein sprödes Material. Dieses Ergebnis beruht darauf, dass die charakteristische Salztektonik in diesem Experiment besser ausgebildet ist als in dem spröden Vergleichsexperiment.

Im Folgenden (Kapitel IV) soll aufgezeigt werden bei welcher Viskosität am ehesten ein Keil mit einem viskosen Décollement entsteht. Hierfür wurde der Einfluss von verschiedenen viskosen Materialien auf das Deformationsverhalten analysiert in dem die Viskosität variiert wurde. Neben den beschriebenen Faktoren wurde vor allem der Massentransport der Partikel durch den Akkretionskeil verglichen. Die Analyse zeigt, dass die Keilmechanik sehr stark von der Viskosität der viskoelastisch-plastischen Lage abhängt. Während bei einer hoch viskosen Lage der Einfluss vernachlässigbar ist, zeigt sich bei einer geringen Viskosität ein deutlicher Einfluss auf den Akkretionsmodus (frontale und basale Akkretion), die internen Störungen, den Massentransport und die Hebungspfade. In diesem Fall entwickelt sich innerhalb der viskoelastisch-plastischen Lage ein neues Décollement, das den frontalen Keil von dem basalen Duplex trennt. Darüber hinaus bildet die gering viskose Lage eher das Verhalten von viskosen Materialien wie Salzen nach. Hierbei entwickeln sich relativ symmetrische Störungen, typische flache Materialpfade im frontalen Keil und steile Hebungspfade in der basalen Duplexstruktur.

Im Anschluss (Kapitel V) wird das kalibrierte, heterogene Model für eine Studie verwendet, die den Einfluss der Sedimentmächtigkeit auf das Störungssystem und die Akkretionsprozesse testen soll. In diesem Fall werden die Mächtigkeiten der viskoelastisch-plastischen und der oberen spröden Lage vom Mittelmeerrücken übernommen. Für diese Studie wird neben dem Störungssystem, die internen Spannungswerte zwischen den verschiedenen Lagen analysiert. Bei einer dünnen, spröden, hangenden und einer dünnen, eingebetteten Lage ähnelt das Deformationsverhalten eher einem spröden, schuppenartig-gestapelten Keil. Dagegen ähnelt das Deformationsverhalten bei einer mächtigen Auflast und einer mächtigen eingebetteten Lage eher dem eines Keiles, der sich im Hangenden von Salzen entwickelt. Ab einer bestimmten Mächtigkeit der eingebetteten Lage stagniert ihr Einfluss auf das

Deformationssystem. Im Gegensatz dazu zeigt eine mächtige hangende Lage einen großen Einfluss auf das Störungssystem. Diese Ergebnisse helfen die verschiedenen Akkretionsmechanismen am westlichen und östlichen Mittelmeerrücken zu verstehen.

Die hier präsentierten numerischen „Sandkisten“-Experimente ermöglichen die Mechanismen von wachsenden Akkretionskeilen im Allgemeinen und am Mittelmeerrücken im Speziellen besser zu verstehen. Die Ergebnisse stimmen mit früheren Studien überein und zeigen darüber hinaus neue detaillierte Einblicke in den Massentransport, den Akkretionsmodus und das Störungssystem sowie in die internen Spannungen eines akkretierten Keiles.

Neben dieser Studie wurde eine weitere Studie mit einem ähnlichen Modellaufbau durchgeführt, um zu analysieren, welchen Einfluss die Décollement- und Geometrieigenschaften der unteren Kruste auf die Entwicklung der oberen Kruste haben. Dieser Ansatz ermöglicht den Zusammenhang zwischen Prozessen in der unteren und oberen Kruste zu untersuchen und ein Verständnis dafür zu bekommen, wie die Eigenschaften der unteren Kruste die Exhumierungsgeschichte von Gesteinen beeinflussen. Hierfür werden in numerischen „Sandkisten“-Experimenten doppeltvergente Keile entwickelt, deren Reibungen am Décollement und Geometrien sich unterscheiden. Mit den Daten aus diesen Keilen wird im Anschluss eine Apatit-Spatspurenanalyse (AFT) durchgeführt, um die Exhumationsgeschichte zu rekonstruieren. Somit verwenden wir einen kombinierten Ansatz, bei dem numerische „Sandkisten“-Experimente mit einer AFT Analyse gekoppelt werden. Hierbei werden für ausgewählte Partikel der numerischen „Sandkiste“ synthetische AFT-Alter durch eine thermalgeschichtliche Modellierung von Zeit-Temperatur-Pfaden berechnet. Die AFT-Muster der verschiedenen Experimente werden im Anschluss verglichen. Diese Studie zeigt, dass anhängig von der Stärke des Décollements und den geometrischen Bedingungen Hebungen in unterschiedlichen Bereichen dominieren, wodurch unterschiedliche charakteristische AFT-Muster entstehen. Aus den Ergebnissen schließen wir, dass verschiedene Exhumationsmuster durch unterschiedliche Eigenschaften der unteren Kruste entstehen. Die präsentierte Kombination der zwei Methoden hilft die Zusammenhänge zwischen der oberen und unteren Kruste zu verstehen und kann verwendet werden um konzeptionelle Modelle zu entwickeln.

Table of Contents

Abstract	I
Zusammenfassung	V
Chapter I: Introduction	1
1. Subduction zone	1
2. Mechanics and dynamics of brittle MC accretionary wedge	5
2.1 Material behavior in case of elasto-plastic rheology	5
2.2 Critical Taper theory	7
2.3 Mechanics and kinematics of accretionary wedges	8
2.4 Simulation of wedge kinematics and mechanics	11
2.5 Factors affecting the evolution of accretionary wedges	12
3. Mechanics and dynamics of non-MC accretionary wedges	21
3.1 Creep behavior of rocks	21
3.2 Natural wedges and wedge models with viscous layers	23
3.3 Case study: Mediterranean ridge complex	24
3.4 Simulation of non-Mohr-Coulomb accretionary wedges	27
Chapter II: Motivation and Objectives of this study	33
Chapter III: Rheology study	39
1. Introduction	40
2. Method	41
2.1 Discrete Element Method	41
2.2 Mechanical concepts and rheological models	42
2.3 Model setup	44
2.4 Analysis and interpretation techniques	47
3. Results	48
3.1 Bulk properties	48
3.2 Structural geology of the evolving wedges	49
4. Discussion	54
5. Conclusion	57
ACKNOWLEDGEMENTS	58
Chapter IV: Viscosity study	59
1. Introduction	61

2. Method	64
2.1 Discrete Element Method	64
2.2 Rheologies simulated with the DEM	64
2.3. Model configuration.....	67
2.4 Model simplifications	69
2.5 Model analysis and interpretation techniques.....	69
3. Results.....	71
3.1 Bulk material parameters	71
3.2 Mechanics of the experiments H and V1-V6.....	73
4. Discussion.....	82
4.1. Homogeneous wedge (H)	82
4.2. Heterogeneous wedge (V1-V6)	84
5. Conclusion and Outlook	89
ACKNOWLEDGEMENTS.....	91
Chapter V: Layer thickness study	93
1. Introduction.....	95
2. Geological setting Mediterranean Ridge	96
3. Method	98
3.1 Discrete Element Method	98
3.2 Natural rheological behavior and material implementation in PFC2D	99
4. Model configuration.....	100
4.1 Model approach	100
4.2 Model analysis and interpretation techniques.....	103
5. Results.....	103
5.1 Bulk properties.....	103
5.2 Structural evolution of the wedges	104
6. Discussion.....	109
6.1 Effects of the thickness of the embedded layer (series I)	110
6.2 Effects of the thickness of the Plio-Quaternary cover (series II).....	111
6.3 Comparison with the Mediterranean Ridge	112
7. Conclusion	114
ACKNOWLEDGEMENTS.....	115
Chapter VI: Conclusion and Outlook	117

References.....	121
Danksagung.....	131
Appendix I: Combined DEM and AFT study.....	133
1. Introduction.....	135
1.1 Evolution of double-vergent wedges	137
2. Method	138
2.1 Discrete Element Method	138
2.2 Apatite fission track analysis	139
2.3 Model setup.....	140
2.4 Model limitations	142
2.5 Analysis and interpretation techniques	142
3. Results.....	147
3.1 Experiment Sc1 (high friction detachment, indenter, lcf).....	147
3.2 Experiment Sc2 (low friction detachment, indenter, lcf).....	152
3.3 Experiment Sc3 (high friction detachment and indenter)	156
4. Discussion.....	159
4.1 Influence of detachment strength (coefficient of friction of lower crust).....	160
4.2 Influence of deep seated geometries	165
5. Conclusions.....	166
ACKNOWLEDGEMENTS.....	168
Erklärung.....	169

Chapter I: Introduction

1. Subduction zone

Forearc regions of subduction zones belong to the most tectonically active regions in the world and are responsible for geohazards, such as volcanism, earthquakes, and tsunamis (Fig. I-1). The uplift and the topography of these regions influence the amount of sedimentary input and are responsible for the evolution of mass wasting events (e.g., Gutscher et al., 1998b; Lucente and Pini, 2008). The mechanics of forearc regions in subduction zones has been in the focus of geoscientific studies for many years (e.g., Davis et al., 1983; Dahlen, et al., 1984; Mulugeta, 1988) because understanding these mechanisms is an important task not only of scientific interest, but also for the development of early warning systems for humans living along the coastline (e.g., Tappin, 2009).

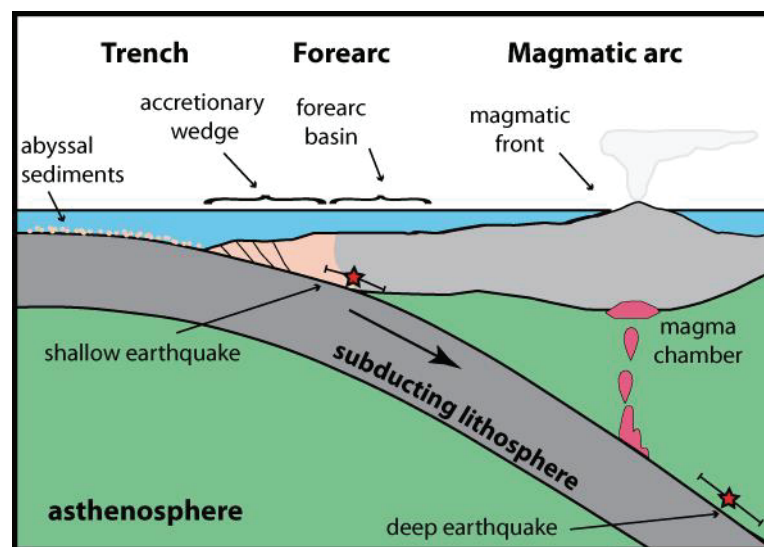


Fig. I-1: Subduction zone with the forearc region, magmatic front, and earthquake positions marked by red stars (modified after Frisch and Meschede, 2007).

At subduction zones of convergent margins, an oceanic plate descends beneath a continental plate and sinks into the earth mantle (Fig.I-1). Active margins can be divided into two categories: accretive and non-accretive systems (e.g., Lohrmann, 2002; Frisch and Meschede, 2007). At accretive margins the sediments or rocks of the upper brittle crust are horizontally compressed as a result of the submerging of the subducting crust and the pressure induced by the opposite movement of the upper crust. This continuous off-scraping of sediments from the oceanic plate and uplifting or accumulation along the

continental plate results in the evolution of an accretionary wedge (Fig. I-1, Frisch and Meschede, 2007). In contrast, at non-accretive margins, no or only a reduced wedge evolves.

Accretionary wedges, which are usually submarine, can be seen as a subset of fold-and-thrust belts where new sediments are added or incorporated (Davis et al., 1983). They show large variations in their form and can evolve widely extended (e.g., Barbados wedge; Westbrook, 1975) or short (e.g., Tonga wedge; Giardini and Woodhouse, 1984) and with a steep frontal slope (e.g., the Oregon wedge; DeMets et al., 1990) or in an extremely flat shape (e.g., Mediterranean Ridge; Reston et al. 2002b). Nevertheless, a few common observations can be made (e.g., Chapple, 1978):

- (1) the base of the accretionary wedge is formed by a mechanically weaker basal detachment or décollement embedded in the stratigraphy, dipping towards the subduction zone;
- (2) the evolving thrusts dip towards the hinterland and become systematically younger in the direction of the foreland;
- (3) the surface slope angle dips towards the foreland.

At these accretionary wedges, sediment accretion occurs either by accumulation of the off-scraped material at the deformation front (frontal accretion mode) or at the bottom of the prism structure (basal accretion mode), resulting in a triangular wedge form (e.g., Platt, 1989; Fig. I-2a, b). In case of frontal accretions, the wedge grows by progressive frontal thrust faults e.g., piggy back thrusts or pop-ups (e.g., Mediterranean Ridge; Reston et al. 2002b; Fig I-2a) and in case of basal accretion the material can be far underthrust under the wedge structure and afterwards basally accreted (northern Barbados accretionary wedge; Westbrook et al., 1982; Fig. I-2b). Thereby, a duplex structure can evolve and, depending on the uplift rates, an exhumation of the wedge material will occur (Cloos and Shreve, 1988; Von Huene and Scholl, 1991; Gutscher et al., 1998a, b; Glodny et al., 2005). As a result of the exhumation, slope destabilization with mass wasting events can occur along the uplifted wedge (Gutscher et al., 1998b). Moreover, both accretion modes can act at the same time if besides a stronger basal décollement a weaker mid-level décollement is evolved within the incoming sediments (Fig. I-2c; e.g., Makran accretionary wedge; White et al., 1977; Fruehn et al., 1997).

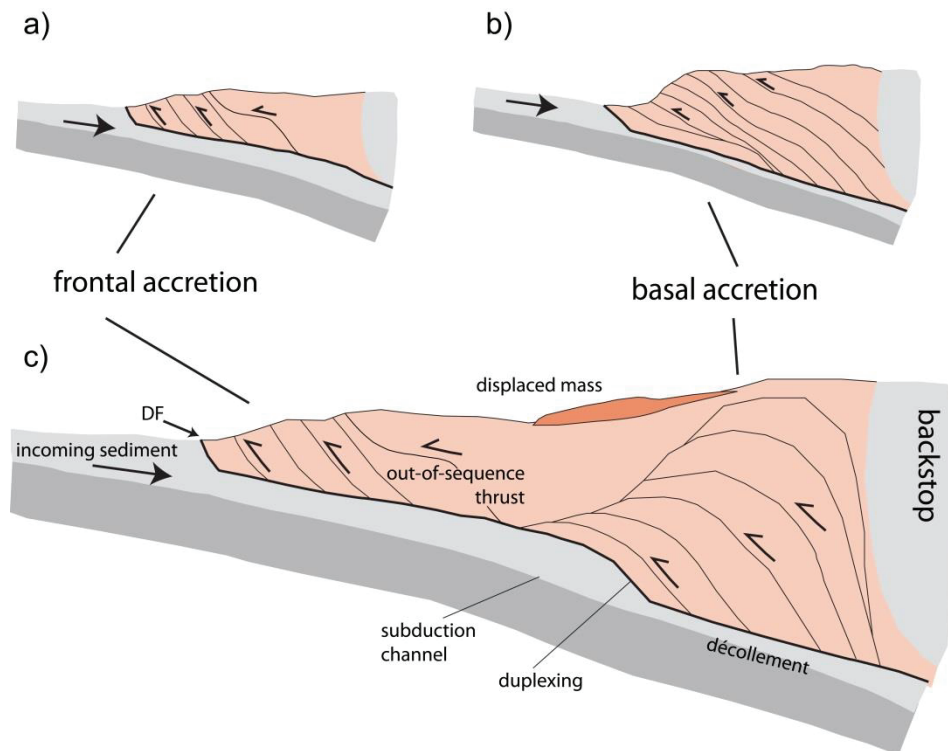


Fig I-2: Frontal and basal accretion in single mode and simultaneously occurring due to an active mid-level décollement (modified from Cawood et al., 2009; Kusky et al. 1997 (a, b); Gutscher et al., 1996 (c)).

Both accretion modes result in a horizontal and vertical growth of the wedge structure, however horizontal spreading is more pronounced in the case of frontal accretion and a vertical thickening is more pronounced in case of basal accretion. Additionally, the wedge thickens due to the evolution of out-of-sequence thrusts, which evolve distant from the deformation front (Fig. I-2).

The evolution of the thrust system also defines the mass transport pattern of the incoming sediments and can be subdivided into frontal and basal accretion (Cloos and Shreve, 1988). If frontal accretion occurs, a slightly linear uplift of the material can be distinguished while the material is transported away from the deformation front (Fig. I-3). In contrast, if the material is basally accreted it is first horizontally transported deep into the wedge structure and, subsequently, steeply vertically uplifted (Cloos and Shreve, 1988; Fig. I-3).

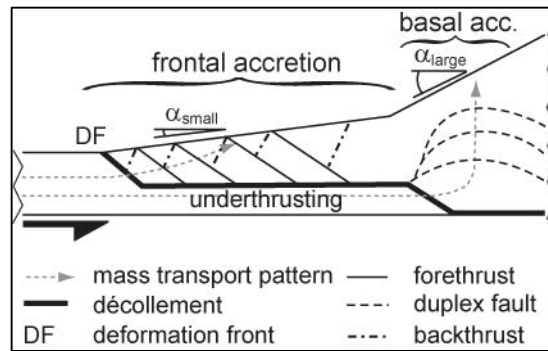


Fig. I-3: Mass transport through an accretionary wedge due to frontal and basal accretion (modified after Cloos and Shreve, 1998).

To understand the structure of accretionary wedges and, respectively, their mechanics recorded data, such as seismic profiles or bathymetry data, are used (e.g., Mascle and Chaumillon, 1998; Bohnhoff et al., 2001). Nevertheless, these data sets only represent snapshots in time of the recent situation. To understand the structural geological principles, the reconstruction of the kinematic history and the growing mechanisms are necessary. An important step in the last 30 years for understanding the thrust mechanics of accretionary wedges was done by Chapple (1978), Davis et al. (1983), and Dahlen et al. (1984). They developed the Critical Taper theory which explains the mechanics of a pure brittle accretionary wedge. This theory is based in the Mohr Coulombs law which describes the mechanical behavior of upper brittle crustal materials (Coulomb, 1776; see Sec. 2.2). Following this theory, the wedge deformation and kinematic are defined by different factors influencing the system such as geometrical conditions (e.g., plate dipping; Davis et al., 1983) and physical properties of the incoming sediments (e.g., coefficient of friction, density or pore pressure; e.g., Davis et al., 1983; Dahlen, 1990, Lallemand et al., 1994). In Section 2.2 the effect of some selected factors influencing the wedge growing are explained, whereas in Section 2.3 and 2.4 a detailed overview is given about analog and numerical studies dealing with the quantification of different aspects.

Besides the Mohr Coulomb wedges numerous data reveal also non-Mohr Coulomb wedges which contain besides brittle also viscous material. These wedges show due to the weak viscous material which is incorporated into the accretionary process a different mechanical and kinematical evolution than pure brittle wedges (for details see Sec. 3). One prominent example for such kind of wedges is the Mediterranean Ridge (see Sec. 3.5).

2. Mechanics and dynamics of brittle MC accretionary wedge

2.1 Material behavior in case of elasto-plastic rheology

Brittle sediments, which are deformed under acting forces, show an elasto-plastic material curve (Fig. I-4a). If the applied forces are small, the initial elastic material deformation is reversible and follows the Hooke's law. When further forces act and the critical shear strength of the material is reached, the elastic deformation is, subsequently, replaced by plastic deformation and non-oriented, irreversible microcracks are generated (strain hardening, Fig. I-4a). This deformation-phase is irreversible and starts before the maximal peak stress is reached. After reaching the peak stress, the shear strength of the material decreases (strain softening) and the generation of microcracks is substituted by the development of large, irreversible shear plains and rock failure (Fig. I-4a). The strain hardening and strain softening has an important influence on the thrust zone formation (e.g., Adam et al., 2005). If the stress/strain curve of brittle sediments is compared with those of the upper brittle crust a similar form comprising elastic and plastic deformation can be distinguished (Fig. I-4a, b). In this case, starting at the peak point, microcracks occur that are known as Riedel-shears (Fig. I-4b).

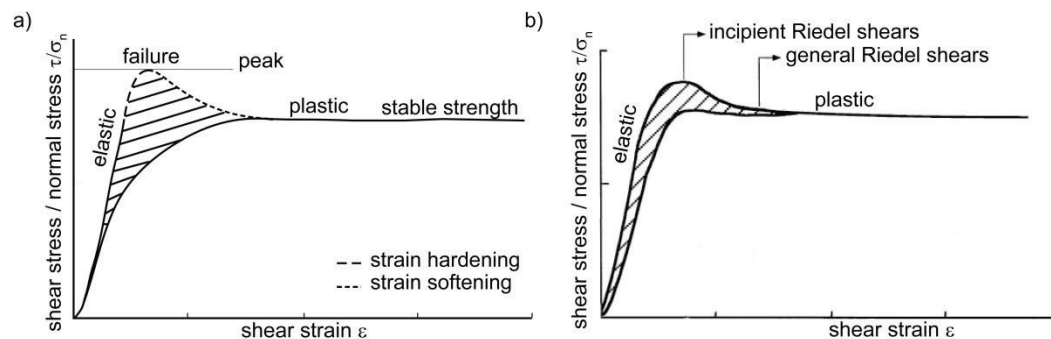


Fig. I-4: Material curve of a) sand and b) a natural rock of the upper crust
(modified after Marone, 1988 and Lohrmann et al., 2003).

To calculate if a rock failure occurs, the Mohr-Coulomb criterion can be used. This criterion describes the ratio of the shear stress (τ) to the normal stress (σ_N). Therein, failure appears when the critical shear stress (τ_{crit}) is reached according to the equation (eq. I-1, Coulomb, 1776):

$$|\tau_{crit}| = C + \mu_{int} \cdot \sigma_N, \quad (\text{eq. I-1})$$

where C is the cohesion and μ_{int} is the internal friction coefficient of the material. In accordance with this theory, brittle fractures occur in the stiff upper crust if the critical shear stress is reached. Consequently, the Mohr-Coulomb criterion can be used to describe the deformation behavior under the temperature conditions existing in the small depths of typical accretionary wedges (Davis et al., 1983; Dahlen et al., 1984). In general, the Mohr-Coulomb criterion depends on the stresses within the material, but is time *independent*.

Pore fluids, which occupy the pore spaces in natural rocks, have a further influence on the thrust evolution and the stress field. These fluids reduce the normal stress on the sidewalls in accordance with the pore pressure. The principal stresses change and the Mohr Coulomb circle is shifted along the normal stress axis towards the shear stress axis (Fig. I-5).

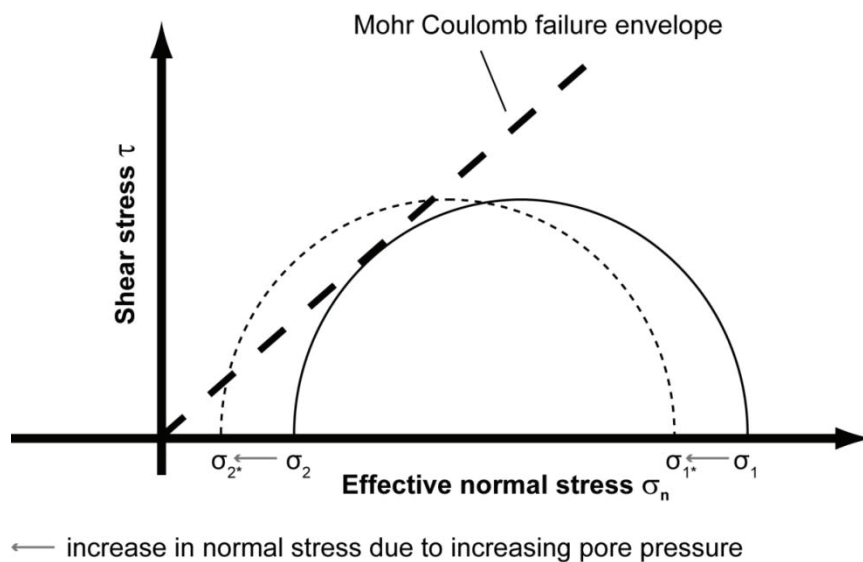


Fig. I-5: *In-situ* stress and fault reactivation associated with pore pressure increase (modified after Hung and Wu, 2012).

In regions where pore fluids are involved, fracturing or faulting occurs at lower strain rate than in dry natural rocks (Detournay et al., 2007). The resulting effective normal stress (σ'_N) can be described by equation (eq. I-2; Terzaghi, 1925):

$$\sigma'_N = \sigma_N - P_f. \quad (\text{eq. I-2})$$

where P_f is the pore pressure.

The shear stress is not affected. Hence, the frictional strength with the Mohr Coulomb criterion is reduced to:

$$\tau_{krit} = C + \mu(\sigma_N - P_f), \quad (\text{eq. I-3})$$

with $\mu = \tan \theta$, where θ is the angle of friction. Consequently, as water is not homogeneously distributed in rocks, in those areas where water is located failures occur under lower normal stress than in dry regions because pore pressure reduces the brittle strength of rocks (Davis et al., 1983).

2.2 Critical Taper theory

The mechanical behavior and the evolution of a Mohr Coulomb wedge have been successfully described by the Critical Taper (CT) theory (Davis et al., 1983; Dahlen, 1984; Dahlen et al., 1984; Lallemand et al., 1994). This theory provides an analytical solution for the critical taper (sum of the surface slope angle (α) and basal slope angle (β)), the orientation of the stresses (σ_1, σ_2), the mass transport pattern of accreted prisms and the evolution of thrust angles (δ_f, δ_b) as function of internal material strength of the incoming sediment sequence and basal strength at the décollement (Davis and Engelder, 1985; Cloos and Shreve, 1988; Fig. I-6). Despite the explanation for the geometry of wedges which is provided by the CT theory, this theory does not contain an explanation for the evolution of the wedge structure.

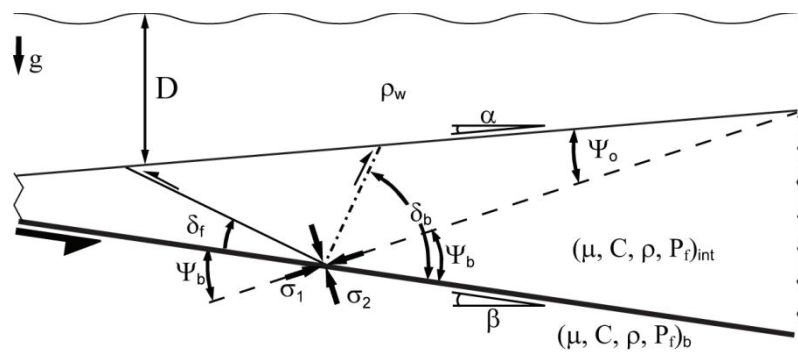


Fig. I-6: Stress orientation for a cross-section through a wedge with a critical taper angle ($\alpha + \beta$), Ψ_β : the angle between the maximum compressive stress σ_1 and the base of the wedge, Ψ_0 : angle between σ_1 and the top, σ_2 : minimum compressive stress, C : Cohesion, P_f : pore pressure, μ : coefficient of friction, ρ : density, ρ_w : water density; g : gravitational acceleration, δ_f : dip angle of forward thrusts, δ_b : dip angle of back thrusts, D : depth (modified after Dahlen and Suppe, 1988).

Besides the importance of a time-independent Coulomb material further assumptions for the material conditions have to be made for the CT theory. These conditions are for the hanging or the internal material a homogeneous and isotropic lithology in space and time incorporating the friction coefficient (μ_{int}), the pore pressure (P_{fint}) and the stress orientation (Fig. I-6; Dahlen, 1984). These factors are also valid for the basal décollement (e.g., basal coefficient of friction (μ_b), basal pore pressure (P_{fb})). Additionally, reactivation of thrust faults in weakened material is not taken into account. These conditions allow for static stress conditions which are assumed to be approximated by linear elasticity (Wang and Hu, 2006) and that the material is uniform on the verge of failure (Lohrmann et al., 2003; Wang and Hu, 2006). Hence, the theory gives the best solution for the deformation front where new material occurs in the undeformed sediment (Stockmal et al., 2007; Simpson, 2011). Furthermore, a negligible cohesion ($C_{int/b}$) is needed within the whole prism and the décollement (Davis et al., 1983).

2.3 Mechanics and kinematics of accretionary wedges

Using a Coulomb material approach the mechanics and accretion mode of an accretionary wedge can be explained by the Critical Taper theory. Following this theory, a wedge will deform until a critical taper is reached. If the wedge has reached this critical state, stress equilibrium exists between the development of internal thrusts and basal sliding. The critical taper evolves as follows (Davis et al., 1983; Dahlen, 1984; Dahlen et al., 1984; Dahlen, 1990; Buitert, 2012):

$$\alpha + \beta = \Psi_\beta + \Psi_0 \quad (\text{eq. I-4})$$

where α is the surface slope, β the basal slope, Ψ_β is the angles between the maximum principal stress σ_1 and the base, and Ψ_0 is the angle between maximum principal stress σ_1 and the top of the wedge.

For a cohesionless wedge we have:

$$\Psi_0 = \frac{1}{2} \arcsin \left(\frac{\sin \phi'_b}{\sin \phi} \right) - \frac{1}{2} \phi'_b \quad (\text{eq. I-5})$$

$$\Psi_0 = \frac{1}{2} \arcsin \left(\frac{\sin \alpha'}{\sin \phi} \right) - \frac{1}{2} \alpha' \quad (\text{eq. I-6})$$

$$\tan \phi'_b = \tan \phi_b \left(\frac{1-\lambda_b}{1-\lambda} \right) \quad (\text{eq. I-7})$$

$$\alpha' = \arctan \left(\left(\frac{1-\rho_w/\rho_{int}}{1-\lambda} \right) \tan \alpha \right) \quad (\text{eq. I-8})$$

where ϕ_b is the angle of basal friction, ρ_{int} is the internal density, ρ_w is the water density, λ is the pore fluid factor within the wedge and λ_b is the pore fluid factor at the base. The pore fluid factor is defined as the pressure of the pore water in dependence of the depth. These parameters can be calculated dependent on the known pressure (P) and pore pressure (P_f) along the basal detachment as follows:

$$\lambda = \frac{P - \rho_w g D}{\sigma_z - \rho_w g D} \quad (\text{eq. I-9})$$

$$\lambda_{fl} = \frac{P_f - \rho_w g D}{\sigma_z - \rho_w g D} \quad (\text{eq. I-10})$$

where σ_z is the vertical stress, g is the gravity, and D is the water depth for the submarine wedge.

The opening angle of an accretionary can be calculated by the following equation (Davis et al., 1983):

$$\alpha + \beta = \frac{(1-\lambda_b)\mu_b + \left(1 - \frac{\rho_w}{\rho_{int}}\right)\beta}{\left(1 - \frac{\rho_w}{\rho_{int}}\right) + (1-\lambda)K} \quad (\text{eq. I-11})$$

In the case of a subaerial wedge ($\lambda = 0$; $\lambda_b = 0$), $D = 0$ and $\rho_w = 0$ and, thus the equation simplifies to

$$\alpha + \beta = \frac{\mu_b + \beta}{1+K} \quad (\text{eq. I-12})$$

The dimensionless term (K) will be approximate:

$$K = \frac{\sin \phi}{1 - \sin \phi} + \frac{\sin^2 \phi_b + \cos \phi_b (\sin^2 \phi - \sin^2 \phi_b)^{1/2}}{\cos^2 \phi_b - \cos \phi_b (\sin^2 \phi - \sin^2 \phi_b)^{1/2}} \quad (\text{eq. I-13})$$

The critical taper ($\alpha + \beta$) can be calculated by substituting the equation (eq. I-13) in (eq. I-12). The taper increases with an increase of the coefficient of basal friction angle ϕ_b , whereas it decreases with an increase in the internal friction angle ϕ (e.g., Dahlen, 1990).

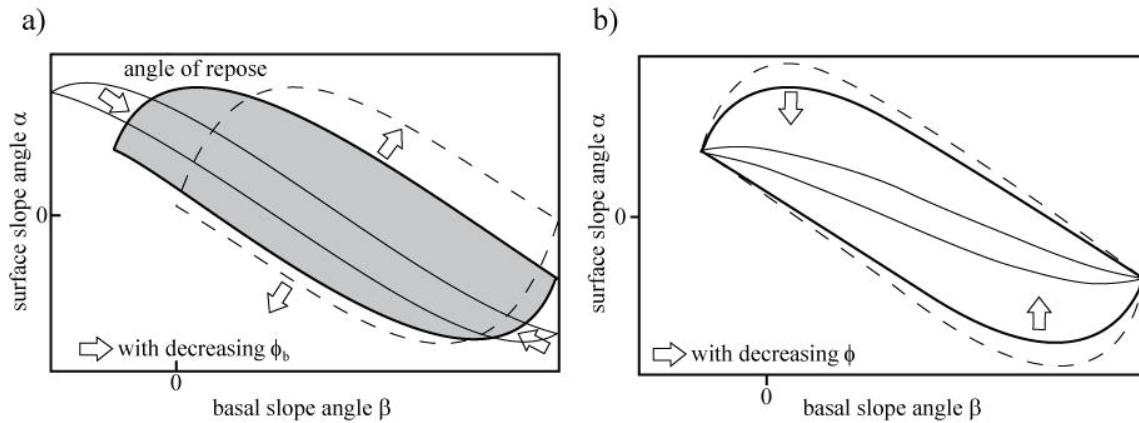


Fig I-7: Evolutions of wedge stability fields with (a) decrease of ϕ_b (direction of arrow) resulting in a reduction of the horizontal extension and an increase of the vertical extension as well as with (b) decreasing ϕ (direction of arrow) resulting in a decrease of the vertical extension (modified after Dahlen, 1984).

Consequently, the ‘critical’ surface slope angle (α_{krit}) can be calculated for all basal slope angles β . The maximum surface slope for a dry and subaerial wedge is the angle of repose, $\alpha_{max} = \phi$ (Dahlen, 1984). By using equations I-5 - I-8 , two stability curves can be calculated for a lower and an upper surface ‘critical’ slope value for any given basal dip. Wedges evolving out of a nearly horizontal incoming sediment sequence, achieve in most cases the lower critical taper angle and adapt their geometry by reverse faulting to the critical taper solution (e.g., Dahlen, 1984). In contrast, preexisting wedges will evolve in accordance to the upper critical taper by normal faulting. In either circumstance, the condition that $0 \leq \alpha + \beta \leq \pi$ must be fulfilled.

To gain a better understanding of the relationship between the surface angle and the basal slope angle a “stability diagram” can be drawn to enable the identification of the stability domains (Fig. I-7). Outside the stability domain, the wedge is overcritical or undercritical and, thus, is in a non-equilibrium state. A shift of the stability-domain can occur when the strength of the basal detachment or of the strength of the internal material changes. In this case, the wedge will deform internally by extension or compression until the critical taper is reached while increasing or decreasing its surface slope angle. For the adaption of the surface slope angle different deformation technics, such as frontal accretion, underplating, duplexing, out-of-sequence thrusting or even the formation of a new basal décollement at the new weakest horizon is used (Dahlen, 1984). Hence, different factors lead to the evolution of new thrust zones based on the Mohr Coulomb criterion. Afterwards, if new

material is added, the wedge grows self-similar at its critical taper value with a constant stress orientation through the interior. If the material input stops, the wedge will slide stably along the base without internal deformation.

2.4 Simulation of wedge kinematics and mechanics

To analyze the dynamic evolution of accretionary wedges small scaled analog or numerical experiments have been used since decades (e.g., Byrne et al., 1993; Costa et al., 2002, Buitter et al., 2006). Analog experiments are typically undertaken in a box, which consists of glass-walls at the sides and a moveable bottom, out of a more or less rough material such as a sand-paper. This material is pulled in one direction similar to a subduction plate. On top different anorganic or artificial granular materials of low strength such as quartz sand, clay or microbeads are used to simulate the material behavior of the upper crust (e.g., Lohrmann et al., 2003; Schreurs et al., 2006; Storti et al., 2007). Mainly cohesionless quartz sand is a widespread material to reproduce rock deformation since both have a similar stress/strain-material-curve (see Sec. 2.1, 2.2). To calibrate the material (e.g., frictional properties) measurements with ring-shear testers (e.g., Panien et al., 2006) or a Hubbert-type shear box (e.g., Hubbert, 1951; Schellart, 1994) are performed. For quartz sand commonly a friction coefficient (μ) of the order of ca. 0.6-0.7 is used. The calibration of the coefficient of friction, the natural stress-strain material behavior (see Sec. 2.1) and the time-independence of the Mohr Coulomb material are the main arguments why the upper brittle crust can be modeled in a much shorter time frame by using small-scaled sandbox models (Jaeger et al., 2007).

If natural fold-and-thrust belts should be simulated partially additional materials are necessary to simulate the various rheological behaviors. To simulate a viscous material such as evaporites also glass beads have been used (e.g., Kukowski et al., 2002). This brittle material has a low coefficient of friction of $\mu \sim 0.37$ (e.g., Koyi and Vendeville, 2003), but it cannot reproduce the rheological behavior correctly. As a result, in analog experiments viscous silicon layers such as SGM36, a transparent PDMS polymer, are used to simulate evaporitic behavior (e.g., Costa et al., 2009). These materials are much more suitable to model the creep behavior of natural evaporites.

In contrast to analog models, numerical models are extremely flexible concerning the choice of the rheology, the material properties, and its calibration. In this case, a large range of parameters can be directly tested, such as stress, strain or velocity. One numerical method is the Finite Element Method (FEM), which is suitable for approximative solutions of partial differential equations. These differential equations describe boundary valued problems of different forms. The FEM subdivides the forms in small domains. In these domains, the partial differential equations are locally approximated by simpler element equations. FEM is suitable to calculate stress and strain by analyzing local shifts of knots in the subdomain-grid, but simulations of thrust along long distances are still complicated.

Another numerical method, which is used for the study, is the Discrete Element Method (DEM). This method contains discrete particles of simple shape which can be displaced in different directions of a two-dimensional (2D) or three-dimensional (3D) simulation space. Moving direction and displacement of a single particle are calculated depending on its interaction with neighboring particles by simple physical laws. A detailed explanation of the 2D Discrete Element Method, which is used for this thesis, is given in Chapter III (Sec. 2.1), IV (Sec. 2.1) and V (Sec. 3.1). Due to the set of individual particles thrusting can easily be simulated which is an advantage to the FEM. To simulate a variety of natural materials, rheological models have been developed which approximate the material behavior by using simple components such as springs (*Hookean model*) or dashpot (*Newtonian model*, e.g., Barnes, 2000; Malkin and Isayev, 2006). The here used rheological models are explained in Chapter III (Sec. 2.2) and IV (Sec. 2.2).

2.5 Factors affecting the evolution of accretionary wedges

The evolution of an accretionary wedge is influenced by different factors which can be derived from the Critical Taper theory, such as:

- geometrical factors
 - plate dip angle (β)
- physical properties
 - basal coefficient of friction (μ_b)
 - internal coefficient of friction (μ_{int}).

- pore pressure (P_f)
- thickness, sedimentation, erosion (effect on: σ_n , τ , ρ , α , β)

Besides the known factors, various analog and numerical studies (e.g., Sassi et al., 1993; Lohrmann et al., 2003) have distinguished further factors influencing the mechanics and the evolution of accretionary wedges, such as:

- additional factors
 - preexisting heterogeneities and material compaction
 - internal variations of the material.

In the following, the effect of these factors on the accretionary wedge evolution will be explained.

2.5.1 The role of geometrical factors

Plate dip angle (β)

One geometrical factor which has an important effect on the wedge evolution is the basal dip angle of the down-dipping plate. An accretionary wedge grows until the Critical Taper is reached. As the taper consists of the surface slope angle α and the dipping angle β , a change in β affects the whole wedge mechanics (Dahlen, 1990). Koyi and Vendeville (2003) performed a series of analog models shortened asymmetrically above a dipping frictional décollement. They found that the amount and the direction of the décollement dip strongly influences the geometry and the deformation process in the resulting wedge. An increasing basal dip angle of a décollement towards the hinterland leads to a larger wedge taper with a steeper and higher accreted wedge structure. Additionally, the wedge evolves shorter. This development is more pronounced if high basal friction acts at the décollement and reduced in case of low basal friction (Koyi and Vendeville, 2003).

2.5.2 The role of physical properties

Basal coefficient of friction μ_b

The Critical Taper theory shows that the basal coefficient of friction is one major factor determining the kinematics and mechanics of accreted wedges (μ_b ; e.g., Gutscher et al., 1998b; Hardy et al., 1998; Davis et al., 1983; Dahlen, 1984; Huiqi et al., 1992; Burbidge

and Braun, 2002). If the basal strength at the detachment increases by an increase in basal friction (μ_b) the stability fields will be changed. Tests under this topic have been conducted by Agarwal and Agarwal (2002). They increased the basal strength by testing different material at the base.

In Figure I-7a the effect of an increasing friction coefficient on the stability field is indicated by (contrary to the arrows). In this case, the stability field extends horizontally (extension of dip angle field) and narrows vertically (narrowing in slope angle field). Consequently, the taper angle increases and the wedge is more compressed while shortening (Fig. I-8).

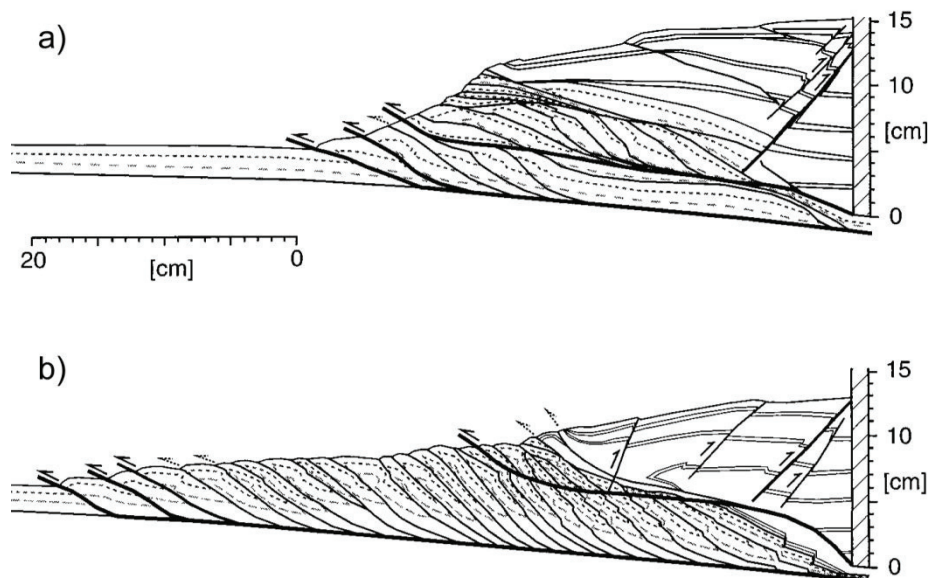


Fig. I-8: Wedge growing on high (a) and low (b) basal friction décollement (modified after Gutscher et al., 1996).

This has been shown by e.g., Dahlen et al. (1984), Mulugeta (1988), Huiqi et al. (1992), Gutscher et al. (1996). The increase is accompanied by changes in the deformation style (e.g., dip angles of thrusts), which goes along with a rotation of the stress-field (Fig. I-6; Davis and Dahlen, 1983). The forethrusts reduce their dipping angles whereas the conjugated backthrusts increase their dipping angles. This asymmetrical thrust formation can be termed as foreland-vergent with a steep σ_1 -axis dipping toward the foreland (large Ψ_b , Fig. I-6; Hafner, 1951; Chapple, 1978; Mandl and Shippam, 1981; Davis and Engelder, 1985). In this case, the material is accreted and far transported along the flat forethrusts

with large offsets and steep dipping backthrusts with low offsets (Fig. I-8a, I-9a). For a high basal strength an episodic variation between frontal and basal accretion at the frontal wedge part is observed (Gutscher et al., 1996).

In contrast, if the basal strength of the detachment decreases a reduction of the lower critical taper angle and, simultaneously, an increase of the upper angle occurs (Fig. I-7a, direction of arrows). This decrease in the lower critical taper is shown by several analog and numerical models (Fig. I-8b; Mulugeta, 1988; Willett, 1992; Lallemand et al., 1994; Gutscher et al., 1998a; Nieuwland et al., 2000; Burbidge and Braun, 2002; Koyi and Vendeville, 2003; Teixell and Koyi, 2003; Naylor et al., 2005; Nilfouroushan et al., 2008).

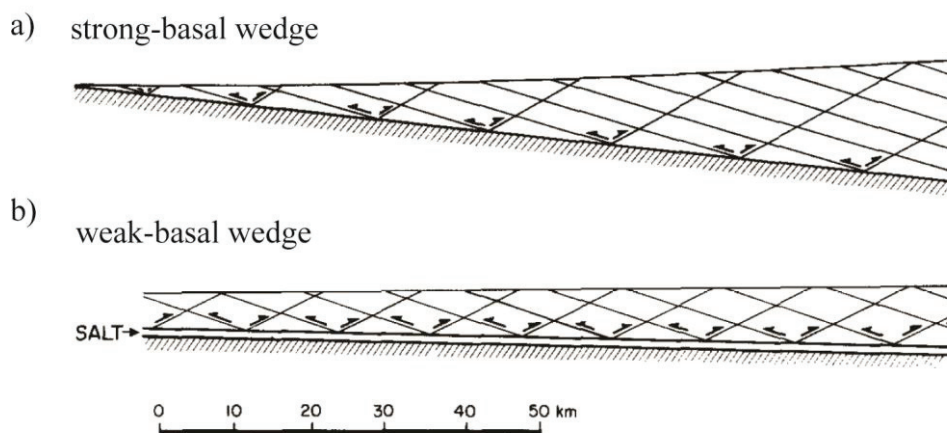


Fig. I-9: Slip plane orientation on a weak and a strong-basal décollement (modified after Davis and Engelder, 1985).

The forethrust evolve steeper whereas a flatter evolution of backthrusts occurs (Davis and Engelder, 1985; Huiqi et al., 1992). Consequently, forethrusts (δ_f) and backthrusts (δ_b) develop more symmetrically (Fig. I-9b). Material is slightly uplifted and accreted along steep dipping forethrusts with lower offsets and mean stress σ_1 (small Ψ_b) evolves shallow (Fig. I-8b). Backward thrusts get more dominant and more abundant as shown by Huiqi et al. (1992), Lallemand et al. (1994) and Mulugeta (1988).

Internal coefficient of friction (μ_{int})

The Critical Taper theory also shows the importance of the internal coefficient of friction (μ_{int}). An increase in the coefficient of friction, leads to a vertical extension of the stability field (Fig. I-7b, contrary to arrows). Such a variation results in a similar effect as a relative decrease in basal strength does (Davis et al, 1983). Thereby, the lower critical surface slope

is reduced and the higher critical surface slope increases (Fig. I-7b). In this case, the wedge taper decreases as a result of the internal material strengthening while the décollement strength remains constant. Simultaneously, the fore- and backthrusts evolve more symmetrically, foreland-vergence reduces and the main stress σ_1 evolves flatter. A decrease in bulk strength reduces the stability field for critical wedges and the wedge shows the opposite evolution (Fig. I-7b, direction of arrows). In addition, the thrust system adapts and evolves more asymmetrically, as a result of the reduced strength contrast between the internal material and the décollement.

Pore pressure factor (P_f)

Another factor influencing the material strength is the pore pressures and its variations. Strayer et al. (2001) studied the development of thrusts by coupling a fluid flow model with a compressional finite-element model. In their model the basal friction is reduced and failure is facilitated due to the presence of water within a wedge. Additionally, fluids are more focussed within faults zones. Also Cobbold et al. (2001) as well as Mourgues and Cobbold (2006) dealt with this question. They used inclusion of fluids in analog sand models by using compressed air as a pore fluid.

Thickness, sedimentation and erosion (effect on: σ_n , τ , ρ , α , β)

The thicknesses of the incoming 'sediment' layers as well as the variations in thickness due to erosion and sedimentation processes have an important influence on the normal stress (σ_n), shear stress (τ) and on the wedge mechanics (e.g., Vendeville and Cobbold, 1988; Huiqi et al., 1992; Gutscher et al., 1998a; Bonnet et al., 2007; Konstantinovskaya and Malavieille, 2011).

Huiqi et al. (1992) tested different initial thicknesses of the incoming layer of an accretionary wedge. They found that a decrease in the initial thickness results in a decrease of the thrust spacing and an increase of the critical taper (Fig. I-10, e \rightarrow a). This confirms with studies of Marshak and Wilkerson (1992) as well as Panian and Wiltschko (2007).

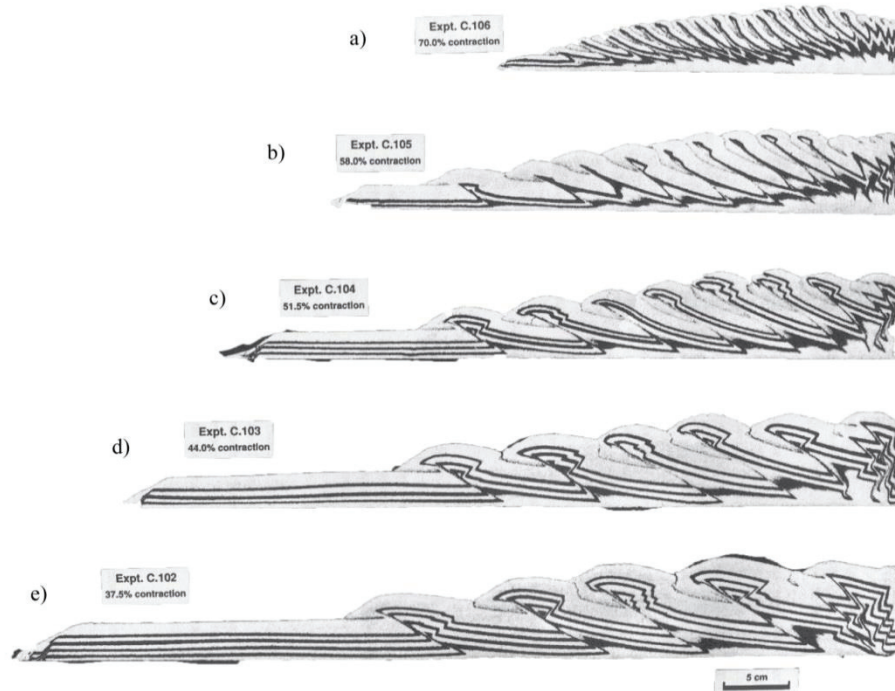


Fig. I-10: Sand models of five different initial thicknesses. a) 3 cm model, b) 2.5 cm model, c) 2 cm model, d) 1.5 cm model, e) 1 cm model (modified after Huiqi et al, 1992).

To understand the effect of erosion and sedimentation various analog and numerical models have been undertaken (e.g., Mulugeta and Koyi, 1987; Willett, 1999; Persson and Sokoutis, 2002; Konstantinovskaya and Malavieille, 2005; Hoth et al., 2006; Stockmal et al., 2007; Selzer et al., 2007; Bigi et al., 2010; Cruz et al., 2010). If material is removed at the surface due to erosion or added due to high sedimentation rates the taper angles change (increase or decrease of α). To maintain the critical taper, a rearrangement of the thrust system occurs and new thrusts evolve or older thrusts get re- or deactivated (Koons, 1990; Beaumont et al., 1992).

Erosional processes reduce the stress at the base and, consequently, can be seen as a weakening process in which new thrusts evolve more localized (e.g., Willett, 1999; Malavieille and Konstantinovskaya, 2010). In contrast, sedimentation can be seen as a strengthening process (Beaumont et al., 1992, Selzer et al., 2007) which has a delocalizing effect on the deformation. This material strengthening influences the internal stresses resulting from an increase in material compaction and density (ρ), what further influences the wedge mechanics as analyzed by Zhao et al. (1986) and Lohrmann et al. (2003) and is discussed in the next section.

Furthermore, thinning or thickening can lead to an isostatic response resulting in an exhumation or subsidence of the wedge material. Konstantinovskaya and Malavieille (2005) found that the exhumation due to erosion is controlled by the thrust systems and further by the basal friction values.

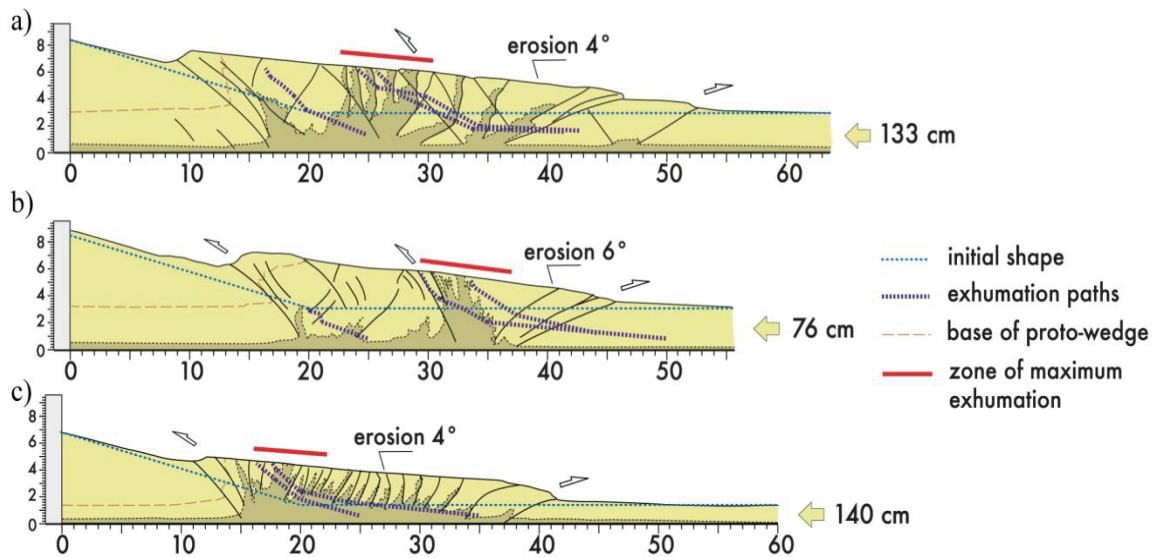


Fig. I-11: Sand models with erosion at 4° (a) and 6° (b, c) with reduced incoming sediment thickness. Thin blue line shows the initial shape. Thick blue line shows the material paths through the wedge. Shortening (in cm) is depicted at the end of each experiment (modified after Konstantinovskaya and Malavieille, 2005).

In Figure I-11 their results for a low basal friction wedge is displayed. The material is exhumed along a group of high-angle thrusts (Fig. I-3b). The flat forethrusts become increasingly steeper until they evolve nearly vertically in the central part of the wedge while ongoing shortening. An increase of the basal shear plane reduced the wedge length about 12-13% (Fig I-3c) whereas a decrease of the incoming ‘sediment’ thickness has more an influence on the thrust spacing (Fig. I-11c).

2.5.3 Additional factors beside the Critical Taper theory

Besides the geometrical and physical properties, further factors influencing this strength have been detected in different studies (e.g., Lohrmann et al., 2003; Anthony and Marone, 2005).

Material compaction and preexisting heterogeneities

The strength of the internal material is influenced by the material compaction or pre-existing heterogeneities (e.g., Zhao et al., 1986; Sassi et al., 1993; Strayer et al., 2001; Bonini, 2003; Smit et al., 2003; Selzer et al., 2007). While material gets incorporated into the wedge or material is added on top due to sedimentation it is compacted. In these compacted regions, the internal strength increases locally and reduces the critical taper angle (Zhao et al., 1986). In natural settings an increase of cohesion would be expected and the wedge would evolve in a convex shape. Nevertheless, also in case of granular materials a compaction and a convex shape has been observed (Lohrmann et al., 2003; Kopp and Kukowski, 2003; Miyakawa et al., 2010). These authors concluded that a convex shape may result from an increase in the bulk strength in the inward direction of the frontal wedge.

Pre-existing heterogeneities as shown by e.g., implemented pre-cut faults in a scaled sandbox experiment change the internal strength and result in localization of later thrusts and, hence, influences the thrust style (Sassi et al., 1993). Lohrmann et al. (2003) confirmed with this result and showed that the strength of a brittle material is controlled by its pre-existing heterogeneities which are often thrusts or faults along which stable gliding occurs. They showed that the bulk strength of the evolving critical wedge is mainly controlled by the frictional strength of the weakest and/or already thrust regions, as at these positions stable sliding occurs.

Internal variations of the material

Kukowski et al. (2002), Selzer et al., (2007) and Konstantinovskaya and Malavieille (2011) varied the internal material strength by embedding one or several low friction layers within the incoming sediment section. These layers act weaker than the preexisting basal décollement and, hence, can be activated as new mid-level décollement (Fig. I-12; Kukowski et al., 2002). Often these models show an alternate activation between the internal weak layer and the base. The activation of two décollements allows for a simultaneous occurrence of frontal and basal accretion and the evolution of flat-ramp shear zone geometries and duplex structures (Fig. I-2, I-9, I-12). The latter ones can either be stacked laterally as hinterland-/ foreland-duplex or vertically as an antiformal stack (Mitra and Boyer, 1986). In which form they are stacked depends on the strength of the embedded

material and on the strength of the décollement (Couzens-Schulz et al., 2003; Wenk and Huhn, 2013b).

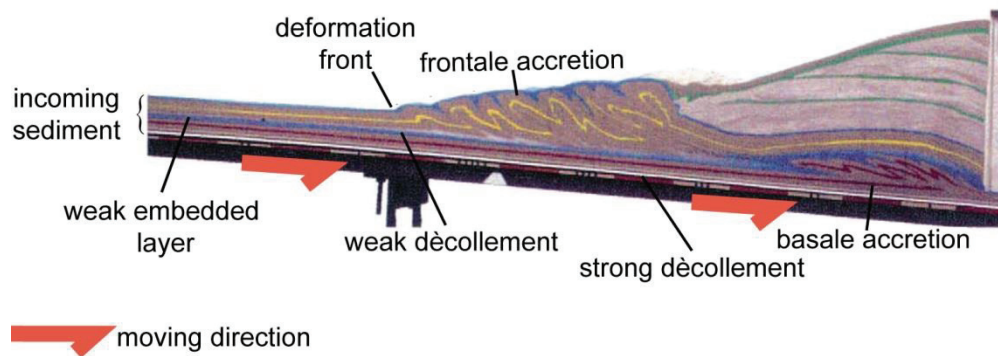


Fig. I-12: Analog sandbox wedge growing by frontal and basal accretion as a result of a weak mid-level décollement and a strong basal décollement (modified after Kukowski et al., 2002).

3. Mechanics and dynamics of non-MC accretionary wedges

3.1 Creep behavior of rocks

Evaporites such as halite always contain some brine. Mechanical tests have shown that the material has a high ductility and reacts very weak already at low temperature and low pressure conditions occurring in shallow depths (Fig. I-13; Urai et al., 1986; Carter et al., 1982; Carter and Hansen, 1983; Davis and Engelder, 1987; Weijermars et al., 1993).

Other evaporites such as gypsum and anhydrite behave brittle at shallow depth. The transformation from brittle to ductile occurs during burial at depth >1000 m (Shearman, 1983) or at temperatures from 75° to 125°C and from 1.6 to 2.5 km depth (Müller et al., 1981). Consequently, halite acts as an extremely weak layer but also other evaporites such as anhydrite are weak and show a viscous creep behavior, but to a slight lesser degree (Davis and Engelder, 1985).

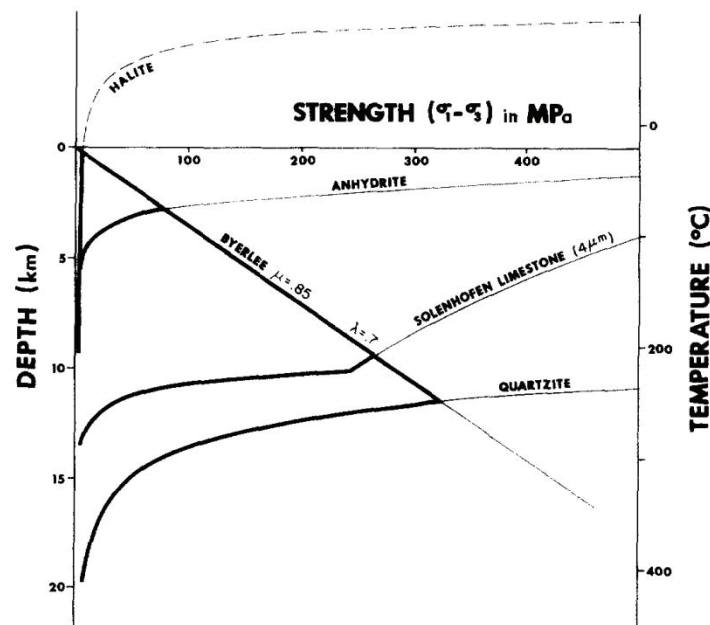


Fig. I-13: Strength versus depth of various rock types (modified after Davis and Engelder, 1985).

A typical creep curve (Fig. I-14) has three different sections: the primary (transient), the secondary (steady-state) and the tertiary phase of creep (Jeramic, 1994). After application of the load, an instantaneous elastic strain is acting followed by the primary creep phase, which is recoverable on unloading (Carter and Hansen, 1983).

The primary creep is followed by the secondary creep phase. Here permanent deformation takes place. Depending on the stress level the secondary creep will be displaced by accelerated creep of the tertiary phase leading to failure (Carter and Hansen, 1983). In nature, the true steady-state creep is not present in hard rocks (Dusseault and Fordham, 1993).

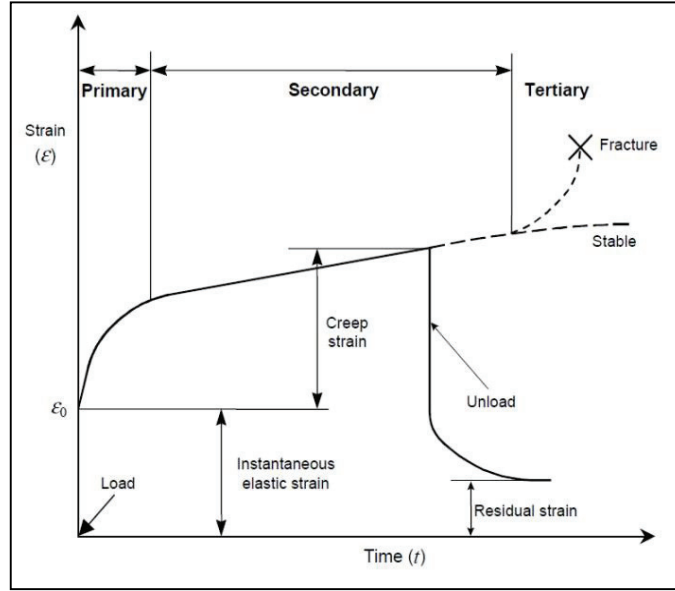


Fig. I-14: Theoretical time-strain curve at constant stress
(modified after Lama and Vutukuri, 1978).

To calculate the total strain ($\varepsilon_{total}(t)$) for creep the following equation can be used (e.g., Carter et al., 1993):

$$\varepsilon_{total}(t) = \varepsilon_0 + \varepsilon_p(t) + \dot{\varepsilon}_{ss}t + \varepsilon_r(t) \quad (\text{eq. I-14})$$

where t is time, ε_0 is the instantaneous elastic strain, $\varepsilon_p(t)$ is a function expressing the slowly creep of the primary phase, $\dot{\varepsilon}_{ss}t$ is the rate of steady-state creep and $\varepsilon_r(t)$ the rate of the tertiary phase.

Most empirical laws, which have been used to calculate the primary creep $\varepsilon_p(t)$, can be expressed in the form:

$$\varepsilon_p(t) = Bt^{-m} \quad (0 \leq m \leq 1) \quad (\text{eq. I-15})$$

where B is a constant, which describes the strain after $t=1$. For $m = 1$, the equation is the logarithmic creep law (Robertson, 1964).

For the secondary or steady state creep $\dot{\epsilon}_{ss}t$ of rocks, the following law is commonly used:

$$\dot{\epsilon}_{ss}t = A(\sigma_1 - \sigma_2)^n e^{-\frac{Q}{RT}} \quad (\text{eq. I-16})$$

where A is a constant, $(\sigma_1 - \sigma_2)$ is the maximal and minimal stress, R is the universal gas constant ($R=8.31 \text{ JK}^{-1}\text{mole}^{-1}$), T is the temperature and Q is the creep activating energy.

For the tertiary creep phase until now no accepted fundamental equation has been found describing this phases (Carter and Hansen, 1983). As time (t) is evolved in the solutions a rheology simulating creep is in contrast to the Mohr Coulomb criterion *time-dependent*.

3.2 Natural wedges and wedge models with viscous layers

Some accretionary wedges or fold-and-thrust belts grow on top of evaporitic detachment such as the Southern Jura (Fig. I-15a; Laubscher, 1977; Philippe et al., 1996), the Pakistan Salt Range (Fig. I-15b; Cotton and Koyi, 2000), the Parry Islands, Arctic Canada (Fig. I-15c, Harrison, 1995), the central Appalachian (Davis and Engelder, 1985, 1987), the Mediterranean Ridge (Reston et al., 2002a; see Sec. 3.3) and the Cascadian margin (Fig. I-15d; Gutscher et al., 2001).

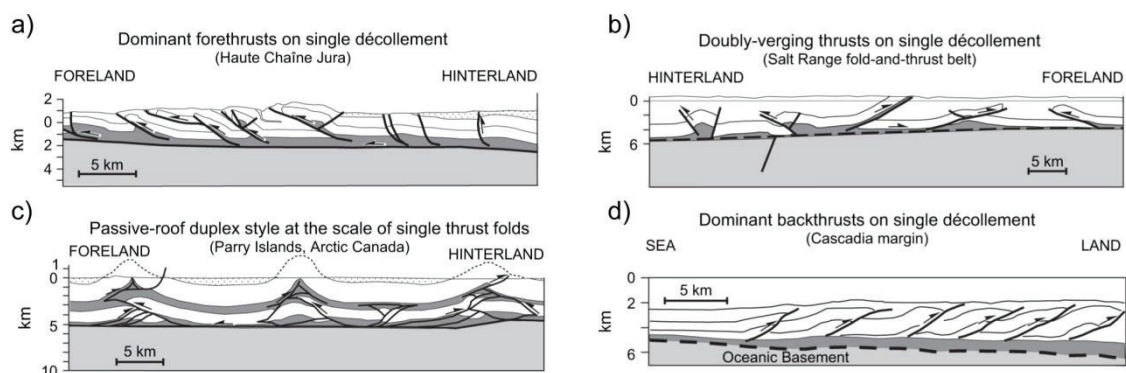


Fig. I-15: Fold-and-thrust belts or accretionary wedges at (a) Haute Chaîne Jura, (b) Salt Range, Pakistan, (c) Parry Island, Arctic Canada, (d) Cascadian Margin (modified after Bonini, 2007).

These wedges or fold-and-thrust belts growing on viscous décollement or with embedded viscous layer do not evolve in accordance with the Critical Taper theory. They show a different mechanical behavior with characteristic features as the viscous material reacts in contrast to the brittle material mechanically weak (e.g., Chapple, 1978; Davis and Engelder, 1985, 1987; Letouzey et al., 1995). One of these features is a faster and further propagation of the deformation front and a reduced taper angle as a result of the reduced basal coupling (e.g., Geiser, 1988; Macedo and Marshak, 1999). All known fold-and-thrust belts, which are located on top of evaporites, maintain a much narrower cross-sectional taper of 1° or less compared with pure brittle wedges or belts (Davis and Engelder, 1987). Additionally, the mechanical preference for the evolution of foreland-vergent thrusts is often reduced. Instead, a tendency for an increasing appearance of hinterland-vergent structures (Fig. I-15d) or the formation of structures without a preferred vergence can be distinguished (Fig. I-15b; Davis and Engelder, 1985). The occurrence of symmetrical fore- and backthrusts are very characteristically on top of a viscous décollement which results from the evolution of pop-up structures (e.g., Brun and Fort, 2004).

Furthermore, dually-vergence occurs within the deformed incoming material. Additionally, such wedges show an anomalous width of the folded zone which compromises symmetrical folds with broad synclines or box folds as occurring in the Jura Mountains (Fig. I-15a; Laubscher, 1972). Folds growing on top of evaporites have commonly a long wavelength of 100 km or more and sharp anticlines occur due to the weak base. One example for an accretionary wedge with an embedded weak evaporitic layer is the Mediterranean Ridge. In the next section a short introduction into this accretionary is given, which serves as a case study for Chapter V.

3.3 Case study: Mediterranean ridge complex

The Mediterranean Ridge complex at the Hellenic subduction zone is located at the plate boundary between the African and the Eurasian plates (Fig. I-16(I); e.g., Taymaz et al., 1990; Bohnhoff et al., 2001). This accretionary wedge is ~1200 km wide (EW-direction) and around 300-400 km long (NS-direction). The incoming sediment sequence consists of five stratigraphic layers (de Voogd et al., 1993; Chaumillon and Mascle, 1995; Chaumillon and Mascle, 1997; Polonia et al., 2002; Reston et al. 2002b). On top of the basement which is presumed to be oceanic crust, Mesozoic carbonates are located. This layer is overlain by

clastics from late Mesozoic to Tertiary age such as terrigenous siltstones, sandstones and shales which have a thickness of 1600 m in the Ionian domain and 4200 m in the Levantine domain. On top the Messinian evaporites are deposited at various positions in the subduction zone, resulting from the Messinian desiccation of the Mediterranean Sea (Hsü et al., 1973; Tay et al., 2002). The evaporites consist of gypsum/anhydrite, massive carbonates and marls as well as halite and potassium (Shipboard Scientific Staff DSDP Leg 13, 1973a, 1973b, 1973c; Kastens et al., 1992).

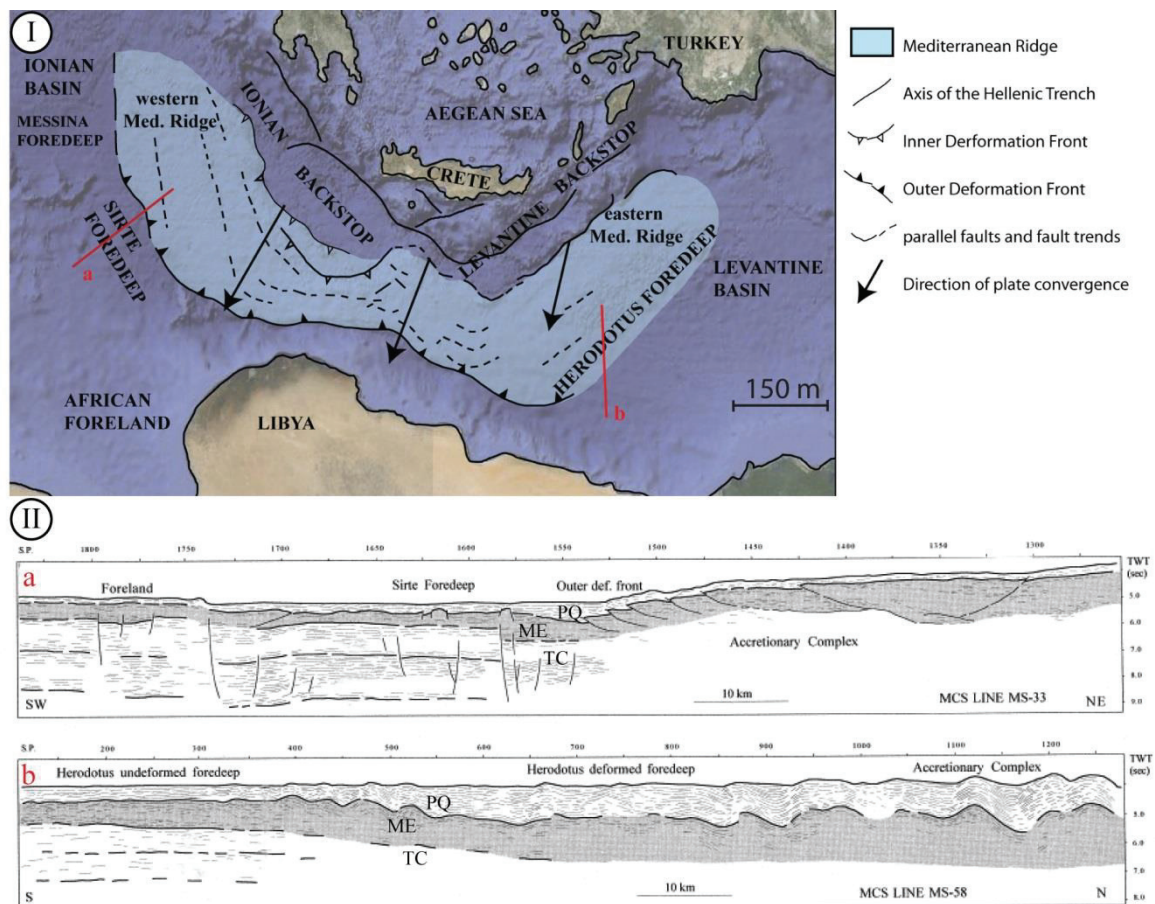


Fig. I-16: I) Location map of the Mediterranean Ridge with structures, deformation front and direction of plate convergence. Additionally the positions of two seismic section (a and b) are shown; II) seismic lines of the western (a) and eastern (b) Mediterranean Ridge (modified after Belderson et al., 1981; Le Pichon et al., 1995; Polonia et al., 2002)

Explorations wells in the marginal areas of the Nil Delta indicate that anhydrite is the prevailing Messinian mineral (Abdel Aal et al., 2000). The Messinian evaporites reach a thickness of 1000 m in the Ionian domain and around 2500 m in the Levantine domain.

The strata is closed by the Plio-Quaternary cover which is thin formed at the Ionian domain (200-400 m) and well formed in the Levantine domain (3000 m) due to high sediment input of the Nile river (Chaumillon et al., 1996; Chaumillon et al., 1997; Kastens et al., 1992). The Plio-Quaternary deposits are composed of pelagic marl, turbiditic mud and silt as well as occasional sapropels and ash-layers (Parisi et al., 1987).

The deposited evaporites have an important influence on the mechanics of the accretionary wedge (Tay et al., 2002). At the outer Mediterranean Ridge the main detachment is located either within the Messinian evaporites (Mascle et al., 1994; Mascle and Chaumillon, 1998; Polonia et al., 2002) or underneath this layer (Reston et al., 2002a). This detachment becomes gradually deeper, below the inner parts where it is located on top of the Mesozoic carbonates along clay-rich horizons (Reston et al., 2002a). Consequently, it can be inferred that the Messinian evaporites represent the weakest horizon in the deep basins of the eastern Mediterranean Ridge.

The structural style of the Mediterranean Ridge varies along the plate boundary. In the central part of the Mediterranean Ridge the oceanic plate has been nearly completely subducted and a continent-continent collision has been initiated. As a result also the sedimentary package has been uplifted to shallowest water depths which prevented an accumulation of the evaporites. In contrast, at the western Mediterranean Ridge still subduction takes place and the Plio-Quaternary cover is added to the wedge structure by imbrication. In this area the incoming sediment sequence is mainly deformed along landward-dipping forethrusts. As a result, an anxious morphology with small breaks and offsets occurs due to thrusting in the Messinian evaporites and the surface slope angle is 1.8° (Le Pichon et al., 1982; Ryan et al., 1982; Chaumillon et al., 1996; Polonia et al., 2002).

In contrast to the western Mediterranean Ridge, the eastern part shortens due to the evolution of gentle asymmetrically folds of both the Messinian evaporitic sequence and the overlying Pliocene-Quaternary terrigenous cover. In this area no abrupt deformations occur or mark the transition between the abyssal plain and the outer accretionary wedge. These folds evolve symmetrical along the southern edge of the Mediterranean Ridge but with seaward vergent thrusts in the north. Many asymmetrical folds are probably related to thrusts dipping to the north and splaying from the sole thrust located at the base of the Messinian evaporites (Chaumillon and Mascle, 1997; Polonia et al. 2002).

The different structural styles between the western and the eastern Mediterranean Ridge are accompanied by different factors such as an irregular shape of the converging plate boundaries, varying angle of convergence or lateral changes in the backstop geometry which is tapered and trenchward dipping (Finetti, 1976; Kastens, 1991; Kastens et al., 1992; Byrne et al., 1993, Le Pichon et al., 1995; Camerlenghi, 1998; Reston et al., 2002a, b).

A further important factor that varies along the subduction zone is the thickness and lithology of the incoming sedimentary sequence, what has been detected as a major factor controlling the structural style (Chaumillon and Mascle, 1995; Polonia et al., 2002). Hence, the structural evolution is influenced by the variable thickness and lateral extent of the Plio-Quaternary cover and the evaporites resulting from the Messinian (late Miocene) desiccation of the Mediterranean Sea (Hsü et al., 1973).

3.4 Simulation of non-Mohr-Coulomb accretionary wedges

3.4.1 'Sandbox' wedges growing above basal viscous décollements

Davis and Engelder (1985) tried to explain the characteristic structures of evaporitic wedges by the use of a brittle wedge growing on a zero friction décollement in accordance with the Critical Taper theory. This approach of a low strength brittle décollement explains the extremely small surface slope angles and pop-up structures (Fig. I-17a), but it is not able to explain the different deformation forms occurring in these extremely weak basal wedges such as the dually-vergence, spacing and folding (Smit et al., 2003; Fig. I-17b). To better reconstruct the characteristic deformation forms in the following viscous or ductile materials (e.g., silicon layer) are incorporated into the different numerical and analog sandbox experiments (e.g., Bonini 2001, 2007; Costa and Vendeville, 2002; Smit et al., 2003).



Fig. I-17: Analog sandbox experiment with accretionary wedges growing above (a) a brittle glass bead layer and (b) a viscous silicon layer (Dooley, 2009; http://www.ig.utexas.edu/jsg/earth_processes/)

Similar to the observations at natural wedges with viscous layer, analog models growing on ductile or viscous décollement show a gentle taper, an increasing backward and decreasing foreland-vergence, a wider thrust-spacing and the coexistence of both forward and backward thrusts above a viscous décollement in contrast to a brittle décollement (Fig. I-17, I-18; Cotton and Koyi, 2000; Bahroudi and Koyi, 2003). Additionally, master backthrusts with conjugated transient forethrusts occur more often in brittle/viscous model than in pure brittle models. In case of an equally importance of fore- and backthrusts, pop-up structures appear (Fig. I-18; e.g., Cotton and Koyi, 2000). Besides thrusting, the evolution of fold (e.g., box fold) with kink-band is often observed.

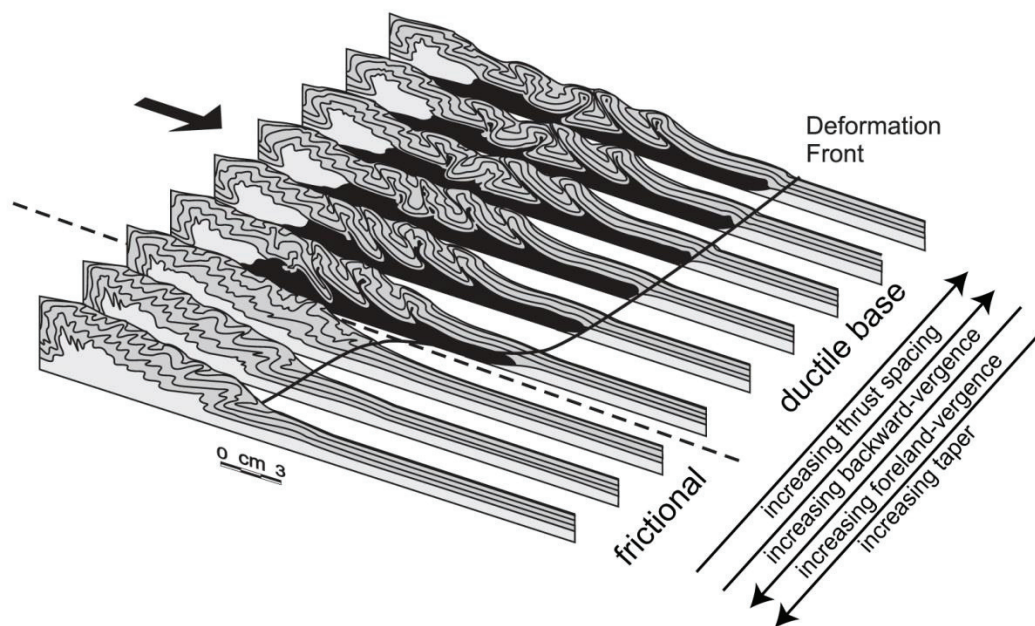


Fig. I-18: Line drawing from vertical cross section of analog sandbox wedge growing above a partly frictional and partly ductile base (modified after Cotton and Koyi, 2000)

Additionally, it has been shown that in contrast to pure brittle experiments in case of weak viscous décollements a non-frontward sequence of thrust development occurs or the evolution of many structures can take place simultaneously (Fig. I-19; Cotton and Koyi, 2000; Costa and Vendeville, 2002; Bonini, 2007).

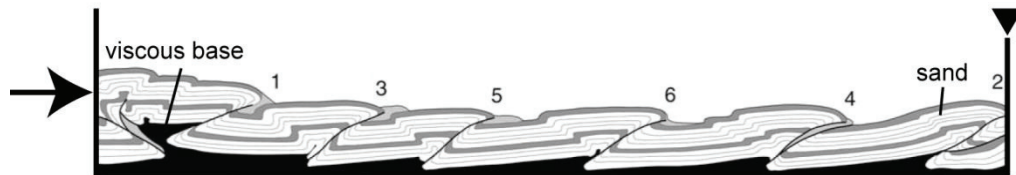


Fig. I-19: Line drawing of vertical cross section from analog sandbox compressed from the left side against a fixed box wall. Numbers depict the order in which the box folds appear (Costa and Vendeville, 2002)

All these characteristics depend on the brittle/ductile coupling (Smit et al., 2003) or the absolute value of décollement strength in relation to the brittle overburden strength (Gutscher et al., 2001; Costa and Vendeville, 2002; Smit et al., 2003). Following Smit et al. (2003) the brittle/ductile (BD) coupling is a function of the magnitude and of the stress ratio between the brittle and the ductile layer. Consequently, a strong BD coupling results in frontward-vergent sequences of narrow spaced thrusts and the resulting wedge evolves similar to a purely frictional wedge. This is also shown by Wenk and Huhn (2013b, Chapter IV). In contrast, an intermediate coupling leads to a thrust evolution which oscillates frontward and backward, whereas in case of a weak BD coupling mainly backward thrusting occurs. Smit et al. (2003) assumed further that the BD coupling is a function of the thickness and the frictional properties of the brittle layers as well as of the viscosity and the shear strain rate in a ductile layer.

Also Bonini (2007) examined the effect of very low basal friction on the relative strength between the brittle overburden and the viscous décollement (brittle-ductile coupling). He shows that the absolute value of shear stress defines the evolution of hinterland- and foreland-verging thrusts. Mainly, the orientation of the stress field, the basal friction and the décollement offset influences the deformation structures and the thrust vergence. Finally, he found that these factors could trigger the dominant backthrust-vergence at the Cascadia margin (Fig. I-15d).

In case of a décollement composed of different materials, the evolving structures are more complex. Bahroudi and Koyi (2003a) undertook a group of experiments in which a sand-layer overlays a partly viscous and partly brittle layer. Additionally, different thicknesses of the viscosity detachment were tested in order to explain the Hormuz salt and the Zagros fold and thrust belt (Pakistan, Mukherjee et al., 2010). Model results confirm with previous studies in which a gentle tapered wedge grows by forward- and backward thrusts on the viscous décollement and a steep wedge of imbricated thrusts evolve above a frictional décollement (Bahroudi and Koyi, 2003b). Between areas with ductile and frictional décollements an inflection occurs and the highest topography is observed.

3.4.2 'Sandbox' wedges with embedded viscous layers

Experiments have been undertaken to test the wedge evolution in case of a brittle incoming sediment sequence with an embedded viscous layer (Bonini, 2001, 2003, 2007; Couzens-Schulz et al., 2003). In these experiments besides the stronger basal décollement a mid-level décollement can evolve along the weak embedded layer (e.g. Bonini, 2007). This model approach is very helpful to study the evolution of duplex systems which are controlled by the coupling between the décollement layer and the roof sequence (Couzens-Schulz et al., 2003; Fig. I-20).

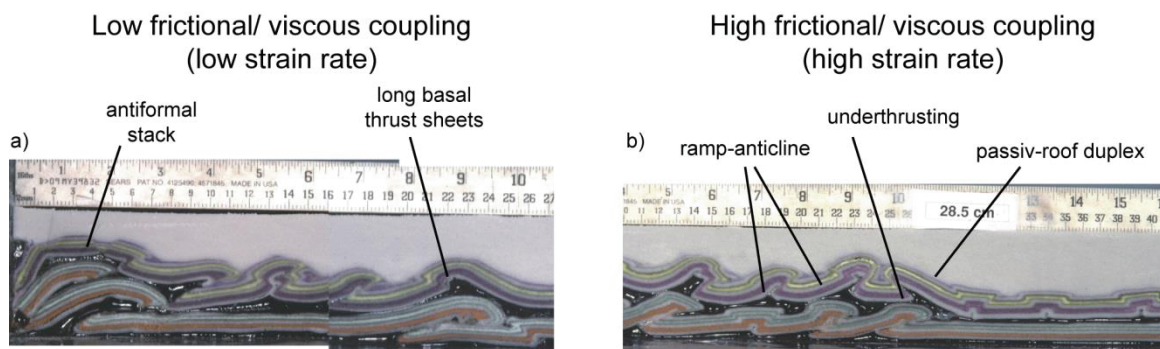


Fig. I-20: Analog wedge experiment above (a) a low frictional and (b) a high frictional décollement (modified after Couzens-Schulz et al., 2003).

It has been shown that the shear stress ratio and the absolute values between viscous layer and the upper as well as the lower brittle layer defines the deformation pattern and the efficiency of the décollement (e.g., Nalpas and Brun, 1993; Bonini, 2001). These parameters are controlled by different factors such as the strain rate, the viscosity and the

thickness ration between the brittle and the viscous layers (Couzens-Schulz et al., 2003; Bonini, 2003; Wenk and Huhn, *subm.*).

Bonini (2003) embedded a weak silicon layer within a brittle incoming sediment sequence. He observed that for a low-viscosity décollement the deformation is localized along a single fold with a negligible propagation. In contrast for a high viscosity décollement a higher horizontal propagation is observed. Therefore, the decoupling of an upper and a lower layer is more efficient if a strong décollement (high viscosity, high strain rate) is used, instead of a weak (low viscosity, low strain rate).

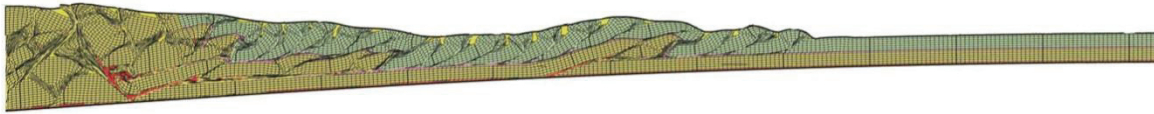
The strength ratios between the layers also define the structures in the lower brittle layer. Here the development of active or passive-roof duplex, translation of individual thrust blocks and spacing of thrust ramps (antiformal stack or individually space ramp-anticlines) has been observed (Couzens-Schulz et al., 2003; Bonini, 2007). Couzens-Schulz et al., (2003) varied the strength of the viscous décollement using different shortening rates. A low convergence rate leads to an effective decoupling of the upper and lower brittle layer while a deformation of the upper layer takes place in front of the stacked floor units. In addition, an antiformal-stacked duplex occurs due long thrust sheets (Fig. I-20a). In contrast, if the convergence rate is increased also the coupling is increased and the upper sequence is underthrust forming a passive roof duplex (Fig. I-20b; Couzens-Schulz et al., 2003). In this case, displacements are short and an individual spaced ramp-anticline evolves. Furthermore, it is found that the thickness ratio of the embedded and the upper brittle layer defines the evolution of the passive-roof-duplex and the degree of the outward folding propagation (Bonini, 2001).

Besides analog experiments also numerical ‘sandbox’ models with the Finite Element Method have been undertaken (e.g., Selzer et al., 2007; Stockmal et al., 2007). Selzer et al. (2007) investigated the sensitivity of active thrust zones to surface processes and strain softening. They found that erosion enhances material transport and slows down the forward progradation of the deformation front. Additionally, an embedded viscous layer of regular spaced intrusions facilitates and focuses the internal deformations. This has an effect on thrust dip, vergence and reactivation of previous active thrusts.

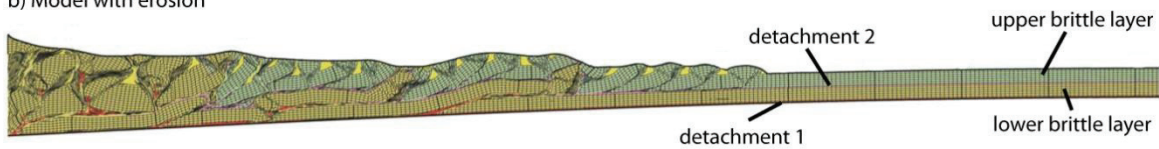
Stockmal et al. (2007) embedded surface processes in a numerical Finite Element study of a two-layer model with strain softening. They found that in contrast to the basic model

without surface processes (Fig. I-21a) the syndeformational surface erosion does not significantly change the structural system, but a slightly enhancement in the evolution of pop-up structures in the upper layer can be distinguished (Fig. I-21b). Additionally, besides erosion also sedimentation has been implemented (Fig. I-21c). In this model with a rapid filling of the foreland basins, piggy-back basins develop by a sequential accretion of the incoming material. From these results Stockmal et al. (2007) inferred that a wedge has no need to thicken, as the critical wedge conditions are achieved due to the sedimentation.

a) Model without erosion or sedimentation



b) Model with erosion



c) Model with erosion and sedimentation

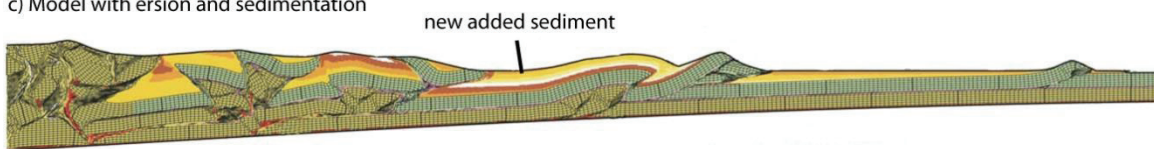


Fig. I-21: Numerical experiments with two brittle layer incorporating surface processes (without and with erosion or sedimentation; modified after Stockmal et al., 2007).

Chapter II: Motivation and Objectives of this study

Since active margins and forearcs are often highly populated areas, understanding the mechanisms of active margins has been of scientific interest for decades. In these regions frequently geohazards such as tsunamis, earthquakes, volcanic eruptions and mass wasting events occur. Along such subduction zones accretionary wedges grow depending on the physical material properties of the décollement and the incoming sediment section, as well as geometrical properties and further factors, which have been found in various ‘sandbox’ experiments (see Sec. 2.4).

Various analog and numerical ‘sandbox’ experiments have been undertaken with the aim to understand the deformation processes occurring along these active margins (e.g., Mulugeta, 1988; Huiqi et al., 1992; Saltzer and Pollard, 1992; Lallemand et al., 1994; Burbidge and Braun, 2002). Some of these studies use high and low frictional Mohr Coulomb materials (e.g., sand, glass beads) to simulate different rocks of the upper crust and associated deformation processes (e.g., Kukowski et al., 2002; see Sec. 2). These settings allow for reproduction and analysis of the mechanics in pure brittle accretionary wedges. Nevertheless, as mentioned in Sec. 3, in some cases, the upper crust in nature comprises not just brittle sand with large strains, but also weak viscous evaporites, which show a different rheological behavior. If such material is involved in the accretionary process of a wedge structure, a brittle rheology is not sufficient for the simulation (e.g., Platt, 2000). In some analog experiments a more natural behavior was achieved by incorporating a viscous or ductile silicone layer, which gave insight into the processes occurring within accretionary wedges growing on evaporitic décollements. However, analog models are still limited in their property range and analysis techniques. For example, an exact material tracking of single particles is not possible (e.g., Adam et al., 2005). Numerical methods, such as the Finite Element Method (FEM), are much more flexible in property calibration, but simulations of movements along long distances are still complicated.

The first aim of this thesis is to develop and evaluate a numerical method in order to study the evolution of accretionary wedges that incorporate different rheologies. Our requirements for the simulation are, amongst others, a flexible property calibration and a detailed tracking of particles and structures. Therefore, we chose the Discrete Element

Method (DEM) to build up numerical 2D experiments, which allow for simulation in a reasonable time frame and for comparisons with previous wedge studies (e.g. Naylor et al., 2005). Furthermore, this method allows for developing numerical ‘sandbox’ experiments consisting of single particles which can be displaced in any direction and, hence, displacements (e.g., thrusts) over long distances can easily be modeled. Additionally, it enables tracking of the single particles or particle groups over the whole wedge experiments. To be able to simulate a viscous material, besides brittle Mohr Coulomb material, the Burger’s model is implemented. This rheological model is suitable to simulate the creep behavior of natural rocks. This is the first time such a model has been used to study the evolution of an accretionary wedge growing on a viscoelastic-plastic décollement.

To gain a better understanding for the mechanics in heterogeneous accretionary wedges, a numerical Discrete Element model with an embedded viscoelastic-plastic layer is first developed and tested for different material properties (Chapter III and IV). Finally, the model is used for a numerical case study at the Mediterranean Ridge (Chapter V). In addition, we analyzed the effect of different deep crustal properties on upper crustal evolutions by using a double vergent wedge. The thesis consists of four manuscripts (Chapter III-V, Appendix I) that are currently in press, under review in international scientific journals/books, or in preparation. The questions that are answered in this study are:

- How much does the wedge mechanics depend on the rheology and what differences occur?
- How does an embedded viscoelastic-plastic layer with different viscosity values affect the mechanics, the thrust system and the mass transport pattern in an accretionary wedge?
- How connected are the different accretion mechanisms to the layer thicknesses (evaporites as well as the brittle cover layer) and does this improve the understanding of the structural system along the Mediterranean Ridge?

Chapter III:

In Chapter III, we compare the thrust system and the mechanics of two accretionary wedges. The wedges grow out of a brittle incoming ‘sediment’ sequence with an embedded low friction brittle layer in the first case and an embedded viscoelastic-plastic layer in the second case. Thereby, we test what differences occur and the importance of the use of a

viscoelastic-plastic material in a simulation of a viscous décollement. The scientific questions that are:

- How much do the wedge mechanics depend on the rheology?
- What differences can be observed if a weak embedded layer with an elasto-plastic versus a viscoelastic-plastic rheology is incorporated into the incoming material?

The manuscript entitled, 'MECHANICS IN HETEROGENEOUS ACCRETIONARY WEDGES – TO TEST IMPLEMENTED RHEOLOGIES' has been accepted and is currently in press in *Continuum and Distinct Element Numerical Modeling in Geomechanics, Proceedings of the 3rd International FLAC/DEM Symposium*, edited by H. Zhu, R. Hart, C. Detournay and M. Nelson, Hangzhou, China.

All numerical experiments, including their setup, their execution and their analysis have been carried out by myself. The Co-authors provided comments and edits on the manuscript.

Chapter IV:

Depending on the rheological type and on its properties a viscous material can act weaker or stronger. Therefore, the viscosity value that best simulates an evaporitic layer is tested. It is important to know the effect of different viscous materials on the structural evolution and the mass transport pattern through the accretionary wedge. The following scientific questions are answered in Chapter IV:

- How does an embedded viscoelastic-plastic layer affect the mechanics of an evolving accretionary wedge, particularly the thrust system and the mass transport pattern in the upper and lower brittle sediment layers?
- Can we identify a critical viscosity threshold to localize deformation along this viscoelastic-plastic layer generating a detachment?

The manuscript entitled, 'THE INFLUENCE OF AN EMBEDDED VISCOELASTIC-PLASTIC LAYER ON KINEMATICS AND MASS TRANSPORT PATTERN WITHIN ACCRETIONARY WEDGES' has been accepted and is currently in press for publication in *Tectonophysics* (<http://dx.doi.org/10.1016/j.tecto.2013.08.015>).

All numerical experiments, including their setup, their execution and their analysis have been carried out by myself. The Co-authors provided comments and edits on the manuscript.

Chapter V

For the last study, we chose the Mediterranean Ridge as a case study. The Mediterranean Sea is one of the most active seismic regions in Europe and understanding the processes along the subduction zone is an important task. In this area, the Mediterranean Ridge has evolved as an accretionary wedge due to the subduction process of the African plate. This accretionary wedge is very characteristic as it grows in its outer parts on Messinian evaporites whereas in its inner parts, it grows on older Mesozoic carbonates. Besides various factors influencing the accretionary process, one main characteristic feature of the Mediterranean Ridge is the varying thickness of the Messinian evaporites and the Plio-Quaternary cover (e.g., Polonia et al., 2002). To gain a better understanding how the layer thickness affects the structural development along the Mediterranean Ridge, we focused on the following scientific questions:

- How connected are the different accretion mechanisms to the layer thicknesses (evaporites as well as the brittle cover layer)?
- How far can this help us to increase the understanding for the Mediterranean Ridge mechanics?

The manuscript entitled, 'HOW DOES THE THICKNESS OF BOTH – AN EVAPORITE AND A COVER LAYER - INFLUENCE THE TECTONIC EVOLUTION OF AN ACCRETIONARY WEDGE? A CASE STUDY FOR THE MEDITERRANEAN RIDGE.' is in review for the Journal *Marine Geology*.

All numerical experiments, including their setup, their execution and their analysis have been carried out by myself. The Co-authors provided comments and edits on the manuscript.

Appendix I

The study aims to investigate the processes along a subduction zone where a double-vergent wedge evolves. The form of the wedge which belongs to the upper crust depends on deep crustal processes and properties such as indenter/backstop geometry or décollement strength. One method to examine the exhumation history of the upper crustal material is the apatite fission track (AFT) thermochronology. Therewith, the exhumation history of the upper crust can be deduced from time-temperature histories, which in turn result from inverse thermal history modeling of AFT cooling ages and the corresponding track length distributions. Herein, the statistical agreement of time-temperature paths with the observed data is determined. Nevertheless, only upper crustal processes and effects can be approached whereas underlying triggers are not easy to specify.

To gain a deeper understanding of how upper crustal processes are connected to deep crustal processes, a 2D numerical Discrete Element experiment is developed in which a wedge evolved under different initial conditions. In this study, the geometrical conditions of the indenter and the physical properties of the décollement are varied. From these experiments selected particle paths are extracted and used to derive synthetic AFT cooling ages by forward thermal history modeling. The combination of the DEM and the AFT analysis improve the understanding of the relationship between upper crustal exhumation paths and deep tectonic processes. Within this study the following questions are examined:

- How can we couple numerical ‘sandbox’ modeling and AFT thermochronology and is this technique suitable to enhance the understanding for geological processes?
- How do deep crustal properties, such as décollement friction and presence of an indenter influence evolution and deformation of the upper crust?

The manuscript entitled, ‘LINKING MECHANIC AND KINEMATIC PROPERTIES WITH UPPER CRUSTAL PROCESSES OF OROGENIC WEDGES I: COMBINING NUMERICAL ‘SANDBOX’ MODELING AND APATITE FISSION TRACK THERMOCHRONOLOGY.’ is in preparation for the *Journal of Geophysical Research (Solid Earth)*.

The Discrete Element numerical experiments, including parts of the setup, their execution and their analysis have been carried out by myself. I contributed to the writing of the manuscript as first author.

Additionally, this combined approach of a numerical DEM model and an AFT-analysis is also used for a case study in the Alps. The manuscript entitled, 'LINKING MECHANIC AND KINEMATIC PROPERTIES WITH UPPER CRUSTAL PROCESSES OF OROGENIC WEDGES II: AN EXAMPLE FROM THE EUROPEAN CENTRAL ALPS.' is in preparation for the *Journal of Geophysical Research (Solid Earth)*.

The Discrete Element numerical experiments, including parts of the setup, their execution and their analysis have been carried out by myself. I contributed to the writing of the manuscript as second author.

Chapter III: Rheology study

MECHANICS IN HETEROGENEOUS ACCRETIONARY WEDGES – TO TEST IMPLEMENTED RHEOLOGIES

Linda WENK¹ and Katrin HUHN¹

¹*MARUM – Center for Marine Environmental Sciences and Faculty of Geoscience, University of Bremen, Leobener Straße, D-28359 Bremen, Germany*

Keywords: accretionary wedge; mid-level décollement; numerical model; viscoelastic rheology; Burger's model

ABSTRACT

Various studies are undertaken gaining a better understanding of the kinematics of accretionary wedges with a heterogeneous sediment input. We used a numerical granular model approach to simulate a heterogeneous accreting sediment sequence consisting of three horizontal layers. Using this approach, the importance of the implemented rheology of the embedded layer is examined utilizing a low friction elasto-plastic, brittle (Mohr-Coulomb) layer versus a viscoelastic-plastic (Burger's) layer.

In both experiments, a stable mid-level detachment evolved in the vicinity of the mechanically weaker embedded layer causing the evolution of an accretionary prism. Hanging and underlying layers are always decoupled. The brittle wedge showed typical foreland-vergent thrusts with small thrust-spacing. In contrast, the wedge with a viscoelastic-plastic layer evolved wider extended, with reduced foreland-vergence, with larger thrust-spacing, with a faster deformation front propagation and with a flatter topography. Hence, a viscoelastic-plastic approach is more suitable to simulate the natural behavior of evaporitic décollements.

1. Introduction

Accretionary wedges growing in forearc regions form due to the compression of the incoming materials or sediments on top of a moving basal detachment – the so called décollement (Moore 1989). To understand the mechanics and kinematics of such systems, various studies with numerical and analog models have been made using Mohr Coulomb (MC) materials (Dahlen et al. 1984; Hardy et al., 1998; Gutscher et al., 1998a; Burbidge and Braun, 2002; Lohrmann et al., 2003; Naylor et al., 2005). These studies have successfully explained the evolution of homogeneous MC wedges based on the Critical Taper (CT) theory (Dahlen, 1984; Dahlen et al., 1984; Davis et al., 1983). Therein, the physical properties of the incoming sediments and, particularly the basal detachment, define the internal fault kinematics, slope topography, and, therefore, the mechanics of the accreted prisms (e.g., Dahlen, 1984; Gutscher et al., 1998a). In case of a mechanically weak décollement, material compression is reduced and a wide, extended, and low tapered wedge with a flat topography evolves (Huiqi et al., 1992; Gutscher et al., 1998b). With increasing décollement strength, the steep conjugated fore- and backthrusts (δ_f , δ_b) develop progressively foreland-vergent with increasing offsets along the shallower forethrusts and with decreasing offset along the steeper backthrusts. The resulting wedge is laterally compressed with a steeper topography (Chapple, 1978; Gutscher et al., 1998a). If the basal friction value of the detachment is further increased, the incoming materials are far underthrust and, subsequently, basally accreted which results in duplex growth (Gutscher et al., 1998a).

Pure brittle experiments can explain some aspects of natural thrust systems, but still one single rheology does not satisfactory explain all the observed geological variables (e.g., Platt, 2000). Natural thrust systems, such as the Mediterranean Ridge (Von Huene and Scholl, 1991; Mascle et al., 1998), the Jura Mountain (Laubscher, 1977; Burkhard and Sommaruga, 1998), or the Salt Range in Pakistan (Butler et al., 1987; Davis and Lillie 1994) incorporate, besides brittle material, a low strength stratum such as halite, gypsum, or anhydrite. These wedges or fold-and-thrust belts often show symmetrical structures, a wide thrust-spacing and a non-preferential, dually- or hinterlandward-vergent system as well as a non-frontward development of thrusts (e.g., Davis and Engelder, 1985; Mulugeta, 1988; Bonini 2003, 2007; Smit et al., 2003). However, these wedges cannot be explained by the CT theory (Platt, 2000).

To investigate the kinematics of such accreted systems, some studies with heterogeneous input layers were undertaken in recent years. These ‘evaporite-like’, embedded layers were in some cases simulated using brittle elasto-plastic materials, such as glass beads and in other cases, viscoelastic materials, such as silicon polymers (e.g., Konstantinovskaya and Malavieille 2011, Yamato et al. 2011, Bonini 2007, 2001, Storti et al. 2007, Selzer et al. 2007, Stockmal et al. 2007, Couzens-Schultz et al. 2003, Costa and Vendeville 2002, Kukowski et al. 2002). Both materials can act as mechanically weak layers, but have, due to their rheological model, different influences on the mechanics and kinematics of such accretionary wedges (Buitter 2012). Bonini (2007) concluded that in his viscous analog experiments, it is difficult to discern the operating factor that influenced the variability of the thrust vergence. Numerical analyses may be useful as here a quantification of the effect of a single parameter on the structural system is possible. In our study, we focused on how much the wedge mechanics depends on the rheology. What differences can be observed, if a weak embedded layer with an elasto-plastic (H-experiment series) versus a viscoelastic-plastic rheology (B-experiment series) is incorporated into the incoming material. We utilized numerical 2D ‘sandbox’ experiments based on the Discrete Element Method (PFC2D, ITASCA Manual 2004) gaining a deeper insight into the key role of the different implemented rheologies in an accretionary wedge. In both models, H and B, a weaker layer is embedded in a brittle Mohr Coulomb stratum. All other settings and material properties for the embedded materials were held constant. The only varied parameter is the rheological model used for the embedded layer.

2. Method

2.1 Discrete Element Method

The Discrete Element Method (DEM) is a numerical particle based simulation technique that enables the computation of the deformation behavior of rocks and sediments over large strain rates (e.g., Morgan and Boettcher, 1999; Huhn et al., 2006; Schöpfer et al., 2006; Yamada et al., 2006). This approach was developed by Cundall and Strack in 1978 and serves as the basis for the commercial code PFC2D (ITASCA Manual, 2004), which is used in this study.

The software simulates a granular material by using a distinct number of simple spherical elements. If neighboring particles come in contact, two kinds of contact forces occur: (1)

shear forces (F_s) parallel to the contact plane and (2) normal forces (F_n) perpendicular to the contact plane. These forces, acting along particle contact points, are calculated depending on the physical properties of the involved particles (e.g., normal and shear particle stiffness ($k_{n,particle}$, $k_{s,particle}$), the coefficient of particle friction ($\mu_{particle}$) and particle density ($\rho_{particle}$)) or the properties of the particle contacts (e.g., normal and shear contact stiffness ($k_{n/s,contact}$, $k_{m/s,contact}$)) via force-displacement laws (Cundall and Strack, 1979; Morgan and Boettcher, 1999; ITASCA Manual, 2004). In the following study we used ideal spherical particles with a linear force displacement law (Mindlin and Deresiewicz, 1953). Subsequently, all forces acting on a single particle are summed in order to calculate the resultant particle displacement using the second Newton's law. For a more detailed description of the code used, please refer to e.g., Cundall and Strack (1983, 1979, 1978), Cundall (1987) or the PFC2D User's Manual (ITASCA Manual, 2004).

Detailed information about particle position and, hence, internal structure of a particle assembly as well as shear and normal stresses at each particle contact are available at each time step for the entire model run. From these data, the bulk friction values as well as the bulk viscosity of an entire particle assembly can be calculated (see Sec. 3.1). This has to be done, as the micro properties in the DEM do not correspond with the macro properties of the particle assemblage (Cundall and Strack, 1979).

2.2 Mechanical concepts and rheological models

2.2.1 Elasto-plastic behavior in PFC2D

Most natural rocks exhibit an elasto-plastic material behavior (Mandl, 1988). If forces are applied to these materials they, first, deform elastically with a reversible deformation that follows the Hooke's law. If further forces are applied, plastic deformation occurs, similar to the Mohr Coulomb rheology (e.g., Morgan and Boettcher, 1999). The numerical DEM approach is able to simulate both elastic, as well as plastic deformation. For elastic deformation, the Hooke's law is implemented with a spring (Fig. III-1a). Therein, strain increases linearly with the acting stress. When further forces act and the critical shear strength of the material is reached, the elastic deformation is, subsequently, replaced by plastic deformation and the frictional contacts between particles break. Hence, the numerical approach is able to describe the deformation behavior of upper, brittle crustal

materials and, therewith, allows for simulating and investigating the deformation processes of accretionary wedges (Miyakawa et al., 2010). Consequently, the numerical material will be, hereafter, referred to as brittle material, defined by normal and shear particle stiffness ($k_{n,particle}$, $k_{s,particle}$), the particle friction ($\mu_{particle}$) and the particle density ($\rho_{particle}$, Table III-1).

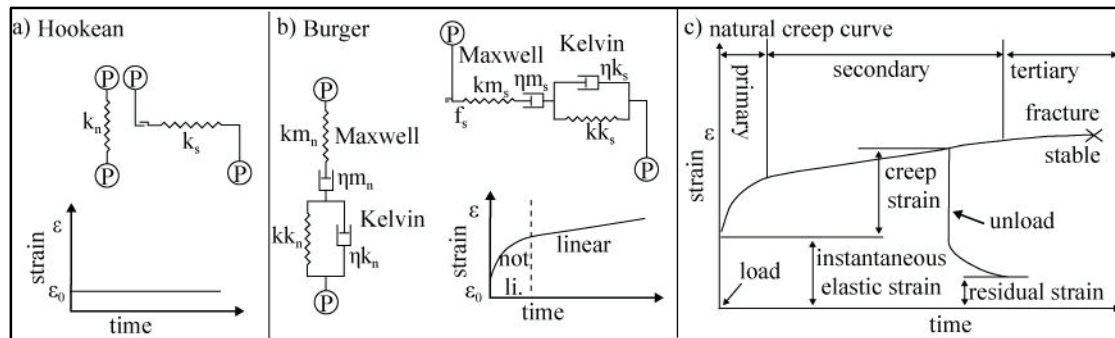


Fig. III-1: a) The mechanical attributes of the *Hookean* model (modified after ITASCA Manual, 2004) and the material curve for an elastic body described by the Hooke's law. Spheres (P) represent interacting particle. b) The mechanical attributes of the *Burger's* model (modified after ITASCA Manual, 2004) and the material curve for a viscoelastic-plastic body described by the Burger's model, similar to the creep behavior of rocks. c) Creep curve of natural rocks.

2.2.2 Viscoelastic-plastic behavior in PFC2D

Evaporites such as halite, anhydrite or gypsum show ductile or viscous behavior already under low temperature conditions (Le Comte, 1965). Such materials break under short acting forces, but starts to creeps under long acting forces e.g., subduction processes at active convergent margins (Baar, 1977). A typical creep curve has three different sections, the transient (primary), the steady-state (secondary), and the tertiary phase of creep (Lama and Vutukuri, 1978; Fig. III-1c). Accordingly, after application of the load and an instantaneous elastic strain, the primary creep phase begins. Primary creep is non-linear and recoverable by removal of forces. This phase is followed by the secondary linear creep phase, where permanent deformation takes place. Depending on the stress level, the secondary creep will be displaced by the accelerated creep of the tertiary phase, which eventually leads to failure. Furthermore, the general creep rate is influenced by temperature. Nevertheless, temperatures between 20° and 100° C, such as those of the flat, extended Mediterranean ridge (Reston et al., 2002b) do not significantly affect the creep rate associated with evaporites (Dusseault and Fordham, 1993). Hence, thermal related aspects are not taken into account in this study.

To achieve viscoelastic-plastic behavior in DEM, contact laws acting between the particles are extended. The rheological model used to simulate creep in this study is the Burger's model, which simulates the creep behavior of natural rocks such as evaporites (Fig. III-1b). This model also uses the *Hookean* model (spring) for the elastic deformation and the *Newtonian* model (dashpot) for the viscous deformation. The dashpot implementation is used to represent the absorption or dissipation of energy and produces an idealized viscous behavior. The Burger's Model is a contact law and is for both - the normal and the shear component, a combination of two springs and two dashpots (Fig. III-1b). The contact forces were calculated based on the combined *Kelvin* and *Maxwell* section, where the former is expressed by a parallel spring and dashpot and the latter by a spring and dashpot connected in series (Fig. III-1b). The combination of the two sections allows for simulating of, both, a primary (nonlinear = *Kelvin* section), as well as the secondary (linear = *Maxwell* section) phase of creep. The responding deformation is controlled by predefined contact stiffness of the *Maxwell* ($km_{n,contact}$, $km_{s,contact}$) and the *Kelvin* section ($kk_{n,contact}$, $kk_{s,contact}$) and viscosity coefficients for the *Maxwell* ($\eta m_{n,contact}$, $\eta m_{s,contact}$) and the *Kelvin* section ($\eta k_{n,contact}$, $\eta k_{s,contact}$) in normal and shear directions as well as particle friction ($\mu_{particle}$, Table III-1).

2.3 Model setup

To investigate the effects of different implemented rheologies on accretionary wedges, a numerical 2D 'sandbox' is developed by adopting general geometries from analog experiments (e.g., Gutscher et al., 1998a; Kukowski et al., 2002; Konstantinovskaya and Malavieille, 2011; Fig. III-2). Such simplified settings were successfully used to investigate key role of single parameters on wedge kinematics while numerical simulations have the advantage that dimensions and properties can be directly link/scale to nature.

This rectangular box had a length of 200 km and a height of 30 km (Fig. III-2a). It consisted of a box bottom and two fixed vertical side walls. The box bottom and walls were made of particles with a homogeneous radius of 125 m and acted as stiff undeformable boundaries. The box bottom had a fixed dip angle of $\beta = 0^\circ$ and moved with a constant velocity in the positive x-direction simulating the subduction of the "oceanic plate". Hence, the surface of the box bottom represented a potential basal detachment. Within the box, 21,000 randomly distributed particles were generated with three particle sizes of 100, 125, and

150 m diameters and a logarithmic normal size distribution. The particles were initially generated with as brittle material with frictional contacts and no particle bonding is used. These particles were deposited on top of the box bottom under gravity ($g = 9.81 \text{ m/s}^2$) to create an undeformed ‘marine’ sediment layer of 7.5 km thickness. This geometries mirrors common natural conditions at forearc regions, e.g., at the Mediterranean Ridge (e.g., Reston et al., 2002a) or the Makran fore arc (e.g., Fruehn et al., 1997). All these settings were held constant throughout all experiments.

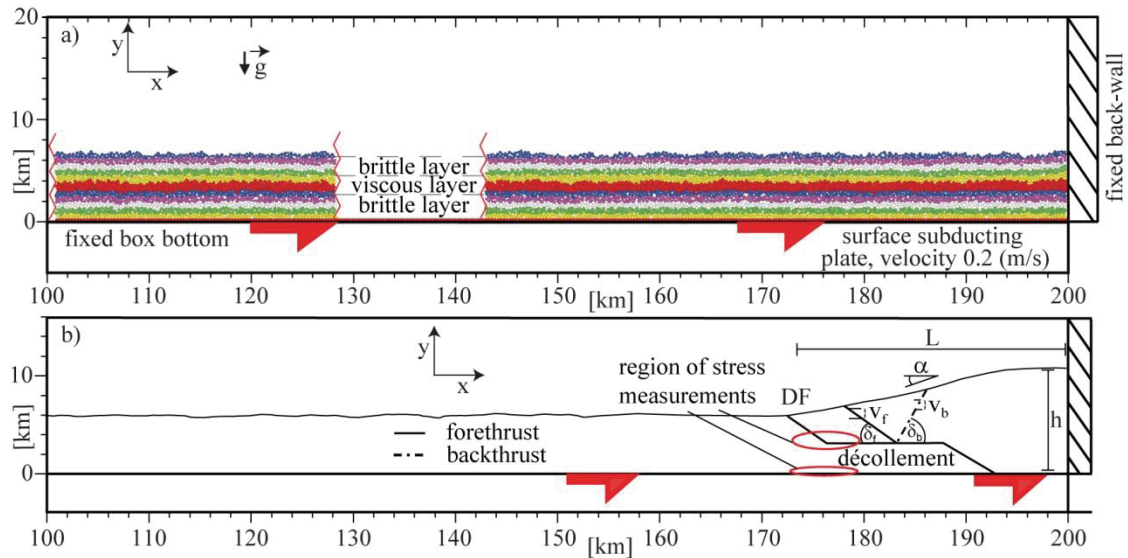


Fig III-2: a) A schematic view of the initial state of all experiments. The different colored layers are used as marker horizons. The red layer indicates the position of the embedded layer, which has a brittle MC rheology in experiment H and a Burger’s rheology in experiment B. Gravity is 9.81 m/s^2 . ‘Subduction’ induced by the moving box bottom is shown by a red arrow. b) Line drawing of evolved prism including the position of the active décollement and the deformation front (DF). One fore- and backthrust are shown exemplarily. Red ellipses mark the area of data extraction where bulk properties were measured.

This undeformed ‘sediment’ input layer is subdivided into three horizontal layers. A lower 3 km-thick layer exhibited brittle material behavior. Above that, a second layer had a homogeneous thickness of 1.5 km. Finally, an upper third 3 km-thick cover layer behaved in accordance with brittle material rheology and was implemented simulating a natural sedimentary cover. Hence in all experiments, a brittle hanging and a brittle underlying sediment sequence were simulated. Material properties of these layers were held constant throughout all experimental runs (Table III-1).

In addition, in all experiments, the second layer was designed to simulate an ‘evaporite-like’, weak embedded layer, such as those that can be found in natural, heterogenic accretionary systems e.g., Mediterranean Ridge (Reston et al., 2002a) or the Jura Mountains

(Laubscher, 1977). As we would like to test the key role of the used rheology, this embedded layer had a Mohr Coulomb rheology with reduced particle friction (μ_{particle}) and stiffness ($k_{n/s,\text{particle}}$) in experiment H similar to glass beads used in analog experiments (Kukowski et al., 2002; Konstantinovskaya and Malavieille, 2011).

Table III-1: Model input particle parameters

Particles/ Contacts	μ_{particle}	ρ_{particle} [kg/m ³]	$k_{n/\text{particle}}$ [N/m]	$kk_{n/s,\text{contact}}$ [N/m]	$km_{n/s,\text{contact}}$ [N/m]	$\eta m_{n/s,\text{contact}}$ [Pa s]	$\eta k_{n/s,\text{contact}}$ [Pa s]
Lower/upper MC particles	0.58	2500	1×10^{12}				
Box bottom	0.2	2500	1×10^{12}				
Viscoelastic- plastic part.	0.1	2300	1.6×10^{11}	8×10^{10}	8×10^{10}	1×10^{19}	1×10^{19}
Weak MC Particles	0.1	2300	1.6×10^{11}				

Model parameters: μ_{particle} is the particle friction, ρ_{particle} is the density, $k_{n/s,\text{particle}}$ is the particle stiffness in normal and shear direction, $km_{n/s,\text{contact}}$ is the normal and shear contact stiffness of the *Maxwell* section, $kk_{n/s,\text{contact}}$ is the normal and shear contact stiffness of the *Kelvin* section, $\eta m_{n/s,\text{contact}}$ is normal and shear viscosity of the *Maxwell* section, $\eta k_{n/s,\text{contact}}$ is normal and shear viscosity of the *Kelvin* section.

Further, in the second experiment B, the embedded second layer consisted of a viscoelastic-plastic material in which the Burger's Model was implemented similar to analog studies (e.g., Smit et al., 2003; Bonini, 2007). For the different rheologies of this embedded layer identical particle friction and particle/contact stiffness values were used. Besides, shear and normal contact viscosity had to be defined for the Burger's model and were calibrated to produce natural behavior of marine sediment (see Sec. 3.1). All material properties were adopted from previous studies (e.g., Ting et al., 1989; Spiers et al., 1990; van Keken et al., 1993; Jensen et al., 1999; Burbidge and Braun, 2002; Turcotte and Schubert, 2002; Naylor et al., 2005).

Pore fluids and cohesion were not taken into account in the simulations. Although these effects can have an influence on the wedge tapers and fault structures (Davis et al., 1983; Smit et al., 2003; Stockmal et al., 2007), these simplifications are reasonable as only relative comparisons between experiments were derived. We were not aiming to transfer

faults angles and slope tapers directly into natural systems. Such simplifications were already successfully applied to study general processes and the influence of different operation factors, e.g., friction distribution, subduction angle, and layer thicknesses on wedge kinematics (e.g., Naylor et al., 2005). Additionally, it should be mentioned that even in this short time period, which was modeled, a reduction of the viscous effects occurs, due to the time scaling (see Sec. 3.1), which is needed to run the model in a reasonable time frame.

2.4 Analysis and interpretation techniques

Generally, all particle positions as well as normal and shear stresses were saved every 0.05 % shortening or 200 m ‘subduction’ during the entire model run of each experiment. The detailed information about particle positions allow for the monitoring of internal deformations, such as fault zone evolution in space and time. For a first impression of the evolving structures, horizontal layers were colored in accordance to analog sandbox experiments in order to highlight offsets and folding within these layers, e.g., as an indicator of thrust evolution (Fig. III-2a).

Furthermore, displacements of each particle in the x-direction were calculated and plotted for each ‘subduction’ increment of 200 m (Fig. III-3). Such relative displacements between particle groups reveal general strain plots in which the direction of movement of large particle assemblages relative to the surrounding particles is shown, this enables mapping of the evolving thrusts (Morgan and Boettcher, 1999; Huhn et al., 2006). Based on the model configuration and the origin of the coordinate system, offsets or thrusts rising outwards or inwards were interpreted as landward dipping forethrusts or seaward dipping backthrusts (Fig. III-3). To define the degree of thrust vergence the dip angles of thrusts were measured and average values were calculated.

For a comprehensive value of thrust offsets ($v_{f/b}$) in positive (inwards) and negative (outwards) x-direction, particle amount and displacement along fore- and backthrusts were calculated and summed to get a total offset along fore- and backthrusts. This calculation was performed for all particles between 120 km and 180 km between 20 % and 70 % shortening to obtain a qualitative picture of the structural vergence and dominance of fore- and backthrusts. Furthermore, shear and normal stresses were extracted for all particle

contacts in the vicinity of the deformation front (DF; Fig. III-2b, area marked by red ellipse). These values together with the particle positions enable the calculation of the bulk friction as well as the bulk viscosity (see Sec. 3.1).

3. Results

3.1 Bulk properties

The bulk material properties were first tested and micro properties were defined to simulate natural material behavior. Therefore, the shear and normal stress as well as the particle positions for the brittle upper and lower layers, the basal box bottoms as well as for the embedded weak layers were extracted for different time steps or every 2.5 % strain (Fig. III-2b; Table III-2). Afterwards, average values were calculated and used to calculate bulk friction values (μ_{bulk}) and bulk viscosity (η_{bulk}) for the embedded layer. The bulk friction was calculated following the equation:

$$\mu_{\text{bulk}} = \tau / \sigma_v \quad (\text{eq. III-1})$$

For calculating the bulk viscosity, the following equation was used:

$$\eta_{\text{bulk}} = \tau / (\partial u / \partial y) \quad (\text{eq. III-2})$$

where τ is the shear stress, σ the normal stress and u the subduction velocity. Equal particle and contact stiffness as well as friction coefficients were used in all experiments resulting the shear and normal stress in experiment B ($\sigma_n = 1.75 \times 10^{10}$ Pa, $\tau = 3.0 \times 10^9$ Pa) and experiment H ($\sigma_n = 1.75 \times 10^{10}$ Pa, $\tau = 3.3 \times 10^9$ Pa) were similar, whereby shear stress is slightly reduced in experiment B. For the experiment B the contact viscosity values ($\eta_{n/s, \text{contact}}$) was set to 1×10^{19} Pas, which resulted in a bulk viscosity of $\eta_{\text{bulk}} = 3.5 \times 10^{13}$ Pas.

Table III-2: Measured bulk properties

Particles/Contacts	σ_v [Pa]	τ [Pa]	μ_{bulk}	η_{bulk} [Pa s]
Lower/upper MC particles	1.92×10^{10}	6.43×10^9	0.33	--
Box bottom	1.37×10^{10}	4.77×10^9	0.35	--
Viscoelastic-plastic particles	1.75×10^{10}	3.0×10^9	0.17	3.5×10^{13}
Weak MC particles	1.75×10^{10}	3.3×10^9	0.2	--

σ_n is the normal stress, τ is the shear stress, μ_{bulk} is the bulk friction and η_{bulk} is the bulk shear and normal viscosity.

In the next step, macro viscosities were scaled to natural conditions. This was done in

accordance to previous analog experiments (Storti et al., 2007) because this parameter is time dependent (Mezger, 2006). Natural convergence rates at subduction zones are in the range of $\sim 4\text{-}5$ cm/y (e.g., at the Mediterranean Ridge; Bohnhoff et al., 2001). Together with the numerical subduction velocity of 0.2 m/s the resultant time scaling factor ($t_{\text{nature}}/t_{\text{bulk}}$) was 1.58×10^8 . The natural viscosity for our model can be obtained by the following equation (Weijermars and Schmeling, 1986):

$$\eta_{\text{nature}} = ((t_{\text{nature}} \times \eta_{\text{bulk}}) / t_{\text{bulk}}) \times ((\rho_{\text{bulk}} g_{\text{bulk}} l_{\text{bulk}}) / (\rho_{\text{nature}} g_{\text{nature}} l_{\text{nature}})) \quad (\text{eq. III-3})$$

where t is time, l is the length and g is gravitation. By assuming a length ratio of $l_{\text{bulk}} = l_{\text{nature}}$, a density ratio of $\rho_{\text{bulk}} = \rho_{\text{nature}}$, and natural gravitation conditions of $g_{\text{bulk}} = g_{\text{nature}}$, the bulk macro viscosity ($\eta_{\text{bulk}} = 3.5 \times 10^{13}$ Pas) of experiment B, resulted in a calculated ‘natural’ viscosity of $\eta_{\text{nature}} = \sim 6 \times 10^{21}$ Pas. This corresponds with natural values for rock salt or evaporites, which are between 10^{18} Pas to 10^{21} Pas (Spiers et al., 1990; van Keken et al., 1993; Chemia and Koyi, 2008; Mukherjee et al., 2010).

3.2 Structural geology of the evolving wedges

In experiments H and B, the brittle stratum with an embedded, mechanically weak layer was shortened above a basal box detachment. Thereby, depending on the implemented rheology of the embedded layer, accretionary wedges with specific lengths (L), maximal thicknesses (h), slope angles (α_{1-3}), and specific internal geometries evolved (Fig. III-3).

In both experiments, a mid-level décollement developed within the weak, embedded layer corresponding to the reduced shear strength in this layer in comparison with those of the upper and lower brittle layers. This mid-level décollement caused the evolution of a frontally accreted wedge (A, Fig. III-3). It stepped down to the basal box detachment at some distance of the fixed back-wall resulting in the development of a basally accreted body just in front of the strong back wall (B, Fig. III-3). Therewith, the active décollement consisted of two detachments, what enabled the accretionary wedges to grow by frontal and, simultaneously, basal accretion. As a result, all wedges were classified by at least two wedge segments (A and B).

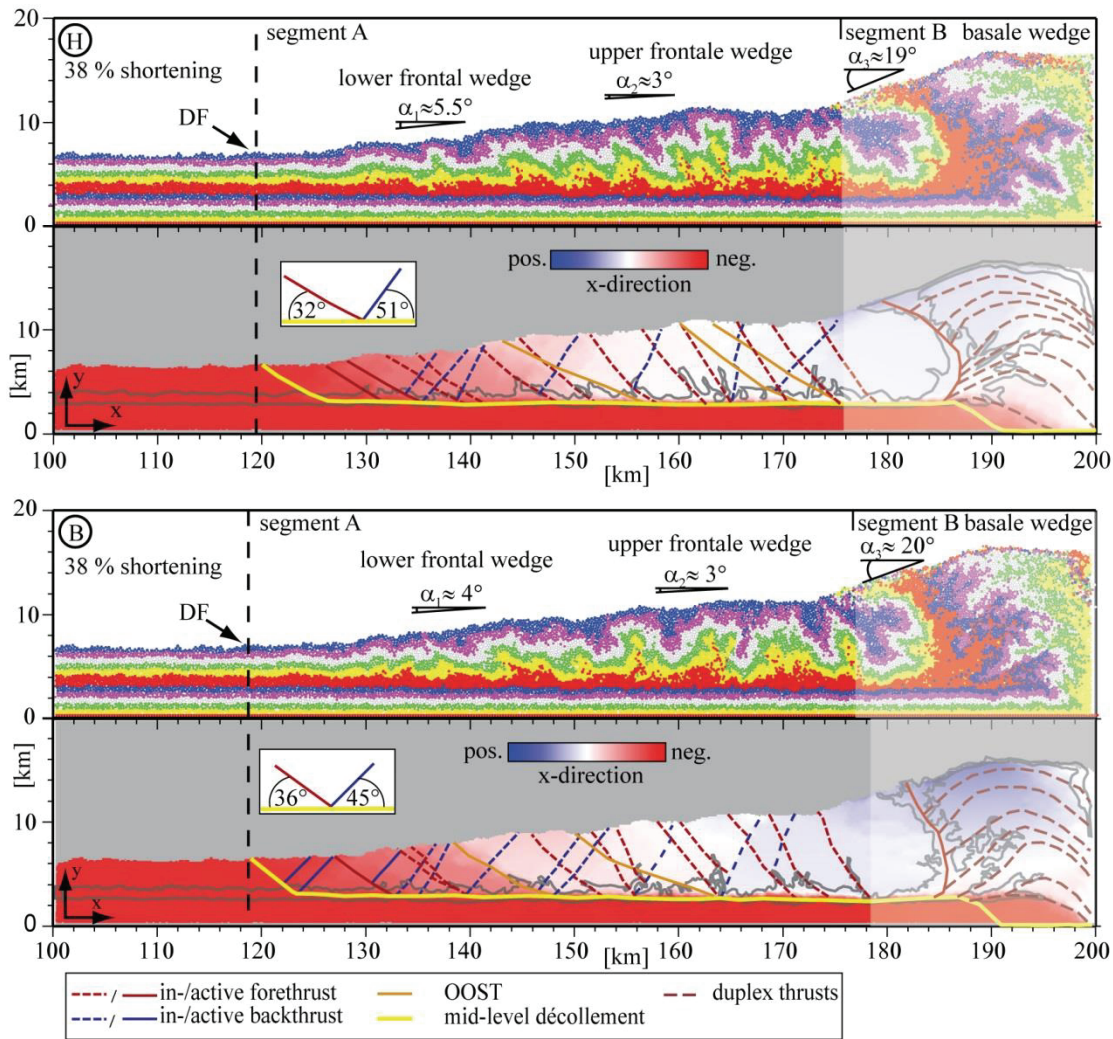


Fig. III-3: Particle configuration view and x-displacement plot of the experiments H and B after 38 % of shortening. The different colors are used as markers of horizons to visualize fault evolution. The red layer has a brittle MC rheology in experiment H and a Burger's rheology in experiment B. The wedge segments, DF (deformation front), and slope angles α_{1-3} are labeled.

3.2.1 Model H: pure MC material wedge

In experiment H, a self-similar growing wedge with stable slope angles evolved after 22 % shortening. This wedge grew continuously by accumulating new material and reached a length of $L = 80.5$ km and a maximal height of $h = 16.7$ km at the end of the experiment (38% shortening; Fig III-3). Directly at the deformation front (DF), new forethrusts cut out of the surface with steep angles of around 32° , which were generated at the embedded, weak MC layer serving as the mid-level detachment (Fig. III-3). The corresponding backthrusts rose with an angle of 51° (Fig. III-3). Hence, fore- and backthrusts developed asymmetrically with a difference in rise angles of $\sim 17^\circ$, which implies a more foreland-

vergent thrust system. The deformation front propagated rapidly forward in short-periods leading to a relatively flat frontal wedge with a slope angle of $\alpha_1 \sim 5.5^\circ$. This forward propagation was followed by an internal rearrangement along thrusts of the upper frontal wedge (Fig. III-3). However, the main activity took place behind or inward of the DF at the lower frontal wedge. There, transient first time reactivated thrusts were observed. Over the experimental run, around thirteen forethrusts were active, whereas only around seven backthrusts were detected. The spacing between the active fore- and backthrusts was around 3.5 km (Fig. III-3).

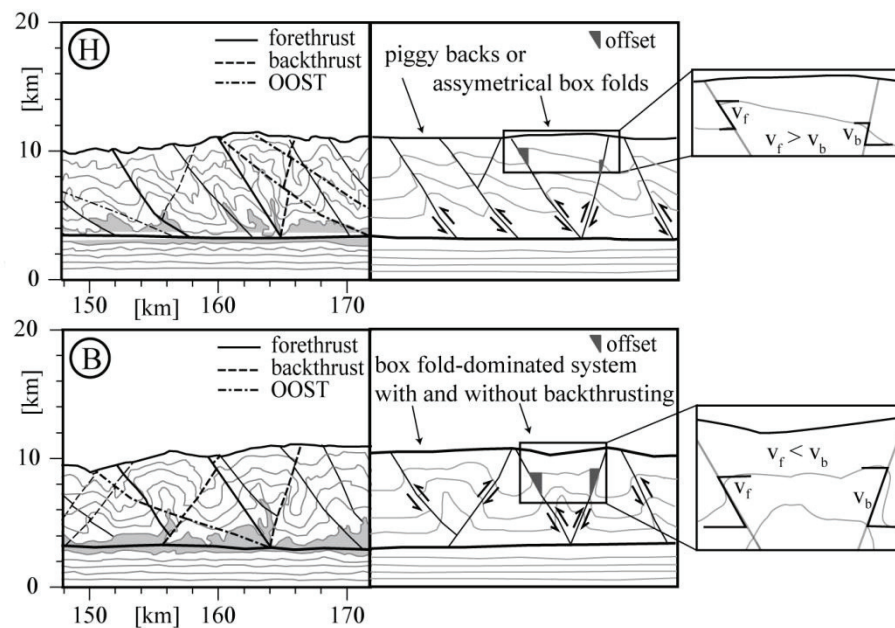


Fig III-4: Line drawings of two sections of experiment H and B after 38 % shortening. The actual position of the viscoelastic-plastic layer is shown in grey.

Furthermore, the offsets (v_f) along the forethrusts seemed to be distinct larger than along backthrusts (v_b), ($v_f > v_b$, Fig. III-4). To get a more detailed picture of this foreland dominance, the amount and mean displacement of particles in fore- and backthrusts was calculated and its portion of outward and inward movements reported in percentage. In total 4016 particles have moved within active forethrust with a mean distance of 191 m. The resulting total offset of all particles is 767,806 m. In contrast, 3089 particles were moved with an average value of 152 m within active backthrusts. Consequently, a total offset of 469,546 m took place along backthrusts. This shows that 63 % of the shortening was accumulated by forethrusts whereas only 37 % along backthrusts. Both results show a foreland dominance of the tectonic system.

In general, the structures formed ‘in-sequence’ although individual thrusts were later re-activated as out-of-sequence thrusts (OOSTs) rearranging the accretionary wedge. The long frontal wedge (segment A) was split by a first generation of OOSTs into an active and a less active part (Fig. III-3). These thrusts rose with an angle of $\sim 30^\circ$. Beyond that, a few more reactivated OOSTs were detected further inwards, where a flat terrace $\alpha_2 \sim 3^\circ$ at the outer edge of the upper, frontal wedge evolved separating the frontally accreted wedge from the steeper uplifted upper slope.

Underneath the embedded weak layer, the brittle material was far-underthrust under the frontal wedge without developing fractures. In the deep or inward portion of the wedge (in front of segment B), the mid-level detachment stepped down to the basal box creating a steep antiformal stacked duplex. At this location the whole material was uplifted next to the fixed back-wall resulting in highest uplift rates of the overlaying material until the material started to overtilt above the frontal wedge. The high uplift rate increased the slope angles to $\alpha_3 \sim 19^\circ$ at the upper wedge (segment B; Fig. III-3). Hence, the frontal accretion in the upper brittle layer and the basal accretion in the lower brittle layer were decoupled by a mid-level detachment, which fail at lower stresses induced by the basal box detachment. The main shearing took place directly in this weak layer (Fig. III-3), which got afterwards, incorporated by intrusions into the fault system of the duplex body. This experiment detected the mid-level décollement directly inside.

3.2.2 Model B: MC material wedge with a viscoelastic-plastic layer (Burger’s rheology)

In experiment B, a self-similar growing wedge with stable slope angles evolved after 20 % accretion. By the end of the experiment (38 % shortening), the wedge reached a length of $L = 81.5$ km and a maximal thickness of $h = 16.4$ km by continuous growing (Fig. III-3). The frontal wedge, with narrow slope angles of around $\alpha_1 \sim 4^\circ$, was built up on top of the weak, viscoelastic-plastic layer by steep fore- and backthrusts. Hence, similar to experiment H a mid-level detachment evolved within the mechanically weak embedded layer, what corresponded to the resulting reduced strength. The forethrusts rose with a slightly steeper angle of $\sim 36^\circ$ than in experiment H to the surface and corresponding backthrusts with a slightly flatter angle of $\sim 45^\circ$ (Fig. III-3). Hence, fore- and backthrusts of the frontal wedge (segment A) differed only by a mean value of 9° , what indicates a more symmetrical and only slight foreland-vergent thrust system (Fig. III-3). Rather these

thrusts show a more box-fold style (Fig. III-4). The DF propagated again rapidly forward and thrusts were active only for a short time period. Similar to experiment H, the main activity took place behind the DF at the lower slope (Fig. III-3). The spacing between the new active fore- and backthrusts was relatively wide at ~ 5 km. In total, around eleven active forethrusts and eleven active backthrusts were detected. Similar to experiment H, the structures formed 'in-sequence' although the individual faults were later re-activated out-of-sequence which led to rearrangements and build-up of an upper frontal accretionary wedge. The lower, 20 km long frontal wedge was separated from a more inactive part by OOSTs, which were regularly activated at a x-position of approximately 170 km (Fig. III-3) and rose with a slightly flatter angle of $\sim 29^\circ$. This upper wedge developed with extremely flat slope angles of $\alpha_2 \sim 3^\circ$.

Whereas in experiment H the offset along forethrusts developed much higher than along backthrust, it seems that in experiment B offsets evolve more similar ($v_f \approx v_b$; Fig. III-4). To verify this assumption, the amount and mean displacement of all particles in model B was calculated similar to the model H. In this case, 4749 particles have moved with a mean displacement of 180 m within active forethrusts. Therewith, the total offset of all particles taking place along forethrusts is 854,911 m. In contrast, 4285 particles have moved within active backthrusts with a slightly lower mean distance of 167 m. This results in a total offset of 716,912 m along backthrusts. Hence, 54 % shortening occurred along fore- and 46 % along backthrusts. This indicates that the foreland-vergence obviously decreased.

In contrast to the brittle layer on top of the weak viscoelastic-plastic layer, the lower brittle material was again far underthrust under the frontal wedge without being fractured. Similar to experiment H, the material was basally accreted, antiformally stacked, and uplifted next to the fixed back-wall resulting in the development of a duplex (segment B). This basal accretion led to an increase of the slope angle to around $\alpha_3 \sim 20^\circ$ at the outer edge of the upper wedge (segment B). The uplifted material was slightly stabilized and, hence, the material showed a slightly delayed overtilt (Fig. III-3).

Again, the upper brittle layer and the lower one were decoupled by the weak mid-level detachment. The stresses were absorbed along this layer and no interaction between the upper and lower MC layers took place. Shearing took place along the embedded layer, but viscoelastic-plastic material was incorporated in the fault system above and below basally

accreted thrusts indicating that the mid-level décollement developed directly inside or at the bottom of the weak layer as also seen from the displacement plots (Fig. III-3).

4. Discussion

The aim of the experiments presented above was to gain a better understanding of how important the use of a viscoelastic-plastic rheology is compared to a weak Mohr-Coulomb rheology for simulations of evaporitic décollements, e.g., as that observed at the Mediterranean Ridge (Reston et al., 2002b). This question is based i.e. on the fact that some of the previous analog experiments dealing with heterogeneous wedges used glass beads with a very low frictional MC rheology to simulate viscous detachments (e.g., Kukowski et al., 2002). Furthermore, analog experiments are restricted to discern high resolution differences of thrust kinematics in space and time as a function of the used rheology or/and the operating factors (e.g., Bonini, 2007).

In this study two ‘sandbox’ experiments H and B documented the growth and evolution of accretionary wedges. These prisms developed out of an undeformed, heterogenic, incoming ‘sediment’ sequence as a result of a continuous convergence of the brittle basal detachment against a fixed back-wall. The ‘sediment’ sequence consisted of two brittle layers with an embedded weak layer which followed in experiment H a MC rheology and in experiment B a Burger’s rheology. All model configurations including material parameters were chosen identically except of the viscosity which must be only defined for the embedded layer with the Burger’s rheology.

The focus of our study was made on the distinctions which occurred in the overlying brittle layer due to the different used material rheologies at the mid-level detachment. For such a rheology sensitivity study, a numerical approach is helpful, as only here the effect of this single parameter can be studied.

In experiments H and B, accreted prisms, consisting of a wide, flat lower slope (segment A) and a steep upper slope (segment B) developed correspondingly to the frontally accreted wedge and the basally accreted and uplifted material, respectively (Fig. III-3, III-5). Hence, due to the reduced shear strength of the embedded layer a mid-level detachment evolved in both experimental runs H and B causing the evolution of a frontally accreted segment (A; Fig. III-3, III-5). Underlying material was far underthrust and, subsequently, basally accreted on top of the basal detachment generated at the top of the moving box bottom. The

décollement consisted of two detachments, because the mid-level detachment stepped down to the basal box bottom detachment in front of the back-wall. The décollement and the regularly occurring OOSTs decoupled the frontally and basally accreted wedge segments. This general wedge mechanics of frontal and basal accretion was in line with former studies of heterogeneous sediment sequences (Costa and Vendeville, 2002; Couzens-Schultz et al., 2003; Costa et al., 2004; Dooley et al., 2007; Reiter et al., 2011) and supported the ability of our approach to simulate evolving accretionary wedges and to investigate their mechanics.

As the focus of our study was on the effect of the mid-level detachment rheology, the evolving basal accreted wedges caused by the deeper positioned moving basal box bottom will not be analyzed and discussed in detail (see gray area, Fig. III-3).

By comparing the wedge topography of both experiments, it can be inferred that the prism in experiment B was slightly longer ($\Delta L = 1$ km) and had a reduced slope angle ($\Delta\alpha_1 = 1.5^\circ$) at the frontal wedge compared to the prism in experiment H (Fig. III-3). Furthermore, it evolved slightly baser ($\Delta h = 0.3$ km). These results coincide with the observation that the DF migrated more rapidly outwards on top of the viscoelastic-plastic mid-level décollement than on top of the brittle MC mid-level décollement. Hence, it can be inferred that the viscoelastic-plastic décollement acted weaker than the brittle décollement as previous studies have shown that the DF propagates faster and further above a weak décollement than above a strong one (Marshak and Wilkerson, 1992; Cotton and Koyi, 2000; Costa and Vendeville, 2002; Bahroudi et al., 2003).

In addition, our numerical studies revealed that shear stresses in the embedded layer are slightly reduced when a Burger's rheology is used compared to a MC rheology whereas the normal stress values in the embedded layers were identical in both experiments H and B. This slight shear stress reduction caused by the use of the Burger's rheology led to the change in topography and internal structures (Fig. III-5). The evolution of a mid-level detachment in the vicinity of a weaker embedded layer has been described in various numerical and analog models (e.g., Kukowski et al., 2002; Bonini, 2003; Couzens-Schultz et al., 2003; Konstantinovskaya and Malavieille, 2005; Bonnet et al., 2007; Yamato et al., 2011). However, these numerical experiments showed quantitatively that this mid-level detachment was located directly inside the embedded weak layer.

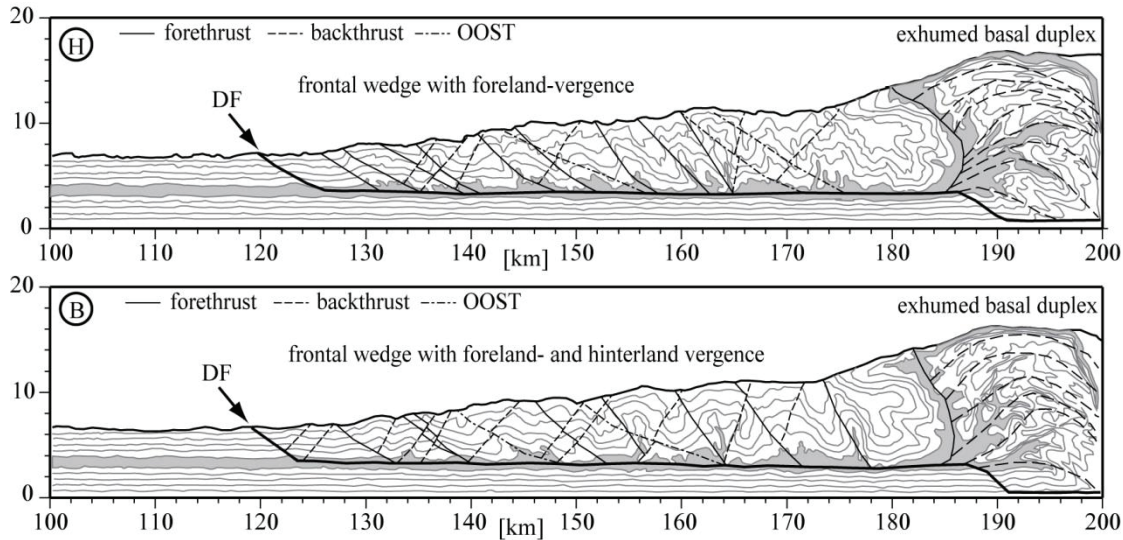


Fig. III-5: Conceptual models for experiment H and B demonstrating the key role of an embedded viscoelastic-plastic layer on wedge shapes and internal structures. The position of the viscoelastic-plastic layer is shown in grey.

The frontally accreted wedges in experiments H and B grew by fore- and backthrusts rising from the active mid-level detachment which led to the evolution of a frontally accreted wedge similar to previous studies (e.g., Zhao et al., 1986; Gutscher et al., 1998a; Naylor et al., 2005; Konstantinovskaya and Malavieille, 2011). The comparison of the thrust systems in detail showed that the forethrusts in experiment B develop slightly steeper ($\Delta\delta_f = 4^\circ$) and the backthrusts flatter ($\Delta\delta_b = 6^\circ$) than in experiment H. Such an angle in- and decrease or a rotation of two conjugates thrusts was explained by a reduced strength or coupling between the overburden brittle layer and the mid-level detachment (Couzens-Schultz et al., 2003; Bonini, 2007). Foreland-verging thrusts were more dominant in both experiments, but in experiment B to a significant lesser degree. In this experiment hinterland-vergent thrusts occurred nearly equally pronounced (Fig. III-4, III-5) what resulted in a more dually-vergent system on top of the viscoelastic-plastic décollement. Box-fold structures were observed in experiment B whereas structures in experiment H were similar to piggy-back thrusts. In addition, the increasing symmetry of the fore- and backthrusts in experiment B and the reduction of the foreland-vergence were validated by the calculated thrust-offsets. In experiment H, only 63% shortening occurred along forethrusts and 37 % shortening occurred along backthrusts. In contrast, in experiment B a nearly identical shortening along fore- and backthrusts with 54 % to 46 % was measured (Fig. III-4).

Such an increasing symmetrical evolution of both foreland and hinterlandward verging thrusts was observed in various studies with a layered brittle MC – viscoelastic-plastic incoming sediment sequence (Cotton and Koyi, 2000; Koyi et al., 2000, Costa and Vendeville, 2002; Lujan et al., 2003; Smit et al., 2003). These studies have shown that the importance of backthrusts increases with decreasing strength along the detachment while offset at the forethrusts decreases and consequently, the structural system changes from piggy back to box fold anticlines structures (Fig. III-4; Davis and Engelder, 1985; Liu et al., 1992; Lallemand et al., 1994; Hardy et al., 2009; Graveleau et al., 2012). Nevertheless, our experiments revealed quantitatively that lowering the frictional strength of a MC décollement caused a decrease of thrust vergence in the piggy-back structures but it is less sufficient to simulate symmetrically thrusts and typical box-folds structures. Rather a viscoelastic-plastic rheology should be applied to simulate the creeping and thrust geometries in case of evaporitic décollements.

Finally, different analog studies have shown a wider spacing and decreasing numbers of thrusts due to a reduced coupling between the overburden and the mid-level detachment when viscous materials are incorporated in the accretionary process (e.g., Mulugeta, 1988; Mandal et al., 1997; Smit et al., 2003). Our results agreed with these observations, as the distance between the evolving forethrusts in experiment B were wider than in experiment H. Simultaneously the numbers of active forethrusts were reduced whereas the number of backthrusts increased. This supports the importance of the used rheology for simulation of ‘evaporitic’ décollements.

5. Conclusion

Within our study we developed a numerical 2D ‘sandbox’ experiment to compare the mechanics of two accretionary wedges which had either an embedded MC rheology layer (experiment H) or an embedded viscoelastic-plastic layer (experiment B). Setting and input material parameters were chosen identically except of the viscosity values that must be defined in experiment B for the Burger’s rheology in the embedded layer.

In both experiments, accretionary wedges evolved which consisted of a frontally accreted segment A correlating with the flatter lower slope and a basal accreted segment B which evolved in front of the back-wall at the position of the steeper upper slope. These segments were decoupled by a mid-level detachment which developed within the embedded weaker

brittle or viscoelastic-plastic layer. In both cases, the frontal segment grew by fore- and backthrusts cutting through the overlying brittle layer from the mid-level detachment to the wedge surface. Simultaneously, the material underneath the mid-level detachment was far underthrust and basally accreted in a steep uplifted duplex structure in front of a strong back-wall.

Our experiments confirmed that the tectonic system and the slope topography changed depending on the rheological properties of the incoming sediment sequence. We were able to show quantitatively and qualitatively that the accretionary wedge above the weak, viscoelastic-plastic layer (experiment B) evolved wider extended, with flatter slope angles, with larger thrust-spacing and a more symmetrical thrust system than above the weak brittle MC layer (experiment H). These characteristics implicated a decrease in material strength in case of the viscoelastic-plastic décollement compared to the weak brittle MC décollement although in both cases identical particle friction was implemented. We could demonstrate that foreland-vergence was less dominant in experiment B while the dip angles and the offsets along fore- and backthrusts already indicate dually-vergent structures. Such structures are typical for a brittle material overlying an ‘evaporitic’ décollement. Consequently, we inferred that using a viscoelastic-plastic rheology can simulate a more ‘evaporitic’-like behavior than a weak MC rheology.

Summarizing, this study showed quantitatively and qualitatively for the first time in a numerical study the importance of the applied rheology, if an evaporitic base should be simulated incorporating thrust spacing, vergence as well as the shortening along thrusts. The embedded detachment in experiment B was, therewith, defined as more suitable to simulate an ‘evaporitic’-like décollement than an embedded very weak MC layer (experiment H). Consequently, Burger’s rheology is most sufficient to simulate an ‘evaporitic’-like décollement in case the mechanics and fault kinematics of accretionary wedges with heterogeneous sediment input.

ACKNOWLEDGEMENTS

Thanks are due to all our colleagues of the MARUM-Center for Marine Environmental Sciences. This research was funded through DFG-Research Center / Cluster of Excellence „The Ocean in the Earth System“.

Chapter IV: Viscosity study**THE INFLUENCE OF AN EMBEDDED VISCOELASTIC-PLASTIC LAYER ON KINEMATICS AND MASS TRANSPORT PATTERN WITHIN ACCRETIONARY WEDGES**Linda WENK^{1*}, Katrin HUH¹¹ *MARUM – Center of Marine Environmental Science and Faculty of Geosciences, University of Bremen, Leobener Straße, 28359 Bremen, Germany**Keywords: accretionary wedge; viscoelastic-plastic mid-level décollement; numerical ‘sandbox’ experiment; Burger’s model***ABSTRACT**

The major aim of this study is to examine the influence of an embedded viscoelastic-plastic layer at different viscosity values on accretionary wedges at subduction zones. To quantify the effects of the layer viscosity, we analysed the wedge geometry, accretion mode, thrust systems and mass transport pattern. Therefore, we developed a numerical 2D ‘sandbox’ model utilising the Discrete Element Method. Starting with a simple pure Mohr Coulomb sequence, we added an embedded viscoelastic-plastic layer within the brittle, undeformed ‘sediment’ package. This layer followed the Burger’s rheology, which simulates the creep behaviour of natural rocks, such as evaporites. This layer got thrust and folded during the subduction process. The testing of different bulk viscosity values, from 1×10^{13} to 1×10^{14} Pa s, revealed a certain range where an active detachment evolved within the viscoelastic-plastic layer that decoupled the over- and the underlying brittle strata. This mid-level detachment caused the evolution of a frontally accreted wedge above it and a long underthrust and subsequently basally accreted sequence beneath it. Both sequences are characterised by specific mass transport patterns depending on the used viscosity value. With decreasing bulk viscosities, thrust systems above this weak mid-level detachment became increasingly symmetrical and the particle uplift is reduced, as would be expected

for a salt controlled forearc in nature. Simultaneously, antiformal stacking is favoured over hinterland dipping in the lower brittle layer and overturning of the uplifted material increased. Hence, we validated that the viscosity of an embedded detachment strongly influences the whole wedge mechanics, both the respective lower slope and the upper slope duplex, shown by e.g., the mass transport pattern.

1. Introduction

The kinematics and mechanics of accretionary wedges utilising the brittle Mohr Coulomb rheology have been in the focus of analog and numerical modelling studies for decades (e.g., Mulugeta, 1988; Mugnier et al., 1997; Lohrmann et al., 2003; Konstantinovskaya and Malavieille, 2011; Burbidge and Braun, 2002; Ellis et al., 2004). These brittle accretionary wedges are characterised by their accretion mode (defined as frontal and basal accretion), subsequent fault kinematics, total taper (amount of the surface slope α and the basal slope β), and the mass transport patterns of the accreted material (Davis and Engelder, 1985; Cloos and Shreve, 1988). These features are functions of the physical properties of the incoming sediments according to the Critical Taper theory by Davis et al. (1983), Dahlen (1984) and Dahlen et al. (1984).

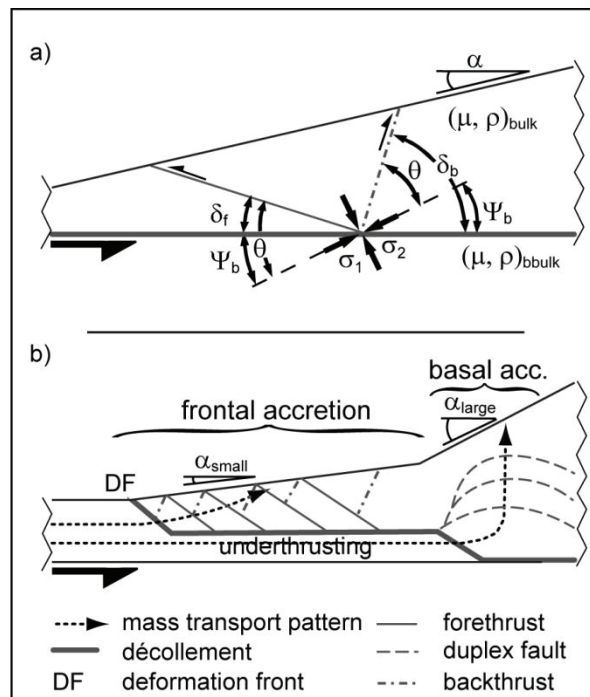


Fig. IV-1: a) The relation between the principal stress field and the conjugated fore- and backthrusts in an accretionary wedge (after Davis and Engelder, 1985). The thick black half-arrow indicates subduction.

Variables: (α) angle of surface slope; (σ_1) max. principle stress; (σ_2) min. principle stress; (Ψ_b) angle between σ_1 and the detachment; (δ_f) rising angle of forethrust; (δ_b) rising angle of backthrusts; (μ) friction; (ρ) density; after the Critical Taper theory by Dahlen et al. (1984). b) The fault geometries and mass transport pattern in the case of frontal and basal accretion after Cloos and Shreve (1988).

In several studies, the role of the friction coefficient of the incoming strata (μ) and, particularly, the friction coefficient at the basal detachment (μ_b) on which the wedge grows

(the so-called *décollement*) are identified as important factors that determine the kinematics and mechanics of wedge evolution (e.g., Moore, 1989; Gutscher et al., 1998b; Hardy et al., 1998).

If a wedge grows above a low friction or mechanically weak *décollement*, a low tapered, frontally accreted wedge evolves (e.g., Davis and Engelder, 1985). In this case, material is slightly uplifted and accreted along steep dipping forethrusts (δ_f) and backthrusts (δ_b) with low offsets. These thrusts develop more symmetrically with similar dipping angles and a low angle between the mean stress σ_1 direction and the *décollement* (ψ_b) (Fig. IV-1a). With increasing basal strength, fore- and backthrusts evolve asymmetrically, with shallow, dominant forethrusts, steep backthrusts (foreland vergence), and a large angle between the mean stress σ_1 direction and the *décollement* (ψ_b) (Chapple, 1978; Davis and Engelder, 1985; Bonini, 2007; Fig. IV-1a). In the case of high basal friction or a strong detachment compared to the internal wedge strength, the material is rather underthrust away from the deformation front (DF) and is subsequently basally accreted (e.g., Davis et al., 1983; Fig. IV-1b). The latter process can cause the development of duplex structures, which, in turn, cause strong vertical uplift of the material. This is associated with an increase in slope taper (e.g., Cloos and Shreve, 1988; Von Huene and Scholl, 1991; Gutscher et al., 1998a). In natural systems, *décollements* are generated along, e.g., embedded clays (e.g., the Kodiak accretionary complex; Sample and Fisher, 1986), turbidity layers (e.g., the Makran wedge; Fruehn et al., 1997) or evaporites (e.g., the Mediterranean Ridge; Reston et al., 2002b). *Décollements* in evaporites are very weak and lead to wide extended wedges with low tapers and a non-preferred or doubly vergent thrust system (e.g., Davis and Engelder, 1985; Marshak and Wilkerson, 1992; Cotton and Koyi, 2000; Costa and Vendeville, 2002; Bahroudi and Koyi, 2003). In recent years, various studies investigate the kinematics of those wedges, incorporating viscous and/or ductile materials (e.g., Bonini, 2001, 2007; Costa and Vendeville, 2002; Couzens-Schultz et al., 2003; Smit et al., 2003; Selzer et al., 2007; Stockmal et al., 2007; Storti et al., 2007; Yamato et al., 2011). Although these studies reveal the role of such mechanically weaker layers that act as potential *décollements* for fault kinematics and accretion modes, there is a lack in knowledge regarding the mass transport pattern of the accreted materials as well as the fault angle evolution as a function of the viscosity magnitude of such detachments. The reasons for this are the limitations of the methods for analysis of material transport in analog models (e.g., Koyi and Vendeville, 2003; Costa and Vendeville, 2002) and the fact that simulations exclude discrete thrusting

and shear surface formation of localised deformations over long distances in most continuum models (e.g., Selzer et al., 2007).

Therefore, we use a particle based granular model approach, the Discrete Element Method (DEM), to develop a numerical 2D ‘sandbox’ experiment. This technique is successfully used to simulate large scale strain and localised deformation as well as complex tectonic processes in brittle, upper crustal materials (Burbidge and Braun, 2002; Naylor et al., 2005; Miyakawa et al., 2010). Furthermore, besides a brittle rheology also viscoelastic-plastic material behaviour can be simulated with this technique (e.g., Kim et al., 2009). This approach allows for the investigation and, particularly, quantification of the influences of a heterogeneous sediment input. However, until now this technique has not been used to simulate accretionary wedges that incorporate a viscoelastic-plastic décollement. We undertake a parameter study, where the viscosity of an embedded layer (experimental series V1-V6) is gradually changed to test the applicability of viscoelastic-plastic DEM experiments for such simulations. Simultaneously, we carry out an experiment with a homogeneous brittle wedge (experiment H), serving as our standard Mohr Coulomb model to allow for a comparison and evaluation with analog sandbox experiments (e.g., Huiqi et al., 1992; Gutscher et al., 1998a; Kukowski et al., 2002; Konstantinovskaya and Malavieille, 2011) and numerical experiments (Miyakawa et al., 2010). Hence, the parameter study is designed to develop and test a conceptual model of viscoelastic-plastic décollements and the associated mass transport pattern rather than the simulation of a specific forearc region.

Our studies quantify the influence of a viscoelastic-plastic layer with different viscosity values embedded in an undeformed incoming brittle ‘sediment’ stratum on the mechanics of an evolving accretionary wedge. We examine the following questions: Is this technique suitable for simulating evaporitic décollements? How does an embedded viscoelastic-plastic layer with different viscosities affect the mechanics of an evolving accretionary wedge, particularly the thrust system and the mass transport pattern in the upper and lower brittle sediment layers? Can we identify a critical viscosity threshold to localise deformation along this viscoelastic-plastic layer generating a detachment?

To address these questions, we analyse the evolving slope geometries, internal structures, such as thrust evolution in space and time, as well as the mass transport patterns.

2. Method

2.1 Discrete Element Method

The Discrete Element Method (DEM) was developed by Cundall and Strack (1978) and Cundall (1987) and serves as the basis for the commercial code PFC2D (ITASCA), which is used for this study. This software simulates granular materials by using distinct rigid elements of any simple spherical shape, such as disks, balls, spheres, and cylinders. Particles can be displaced in any direction forced by the given boundary conditions, while interacting and overlapping with the neighbouring elements (Cundall and Strack, 1978). These interactions simultaneously cause two kinds of contact forces at each particle contact: (1) normal forces (F_n) perpendicular to the contact plane and (2) shear forces (F_s) parallel to the contact plane. Forces are calculated according to the magnitude of the overlap and the physical parameters of the interacting particles (density, particle stiffness, contact stiffness, friction, etc.) via simple physical laws (Mindlin and Deresiewicz, 1953; Cundall and Strack, 1979; Morgan and Boettcher, 1999). Calculated shear forces are used to define if particles are gliding away, in a tangential direction, in association with contact break. Subsequently, all forces acting on a single particle are added together following the Newton's law to calculate the resulting particle displacements (d) via force-displacement laws.

See Cundall and Strack (1978, 1979, 1983), Cundall (1987) or the PFC2D ITASCA Manual (2004) for a more detailed description of the DEM code. Please note that the defined single particle properties vary (e.g., particle friction) from the overall macro properties (e.g., bulk friction) of the entire particle assembly (Cundall and Strack, 1983). Hence, these overall macro properties must be measured and calculated for each individual particle assembly (see Sec 3.1).

2.2 Rheologies simulated with the DEM

The DEM offers a wide rheological spectrum to model different types of natural materials, such as those with elastic, plastic, or viscoelastic-plastic behaviour. Rheologies are implemented by adjusting the contact force calculations or the employed physical laws, respectively (ITASCA Manual, 2004).

2.2.1 Elasto-plastic rheology

Elastic deformation follows the linear Hooke's law and is comparable to the physical behaviour of a spring (*Hookean* model; Fig. IV-2c). The physical parameters normal and shear particle stiffness (k_{particle} , k_{particle}) are thereby comparable to the spring constant. If forces are applied on particles with an elastic behaviour, the responding instantaneous strain-rate (ϵ_0) remains constant over time (t) (Fig. IV-2a). If the contact shear force (F_s) exceeds the critical shear strength, frictional particle contacts break, sliding occurs, and the numerical material is plastically deformed. The contact forces (F_n , F_s) and, subsequently, the particle displacements (d) are calculated depending on normal and shear particle stiffness (k_{particle} , k_{particle}), the coefficient of particle friction (μ_{particle}), and particle density (ρ_{particle}) (Fig. IV-2c). The particle density defines together with the particle radius the weight of the particles and, therewith, the normal loading on lower particles and is also used to define the calculation time step. Using this contact law, an elasto-plastic rheology, similar to Mohr Coulomb can be simulated (Morgan and Boettcher, 1999; Kock and Huhn, 2007). This elasto-plastic material deforms similarly to the brittle upper crust and, therewith, allows for the simulation and investigation of the deformation processes of accretionary wedges (Naylor et al., 2005; Miyakawa et al., 2010). This numerical material is, hereafter, referred to as brittle material.

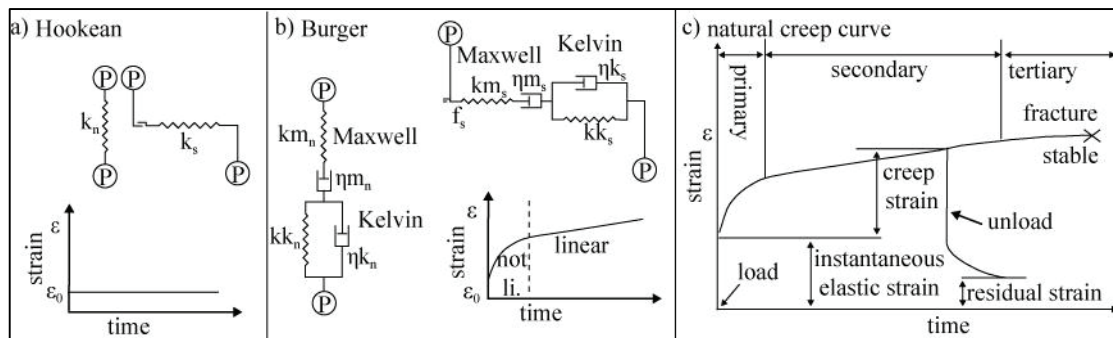


Fig. IV-2: The material curve for an elastic body described by a) the Hooke's law and b) the Burger's law, similar to the creep behaviour of rocks; the mechanical attributes of the c) *Hookean* model (modified after ITASCA Manual, 2004) and d) the Burger's model (modified after ITASCA Manual, 2004). Grey spheres represent interacting particle. Variables: (k_{particle}) normal particle stiffness; (k_{particle}) shear particle stiffness; (μ) coefficient of particle friction; (η_{particle}) normal particle viscosity; (η_{particle}) shear particle viscosity; (t_{bulk}) model time; (ϵ_0) instantaneous strain; (ϵ) strain. e) creep behaviour of natural rocks.

2.2.2 Burger's model

Natural rocks such as evaporites (e.g., halite or anhydrite) break under short acting forces and start to creep under long acting forces already in case of low temperature conditions (Le Comte, 1965). The creep curve of such viscous or ductile materials has three different sections: the transient (primary), the secondary (steady state) and the tertiary phase of creep (Lama and Vutukuri, 1978; Fig. IV-2e). The primary phase, which follows after application of the loading and an instantaneous elastic response, is non-linear and recoverable. The permanent deformation takes place in the secondary phase, which will be displaced by the accelerated creep of the tertiary phase eventually leading to failure.

To simulate such a material behaviour in DEM, the viscoelastic-plastic Burger's model is used for this study. Therefore, the elastic *Hookean* model (spring) is extended by viscous components represented by dashpots (Barnes, 2000; Fig. IV-2d). The strength of the dashpots (*Newtonian* model) is defined by the particle viscosity and they are used to absorb or dissipate tension or compression forces (F_n , F_s) and, therefore, mimic an idealised viscous behaviour. It reveals an instantaneous response with a linear increasing strain ϵ_0 as a function of time (t) and applied forces (Fig. IV-2b). The contact forces are calculated depending on the combination of two springs and two dashpots. First, a spring and a dashpot are connected in parallel for the *Kelvin* section and second, they are connected in series for the *Maxwell* section (Fig. IV-2d). This combination of two sections enables simulation of both the non-linear primary (*Kelvin* section) and the linear secondary phase (*Maxwell* section) of creep for natural rocks (Fig. IV-2b, e).

For both the *Kelvin* and *Maxwell* sections, the particle density (ρ_{particle}) as well as the particle viscosities, and contact stiffness in both the shear (η_{particle} , k_{contact}) and normal (η_{particle} , k_{contact}) direction must be defined. In addition, for the usage of this rheology in PFC2D, a coefficient of particle friction (μ_{particle}) must be defined to give the system an additional plastic component. Consequently, the whole system contact law represents a viscoelastic-plastic rheology that is only active if two or more particles with this rheology come in contact. Otherwise, the Hooke's law is used for the calculation. For more details please see Wenk and Huhn (2013b).

2.3. Model configuration

The model is designed as a numerical ‘sandbox’ adopting the general settings from lab experiments (Fig. IV-3a). Such simplified model settings are successfully used in numerous analog and numerical studies to simulate and analyse accretionary wedges (Kukowski et al., 2002; Konstantinovskaya and Malavieille, 2011; Fillon et al., 2012) and, hence, allows for comparison to analog experiments. Additionally, these simplified settings increase the process-based understanding in order to develop a conceptual model of wedges with viscoelastic-plastic décollements.

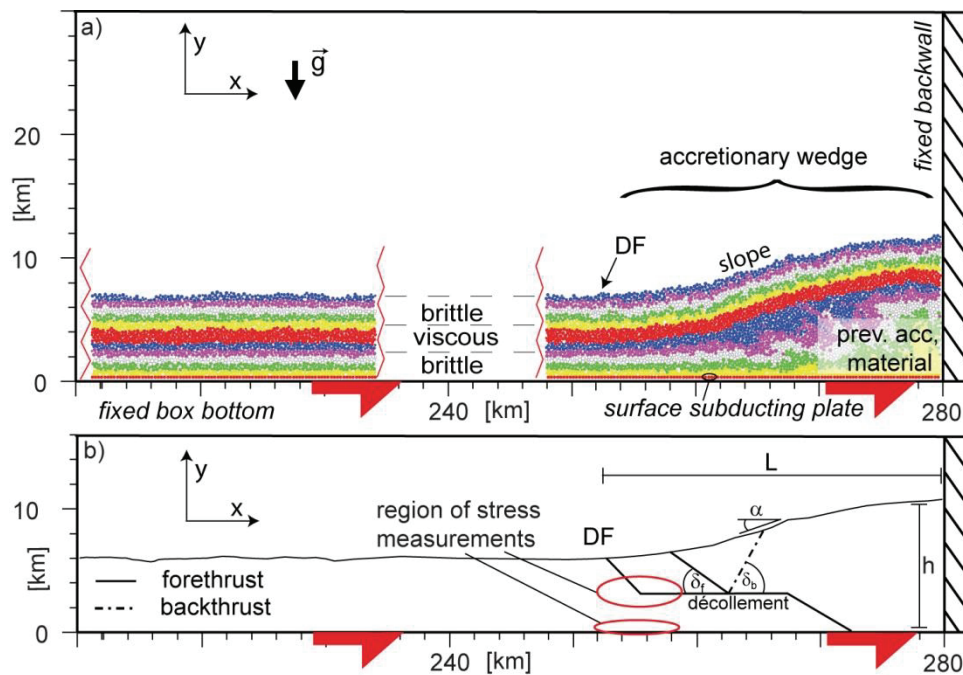


Fig. IV-3: a) A schematic view of the initial stage of the model series after previous material accretion (prev. acc. material). The different colours are used as marker horizons. The red layer indicates the position of the embedded layer having a brittle Mohr Coulomb rheology in experiment H and a Burger’s rheology in series V. ‘Subduction’ induced by the moving box bottom is shown by a red half-arrow. b) Line drawings of the analysed structures: surface slope (α), dip angles of thrusts (δ_f , δ_b), length (L) and height (h). Red ellipses mark the position of regions for normal and shear stress measurements to analyse bulk properties.

The ‘sandbox’ consists of a rectangular box with a fixed box bottom having a total length of 280 (km), and two fixed, vertical side-walls with heights of 30 (km). All walls are composed of spherical brittle particles with a homogeneous diameter of 125 (m) that act as stiff undeformable boundaries. During all experimental runs, the box bottom has a fixed dip angle of $\beta = 0^\circ$ (Fig. IV-3a) and moves with a constant velocity (see Sec. 3.1), in positive x-direction to simulate the subduction of a down-dipping oceanic plate.

The entire box is gradually filled with randomly distributed spherical particles of three different diameters (100, 125, and 150 μm). The distribution of the particle size follows a logarithmic normal distribution. In accordance to this distribution, the numbers of particles for each of the three diameters are chosen. Afterwards, they settle, under standard gravity ($g = 9.81 \text{ m/s}^2$), on the box bottom to generate the undeformed ‘marine sediment’ layer. These particular settings of three sizes prevent symmetrical particle packing and, hence, unrealistic deformations (Saltzer and Pollard, 1992). Identical particle configurations are used in all experiments. Standard gravity is active during the entire experiment.

The underlying section of the incoming strata is designated as a 3 km thick lower brittle layer (12,000 particles). After generation, this layer is accreted against the fixed right box-wall until a stable wedge taper is achieved. This critical wedge later acts as a deformable previously accreted wedge similar to a backstop (Fig. IV-3a), which is essential to investigate the wedge evolution while reducing boundary effects caused by the right side-wall acting as a fixed back-wall (Byrne et al., 1993). This model is used as an initial stage for all parameter studies, to reduce the calculation times prior to development of a stable wedge model. On top of this wedge, a second layer (6,000 particles), with a homogeneous thickness of 1.5 km, followed by a third 3 km thick cover layer (12,000 particles), is deposited. In total, the incoming section has an absolute thickness of 7.5 km, similar to values from, e.g., the Mediterranean Ridge (Finetti, 1976; Kastens et al., 1992). All geometrical parameters and boundary conditions are held constant throughout the model series H and V1-V6.

All experiments are simulated until a final stage of 57 % shortening. For such a model run 45 days computational time are needed on a 2 Quad CPU Core computer with 2.83 GHz. Therewith the modelled time step of one cycle step is on average $2.5 \times 10^{-2} \text{ s}$ defined by the program itself.

In experiment H, the entire incoming sediment sequence has a Mohr Coulomb rheology with identical properties for the particles comprising the walls. The particle properties required to simulate the brittle material are held constant for all experiments (Table IV-1). In series (V), the embedded (second) layer follows a viscoelastic-plastic rheology that behaves according to the Burger’s model. For our parameter study, we systematically vary the material behaviour or the respective particle viscosity of this embedded layer (V1-V6). Six different shear and normal particle viscosities (η_{particle} , $\eta_{\text{sparticle}}$), varying from 1×10^{16} ,

5×10^{16} , 7×10^{16} , 1×10^{17} , 1×10^{19} to 1×10^{25} Pa s, are tested (see Table IV-1). All other material properties of this viscoelastic-plastic are held constant.

All defined particle properties for the brittle and viscoelastic-plastic layers are shown in the Table IV-1. These values are chosen and calibrated to reproduce natural behaviour of marine sediments (Spiers et al., 1990; van Keken et al., 1993; Turcotte and Schubert, 2002) which are already used in previous studies to successfully simulate accretionary wedges or viscous material behaviour (e.g., Ting et al., 1989; Jensen et al., 1999; Burbidge and Braun, 2002; Naylor et al., 2005; Chemia and Koyi, 2008).

2.4 Model simplifications

Although we are aware that the incoming sequence in nature has a much finer stratification and a more complex property variation, we simulate a homogeneous brittle sediment packages. Pore fluids and cohesions are not taken into account in our simulations similar to analog experiments using dry sands. One additional simplification is that we use a horizontal detachment with a dipping surface slope of $\beta = 0^\circ$. In this case the surface slope angle α increases. Additionally, the base is rigid as it consists out of fixed particles which move all with a constant velocity in the positive x-direction. This all together has an influence on the absolute values of wedge tapers and thrust angles. Due to this simulation approach, thrust angles and slope geometries cannot be transferred directly into natural systems, but can be compared with analog experiments (Morgan and Boettcher, 1999). Besides, these simplifications are commonly successfully used for modelling accretionary wedges (Davis et al., 1983; Mulugeta, 1988; Burbidge and Braun, 2002; Smit et al., 2003; Stockmal et al., 2007) and enable the testing of controlling factors and the development of conceptual models.

2.5 Model analysis and interpretation techniques

Based on the granular model approach, detailed information about shear and normal stresses and particle positions as well as relative particle displacements at each calculation step are extracted and saved every 0.05 % of shortening corresponding to 200 m of 'subduction', during the entire model run of each experiment to generate a continuous time series.

For a first impression of transport patterns and internal structures, horizontal layers are initially coloured similar to analog sandbox experiments (e.g., Burbidge and Braun, 2002; Costa and Vendeville, 2002; Costa et al., 2004; Konstantinovskaya and Malavieille, 2011) and plotted as a particle configuration view (Fig. IV-3a, IV-5). These plots are further used to measure mean values of surface slope angles. Therefore, depending on the topographic differences, the wedge surface is divided in three or four areas in which the surface slope angles are measured and mean values are calculated. Note that as DEM models consists of spherical particles the surface slope has a rough topography. Such roughness structures are ignored while measuring.

Following on from that, relative displacements of each particle in the x- and y-directions are calculated and plotted for each ‘subduction’ interval of 200 m showing the incremental strain. These reveal zones where particles exhibited large relative offsets between particles moving in blocks in the opposite direction of neighbouring blocks (Morgan and Boettcher, 1999). Zones of large offsets can be interpreted as active thrust zones in these relative displacement plots (Fig. IV-6, IV-7). Based on our model configuration, whereupon the origin of our coordinate system is located in the lower left corner, these thrusts can be interpreted as “landward” dipping forethrusts or “seaward” dipping backthrusts (Fig. IV-6). However, it should be pointed out that only thrusts that are active during this time period of 0.05% or 200 m can be monitored (e.g., Kock and Huhn, 2007). To track older inactive shear zones throughout the experimental run, a combination of the particle configuration view and the relative displacement plot is essential (Huhn et al., 2006). Based on these analyse methods, it is possible to simulate thrust kinematics at a high resolution in both space and time.

In addition, the granular model approach allows for acquisition of high resolution information about the mass transport pattern through the tracking of single particles during the entire experiment (Fig. IV-5). For this, particles are randomly chosen to ensure a representative picture. The combined methods described here allow for wide-ranging analyses of the wedge kinematics and deformational domains.

3. Results

3.1 Bulk material parameters

As already mentioned, the micro particle properties of a single particle do not correspond to the bulk macro properties of the entire particle assemblage. Hence, the values of the bulk material properties are first tested and the micro properties are defined to simulate natural material behaviour. In this case, the average values of the normal stress (σ), the shear stress (τ), and the particle velocity (u) for different time steps are extracted directly in front of the deformation front (Fig. IV-3b; Table IV-1). The latter are used to calculate the shear velocity ($\partial u/\partial y$) and dynamic viscosities (η_{dynamic}) with (x, y) representing the coordinates of the 2D-plane. In the next step, the bulk friction is calculated following the equation (eq. IV-1):

$$\mu_{\text{bulk}} = \frac{\tau}{\sigma} \quad (\text{eq. IV-1})$$

For calculation of the dynamic viscosity, the following equation (eq. IV-2) is used:

$$\eta_{\text{dynamic}} = \frac{\tau}{\partial u/\partial y} \quad (\text{eq. IV-2})$$

All calculated values are presented in the Table IV-1.

For the basal detachment, a low particle friction is used ($\mu_{\text{bparticle}}=0.2$). The resultant bulk friction is $\mu_{\text{bbulk}}=0.33$. The difference between the basal particle friction ($\mu_{\text{bparticle}}$) and the bulk detachment friction (μ_{bbulk}) results from the restriction that the basal particles building up the detachment are not allowed to rotate (Morgan and Boettcher, 1999).

For calculating the critical taper angle α , the following equations are used:

$$\alpha = \left(\frac{\mu_{\text{bbulk}} + \beta}{1+K} \right) - \beta \quad (\text{eq. IV-3})$$

where K is a dimensionless factor (Dahlen et al., 1984). This factor is calculated as follows

$$K = \frac{\sin \phi_{\text{bulk}}}{1 - \sin \phi_{\text{bulk}}} + \frac{\sin^2 \phi_{\text{bbulk}} - \cos \phi_{\text{bbulk}} (\sin^2 \phi_{\text{bulk}} - \sin^2 \phi_{\text{bbulk}})^{1/2}}{\cos^2 \phi_{\text{bbulk}} - \cos \phi_{\text{bbulk}} (\sin^2 \phi_{\text{bulk}} - \sin^2 \phi_{\text{bbulk}})^{1/2}} \quad (\text{eq. IV-4})$$

with $\phi_{\text{bulk}} = \arctan \mu_{\text{bulk}}$ and $\phi_{\text{bbulk}} = \arctan \mu_{\text{bbulk}}$.

As a result, the critical taper angle α in experiment H with is 12° in the case of a μ_{bulk} of 0.33 at the deformation front.

The particle viscosity values (η_{particle}) are inversely proportional to the dynamic viscosity (η_{dynamic}), as the dynamic viscosity decreases with increasing particle viscosity. This results from a decrease in particle overlap, which leads to a decreasing contact plane and a decreasing shear stress. This, consequently, reduces the bulk friction in the case of an increase in the particle viscosity.

For comparison to natural materials, dynamic viscosity values are scaled based on their time-dependency similar to analog experiments (e.g., Storti et al., 2007). Natural convergence rates at subduction zones are in the range of $\sim 4\text{-}5$ cm/y (e.g., at the Mediterranean Ridge; Bohnhoff et al., 2001). The applied numerical subduction velocity of 0.2 m/s results in a time scaling factor ($t_{\text{nature}}/t_{\text{bulk}}$) of 1.58×10^8 where t_{nature} is the time in nature and t_{bulk} is the corresponding model time. The natural viscosity η_{nature} for our model can be obtained by the following equation (Weijermars and Schmeling, 1986):

$$\eta_{\text{nature}} = \frac{t_{\text{nature}} \times \eta_{\text{dynamic}}}{t_{\text{bulk}}} \times \frac{\rho_{\text{bulk}} \times g_{\text{bulk}} \times l_{\text{bulk}}}{\rho_{\text{nature}} \times g_{\text{nature}} \times l_{\text{nature}}} \quad (\text{eq. IV-5})$$

where t is time, l is the length, g is standard gravity, and ρ is density. By assuming a length ratio of $l_{\text{bulk}} = l_{\text{nature}}$, a density ratio of $\rho_{\text{bulk}} = \rho_{\text{nature}}$ and standard gravity conditions $g_{\text{bulk}} = g_{\text{nature}}$ the dynamic viscosity ($\eta_{\text{dynamic}} = 5.4 \times 10^{13}$ Pa s) in experiment V6 results in a calculated ‘natural’ viscosity of $\eta_{\text{nature}} = \sim 7.6 \times 10^{21}$ Pa s. The viscosity in experiment V6 most likely simulates natural values of rock salt or evaporites, which are between 10^{18} Pa s and 10^{21} Pa s (van Keken et al., 1993; Spiers et al., 1990; Chemia and Koyi, 2008; Mukherjee et al., 2010). In contrast, in experiment V1, a higher dynamic viscosity of $\eta_{\text{dynamic}} = 4.8 \times 10^{14}$ Pa s results in a ‘natural’ scaled viscosity of $\eta_{\text{nature}} = \sim 6.7 \times 10^{22}$ Pa s, which is slightly higher than the natural range. As outlined above, an inverse relationship exists between the particle viscosity and the dynamic viscosity. We, hereafter, define a high particle viscosity layer with a low dynamic viscosity as weak material, because the resulting stresses along this layer are low. Likewise a low particle viscosity layer with a high dynamic viscosity is, hence, referred as strong because the resulting stresses are high.

3.2 Mechanics of the experiments H and V1-V6

In all numerical experiments (H, V1-V6), a triangular wedge with certain wedge tapers ($\alpha_1, \alpha_2, \alpha_3, \alpha_4$), lengths (L =distance between DF and back-wall), and thicknesses (h =distance between box bottom and top of wedge surface) develops due to the 'subduction' (Fig. IV-3b, 5, 6). The toe of these wedges always correlates with the deformation front (DF). Thrust angles for fore- and backthrusts, as well as slope angles are average values measured over the whole experimental run.

3.2.1 Homogeneous incoming 'sediment' sequence (experiment H)

A stable convex shaped wedge with a constant slope taper evolves after 15 % shortening (Fig. IV-4). Thereafter, the wedge grows while retaining a constant geometry by accumulating new material at the toe. Wedge evolution is controlled by one accretion mode resulting in one deformation segment. After 57 % shortening, the wedge has a total length of $L = 87.2$ km and a maximal thickness of $h = 23$ km.

In Figure IV-6, it is shown that the youngest forethrusts with average dip angles of $\delta_f \sim 24^\circ$ mark the DF. These thrusts cut through the whole strata and uplift the overlying material slightly towards the back-wall. Accordingly, the particles rise gently close behind the wedge toe with an uplift angle of $\sim 20^\circ$ (Fig. IV-5). These thrusts and material paths mark the position of the lower wedge having a slope angle of $\alpha_1 \sim 15^\circ$.

The forethrusts are rotated further inward and reactivated as long, shallow dipping thrusts ($\delta_f \sim 15^\circ$) imbricating the incoming material (Fig. IV-6). Associated with these forethrusts, conjugated, less-pronounced backthrusts ($\delta_b \sim 75^\circ$) are observed. The material is even more vertically uplifted as indicated by an increase in the uplift angles of the mass transport pattern to angles of $\sim 42^\circ$ (Fig. IV-5). In addition, the slope taper flattens, creating a convex shaped upper wedge, which exhibits a slightly smaller slope angle of $\alpha_2 \sim 12^\circ$ and a flat plane on top with a slope angle of $\alpha_3 \sim 4^\circ$. The highest uplift is exhibited in this area. This upper wedge consists of previous frontally accreted units that are continuously uplifted at a constant angle (Fig. IV-5).

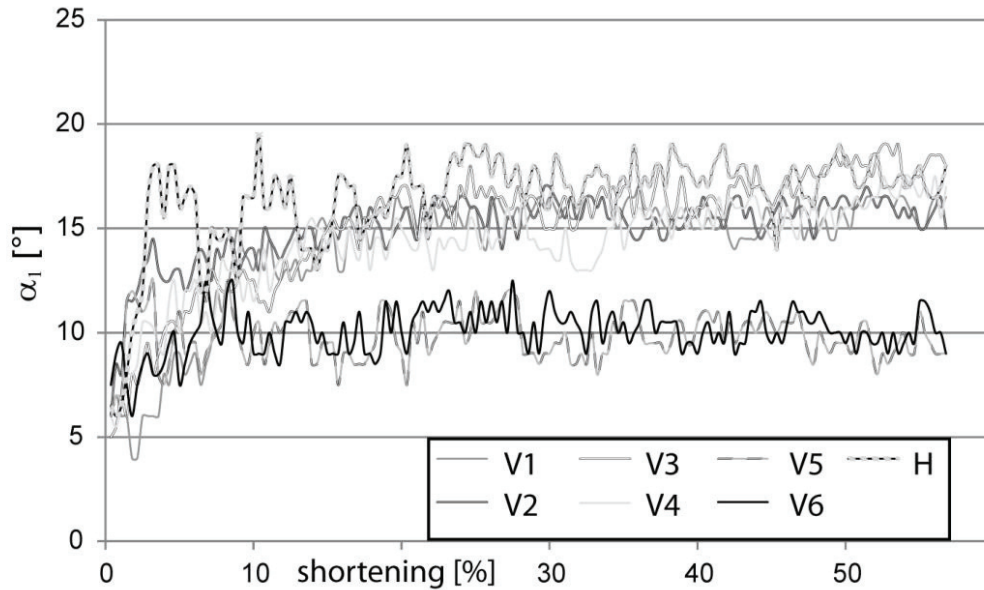


Fig. IV-4: Mean slope angle α_1 at the frontal wedge in the vicinity of the deformation front during shortening.

In addition, out-of-sequence thrusts (OOSTs), with a mean dip angle of $\delta_f \sim 25^\circ$, are frequently activated at the upper slope (Fig. IV-6, IV-7). These OOSTs cut through the entire wedge from the décollement to the surface. They separate the flatter more inactive upper wedge from the previously accreted lower wedge (Fig. IV-6, IV-7).

3.2.2 Heterogeneous incoming 'sediment' input with an embedded viscoelastic-plastic layer (experiment series V)

The heterogeneous models contain a viscoelastic-plastic layer embedded between two undeformed brittle layers. The dynamic viscosity of this layer gradually decreases from 4.8×10^{14} Pa s in V1 to 5.4×10^{13} Pa s in V6 (see Table IV-1). After a shortening of at least 28 %, stable convex shaped wedges with constant slope tapers evolve within all experiments (Fig. IV-4). Once reaching stable tapers, these wedges grow while retaining a constant geometry by accumulating material (Fig. IV-7). All experiments are simulated until a final stage of 57 % shortening.

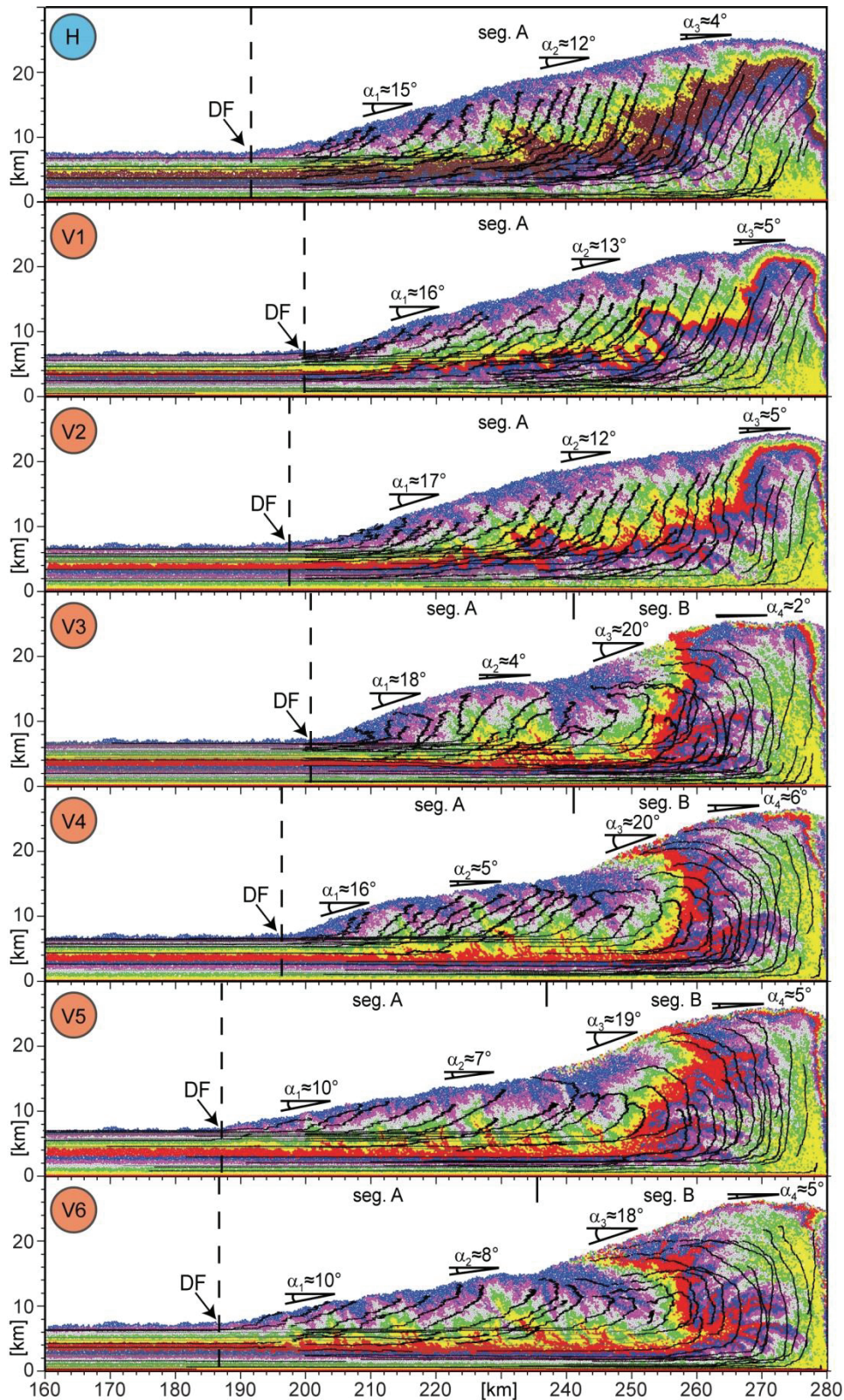


Fig. IV-5: Particle configuration view of the model series H and V1-V6 after 42 % of shortening. The different colours are used as markers of horizons to visualise thrusts. The brown layer in series H has a brittle Mohr Coulomb rheology and the red layers in series V have a Burger's rheology. The wedge segments, DF (deformation front), and slope angles α_{1-4} are labelled for every experiment. The black lines mark the particle tracks or the mass transport pattern respectively.

With respect to the varying dynamic viscosity of the embedded layer, wedges with different total lengths (L), maximal thicknesses (h), slope tapers ($\alpha_1, \alpha_2, \alpha_3, \alpha_4$), different internal geometries and, therewith, accretion modes evolve. Generally, wedges with strong viscoelastic-plastic layers (V1, V2) exhibit only one accretion mode and, therefore, only one wedge deformation segment (A; Fig. IV-6). In contrast, wedges with weaker viscoelastic-plastic layers (V3, V4, V5, and V6) exhibit at least two deformation segments (A, B). Here, the décollement is generated by two distinct layers. The décollement is located along the viscoelastic-plastic layer at the frontal part and stepped down to the basal box detachment next to the fixed back-wall.

3.2.2.1 Wedge tectonics in case of strong embedded layers (V1, V2)

At the end of the experiments, the total length of the accretionary wedges in V1 and V2 are $L = 80$ km and 82.5 km and the maximal thicknesses are $h = 21.5$ km as well as $h = 22.2$ km at the highest position (Fig. IV-6). Within these experiments, the frontal wedges (V1: $\alpha_1 \sim 16^\circ$, V2: $\alpha_1 \sim 17^\circ$) are built by thrusts with dip angles of $\delta_f \sim 24^\circ$, cutting from the box bottom through the whole strata with only a few conjugated backthrusts (V1: $\delta_b \sim 68^\circ$, V2: $\delta_b \sim 69^\circ$; Fig. IV-6). Mass transport patterns indicate that the incoming particles rise slightly behind the DF with an uplift angle of $\sim 19^\circ$ - 22° (Fig. IV-5). These thrusts are back-rotated and first-time reactivated as long imbricated thrusts with low dip angles (V1: $\delta_f \sim 13^\circ$, V2: $\delta_f \sim 15^\circ$), which exhibit similar overall angles compared to those in experiment H. Furthermore, for a short period, the thrust direction is parallel to the deformed embedded viscoelastic-plastic layer such that they rise from the box bottom and then run along the base of the viscoelastic-plastic layer (V1) or within the viscoelastic-plastic layer (V2) before they cut through the hanging material. Finally, the thrusts reach the wedge surface (Fig. IV-6). Offsets along these faults increase in V2 compared to V1 causing a higher internal shortening of the wedge. In addition, when particles pass the low angle forethrusts, the uplift angles of the particles increase to $\sim 41^\circ$ - 43° (Fig. IV-5). This effect is more pronounced in V2 compared to V1 and increase towards the back-wall in V2. In both cases, it remains smaller than in experiment H. The slope taper (V1: $\alpha_2 \sim 13^\circ$, V2: $\alpha_2 \sim 12^\circ$) becomes shallower at the upper wedge above these imbricated thrust units. Near the back-wall, a flat top with $\alpha_3 \sim 5^\circ$ evolve (Fig. IV-5, IV-6).

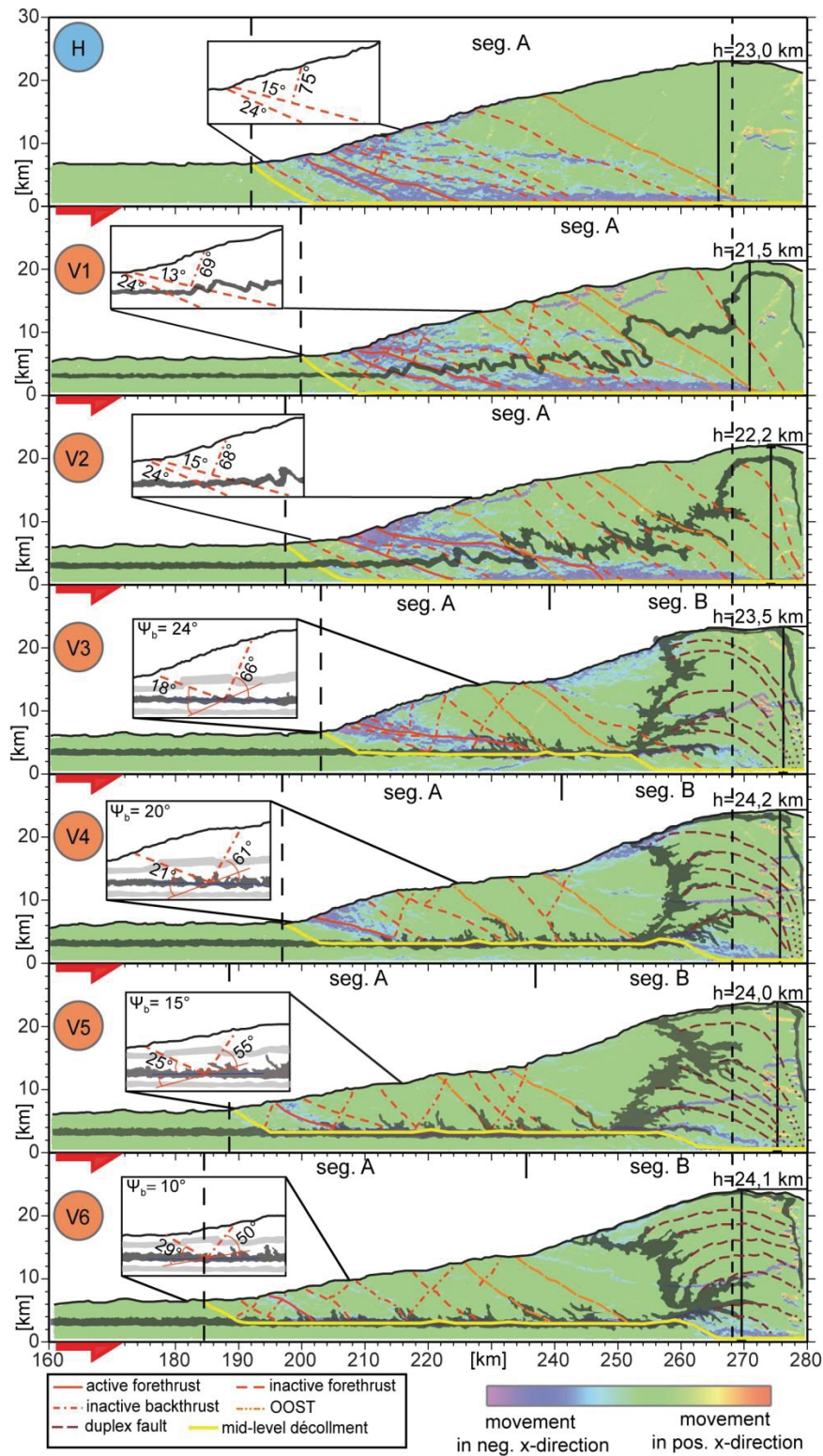


Fig. IV-6: Illustration of the relative displacement plot of the model series H and V1-V6. Red colours the maximum positive relative displacements and in magenta the maximum negative displacements are pictured. The displacements are calculated for 42% - 46% shortening. The actual position of the viscoelastic-plastic layer is shown in grey. Deformational wedge segments for all experiments are marked. For all experiments the mean angle Ψ_b and thrust dip angles $\delta_{e,b}$ are highlighted close to the deformation front. The black dashed line marks the border of the uninfluenced areas, inward structures are influenced by the strong back-wall.

Similar to those in series H, steeper thrusts are frequently re-activated at the upper wedge as second order OOSTs ($\delta_f \sim 27-28^\circ$), which separate the upper wedge from the flat previously accreted wedge. The OOSTs cut through the entire strata and reach the wedge surface (Fig. IV-6). Within the upper wedge, the particles are steeply uplifted in front of the fixed back-wall (Fig. IV-5).

3.2.2.2 *Wedge tectonics in case of an intermediate strong embedded layer (V3)*

The accretionary wedge in experiment V3 is the shortest, reaching a total length of $L = 78$ km and a maximal thickness of $h = 23.5$ km in the final stage (Fig. IV-6). In contrast to experiment H, experiments V1 and V2 reveal different deformation stages during wedge evolution. However, after 35% of shortening a constant wedge taper evolves (Fig. IV-7). Material is either frontally or basally accreted and two deformation segments evolve (A+B).

During the first 28 % of shortening, the wedge evolution is dominated by accretion with steep forethrusts and long, shallow-dipping imbricated thrusts ($\delta_f \sim 13^\circ$) showing similar behaviour as in experiment V1 and V2 (Fig. IV-6). In this stage, the entire wedge is characterised by one segment (A) and particle paths rise similar to those in previous experiments (Fig. IV-5). After 28 % shortening, these shallow dipping forethrusts are replaced by slightly steeper thrusts that rise from a distinct depth located in the undisturbed sediment sequence. These thrusts have dip angles of $\delta_f \sim 18^\circ$ (conjugated backthrusts: $\delta_b \sim 66^\circ$; Fig. IV-6). Their new intermediate detachment correlates with the embedded viscoelastic-plastic layer, which serves, henceforth, as a mid-level detachment (Fig. IV-6). This switch in thrust geometry and, hence, accretion mode (Fig. IV-5) leads to a continuously growing wedge above the viscoelastic-plastic layer and a build-up of the steep frontal slope ($\alpha_1 \sim 18^\circ$). Particle paths indicate that the material is very steeply uplifted with an angle of 65° just beyond the DF and the particle layer is even overturned (Fig. IV-5). The steep lower slope is followed by a flat plane with a slope taper of ($\alpha_2 \sim 4^\circ$) consisting of the previously imbricated units that are covered by the slipped masses from the upper slope. The particle paths within this flat plane have, in the early stage, a nearly vertical uplift that is subsequently replaced, in the latter stage of wedge evolution, by a slight material shift towards the previously accreted wedge (Fig. IV-5).

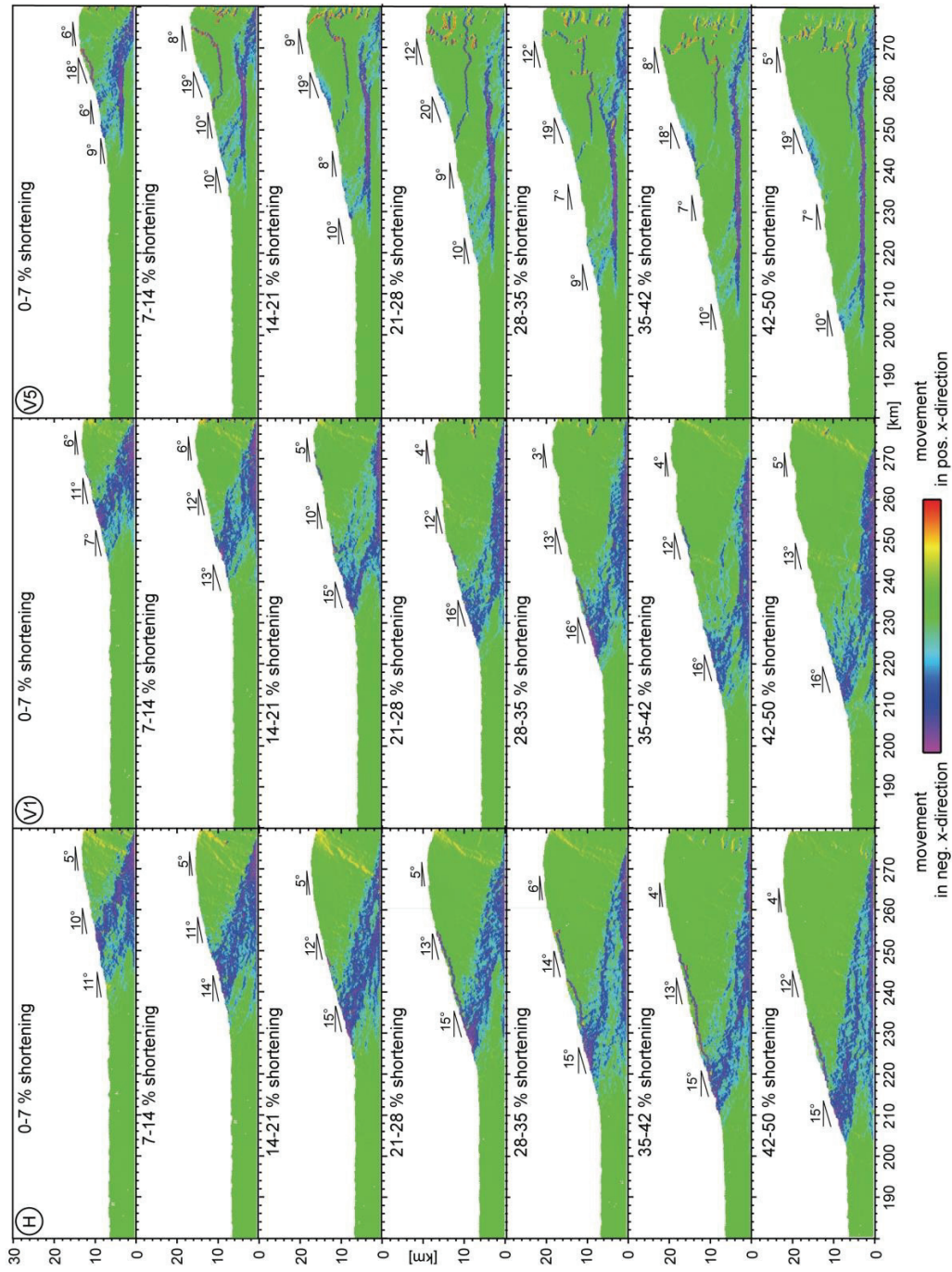


Fig. IV-7: Relative displacement plots for different shortening steps of model H, V1, and V5.

Due to the evolution of a mid-level detachment, material beneath the viscoelastic-plastic layer becomes far-underthrust under the lower slope by the moving basal box bottom. Approximately 40 km inward of the DF, this material is basally accreted while the mid-level detachment steps down to the basal box bottom. A hinterland-stacking and underplated duplex develops while hanging material and accreted strata are nearly vertically uplifted as indicated by steep particle paths (Fig. IV-5). After $\sim 35\%$ of shortening, this hinterland-dipping duplex transforms into an antiformal duplex (segment B), which causes an overtilt in the negative x-direction (Fig. IV-5). Viscoelastic-plastic material is incorporated and smeared along thrusts into the upper and lower brittle layer during basal accretion. Numerous mass wasting events occur and formerly buried brittle strata are exhumed. This is indicated by the outwardly directed particle pattern (Fig. IV-5) and creates a nearly flat, steeply uplifted plateau whose position correlates with the underplated duplex ($\alpha_4 \sim 2^\circ$; Fig. IV-6). Consequently, the steeper upper slope ($\alpha_3 \sim 20^\circ$) marks the position of the outward edge of the duplex structure.

Two main groups of OOSTs occur in experiment V3: (1) rising from the mid-level detachment ($\delta_f \sim 25^\circ$) to the surface splitting the active frontal wedge (segment A) from the flat inwardly located plane (Fig. IV-5); (2) at the border between the flat plane and the steeper slope (segment B) of the duplex structure rising with $\delta_f \sim 27^\circ$ (Fig. IV-6). Hence, they border the flat mid-slope plane while splitting the two main deformation segments identified by their accretion mode: A-frontally accreted and B-basally accreted.

3.2.2.3 *Wedge tectonics in case of weak embedded layers (V4-V6)*

At the end of the simulation, the wedge in experiment V4 has a length of $L = 84$ km. In experiment V5 and V6, the total length increases to $L = 93$ km. The maximum thicknesses are $h = 23.5, 24.2,$ and 24 km in experiments V4, V5 and V6 (Fig. IV-6). The wedges are classified by two segments based on the accretion mode (A and B) similar to V3. This segmentation in a frontal and basal accreted wedge becomes more pronounced with decreasing dynamic viscosity in experiments V4-V6. The décollement consists of two distinct parts: a shallow mid-level detachment, which steps during the whole experimental run down to the deeper positioned basal box bottom (Fig. IV-7). However, the depth position of the mid-level detachment is fixed along the viscoelastic-plastic layer.

Active fore- and backthrusts are still generated at the embedded viscoelastic-plastic layer and intersect the brittle cover of the frontal wedge (Fig. IV-6). The dip angles of the forethrusts increase with decreasing dynamic viscosity. The average values are $\delta_f \sim 21^\circ$ in V4, $\delta_f \sim 25^\circ$ in V5 and $\delta_f \sim 29^\circ$ in V6 (Fig. IV-6). At the same time, dip angles of the associated backthrusts decrease with decreasing dynamic viscosity with average values of $\delta_b \sim 61^\circ$ in V4, $\delta_b \sim 55^\circ$ in V5, and $\delta_b \sim 50^\circ$ in V6 and the taper of the frontal wedge (segment A) shallows with decreasing dynamic viscosity from $\alpha_1 \sim 16^\circ$ in V4 to $\alpha_1 \sim 10^\circ$ in V5 and V6 (Fig. IV-5). Moreover, the length of the frontal wedge increases from 40 km in V4 to 50 km in V6. Simultaneously, the material uplift behind the DF declines with decreasing dynamic viscosities. So, particle rise is much flatter past the DF in experiment V5 and V6 compared to all other experiments (Fig. IV-5). The uplift angles of the particle paths at the frontal wedge decrease from an angle of 38° in V4 to an angle of 22° in V5 and 20° in V6.

Sediments underneath the viscoelastic-plastic layer are underthrust and basally accreted at the rear verified by the mass transport pattern showing a nearly horizontal followed by steep material path (Fig. IV-5, IV-6). The material is imbricated along shallow dipping active shear zones generated at the basal box bottom. During imbrication, new thrusts evolve in front of the duplex and, consequently, the active deformation of this basally accreted duplex migrates together with the wedge toe outwards. Within this duplex structure formerly active thrusts become inactive, but can later also be temporarily reactivated. With increasing shortening, the offset along the shallow dipping thrusts building up the duplex increases and the hinterland-dipping duplex transforms again into an upward growing antiformal stack duplex. With decreasing dynamic viscosity, this transition to antiformal stacking is initiated at an earlier stage, e.g., long-lasting vertical uplift of hanging strata and duplex material (Fig. IV-5). Consequently, steep upper wedges at the outward flank of the duplex evolve. In the later stage, the former basally accreted material slides outwards on viscoelastic-plastic material, which is smeared along basal thrust into the duplex. This consequently reduces the slope angle of the upper wedge ($\alpha_3 \sim 20^\circ$ in V4 and $\alpha_3 \sim 18^\circ$ in V6). Additionally, an overturning of the duplex structure occurs (Fig. IV-5). This results in flank destabilisation in the uplifted upper wedge leading to numerous mass wasting events of the brittle strata, simultaneously causing the exhumation of older basally accreted strata, as well as weaker viscoelastic-plastic materials.

This effect of duplex overturning indicates a significant change in duplex evolution as observed by a break in the particle paths (Fig. IV-5). Afterwards, the material is transported nearly horizontally in the outward direction due to the mass wasting. This process is enhanced with decreasing dynamic viscosity.

Hence, the dynamic viscosity of an embedded layer controls both the frontal wedge (segment A) and the basally accreted duplex (segment B). Both segments are separated by a transition zone marked by a nearly flat mid-slope plane with $\alpha_2 \sim 5^\circ$ in V4 to $\alpha_2 \sim 8^\circ$ in V6 (Fig. IV-5). In the early stage, particle paths in this transition zone are characterised by a slight uplift towards the back-wall, as is typical for frontal accretion. This is followed by a vertical uplift and overturning due to the outwardly propagating uplifted material from the upper wedge, which applies as a result of its vertically spreading pressure from the side on the lower wedge.

Similar to V3, two types of OOSTs occur which again split the different deformation domains: the frontal wedge (segment A) from the flat inward located plane ($\delta_f \sim 25-28^\circ$, segment A) and the plane from the steep upper slope ($\delta_f \sim 30-32^\circ$; segment B). In general, the number of reactivated OOSTs decreases with decreasing dynamic viscosity in V4 to V6.

4. Discussion

4.1. Homogeneous wedge (H)

A triangular stable accretionary wedge with gentle slope tapers decreasing upslope (from $\alpha_{1/2} \sim 15^\circ$ to $\sim 12^\circ$) develops in experiment H. Such convex shapes can be observed in many other analog or numerical wedge studies and may result from an increase in the bulk strength in the inward direction of the frontal wedge (Lohrmann et al., 2003; Miyakawa et al., 2010). Comparing, the angle at the deformation front and the calculated slope angle value for Mohr Coulomb wedges of $\alpha \sim 12^\circ$, it results that the measured value is slightly higher than the calculated one. This may result out of a variation of the basal friction value (μ_{bbulk}) along the basal box bottom due to material compaction and loading as well as thrust evolution (Morgan and Boettcher, 1999).

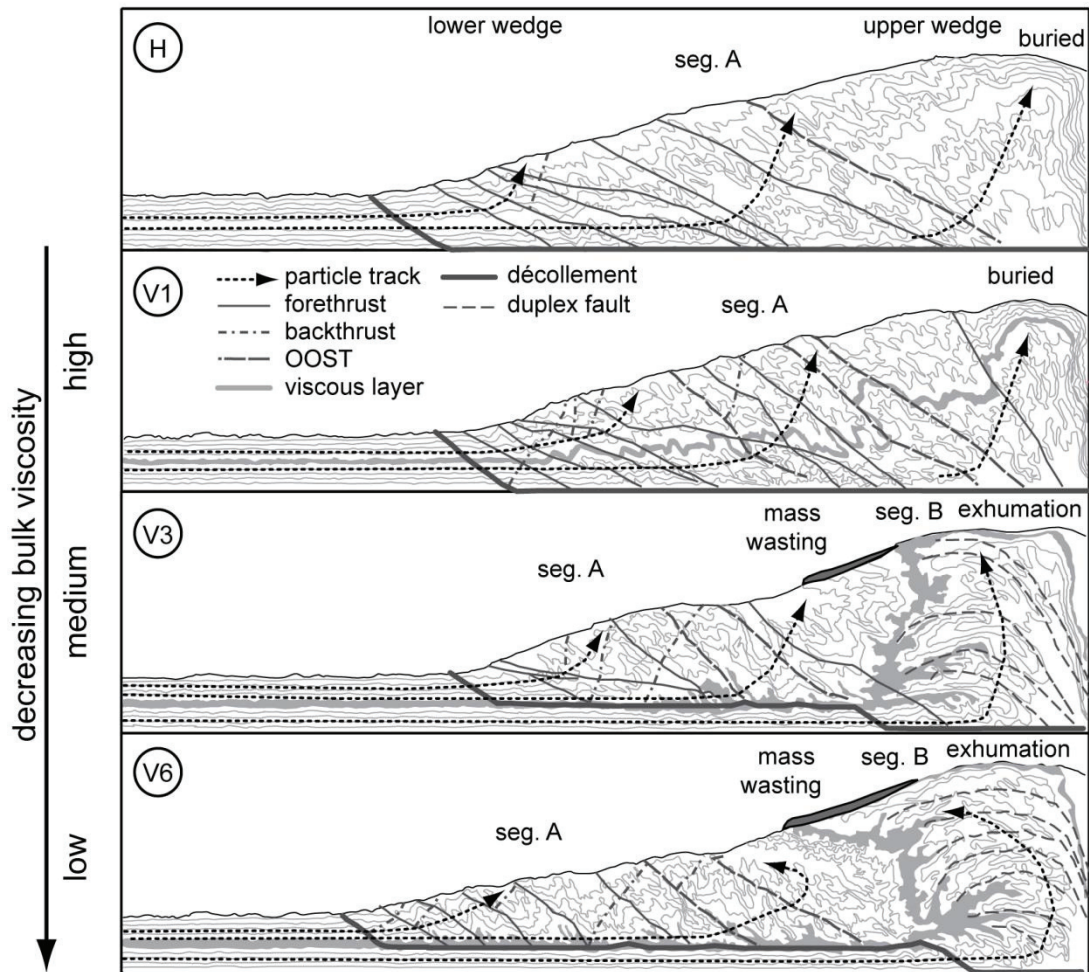


Fig. IV-8: Conceptual models for experiments H and V with varying viscosities at the embedded layers demonstrating the key role of an embedded viscoelastic-plastic layer on the wedge geometry, the internal structures and the mass transport pattern. The position of the viscoelastic-plastic layer is shown in grey. Mass wasting of brittle material occurred mainly in those models with high exhumation. In case of H and V1 the lower brittle layers as well as the viscoelastic-plastic layers did not reach the surface and are buried.

During the experimental run, the incoming material is accreted along steep forethrusts that are then rotated forming flat underthrusting shear zones as observed in the numerical high friction experiments by Gutscher et al. (1998a) and Konstantinovskaya and Malavieille (2011). The internal fore- and their corresponding backthrusts evolve dominant frontward-vergent as is typical for high friction detachments (e.g., Huiqi et al., 1992; Adam et al., 2005; Konstantinovskaya and Malavieille, 2011). Additionally, mass transport pathways are identical through the wedge showing identical large uplift gradients (Fig. IV-8). Such patterns are also described by Cloos and Shreve (1988) as typical for high friction wedges. In addition, active OOSTs decouple the active wedge from the strong back-wall. A similar

segmentation is observed in analog experiments with strong décollements (Lohrmann et al., 2003; Kukowski et al., 2002; Konstantinovskaya and Malavieille, 2011).

Consequently, experiment H shows similar wedge topography, thrust structures, accretion mode and wedge segmentation compared to analog experiments with strong basal detachment (e.g., Davis and Engelder, 1985; Gutscher et al., 1998a; Lohrmann et al., 2003; Konstantinovskaya and Malavieille, 2011). These observations are a first order support of our approach demonstrating the successful simulation of evolving accretionary wedges and investigating of their mechanics similar to previous studies (Saltzer and Pollard, 1992; Naylor et al. 2005). This approach allows for detailed information in space and time about the mass transfer pattern, particularly, uplift and exhumation within the wedge and gives a detailed impression of the geodynamics of growing wedge structures.

4.2. Heterogeneous wedge (V1-V6)

Wedge simulations reveal that the mechanics of the wedge and, hence, the accretion behaviour and the development of the responsible décollement is determined by the presence and, particularly, by the viscosity of an embedded, weak viscoelastic-plastic layer. In summary, this layer determines the spatial and temporal distribution of wedge segments.

4.2.1 Wedge mechanics in case of strong embedded viscoelastic-plastic layer (V1, V2)

In the case of high dynamic viscosities of $\eta_{\text{dynamic}} > 4.8 \times 10^{14}$ Pa s, no mid-level detachment develop, because the embedded layer prevents any internal shearing along this layer. In the strongest case (V1) the embedded layer shows an ‘over’-compaction by the applied loading causing a mechanical strengthening of this layer. In both experiments with high dynamic viscosities, the wedges grow above the basal box bottom. Steep forethrusts are increasingly back-rotated and reactivated as long imbricated OOSTs, while the material is increasingly steeply uplifted (Fig. IV-5, IV-8). Thrusts similar to the pure brittle experiment H evolve (Fig. IV-5) and typical accretion with underthrusting is observed similar to numerous analog studies (e.g., Lallemand et al., 1994; Gutscher et al., 1998a; Konstantinovskaya and Malavieille, 2011). Hence, the wedge evolves in a forward-vergent manner. These results are comparable with results for strong viscous décollements by Couzens-Schultz et al. (2003), who simulates wedges with viscous embedded detachments. Therein, the thrust system evolves asymmetrically and the amount of backthrusts is reduced as observed in

our DEM experiments. Furthermore, our experiments quantify detailed material paths and, in particular, uplift angles, supporting the hypotheses by Cloos and Shreve (1988) for strong detachments.

To summarise, in this experiments, the particle paths rise in the frontal wedge slightly more steeply than those in experiment H, whereas the mass transport in the upper wedge evolves more similarly. An embedded layer with a high dynamic viscosity of $\eta_{\text{dynamic}} > 4.8 \times 10^{14}$ Pa s has only a minor effect on the particle paths which evolve similar to a homogeneous brittle wedge growing on top of a high friction décollement. Additionally, shear zone geometry, e.g., thrust dip angles are slightly reduced in the vicinity of the viscoelastic-plastic layer. Nevertheless, no overall effect on accretion mode and segmentation can be inferred.

4.2.2 Wedge mechanics in case of an intermediate strong to weak embedded layer (V3-V6)

In experiments V3-V6, the viscoelastic-plastic embedded layer (low dynamic viscosities $\eta_{\text{dynamic}} \leq 1.6 \times 10^{14}$ Pa s) is deformed and, subsequently, internally sheared due to the stresses induced by the moving basal box bottom. Hence, a stable mid-level detachment is formed along this viscoelastic-plastic layer due to a reduced dynamic viscosity, which steps down to the basal box bottom just in front of the duplex (Fig. IV-5). As a result, the wedge mechanics are determined by these two active detachments creating the décollement. Based on our numerical studies, it is possible to show that the mid-level detachment is active during the entire accretion process (Fig. IV-7).

On top of the mid-level detachment the brittle ‘sediment’ sequence is frontally accreted creating the shallow lower slope (segment A; see Sec. 4.2.2.1). The underlying incoming material is far underthrust and basally accreted on top of the lower high friction box bottom detachment. This caused the evolution of a stacked duplex (segment B), which lifts the upper wedge (Fig. IV-8; see Sec. 4.2.2.2). Such decoupling of upper and lower sediment strata through a viscoelastic-plastic or weak mid-level décollement is also explained and postulated by several authors in analog and numerical experiments (Stockmal et al., 2007; Selzer et al., 2007; Kukowski et al., 2002; Konstantinovskaya and Malavieille, 2011; Yamato et al., 2011). Furthermore, the resulting wedge segmentation (segment A, B), associated wedge geometries, and wedge mechanics are in line with former studies (Bonini, 2001; Costa and Vendeville, 2002; Bahroudi and Koyi, 2003; Dooley et al., 2007; Costa et al., 2004; Reiter et al., 2011).

This study reveals, similarly to the previous studies, that an effective decoupling is only achievable under a dynamic viscosity of $\eta_{\text{dynamic}} < 1.4 \times 10^{13}$ Pa s. Under the aforementioned time scaling, which is used to achieve natural conditions, the resulting value is $\eta_{\text{nature}} < 2 \times 10^{22}$ Pa s. A further decrease of the dynamic viscosity in experiments V4-V6 (V4: $\eta_{\text{nature}} = 9.4 \times 10^{21}$ Pa s and V6 $\eta_{\text{nature}} = 7.6 \times 10^{21}$ Pa s) lead to a further decrease in the shear stress and to an increasing stabilisation of the mid-level detachment. These viscosity values are in the range of natural materials (Spiers et al., 1990; van Keken et al., 1993; Chemia and Koyi, 2008; Mukherjee et al., 2010).

The wedge mechanics correspond with this decrease in shear stress with respect to an earlier failing of the viscoelastic-plastic material resulting in a faster outward propagation of the DF and a decline of the slope taper angles from 16° - 18° in V1-V4 to 10° in V5 and V6 (Fig. IV-8). This is in agreement with various other studies (e.g., Davis and Engelder, 1985; Marshak and Wilkerson, 1992; Cotton and Koyi, 2000; Costa and Vendeville, 2002; Bahroudi and Koyi, 2003; Couzens-Schultz et al., 2003), which show that at high dynamic viscosity values a high frontal taper evolves and at low viscosities, a gentle topography is observed.

The mid-level detachment within such a system may be positioned either within the weak layer or at the material interface between weak and underlain brittle material (Polonia et al., 2002; Reston et al., 2002b). However, maximum relative displacement is observed between viscoelastic-plastic particles, in the lower third of the mid-level detachment, as the upper part is smeared into the thrusts occurring within the upper brittle layer. We conclude that the décollement is positioned along the weak embedded layer.

Hence, our experiments validate that the dynamic viscosity is a main factor controlling wedge mechanics and reveal the corresponding mass transport pattern of the frontally accreted wedge segment (see Sec. 4.2.2.1) and the basal duplex (see Sec. 4.2.2.2).

4.2.2.1 Frontal accretion mode

In experiment V3-V6, a typical frontal imbricated wedge evolves on the active mid-level detachments with flat forethrusts and steep backthrusts (Fig. IV-8). This is consistent with analog experiments using viscous décollements (e.g., Bonini, 2007; Couzens-Schultz et al., 2003). Similar to the structural system observed in previous analog experiments the resulting particle paths observed in this study rise gently (Fig. IV-5).

A decreasing dynamic viscosity causes a steepening of forethrusts and a flattening of backthrusts (V6; Fig. IV-6) and leads to a reduction in the foreland vergence and a more symmetrical development of the fore- and backthrusts. The evolution of these shear zone geometries corresponds to the reduction of the shear stress and the friction value along mid-level detachment with decreasing dynamic viscosity. Hence, the angle Ψ_b (direction of mean stress σ_1) depends on the viscosity value (Fig. IV-6).

To verify this relation, we use the approach developed by Hafner (1951), whereupon the failure planes are symmetrical with respect to the principle σ_1 axis (Fig. IV-1a). The orientation of the σ_1 axis can be calculated by measuring the conjugated thrusts in the experiments (Davis et al., 1983; Dahlen et al., 1984) by using equation (eq. IV-6):

$$\theta = \frac{(\delta_f + \delta_b)}{2} \quad (\text{eq. IV-6})$$

where δ_f and δ_b are the angles between thrust planes and the box bottom, and θ is the angle between the shear zone and σ_1 (Fig. IV-1a). The angle between σ_1 and the detachment is defined as Ψ_b and can be calculated by equation (eq. IV-7):

$$\theta - \delta_f = \Psi_b \quad (\text{eq. IV-7})$$

In our experiments, angle Ψ_b decreases from 20.2° in V4 to 10.0° in V6 (Fig. IV-6, insets). The decline of this angle Ψ_b or a decrease of the forward vergence is caused by the weakening of the detachment or a decrease in the shear strength. The corresponding detachment of V6 is most likely the weakest, as it has the lowest dynamic viscosity of $\eta_{\text{dynamic}} = 5.4 \times 10^{13}$ Pa s, frontal thrusts are steepest, and backthrusts most gradual. Such a thrust rotation is already described by Bonini (2007) and similar observations are made by Couzens-Schultz et al. (2003). They show that at low dynamic viscosity values, structures evolve more symmetrically in association with the low layer-parallel shear stress. We further show that the particle paths evolved flatter in accordance with the increasing symmetry, whereby the difference between the rising angles of particle paths in the frontal wedge of V5 and V6 is, with only 2° , small (Fig. IV-5). In the vicinity of mid-slope plane or the transition zone between both accretion modes detailed analysis of particle paths reveal a significant change in material transport (Fig. IV-5, IV-8). This region is first characterised by a steep material uplift inward of the frontal wedge (Fig. IV-5). At a later evolution stage, the particle paths become steeper or rather overturned due to the influence

of the duplex growth that increasingly propagates outward on top of the mid-level décollement (Fig. IV-5).

4.2.2.2 Hinterland-dipping and anti-formal stacking (lower brittle layer)

Below the active mid-level detachment, the material is long underthrust in experiments V3-V6, which is mirrored by a horizontal particle transport pattern (Fig. IV-5). The leading factor, therefore, is the brittle basal detachment located at the top of the moving box bottom. Subsequently, material is basally accreted creating a duplex of variable shape, whereas accreted stratum is nearly vertically uplifted with steep particle paths (segment B). This is observed in numerous analog experiments (Gutscher et al., 1998a; Lohrmann et al., 2003; Couzens-Schultz et al., 2003; Glodny et al., 2005; Konstantinovskaya and Malavieille, 2011). The duplex grows in two phases: 1) steep hinterland-dipping thrusts evolve where the mid-level detachment steps down and 2) these thrusts are, thereafter, rotated and antiformally stacked while material is vertically uplifted by younger basally accreted thrusts. This alteration between hinterland-dipping thrusts followed by underthrusting is described by Kukowski et al. (2002), Glodny et al. (2005), Bonini (2001, 2007), Couzens-Schultz et al. (2003) and Konstantinovskaya and Malavieille (2011).

In addition, our parameter studies show that the magnitude of the dynamic viscosity of the mid-level detachment controls the mass transport within the duplex and its geometry. With decreasing dynamic viscosity of the mid-level décollement, hinterland-dipping of the duplex decreases (V4) whereas the basally accreted material is increasingly vertically uplifted or even earlier overturned as shown by the particle paths (V5) (Fig. IV-5). Additionally, the duplex incorporated progressively more viscoelastic-plastic material, which is smeared into the duplex by single thrusts (Fig. IV-5, IV-6; offset of grey layer). As these mostly ‘well-lubricated’ thrusts show lower shear strength, they exhibit larger offsets resulting in steeper duplexes and in higher uplift or even in higher material exhumation of older buried strata. Simultaneously, overlying material at the upper slope is transported down-slope by numerous mass wasting events nicely illustrated by the overturning particle paths (Fig. IV-5). This overturning occurs increasingly earlier with decreasing viscosity. The higher uplift increases the overall taper of the whole wedge structure. In contrast, a high dynamic viscosity results in a reduced uplift angle with no obvious overturning of the particles paths in the upper wedge and, therewith, a reduced taper in the vicinity of the duplex structure.

As a consequence, our studies reveal that besides the basal friction, the mid-level detachment viscosity value also controls the basal accretion mode. These structural observations agree with studies by Couzens-Schultz et al. (2003), who discovered that the duplex structure depends on the coupling between the stacked blocks and that a high dynamic viscosity value reduces the uplift in the lower sand sequence. Additionally, our study shows the dependence between the rising angle as well as overturning of the particle paths and the dynamic viscosity value. Our approach allows for the quantifications of the relationship between dynamic viscosity and uplift patterns and also potential for quantification of supplementary data for, e.g., fission track analyses quantifying exhumation and denudation rates through time and space. This will give a deeper insight into geodynamic processes and a better understanding of, e.g., the coupling between deep-seated crustal and surface processes (Wenk and Elfert, unpubl. data).

5. Conclusion and Outlook

To quantify the influences of an embedded viscoelastic-plastic layer on the kinematics and mass transport of growing sediment wedges, we combine a Discrete Element model utilising the Burger's Model. With this method we simulate a series of wedge experiments that incorporates two different rheologies in the incoming, undeformed strata: brittle (Mohr Coulomb rheology) and viscoelastic-plastic materials (Burger's rheology). The numerical DEM approach allows for the development of conceptual models of the function of viscoelastic-plastic décollements through detailed analyses of viscosity and stress values as well as an exact tracking of temporal and spatial evolution of thrusts and material tracers through the evolving accretionary wedge. Within this study, we focus on the effects of different viscosity magnitudes of an embedded viscoelastic-plastic layer on the thrust geometries, the accretion modes, and the mass transport pattern.

In the case of high dynamic viscosities (V1-V2; $\eta_{\text{dynamic}} > 4.1 \times 10^{14}$ Pa s; $\eta_{\text{nature}} > 5.7 \times 10^{22}$ Pa s; V1-V2), the wedge grows by one accretion mode and no decoupling occurs. Internal structures, e.g., long underthrusting frontal thrusts, as well as wedge geometries, are similar to a pure homogeneous brittle wedge (H). With decreasing dynamic viscosity (V3-V6; $\eta_{\text{dynamic}} \leq 1.6 \times 10^{14}$ Pa s; $\eta_{\text{nature}} \leq 2.3 \times 10^{22}$ Pa s; V3-V6), a mid-level detachment evolves along the weak embedded layers stepping down to the basal box

bottom detachment far away and inward of the deformation front. Consequently, the accretionary wedge grows by two different modes: frontal accretion above the viscoelastic-plastic mid-level detachment creating the frontally accreted lower slope, whereas the material below is underthrust and basally accreted on top of the strong basal detachment. This causes the evolution of a duplex structure below the upper wedge segment. Our simulations demonstrate that both detachments are active throughout the entire experiments. We validate that the reduction of the dynamic viscosity and the shear stress corresponds to a decrease of the foreland-vergence in the frontal wedge and a faster outward propagation of the deformation front, while increasing the horizontal length and decreasing the wedge taper of the frontal wedge. In addition, the embedded viscoelastic-plastic material influences the geometry of the basally accreted duplex as it gets increasingly incorporated into the duplex. In the case of a decreasing dynamic viscosity, we show that the basal thrusts exhibits increasingly higher offsets and material is more vertically uplifted and even exhumed in case of weakest dynamic viscosity. This process occurs together with an increase of mass wasting. Simultaneously, we show that with an increase in dynamic viscosity the material of the frontal wedge is increasingly less uplifted towards the back-wall. The mass transport pattern at the outward edges of segment B is first more influenced by the frontal accretion mode, as shown by the continuous rise, and later is more influenced by the basal accreted segment, which starts to migrate outward. This is indicated by an overturning of the particle paths. The upper wedge shows in all cases a steep uplifting followed by an overturn. The height of overturning, thereby, depends again on the viscosity of the embedded layer.

At low dynamic viscosities (η_{dynamic} : 5.4×10^{13} - 6.7×10^{13} Pa s), the scaled natural viscosity of the viscoelastic-plastic material corresponds to published values for natural evaporitic detachments and the resulting wedge kinematics best correspond to observations made at accretionary wedges growing on top of viscous décollements determined by quantitative information regarding mass transport patterns particularly related to the uplift. In summary, we propose that the dynamic viscosity of an embedded weak viscoelastic-plastic layer is one main factor controlling wedge mechanics and, therewith mass transport. This includes (A) localisation of the décollement, (B) shear resistance within the viscoelastic-plastic, between the viscoelastic-plastic and the brittle material, and (C) the mass transport pattern of the whole accretionary wedge.

The next step is to compare the numerical results with natural examples which will be part of additional publications. Existing examples for natural wedges incorporating weak viscous layers such as evaporites are the Mediterranean Ridge accretionary complex (Finetti, 1976; Reston et al., 2002b) and the Cascadian Arc (Rossi and Sartori, 1981). The accumulated evaporites have in both wedges an important influence on the structural geology (Reston et al., 2002a; Minelli and Faccenna, 2010). Similar to our numerical simulations, frontal accretions occurs in the upper sediment sequence which is located on top of the viscous material building the décollement. Underneath this décollement underplating processes and duplex formations are active (Reston et al., 2002b; Polonia et al., 2011). Furthermore, also in nature and in numerical models, it is found that the out-of-sequence thrusts split the wedge in an active and inactive part. Additionally, the variations of the wedge morphology such as taper angle, uplift rates and seafloor morphology are expected to result out of the differences in plate coupling which is simulated here by using of different viscosity values. Consequently, the numerical models have a great potential to increase the understanding for the processes at accretionary wedges along subduction zones. Therefore, different physical and geometrical parameters which vary along the subduction zone in the Mediterranean can be tested such as the thickness variations of incoming sediment section (Wenk and Huhn, *subm.*).

ACKNOWLEDGEMENTS

Thanks are due to all our colleagues of the MARUM-Center for Marine Environmental Sciences. This research was funded through DFG-Research Center / Cluster of Excellence „The Ocean in the Earth System“. We are grateful to the reviewers and the editor for their constructive comments and discussions.

Chapter V: Layer thickness study

HOW DOES THE THICKNESS OF BOTH – AN EVAPORITE AND A COVER LAYER - INFLUENCE THE TECTONIC EVOLUTION OF AN ACCRETIONARY WEDGE? A CASE STUDY FOR THE MEDITERRANEAN RIDGE.

Linda WENK^{1*}, Katrin HUHN¹

¹ *MARUM – Center of Marine Environmental Science and Faculty of Geosciences, University of Bremen, Leobener Straße, 28359 Bremen, Germany*

Keywords:

accretionary wedge; numerical DEM model; evaporitic décollements; input layer thicknesses; Mediterranean Ridge

Abstract

The layer thickness and stratigraphy of the incoming sediment section has an important influence on the structural development of an accretionary wedge. The Mediterranean Ridge is a key example of a growing prism with variations in the sediment thicknesses along the subduction zone. Besides, this wedge incorporates massive Messinian evaporites which also vary in thickness along strike. As a result, different deformation behavior occurs in its western and eastern domain. To the best of our knowledge, no specific study has been undertaken to explain to what extent these deformational behaviors within the wedge are controlled by the variation in thickness of the incoming sediments and of the embedded evaporite sequence. Therefore, two sets of numerical ‘sandbox’ experiments are developed to gain a better understanding concerning the effects of the cover material thickness and the evaporitic layer thickness on the growth and mechanics of the Mediterranean Ridge accretionary complex. Therefore we utilize the Discrete Element Method implementing constitutive laws for brittle sediments and viscoelastic-plastic rheology for the evaporites. Results show that variations in the thicknesses of an embedded viscoelastic-plastic layer

and of a cover layer control the thrust evolution, thrust-vergence, topography, accretion mechanisms and, hence, the mechanics of the wedge. Therein, the viscoelastic-plastic layer serves depending on its thickness as a weaker (> 400 m) or stronger (< 400 m) mid-level décollement. By combining our experimental wedges with the Mediterranean Ridge, we show that the thickness variations of the cover layer (Plio-Quaternary cover) are more suitable to explain the different accretion mechanisms occurring at the Mediterranean Ridge than the changes in the embedded viscoelastic-plastic (Messinian evaporites) thickness.

1. Introduction

Accretionary wedges are formed due to continuous sediment off-scraping from the lower, oceanic plate and a subsequent accumulation of the material along the upper, continental plate at the forearc of subduction zones. The wedge mechanics of these accretionary wedges is controlled by the strength of the incoming material and of the basal detachment known as the décollement (e.g., Davis et al., 1983; Dahlen et al., 1984). The material strength is affected by the loading or the thickness of the incoming sediment section (e.g., Gutscher et al., 1998b; Adam et al., 2004). An increase in loading raises the material strength and influences the internal stresses and, hence, the thrust generation (Biju-Duval et al., 1982; Platt, 1990).

In most studies, a brittle Mohr Coulomb (MC) is assumed for the incoming sediment sequence at subduction zones. During the growth of such brittle wedges, new material is accumulated either at the wedge toe by imbrication (frontal accretion mode) and/or at the bottom (basal accretion mode) by duplex growth (e.g., Cloos and Shreve, 1988; von Huene und Scholl, 1991). The latter is more pronounced when the décollement strength is high (e.g., high basal friction), whereas frontal accretion occurs when the detachment strength is low (e.g., low basal friction; Dahlen et al., 1984; Moore, 1989; Gutscher et al., 1998b; Hardy et al., 1998). Materials that provide very low-strength décollements are evaporites that have a viscous rheology (e.g., Davis and Engelder, 1985). If a wedge grows on evaporites, no typical accretion mode will occur. Rather, the material is deformed by the formation of folds or by a symmetrical fore- and backthrust evolution, e.g., pop-up structures (Letouzey et al., 1995). Furthermore, conspicuous wide fault-spacing occurs and the wedge evolves flat and wide-extended (Davis and Engelder, 1985; Mulugeta, 1988; Bonini, 2003, 2007; Smit et al., 2003). Understanding the mechanics of such wedges growing on top of viscous décollements is in the focus of several studies (e.g., Bonini 2001, 2003; Cotton and Koyi, 2000; Costa et al., 2002; Smit et al., 2003; Costa et al., 2004). They showed, by using analog experiments, that the surface slope angle increases with a reduction in the viscous layer thickness. Additionally, these studies tested the influence of different sediment loadings or cover layer thicknesses. Therein, they found that the number of thrusts decreases when the overburden loading is increased and a larger faults spacing occurs.

An example of an accretionary wedge that incorporates weak evaporites with varying thickness is the Mediterranean Ridge (Fig. V-1; Finetti, 1976). This wedge grows by imbrication in the western domain and by rather typical salt tectonics in the eastern domain. In order to explain these structural variations, different assumptions have been made, such as lateral changes in sediment loading (Chaumillon and Mascle, 1995; Polonia et al., 2002; Reston et al., 2002b). Hence, this complex accretionary wedge growing on a viscous décollement also allows for the study of the role of sediment thickness variations along the strike (Fig. V-1, Finetti, 1976; Polonia et al., 2002).

However, there is still a lack in ground truthing because as until now, only a few analog sandbox experiments dealing with embedded mechanically weaker layers have been undertaken to understand the structural development of the Mediterranean Ridge (Kukowski et al., 2002; Costa et al., 2004). Hence, no direct experiments have been made to determine to what extent the different deformation modes at the Mediterranean Ridge are linked to the varying cover thickness, particularly, on top of the evaporites as well as the evaporites itself.

For that reason, we undertake a group of 2D numerical ‘sandbox’ experiments utilizing the Discrete Element Method, to gain a better insight into the key role of both the sediment stratigraphy of the incoming layer, as well as the thickness of different sequences. This means in particular: how far are different accretion mechanisms connected to layer thicknesses (evaporites as well as the brittle cover layer) with the overall aim to increase the understanding of the Mediterranean Ridge mechanics. Therefore, we vary the thickness of an embedded viscoelastic-plastic layer (series I: $V_{\text{small}}-V_{\text{large}}$), as well as the cover material thickness (series II: $C_{\text{small}}, C_{\text{large}}$) in accordance with the conditions at the Mediterranean Ridge. The numerical simulation technique is used because it allows for the extraction of detailed information on thrust evolution and the stress field in the interior of the wedge.

2. Geological setting Mediterranean Ridge

The Mediterranean Ridge is located at the Hellenic subduction zone where the African plate dips under the European plate, a process that has been ongoing for the last 30 Myrs (Mascle and Chaumillon, 1997; Fig. V-1). This accretionary wedge has an extension of 1000 km in the EW direction and an extension of 150-300 km in the NS direction. One property of the

Mediterranean Ridge is that large evaporitic sequences are incorporated in its western and eastern domain (Fig. V-1 II). These evaporites result from the Messinian desiccation of the Mediterranean Sea (Hsü et al., 1973; Ryan et al., 1973; Kastens et al., 1992; Tay et al., 2002; Reston et al., 2002a, b). Samples from exploration wells in the marginal areas of the Nile Delta indicate that anhydrite is the dominant Messinian mineral (Abdel Aal et al., 2000). These Messinian evaporites reach a thickness of 1000 m in the Ionian domain and around 2500 m in the Levantine domain (Fig. V-1 Ila, b; Chaumillon and Mascle, 1995).

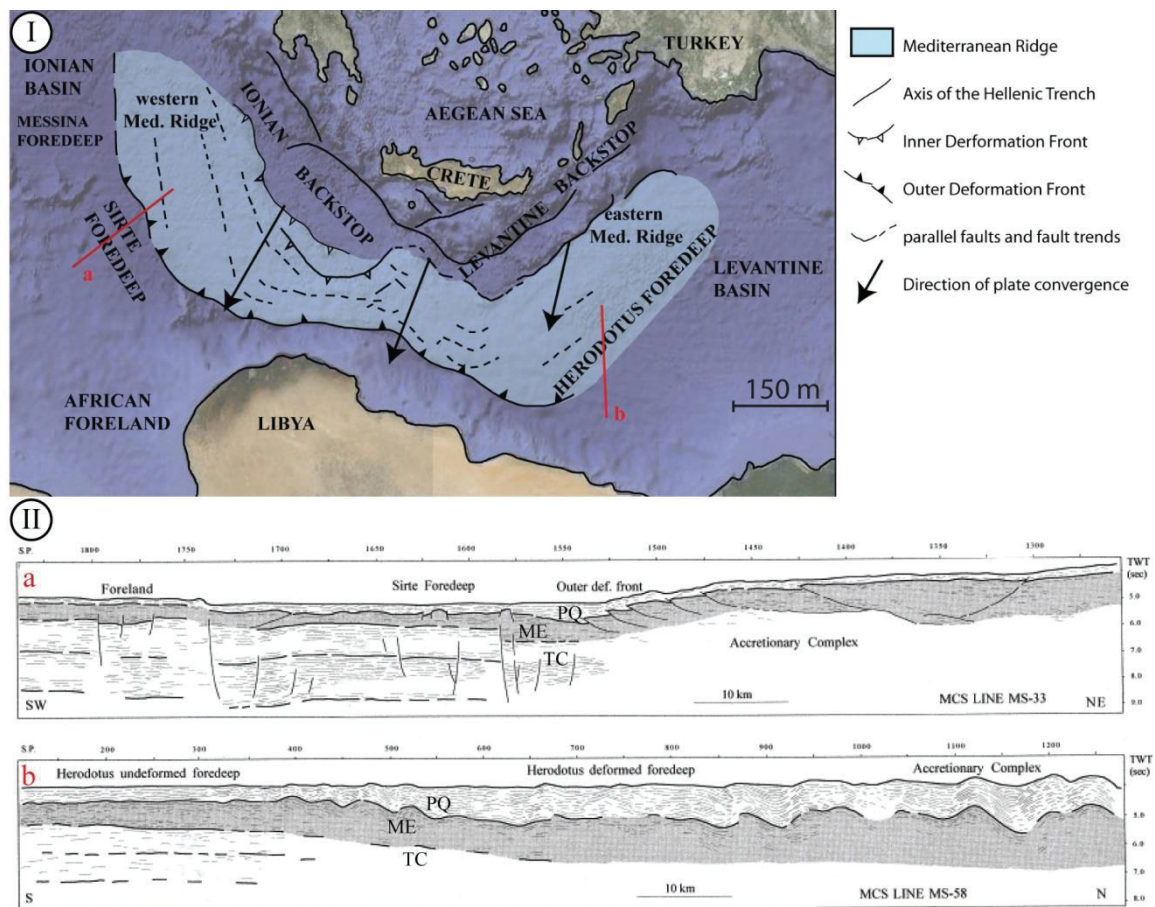


Fig. V-1: I) Map of the Mediterranean Ridge. In red, the positions of two seismic sections are marked. II) Two seismic lines for the western (a) and the eastern (b) Mediterranean Ridge. (PQ) Plio-Quaternary cover; (ME) Messinian evaporites; (TC) Tertiary clastics (modified after Polonia et al., 2002).

Along the entire Mediterranean Ridge, these evaporites are underlain by Tertiary clastics with a mean thickness of ~3000 m (Kasten et al., 1992; de Voogd et al., 1993; Chaumillon and Mascle, 1995; Chaumillon and Mascle, 1997; Polonia et al., 2002; Reston et al. 2002b). On top of the Messinian evaporites, the Pliocene-Quaternary cover is accumulated, which is thin in the Ionian domain (200-400 m) and well-formed in the Levantine domain

(3000 m) due to high sediment input of the Nile River (Fig. V-1 IIa,b; Chaumillon et al., 1996; Chaumillon et al., 1997; Kastens et al., 1992).

Within the western Ionian wedge, the incoming sediment sequence is deformed along landward-dipping thrusts that rise from the evaporites (Fig. V-1 IIa; Chaumillon et al., 1996). This leads to an atypical morphology with small breaks and offsets due to thrusting in the Messinian evaporites (Polonia et al., 2002). Consequently, the domain evolves with a slope angle of 1.8° more similar to an imbricated wedge (Le Pichon et al., 1982; Ryan et al., 1982; Chaumillon et al., 1996). The incoming sediment sequences in the eastern Levantine domain are deformed by asymmetrical folding and reverse faulting (pop-up), which are typical for evaporites (Fig. V-1 IIb). Here, the wedge is wide and flat with slope angles of $\sim 0.3^\circ$ (Chaumillon and Mascle, 1997; Polonia et al., 2002).

3. Method

3.1 Discrete Element Method

The Discrete Element Method (DEM) is a granular model approach. This technique has been successfully used to model discontinuities in different macro- and microscopic scientific processes, such as shear zones (e.g., Kock und Huhn, 2007) or thrust systems within accretionary wedges (e.g., Naylor et al., 2005). We use the commercial code PFC2D (ITASCA) for our study, which is originally developed by Cundall and Strack in 1978. With the DEM, a rock or sediment mass is treated as an assemblage of distinct rigid elements of any simple spherical shape. These particles can be displaced in any direction forced by the given boundary conditions while interacting and overlapping with the neighboring elements (Cundall and Strack, 1978). As a result of these interactions, normal and shear forces occur at the particle contacts. The normal forces (F_n) act perpendicular to the contact plane and are used to define the impulse of a reflected particle. Shear forces (F_s) act parallel to the contact plane and are used to define if particles gliding away in a tangential direction. To calculate the forces of the interacting particles, physical laws are used together with the magnitude of the overlap and the material parameters of the single particles, e.g., density, stiffness, and coefficient of friction (Mindlin and Deresiewicz, 1953; Cundall and Strack, 1979). Subsequently, all forces acting on a single particle are added together to calculate the resulting particle displacements (d) and direction using the 2nd

Newtonian law. For a more detailed description of the code, refer to Cundall and Strack (1979, 1983), Cundall (1987) or the PFC2D ITASCA Manual (2004).

3.2 Natural rheological behavior and material implementation in PFC2D

The DEM offers a wide rheological spectrum to model different natural materials, such as those with elastic or viscoelastic-plastic behavior (ITASCA Manual, 2004). Specific rheology types are implemented by adjusting the employed physical laws.

3.2.1 Elasto-plastic rheology

Under small acting forces, most natural rocks show an elastic deformation that is reversible and can be explained by Hooke's law. This law is implemented in the DEM as a spring referred to as the *Hookean* model. The strength of the spring is defined by the normal and shear stiffness ($k_{n/s,particle}$), as well as the coefficient of friction ($\mu_{particle}$). If the shear forces at a particle contact reach the critical shear strength of the material, non-reversible plastic deformation occurs and particle contacts break results in localized deformations along thrusts. This numerical approach can simulate the brittle deformation behavior of the upper crust and allows for simulation of the deformation processes of accretionary wedges (Miyakawa et al., 2010; Wenk and Huhn, 2013b).

3.2.2 Viscoelastic-plastic rheology

Evaporites, such as anhydrite, exhibit a ductile or viscous material behavior at depths of >1000 m or at temperatures between 75 to 125 °C (Müller et al., 1981; Shearman, 1983). In such cases, the material breaks under short acting forces, but creeps under long acting forces similar to the process at accretionary wedges. For DEM simulation of viscous materials, in addition to the spring, a dashpot termed the *Newtonian* model is used (Barnes, 2000). This dashpot represents the absorption or dissipation of energy and reproduces idealized viscous behavior (ITASCA Manual, 2004). The combination of these two rheological models, the *Hookean* and the *Newtonian* models, is called the *Burger's* model and has been used to simulate creep (e.g., Chin and Rogers, 1987; Collop et al. 2004) and natural viscoelastic-plastic materials (Wenk and Huhn, 2013b).

In this case, besides the particle friction (μ_{particle}), the normal and shear contact stiffnesses ($k_{m_{n/s, \text{contact}}}$, $k_{k_{n/s, \text{contact}}}$) and the viscosity coefficients ($\eta_{m_{n/s}}$, $\eta_{k_{n/s}}$) must be defined for the *Burger*'s materials (Table V-1). To ensure natural conditions, the input particle properties must be calibrated to the overall macro material properties of the whole assemblage in both brittle and viscous behavior cases (see Sec. 4.1; Cundall and Strack, 1983). Moreover, the time must be scaled in the case of viscoelastic-plastic materials (see Sec. 4.1). For details about material calibration, implementation and scaling of viscoelastic-plastic rheology at evolving accretionary wedges please see Wenk and Huhn (2013a).

4. Model configuration

4.1 Model approach

In accordance with the general geometries of the Mediterranean Ridge (e.g., Finetti, 1976; Reston et al., 2002b; Polonia et al., 2002) and the settings from previous analog sandbox experiments simulating the Mediterranean Ridge (e.g., Kukowski et al., 2002), a numerical 'sandbox' is developed (Fig. V-2). This rectangular box consists of a 280 km long horizontal box bottom and two fixed 30 km high vertical side-walls. Walls and bottom are created by particles with a homogeneous diameter of 125 m and act as stiff undeformable boundaries. The box bottom moves during all experimental runs at a constant velocity in positive x-direction (0.2 m/s). Consequently, it acts as a potential basal detachment at a plate interface of a subducting plate.

Prior to initiation, the entire box is gradually filled with ~30,000 randomly distributed particles. To prevent symmetrical particle packing (Saltzer and Pollard, 1992), we use a logarithmic normal distribution of three different particle diameters (100, 125, and 150 m). After generation, the particles are settled under applied gravity ($g = 9.81 \text{ m/s}^2$) on the box bottom to reproduce the undeformed incoming 'sediment' layer (Fig. V-2a). Gravity is active during the entire experiment. The incoming 'sediment' sequence consists of three different units simulating the different stratigraphic layers (B: Tertiary clastics (TC), V: Messinian evaporites (ME), and C: Plio-Quaternary cover (PQ)) at the Mediterranean Ridge (see Sec. 1.2). The lower bottom layer B (Fig. V-2b) of the initial strata is 2500 m thick in all four experiments and simulates the Tertiary clastic material. This layer is first accreted against the fixed back-wall to build up a pre-Messinian wedge structure (Reston et al., 2002b). On top of this layer, a second layer (V) is created simulating the viscous

Table V-1: Material properties

Particles/ Contacts	μ_{particle}	ρ_{particle} [kg/m ³]	$k_{n/s,\text{particle}}$ [N/m]	$k_{m_n,\text{contact}}$ $k_{m_s,\text{contact}}$ [N/m]	$k_{k_n,\text{contact}}$ $k_{k_s,\text{contact}}$ [N/m]	$\eta_{m_n/s,\text{particle}}$ $\eta_{k_n/s,\text{particle}}$ [Pa s]	$\eta_{n/s,\text{nature}}$ [Pa s]
Lower/upper MC	0.58	2500	1×10^{12}				
Box bottom	0.2	2500	1×10^{12}				
Viscoelastic- plastic	0.1	2300		$8 \times 10^{10}/$ 8×10^{10}	$3 \times 10^{11}/$ 1×10^{11}	1×10^{19} 1×10^{19}	$\sim 7.7 \times 10^{21}$

The second embedded layer follows a viscoelastic-plastic rheology that behaves according to the *Burger's Model*. The particle viscosity is set in the range of known anhydrite values (Table V-1, V-2), which have been calibrated and successfully used in previous studies on accretionary wedges (e.g., Ting et al., 1989; Jensen et al., 1999; Burbidge and Braun, 2002; Naylor et al., 2005; Wenk and Huhn, 2013b). For calibration details of the viscosity value please see Wenk and Huhn (2013b). For scaling the modeled time-dependent viscosities the convergence rate at the Mediterranean Ridge of ~ 5 cm/y is used (Bohnhoff et al., 2001). In order to test the mechanics under variable layer thicknesses, two series with varying thicknesses of the viscoelastic-plastic (V, series I) and of the cover layer (C, series II) are generated (Fig. V-2b). For series I, experiments V_{small} ($V = 400$ m), V_{medium} ($V = 1000$ m) and V_{large} ($V = 2500$ m) are compared (Fig. V-2b) and all had a constant cover layer (C) thickness of 1000 m. In series II, the C_{small} ($C = 400$ m) and C_{large} ($C = 2500$ m) experiments are compared (Fig. V-2b) and both had a constant viscoelastic-plastic layer of 1000 m. These thicknesses are chosen in accordance with the Mediterranean Ridge (Chaumillon and Mascle, 1995; Chaumillon et al., 1996; Polonia et al., 2002). Experiment V_{large} mirrors the incoming sequence of the eastern Mediterranean Ridge and experiment C_{small} that of the western Mediterranean Ridge. However, as PFC2D does not take pore fluids and cohesion into account, a direct comparison to natural wedge geometry and dip angles of thrusts is not possible (Davis et al., 1983; Smit et al., 2003; Stockmal et al., 2007). Only relative comparisons between the different experiments are considered while carrying out the study to test influences of the layer thicknesses on wedge dynamics. A similar strategy has already been successfully used in numerous analog studies that used dry, homogenous sand packages to investigate the evolution of accretionary wedges (Lallemand et al., 1994; Adam et al., 2005; Schreurs et al., 2006; Malavieille and Konstantinovskaya, 2010).

4.2 Model analysis and interpretation techniques

For a first impression of the internal structures, horizontal layers are initially colored similar to analog sandbox experiments and plotted in a particle configuration view (Fig. V-2a, 3). Particle positions are then extracted and saved for every 0.05 % shortening or every 200 m of ‘subduction’ throughout the entire model run of each experiment to generate a continuous time series. This allows for calculation of the relative displacements for each particle in the x- and y-directions at each subduction increment. This technique reveals zones where particles move with different magnitudes or perhaps also in opposite directions. These zones of different offsets can be interpreted as active thrust zones (Fig. V-4; Morgan and Boettcher, 1999). Based on our model configuration, faults can be interpreted as inward dipping forethrusts (dipping angle δ_f , Fig. V-2c) or outward dipping backthrusts (dipping angle δ_b , Fig. V-2c). However, only thrusts that are active during a specific ‘subduction’ increment can be visualized. To track older inactive faults throughout the experimental run, a combination of particle configuration view and relative displacement plots is essential (Huhn et al., 2006). By tracking both active and inactive faults using these methods, an improved understanding of thrust kinematics can be achieved at a high resolution.

For quantitative comparison between the models, the individual normal (σ_{particle}) and shear stresses (τ_{particle}) are extracted at all particle contacts directly at the DF (Fig. V-2c). This is done for every 0.05% of shortening. With these data, average stresses are calculated (σ_{bulk} , τ_{bulk}) and applied to derive bulk friction (μ_{bulk} , eq. V-1):

$$\mu_{\text{bulk}} = \tau_{\text{bulk}} / \sigma_{\text{bulk}} \quad (\text{eq. V-1})$$

5. Results

5.1 Bulk properties

In Series I (V_{small} , V_{medium} , and V_{large}), the normal stress ($\sigma_{c,\text{bulk}}$) within the upper brittle layer (C) increases slightly with increasing layer thickness, whereas the shear stress ($\tau_{c,\text{bulk}}$) decreases (Table V-2). Hence, the resultant bulk friction ($\mu_{c,\text{bulk}}$) decreases slightly with increasing thickness (V_{small} to V_{large}). In contrast, the normal stresses ($\sigma_{v,\text{bulk}}$) remain constant in the viscoelastic-plastic layer (V) with increasing layer thickness but the shear stress ($\tau_{v,\text{bulk}}$) decreases similar to that in the upper brittle layer. This also leads to a decrease

in the viscous bulk friction coefficient ($\mu_{v,bulk}$). Within the lower brittle layer (B), the normal stress ($\sigma_{b,bulk}$) increases with increasing cover layer thickness (C), whereas the shear stress ($\tau_{b,bulk}$) remains constant. In this case, however, the bulk friction ($\mu_{b,bulk}$) decreases slightly. In Series II, the thickness of the Plio-Quaternary cover (C) material is varied. By comparing experiments C_{small} and C_{large} , it can be observed that the increases in shear ($\tau_{c,bulk}$) and normal stresses ($\sigma_{c,bulk}$) are due to the increase in layer thickness. In contrast, the resulting bulk friction ($\mu_{c,bulk}$) decreases. Similarly, the thickening of the cover layer leads to a decrease in the coefficient of friction ($\mu_{v,bulk}$) in the embedded viscoelastic-plastic layer (V), while the shear stress ($\tau_{v,bulk}$) and normal stress ($\sigma_{v,bulk}$) again are increased. In the lower brittle layer (B), the normal ($\sigma_{b,bulk}$) and the shear ($\tau_{b,bulk}$) stress increase with increasing cover layer thickness (C), whereas the corresponding bulk friction ($\mu_{b,bulk}$) decreases.

Table V-2: Extracted and calculated bulk properties

Layer		V _{small}	V _{medium}	V _{large}	C _{small}	C _{large}
C	$\sigma_{c,bulk}$ [Pa]	1.63×10^{10}	1.62×10^{10}	1.78×10^{10}	4.94×10^9	1.62×10^{10}
	$\tau_{c,bulk}$ [Pa]	4.7×10^9	4.29×10^9	3.99×10^9	1.45×10^9	4.29×10^9
	$\mu_{c,bulk}$ [-]	0.32	0.26	0.25	0.3	0.26
V	$\sigma_{v,bulk}$ [Pa]	2.09×10^{10}	2.01×10^{10}	2.34×10^{10}	1.05×10^{10}	2.01×10^{10}
	$\tau_{v,bulk}$ [Pa]	4.95×10^9	3.89×10^9	3.73×10^9	2.44×10^9	3.89×10^9
	$\mu_{v,bulk}$ [-]	0.24	0.19	0.16	0.23	0.19
B	$\sigma_{b,bulk}$ [Pa]	3.31×10^{10}	3.86×10^{10}	3.71×10^{10}	2.31×10^{10}	3.86×10^{10}
	$\tau_{b,bulk}$ [Pa]	1.0×10^{10}	1.07×10^{10}	9.98×10^9	6.97×10^9	1.07×10^{10}
	$\mu_{b,bulk}$ [-]	0.32	0.29	0.30	0.32	0.29

5.2 Structural evolution of the wedges

In all experiments, wedges evolve out of the upper brittle (C) incoming ‘sediment’ sequence due to the horizontal movement of the basal box bottom (Fig. V-2, V-3). These wedges become stable at least after 16 % shortening. Depending on the thickness of the embedded viscoelastic-plastic (V) layer and the overlying cover (C), the accreted prisms evolve with different topographies with respect to wedge tapers (α), specific thrust geometries, e.g., foreland- or hinterland-vergences, and accretion mode (Fig. V-3). The wedge toes always correlate with the deformation front (DF).

In all experiments, the embedded viscoelastic-plastic layer decouples the upper brittle (C) layer and lower brittle (B) layer and, hence, acts as mid-level detachments on which a lower, frontal wedge grows. At the same time, the lower brittle layer (B) is underthrust underneath the mid-level detachment and is, subsequently, basally accreted. However, as

the study is focused on the key role of the embedded viscoelastic-plastic layer (i.e. Messinian evaporites) on the mechanics of the frontal accretionary wedge, the underthrusting and basal accretion at the upper wedge are not analyzed. In the following section, characteristics of the individual wedges are described briefly.

5.2.1 'Sediment' sequence with a thin embedded layer and a thick cover (V_{small})

The wedge in V_{small} evolves similar to an MC wedge on top of a low friction décollement. At the location of the slow outward propagating DF, forethrusts crop out of the surface from the mid-level detachment in flat, but variable angles ($\delta_f \sim 25-38^\circ$). The forethrusts cut through the overlaying incoming sediment sequence (C), which is, simultaneously, imbricated, compressed, and slightly uplifted towards the fixed back-wall. Associated with these imbricated forethrusts, steep corresponding backthrusts are observed having angles between $\delta_b \sim 48$ and 61° . As a result, a frontal wedge evolves with a slope angle of $\alpha_1 \sim 10^\circ$. The tectonic system evolves foreland-vergent.

Further inwards, the frontal lower slope is followed by a flatter terrace with a slope angle of $\alpha_2 \sim 8^\circ$. In this terrace, the formerly active forethrusts, between the previously imbricated units, are outwardly rotated towards lower angles. These are temporarily reactivated as first ($\delta_f \sim 32^\circ$) and second order ($\delta_f \sim 20^\circ$) out-of-sequence-thrusts (OOSTs). The first order OOST splits the frontal active wedge from the inactive terrace and the second order OOSTs decouple the frontal wedge from upper wedge (Fig. V-3).

5.2.2 'Sediment' sequence with a medium thick embedded layer (V_{medium} and C_{large})

The DF in V_{medium} and C_{large} migrates faster forward than in experiment V_{small} resulting in a more widely extended frontal wedge. Imbrication and compression within this frontal wedge are reduced compared to the wedge in V_{small} . In this case, the upper brittle (C) layer is affected by forethrusts ($\delta_f \sim 36^\circ$) and backthrusts ($\delta_b \sim 45^\circ$) with a small offset, as well as folds, such as asymmetrical box folds with small offsets along kink bands (Fig. V-3). More backthrusts evolve with larger offsets than in V_{small} . The resulting frontal wedge evolves flatter with slope angles of $\alpha_1 \sim 5^\circ$.

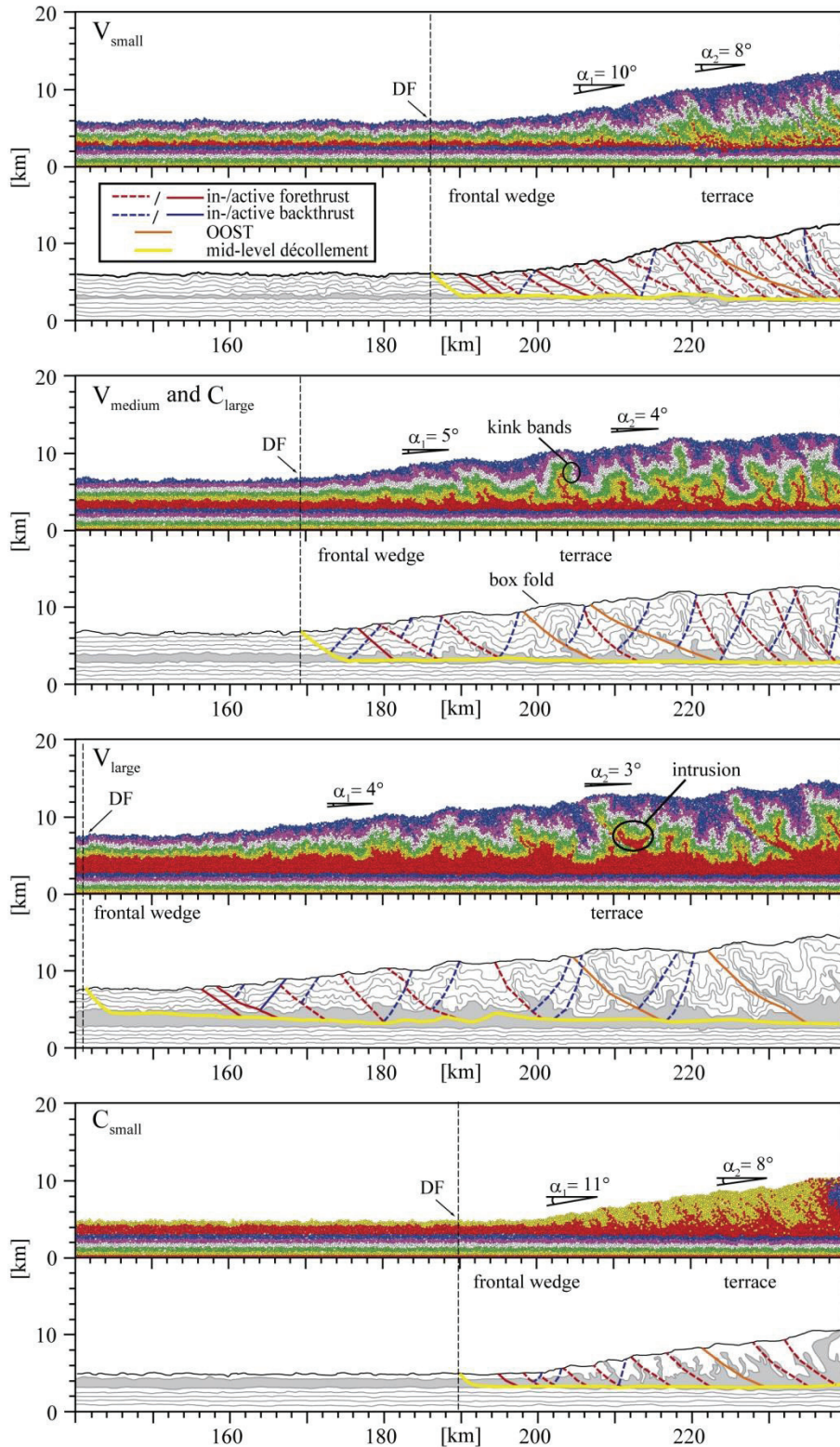


Fig. V-3: Particle configuration view and schematic sketch of the experiments V_{small}, V_{medium} and C_{large}, V_{large}, and C_{small} after 53 % of shortening. The different colors are used as markers of horizons to visualize fault evolution. The red layers have a Burger's rheology. The DF (deformation front) and slope angles α_{1-3} are labeled for each experiment.

Hence, the foreland-vergence is slightly reduced in the frontal wedge. Further inwards, the frontal lower slope slightly flattened and a flatter terrace with a slope angle of $\alpha_2 \sim 4^\circ$ evolves. At this terrace, the formerly active fore- and backthrusts are slightly outwardly rotated toward lower dip angles. Temporarily, additional reactivated dominant backthrusts also cause the evolution of a new forethrust (forethrusting) and backthrust (backthrusting; Fig. V-4). Frequently, thrusts are first ($\delta_f \sim 35^\circ$) order reactivated as OOSTs separating the frontal active from the in-active terrace. Additionally, second order OOSTs ($\delta_f \sim 24^\circ$) split the frontal wedge from the upper wedge (Fig. V-3).

Compared to the previous experiment, the topography of the frontal wedge and the terrace is wavy due to the folding of the material. The embedded layer is smeared along all types of thrusts or folds. This shows the increasing importance of the backthrusts versus the forethrusts, and the folding processes.

5.2.3 'Sediment' sequence with a thick embedded layer (V_{large})

The DF in V_{large} propagated faster forward compared to those in the other experiments. Similar to the previous experiments, forethrusts rise from the mid-level detachment and crop out directly at the DF (Fig. V-3).

The dipping angles of forethrusts are steeper ($\delta_f \sim 40^\circ$) and the corresponding backthrusts dip flatter ($\delta_b \sim 44^\circ$) than in the previous experiments. Fore- and backthrusts evolve nearly symmetrically with an angle-difference of 4° and cause pop-up structures or deep viscoelastic-plastic intrusions into the upper brittle layer (Fig. V-3). Consequently, the system is only slightly foreland-vergent. Similar to V_{medium} and C_{large} , forethrusting, as well as backthrusting, is observed and the corresponding frontal wedge evolves as flattest of all experiments with $\alpha_1 \sim 4^\circ$ in V_{large} . Moreover, the upper (C) brittle layer is increasingly folded and the compression of the frontal wedge is reduced. The amount of active fore- and backthrusts decrease and the fault-spacing is large.

The frontal wedge is separated by first order OOSTs ($\delta_f \sim 39^\circ$) from the terrace. These thrusts smear the viscoelastic-plastic material as intrusions deep into the upper (C) brittle layer (Fig. V-3). Hence, the offsets along these reactivated faults are much larger compared to the temporarily activated thrusts in the frontal part of the wedge. The terrace evolves flatter with an angle of $\alpha_2 \sim 3^\circ$. The second order ($\delta_f \sim 27^\circ$) OOSTs separate the frontal wedge from the upper wedge.

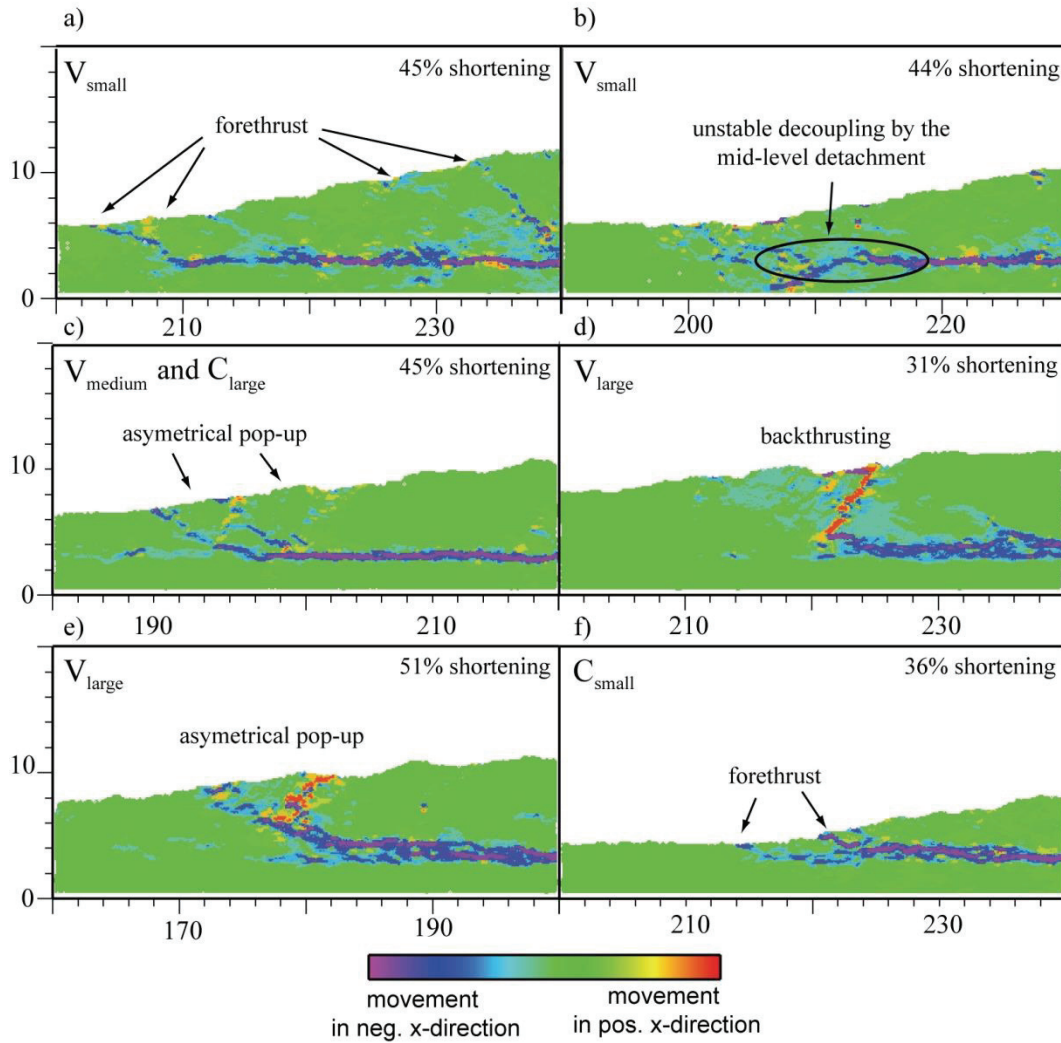


Fig. V-4: Illustration of the gradient of displacement field for different structures and shortening phases (marked in figure) of V_{small} , V_{medium} , and C_{large} , V_{large} , and C_{small} .

The position of the mid-level detachment in experiment V_{large} varies slightly more than in the previous experiments. With decreasing distance to the DF, the mid-level detachment rise from a lower position within the weak viscoelastic-plastic layer to a higher position (Fig. V-4).

5.2.4 'Sediment' sequence a small cover and a medium embedded layer (C_{small})

In the second series, we investigated the key role of the cover layer. The effect of a thick cover layer is explained and analyzed within experiment V_{medium} and C_{large} (see Sec. 5.2.2). Due to the reduction of the cover layer thickness (C), the frontal wedge in C_{small} evolves shorter than in the other experiments. The tendency of the DF to migrate rapidly outward

is reduced. This leads to a relatively steep slope angle of $\alpha_1 \sim 11^\circ$ (Fig. V-3). The upper (C) brittle material deforms mainly by thrusting and no folding is observed. At the frontal wedge, forethrusts rise with $\delta_f \sim 28^\circ$ from the embedded layer and crop out at the DF. These forethrusts are very short due to the thin brittle cover in which they spread. The corresponding backthrusts in this frontal part are rare and have dip-angle of $\delta_b \sim 55^\circ$. Consequently, the system again is distinctly foreland-vergent. The forethrust dip angles are steeper and higher compression occurs than in experiment V_{medium} and C_{large} even though the viscoelastic-plastic layer thicknesses are identical.

Further inwards, the terrace evolves slightly flatter with an angle of $\alpha_2 \sim 8^\circ$. First order OOSTs ($\delta_f \sim 28^\circ$) split the wedge from the active frontal section and an in-active terrace. Second ($\delta_f \sim 24^\circ$) order OOSTs separate the terrace from the upper wedge (Fig. V-3).

6. Discussion

To gain a deeper insight into the influence of different cover and evaporitic layer thicknesses on structural systems, four numerical experiments (V_{small} , V_{medium} , and C_{large} , V_{large} , and C_{small}) are undertaken. The viscosity of the embedded layers is set at $\eta_{\text{nature}} \sim 8 \times 10^{21}$ (Pa s), which is consistent with ‘natural’ viscosity in the range of natural values of evaporites, mainly anhydrite (10^{19} Pas- 10^{21} Pas; van Keken et al., 1993; Spiers et al., 1990; Chemia and Koyi, 2008; Mukherjee et al., 2010).

In all experiments, a wedge evolves out of the upper (C) brittle material, which is decoupled from the underlying (B) brittle strata by a mid-level detachment. This detachment evolves in the lower part of the embedded weak (V) layer, at the latest, after 15 % shortening. Such decoupling due to a weak embedded layer in general corresponds to previous experiments (Bonini, 2001, 2003; Kukowski et al., 2002; Couzens-Schultz et al., 2003; Konstantinovskaya and Malavieille, 2011; Wenk and Huhn, 2013). In this study, the stability and strength of the mid-level detachment and, therewith, the thrust system varies depending on the individual thicknesses of the embedded viscoelastic-plastic layer and the brittle cover layer. In all experiments except V_{small} , the mid-level detachments are stable. In experiment V_{small} , the mid-level décollement is temporally inactive, because the viscoelastic-plastic layer (V) is, at 400 m, extremely thin and, therefore, partly pinches out (Fig. V-4). In such cases, the brittle upper (C) layer is placed on top of the brittle lower (B) layer, which rapidly initiates coupling due to the increased shear resistance. The resulting

stress is directly transported from the basal detachment into the upper (C) layer (Table V-2). Hence, it can be inferred that an embedded layer (V) of more than 400 m thickness is required to allow for evolution of a stable mid-level detachment.

6.1 Effects of the thickness of the embedded layer (series I)

The frontal wedges in all experiments are characterized by a steeper frontal slope followed inwards by a flatter terrace (Fig. V-3). The slope topography of the frontal wedges steepens with decreasing embedded layer thickness (Fig. V-5). This coherence is also shown qualitatively in previous studies of Cotton and Koyi (2000), Bahroudi and Koyi (2003) and Bonini (2003). Here, we are able to give a quantitative explanation. If we increase the thickness of the embedded layer the normal stress within the embedded layer, remains relatively stable at $\sim 2 \times 10^{10}$ Pa. The stability of this value shows that the loading increase, due to the material thickening of the embedded layer, is not responsible for topographic steepening. However, further analysis shows that the shear stresses decreased from 4.95×10^9 Pa in V_{small} to 3.73×10^9 Pa in V_{large} . Consequently, larger strains can be accumulated due to the reduced stress in accordance with a reduction of the embedded material thickness. The resulting slope angle increase from experiment V_{small} to V_{medium} is distinct, with an angle increase of 5° at the frontal wedge and 4° at the flatter terrace (Fig. V-3). Between V_{medium} and V_{large} , the surface slope difference is small at only 1° along the wedge structure. Hence, after the layer reaches a certain thickness of more than 1000 m, a further thickness increase does not significantly change the décollement strength and the wedge topography. Additionally, as a result of the higher shear stress in case of the thin embedded layer (V_{small}), forethrusts and backthrusts evolve asymmetrically. Variation in the fore- and backthrust dip-angles can be explained by the pinch-out of the embedded layer, which leads to increased shear strength.

In general, an imbricated frontally accreted wedge evolves with a foreland-vergent structural system when a thin embedded layer thickness of 400 m is used. With increasing embedded layer thickness (V_{medium} and V_{large}) the thrusting within the brittle cover decreases, while folding increases. Nevertheless, fore- and backthrusts are still observed in experiment V_{medium} and V_{large} , but with a reduced foreland-vergence as the forethrusts and corresponding backthrusts show similar dip-angles (differences of 9° in V_{medium} and 4° in V_{large}). Furthermore, pop-up structures occur and the number of backthrusts as well as their

influence increases (Fig. V-3, V-4). Consequently, the increasing symmetry and the increasing occurrence of folds correspond to the decreasing shear strength at the detachment. A thick embedded layer with a thick cover layer, therefore, induces a far-propagating and flat accretionary wedge, which includes fore- and backthrusting, pop-up structures, and increasing material folding (Fig. V-3, V-4, V-5).

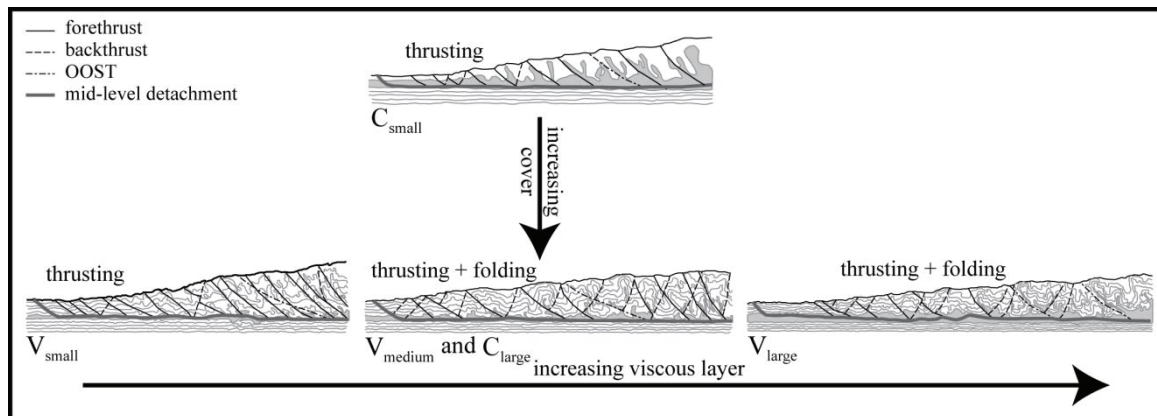


Fig. V-5: Conceptual models demonstrating the key role of the thickness of the incoming strata on wedge shape and internal structures. The viscoelastic-plastic layer is shown as a grey layer.

In summary, the thickness of the embedded layer (V) has an important influence on the structural system within the cover material (C) based on the changes in the shear stress. Moreover, it can be inferred that after a critical thickness (1000 m) is reached, a further increase of the material thickness has a minimal influence on the wedge mechanics. To achieve natural salt-like behavior, a thickness of at least 300-400 m should be used in a numerical model.

6.2 Effects of the thickness of the Plio-Quaternary cover (series II)

By comparing the results of C_{small} and C_{large} , it can be inferred that the topography steepens with decreasing cover material thickness (Fig. V-5). Such a steepening occurs when the strength of the décollement increases (e.g., Mulugeta, 1988; Moore, 1989; Davis et al. 1983; Hardy et al., 1998). Consequently, the loading has an important effect on the stresses along the décollement. This result resembles those of Mulugeta (1988), Marshak and Wilkerson (1992), Gutscher et al. (1998b), Bonini (2003) and Adam et al. (2004). In contrast, to those previous studies, we show, additionally, that the shear stress within the

embedded layer decreases slightly, whereas the normal stresses decrease significantly from C_{large} to C_{small} . The material reacts, thus, weaker under an increase in loading. The resulting wedge taper increase between C_{large} and C_{small} ranges from 5° to 11° at the frontal wedge and from 4° to 8° at the flat terrace.

Additionally, due to the higher strength of the décollement, the brittle cover is thrust and not folded in C_{small} . The latter mechanism is more dominant in C_{large} (Fig. V-5). Forethrusts and their corresponding backthrusts evolve distinctly foreland-vergent in C_{small} and an imbricated frontally accreted wedge evolves with a foreland-vergent structural system. The fault spacing is small, which leads to a short and compressed wedge shape. This finding corresponds with studies of Mulugeta (1988), Gutscher et al. (1996) and Bonini (2003) and shows that the number of folds and thrusts is inversely proportional to the thickness of the cover layer and, furthermore, that the corresponding fault-spacing develops proportional to the layer thickness, which is in agreement with studies of Koyi and Cotton (2000).

In contrast, the thick cover in C_{large} results in a typical far-propagating and flat accretionary wedge, which includes more typical salt-tectonic characteristics, such as fore- and backthrusting, pop-up structures or folding (Fig. V-3, V-4, V-5). In summary, the thickness of the cover layer has an important influence on the wedge mechanics. It is shown that a reduction of the cover material can, despite the presence of a weak viscoelastic-plastic layer, result in the evolution of a rather imbricated wedge with similarities (e.g., foreland-vergence) to a Mohr Coulomb wedge.

6.3 Comparison with the Mediterranean Ridge

Due to different geological boundary conditions, such as sediment input thickness and stratigraphy, the structural system of the Mediterranean Ridge varies along the continental margin. In the western domain, a steeper wedge evolves out of imbricated thrust sheets, whereas in the eastern domain, a flatter wedge grows out of a broad band of gentle folds and reverse faults.

At the eastern domain of the Mediterranean Ridge the evaporitic layer reaches a thickness of 2500 m and the Plio-Quaternary cover has a thickness of 3000 m. Similar values are applied for the Messinian evaporites (V) and the Plio-Quaternary cover (C) in V_{large} . The results of V_{large} correspond well with the observations at the eastern part of the Mediterranean ridge. Both the natural, as well as the numerical accretionary wedges, evolve

as a wide, broad, and flat frontal wedge more dominated by folding and backthrusts than in the other experiments. In both cases, foreland-vergence, hinterland-vergence, and folding occurs, which are a typical characteristics of wedges growing on evaporitic décollements (e.g., Davis and Engelder, 1985; Marshak and Wilkerson, 1992; Cotton and Koyi, 2000; Bonini, 2001, 2007; Costa and Vendeville, 2002; Bahroudi and Koyi, 2003). However, in the numerical experiments, forethrusts occur and the resulting slope angle is approximately $\sim 4^\circ$ higher than that in nature, where angles of 0.7° are measured (Polonia et al., 2002). This difference results, besides other factors, out of the lack of fluids in the numerical DEM approach.

In contrast, at the western domain of the Mediterranean Ridge the evaporitic layer reaches a thickness of 1500 m and the Plio-Quaternary cover has a thickness of 300-400 m. Furthermore, the inner domain is described as an atypical salt wedge consisting of imbricated thrust sheets (Chaumillon et al. 1996; Polonia et al., 2002). Again, similar ratios are applied for the numerical experiment (C_{small}).

To compare experiment V_{large} and C_{small} , we need two separate layer reductions to isolate the influence of the thickness reduction of the embedded evaporites (from V_{large} to V_{medium} and C_{large}) and of the brittle cover (from V_{medium} and C_{large} to C_{small}) on the structural styles of the accretionary wedge.

In the first step, we reduce the thickness of the embedded layer (from V_{large} to V_{medium} and C_{large}). Our results show that the reduction of the embedded viscoelastic-plastic layer, from 2500 m in the eastern part to 1500 m in the western part, do not significantly change the mechanics, because the wedge in experiment V_{medium} and C_{large} still evolves typical of evaporitic décollements. Additionally, by comparing the folded broad wedge of experiment V_{medium} and C_{large} with the steep imbricated wedge of experiment V_{small} , we can infer that a 1000 m thick embedded viscoelastic-plastic layer is required to achieve typical salt-like tectonic features, whereas with <400 m of brittle material, the incoming material is only thrust and shows typical brittle material behavior. Consequently, the results of the Series I show that this reduction of the embedded weak layer is not the key factor influencing the differences in the structural system of the western and the eastern Mediterranean prisms.

In the next step, we reduce the thickness of the cover material from 2500 m to 400 m (from C_{large} to C_{small}). Due to this reduction the former broad and flat numerical wedge of C_{large} changes significantly to a steeper, imbricated wedge in C_{small} . The foreland-vergence

increases and no deformations by folding are observed. These results of Series II fit with observations at the western Mediterranean Ridge, where an atypical imbricated accretionary complex, deformed by faults, grows above the evaporitic detachment.

The atypical evolution of the Mediterranean Ridge growing on a salty décollement is explained by different factors, such as convergence angles and rates, increasing strength related to increasing sediment compaction, fluid escape, and different collisional stages (Le Pichon et al., 1982; Lallemand et al., 1994; Chaumillon and Mascle, 1997; Polonia et al., 2002; Reston et al., 2002). Our numerical experiments do not consider all these factors due to necessary numerical simplification. However, we show that an imbricated wedge can evolve on an evaporitic décollement only due to a decrease in cover material, which decreases in the normal stress. A decrease in normal stress (in the case of stable shear stress) results in a stronger décollement shown by the thrust system and the friction value. Such a phenomenon would more likely occur for a décollement in anhydrite as these rocks exhibit a pressure dependent ductile phase that occurs at depths of >1000 m (Shearman, 1983) or between 75°C and 125 °C (Müller et al., 1981). Hence, although the cover thickness is not the only aspect that influences the mechanics of the Mediterranean Ridge, we are able to show that this factor solely allows for reconstruction of a similar system behavior with the evolution of flat salt tectonic dominated wedge on the eastern side (V_{large}) and an imbricated steep wedge on the western side (C_{small}).

7. Conclusion

Within our study we focus on the role of the thickness of the brittle cover and the viscoelastic-plastic embedded weak layer on the wedge kinematics and the structural style of a growing accretionary wedge. To quantify the influences, we simulate a series of numerical wedge experiments (V_{large} , V_{medium} , and C_{large} , V_{small} as well as C_{small}) using the Discrete Element Method (DEM) by incorporating two different rheologies for brittle (Mohr Coulomb rheology) and viscoelastic-plastic materials (Burger's rheology). The numerical DEM approach allows for a detailed analysis of particle movements and stresses, which are required to understand the deformation system. The results are later compared with observations along the Mediterranean Ridge, which is the target area of our study showing different structural styles in the western Ionian and eastern Levantine domain. To ensure realistic comparisons strata thicknesses employed in the model are taken from the

known values at the Mediterranean Ridge. The viscosity of the viscoelastic-plastic layer is in the range of anhydrite, which is the most common evaporite in the Mediterranean Sea (Abdel Aal et al., 2000; Chemia and Koyi, 2008; Mukherjee et al., 2010).

With the results, we find that an embedded layer of 400 m thickness is necessary to allow the evolution of a stable mid-level detachment in such a numerical approach. Furthermore, the thickness of the embedded layer has an important influence on the structural system in the cover material. When the embedded weak layer is thick, the material deforms rather by folding or symmetrical fore- and backthrusts whereas when the layer is thin, even flat forethrusts and steep backthrusts occur. Nevertheless, at thicknesses greater than 1000 m, significant effects on the structural development are no longer observed. Consequently, the different structural evolution of the eastern and the western Mediterranean ridge cannot be explained by the evaporitic reduction to the western parts, because there the evaporites reach a thickness of 1000 m.

Concerning the cover layer, further, patterns emerge with variation of thickness. With a decrease, the shear strength remains stable, but the normal stress reduces and the material strength increases resulting in the evolution of a foreland-vergence and an imbricated wedge. In contrast, if the thickness of the cover layer is increased, the foreland-vergence reduces, backthrusting dominance increases, and folding occurs. If we transfer the results to the observations at the Mediterranean ridge, the consequence could be that the western part exhibits a more imbricate form due to the extremely reduced Plio-Quaternary cover and the eastern part a more folded form with rather symmetrical structures. In summary, despite all different factors that vary along the continental margin, with only a change in loading, it is possible to reconstruct the structural systems along the Mediterranean Ridge based on the creep behavior of the evaporites. Consequently, if anhydrite is the main rock of the evaporites, the cover layer thickness (i.e., loading) has an important influence on the creep behavior and, therewith, on the shapes that occur at the western and the eastern Mediterranean ridge complex.

ACKNOWLEDGEMENTS

Thanks are due to all our colleagues of the MARUM-Center for Marine Environmental Sciences. This research was funded through DFG-Research Center / Cluster of Excellence „The Ocean in the Earth System“.

Chapter VI: Conclusion and Outlook

In this work, four studies based on numerical Discrete Element ‘sandbox’ experiments are presented. In these studies the mechanics and the thrust systems of accretionary wedges evolving of a heterogeneous incoming ‘sediment’ section are analyzed. The section in all studies consists of a weak layer which is embedded between an upper and a lower brittle layer. By changing the rheology, viscosity and thickness of the embedded layer the effects on the mechanical behavior and the evolution of thrusts are examined. Additionally, the influence of the upper layer thickness is analyzed. In the following, the conclusions of all three studies are presented.

The first study (**Chapter III**) analyzes the differences in the thrust system and the mechanics of two accretionary wedges which incorporate either a low friction layer (Mohr Coulomb rheology) or a viscoelastic-plastic layer (Burger’s rheology) embedded in a higher frictional incoming ‘sediment’ sequence. Therefore, identical property values for the particle stiffness and the coefficient of friction in the two weak embedded layers are used. The only exception is the viscosity, which only must be defined for the viscoelastic-plastic layer. As a result, in both cases a mid-level décollement evolves on which the frontal wedge grows by fore- and backthrusts. Nevertheless, depending on the used rheology the weak embedded layer and the upper brittle layer deform differently in the two experiments. The segment above the viscoelastic-plastic décollement spread wider, with flatter slope angles, larger thrust spacing and a more symmetrical thrust system as in the case of the weak brittle décollement. Additionally, backthrusts are more dominant and a dually-vergence occurs. These factors are typical for ‘evaporite’-based wedges and, consequently, we inferred that using a viscoelastic-plastic rheology is more suitable to simulate an ‘evaporitic’-like behavior than a weak Mohr Coulomb rheology.

The second study (**Chapter IV**) focuses on the influence of a viscoelastic-plastic layer on the wedge mechanics and the mass transport pattern by testing different viscosities. Since we know from the first study (Chapter III), the Burger’s rheology (viscoelastic-plastic) is more suitable to model the behavior of an ‘evaporitic’ décollement, the next step is to test different viscosity values and their effect on the mechanics and mass transport in growing accretionary wedges. Within this study, we show that in case of a high dynamic viscosity in the embedded layer the wedge mechanics and as well as the mass transport pattern are

similar to those in a homogeneous brittle wedge. In this case, no decoupling occurs and thrusts rise directly from the basal box bottom. In contrast, under low viscosity values, a mid-level detachment evolves along the embedded layer which steps down to the basal box bottom far inward of the deformation front. Additionally, the wedge grows simultaneously by frontal and basal accretion. Furthermore, an increase of the viscosity changes the internal structures, the mass transport within the frontal accreted upper section and the duplex section. Under low viscosity values (η_{dynamic} : 5.4×10^{13} - 6.7×10^{13} Pa s) the décollements act more typically as an ‘evaporitic’-décollement. The corresponding naturally scaled viscosity values confirm with the viscosity value of measurements in anhydrite.

After the used numerical ‘sandbox’ experiment has been tested and calibrated to natural conditions in Chapter III and IV, the last study (**Chapter V**) deals with the comparison of wedge mechanics, layer input thickness and stress fields. These wedge experiments incorporate different embedded layer thicknesses and different brittle upper loadings. These values were adopted from the Mediterranean ridge to analyze the effects of thickness variations in the Messinian salts and the Plio-Quaternary cover on the structural evolution and mechanics of this accreted wedge. The Mediterranean Ridge shows a more typical imbricated steeper form in its western part and a more folded and flatter formation in its eastern part (Polonia et al., 2002). As a result, we show that if the embedded layer thickness is enhanced the upper layer is more deformed by fore- and backthrusts with a reduced foreland-vergence. In contrast, if the layer thickness is decreased the incoming layer is rather imbricated in a distinct foreland-vergent mode. The measured stress values support the observations. Nevertheless, after a certain thickness is reached a further increase does not significantly change the structural system anymore. Additionally, if the cover thickness is increased fore- and backthrusts evolve rather symmetrically and backthrusts as well as folds become increasingly important. Simultaneously, the stress ratios increase and the friction value decreases. By comparing the results with the observations along the Mediterranean Ridge, it can be assumed that the reduced cover thickness at the western section of the Mediterranean Ridge would more support imbrication whereas the high cover thickness in the eastern part rather results in a more ‘salt’-tectonic behavior with backthrusts and folds. Also the evaporites have an important impact, but their influence stagnates after a certain thickness has reached. Consequently, the experiments show that although the Mediterranean Ridge is affected by various factors, the use of identical thickness ratios is sufficient to reconstruct a similar structural evolution in the experiments.

The studies of the present thesis provide a better understanding for the structural evolution of heterogenic accretionary wedges with embedded layers having viscous attributes. In these studies, to the best of our knowledge for the first time the Burger's model is used in Discrete Element models to combine different rheological behaviors in an accretionary wedge. The Discrete Element Method allows for analyzing thrust evolution, particle movements and mass transport as well as extracting uplift paths, uplift angles, thrust offsets and dipping angles. Quantitative information are besides the qualitative particle pictures very helpful to examine the influence of the viscoelastic-plastic layer in Chapter III - V. Therefore, an extraction of stress values at each particle contact is helpful to understand the differences in the thrust system of the growing wedges. Summarizing, a viscoelastic-plastic layer with a low viscosity and a large thickness below a thick brittle upper layer acts most likely as a viscous 'salt'-layer. In this case, a mid-level décollement evolves in the viscoelastic-plastic layer and the material above is deformed by typical 'salt'-like structures. In contrast, a thin viscoelastic-layer with a high viscosity or a thin upper brittle layer increases material strength. This can prevent the evolution of a mid-level décollement or at least increase brittle deformation style with typical imbrication or underthrusting in the incoming 'sediment' sequence.

These presented analysis are used to develop conceptional models, which further help to understand the mechanics and kinematics at natural accretionary such as the deformation processes occurring at the Mediterranean Ridge. With our simulation it is possible to show that the different mechanics and thrust systems confirm with the thickness values of the incoming sediment section in this region.

It is suggested in the future to use the calibrated models for testing further properties such as the subduction velocity or the backstop form. These factors have an additional impact on wedge mechanics as shown by e.g., Smit et al. (2003) or Byrne et al. (1993). Also a stress analysis in a finer grid could be helpful to understand how stresses change within the evolving accretionary wedge. Furthermore, contact bonds could be applied to increase the material strength within the brittle layer.

To get a broader picture over the development of accretionary wedges incorporating viscoelastic-plastic materials, it would be interesting to build up a model in three

dimensions. This allows for implementation of e.g., different subduction directions, velocities and thicknesses along the strike of a growing accretionary wedge. Furthermore, an interesting task would be to make a finer stratification of different rheological layers embedded in a brittle stratum e.g., for the Mediterranean Ridge. The incoming ‘sediment’ section here consists of a fine stratification of different rheologies (anhydrite, halite and clays) which have different physical properties and act differently under pressure. Therein, it would be interesting to see, where a décollement evolves and if it evolves stable or if an undulation between different active décollements occurs.

References

- Abdel Aal, A., El Barkooky, A., Gerrits, M., Meyer, H., Schwander, M., Zaki, H., 2000. Tectonic evolution of the Eastern Mediterranean Basin and its significance for hydrocarbon prospectivity in ultradeep water of the Nile Delta. *The Leading Edge* 19, 1086-1102.
- Adam, J., Klaeschen, D., Kukowski, N., Flueh, E., 2004. Upward delamination of Cascadia Basin sediment infill with landward frontal accretion thrusting caused by rapid glacial age material flux. *Tectonics* 23(3), TC3009.
- Adam, J., Urai, J.L., Wieneke, B., Oncken, O., Pfeiffer, K., Kukowski, N., Lohrmann, J., Hoth, S., van der Zee, W., Schmatz, J., 2005. Shear localisation and strain distribution during tectonic faulting - new insights from granular-flow experiments and high-resolution optical image correlation techniques. *Journal of Structural Geology* 27(2), 283-301.
- Agarwal, K.K., Agrawal, G.K., 2002. Analog sandbox models of thrust wedges with variable basal frictions. *Gondwana Research* 5(3), 641-647.
- Anthony, J.L., Marone, C., 2005. Influence of particle characteristics on granular friction. *Journal of Geophysical Research*, 110(B8), B08409.
- Baar, C.A., 1977. *Applied salt-rock-mechanics 1: the in-situ behavior of salt rocks*. North-Holland Inc, Elsevier, New York, NY.
- Bahroudi, A., Koyi, H.A., 2003. Effect of spatial distribution of Hormuz salt on deformation style in the Zagros fold and thrust belt: an analog modelling approach. *Journal of the Geological Society* 160, 719-733.
- Bahroudi, A., Koyi, H.A., Talbot, C.J., 2003. Effect of ductile and frictional décollements on style of extension. *Journal of Structural Geology* 25(9), 1401-1423.
- Barnes, H.A., 2000. *A handbook of elementary rheology*. The University of Wales, Institute of Non-Newtonian Fluid Mechanics, Aberystwyth SY23 3 BZ.
- Beaumont, C., Fullsack, P., Hamilton, J., 1992. Erosional control of active compressional orogens, in: McClay, K.R. (Ed.), *Thrust tectonics*. Chapman and Hall, London, pp. 1-18.
- Belderson, R.H., Stride, A.H., Kenyon, N.H., 1981. Deformation in the Ionian and Levantine basins shown by long range side-scan sonar, in: Wezel, F.C. (Ed.), *Sedimentary Basins of Mediterranean Margins*, C.N.R. Italian Project of Oceanography. Tecnoprint, Bologna, pp. 407-413.
- Bigi, S., Di Paolo, L., Vadacca, L., Gambardella, G., 2010. Load and unload as interference factors on cyclical behavior and kinematics of Coulomb wedges: Insights from sandbox experiments. *Journal of Structural Geology* 32(1), 28-44.
- Biju-Duval, B., Lequellec, P., Mascle, A., Renard, V., Valery, P., 1982. Multibeam Bathymetric Survey and High-Resolution Seismic Investigations on the Barbados Ridge Complex (Eastern Caribbean) - a Key to the Knowledge and Interpretation of an Accretionary Wedge. *Tectonophysics* 86(1-3), 275-304.
- Bohnhoff, M., Makris, J., Papanikolaou, D., Stavrakakis, G., 2001. Crustal investigation of the Hellenic subduction zone using wide aperture seismic data. *Tectonophysics* 343(3-4), 239-262.
- Bonini, M., 2001. Passive roof thrusting and forelandward fold propagation in scaled brittle-ductile physical models of thrust wedges. *Journal of Geophysical Research* 106(B2), 2291-2311.
- Bonini, M., 2003. Detachment folding, fold amplification, and diapirism in thrust wedge experiments. *Tectonics* 22(6), 1065.
- Bonini, M., 2007. Deformation patterns and structural vergence in brittle-ductile thrust wedges: an additional analog modelling perspective. *Journal of Structural Geology* 29(1), 141-158.
- Bonnet, C., Malavieille, J., Mosar, J., 2007. Interactions between tectonics, erosion, and sedimentation during the recent evolution of the Alpine orogen: Analog modeling insights. *Tectonics* 26(6), TC6016.
- Brun, J.P., Fort, X., 2004. Compressional salt tectonics (Angolan margin). *Tectonophysics* 382(3-4), 129-150.
- Buiter, S.J.H., 2012. A review of brittle compressional wedge models. *Tectonophysics* 530-5311-17.
- Buiter, S.J.H., Bebeyko, A.Y., Ellis, S., Gerya, T.V., Kaus, B.J.P., Kellner, A., Schreurs, G., Yamada, Y., 2006. The numerical sandbox: comparison of model results for a shortening and an extension experiment, in: Buiter, S.J.H., Schreurs, G. (Eds.), *Analog and Numerical Modelling of Crustal-Scale Processes*. Geological Society, London, Special Publications, pp. 29-64.
- Burbidge, D.R., Braun, J., 2002. Numerical models of the evolution of accretionary wedges and fold-and-thrust belts using the distinct-element method. *Geophysical Journal International* 148(3), 542-561.

- Burkhard, M., Sommaruga, A., 1998. Evolution of the western Swiss Molasse Basin; structural relations with the Alps and the Jura Belt, in: Mascle, A. (Ed.), *Cenozoic Foreland Basins of Western Europe*. Geological Society of London Special Publication, pp. 279-298.
- Burtner R.L., Nigrini, A., Donelick, R.A., 1994. Thermochronology of Lower Cretaceous source rocks in the Idaho-Wyoming Thrust Belt. *American Association of Petroleum Geologists Bulletin* 78, 1613-1636.
- Butler, R.W.H., Coward, M.P., Harwood, G.M., Knipe, R., 1987. Salt: Its control on thrust geometry, structural style and gravitational collapse along the Himalayan mountains front in the Salt Range of northern Pakistan, in: O'Brien, J.J., Lerche, I. (Eds.), *Dynamical geology of salt related structures*. Academic Press, London, pp. 399-418.
- Byrne, D.E., Davis, D.M., Sykes, L.R., 1988. Loci and maximum size of thrust earthquakes and the mechanics of the shallow region of subduction zones. *Tectonics* 7 (4), 833-857.
- Byrne, D.E., Wang, W.-H., Davis, D.M., 1993. Mechanical role of backstops in the growth of forearcs. *Tectonics* 12(1), 123-144.
- Camerlenghi, A., 1998. The Mediterranean Ridge: A saltbearing accretionary complex in the framework of continental collision, in: Cloetingh, S. (Ed.), *Sedimentary basins—Models and constraints: Proceedings of the International School of Earth and Planetary Sciences* (Siena, September 1996). Elsevier, Amsterdam, pp. 215-241.
- Carlson, W.D., Donelick, R.A., Ketcham, R.A., 1999. Variability of apatite fission-track annealing kinetics: I. Experimental results. *American Mineralogist* 84, 1213-1223.
- Carter, N.L., Hansen, F.D., 1983. Creep of Rocksalt. *Tectonophysics* 92(4), 275-333.
- Carter, N.L., Hansen, F.D., Senseny, P.E., 1982. Stress Magnitudes in Natural Rock Salt. *Journal of Geophysical Research* 87(11), 9289-9300.
- Cawood, P.A., Kröner, A., Collins, W.J., Kusky, T.M., Mooney, W.D., and Windley, B.F., 2009. Accretionary orogens through Earth history, in Cawood, P.A., and Kröner, A., (Eds.), *Earth accretionary systems in space and time*. Geological Society of London Special Publication 318, p. 1-36.
- Chapple, W.M., 1978. Mechanics of thin-skinned fold-and-thrust belts. *Geological Society of America Bulletin* 89(8), 1189-1198.
- Chaumillon, E., Mascle, J., 1995. Lateral variations of the Mediterranean ridge deformation front. *Bulletin De La Societe Geologique De France* 166(5), 463-478.
- Chaumillon, E., Mascle, J., 1997. From foreland to forearc domains: New multichannel seismic reflection survey of the Mediterranean ridge accretionary complex (Eastern Mediterranean). *Marine Geology* 138(3-4), 237-259.
- Chaumillon, E., Mascle, J., Hoffmann, H.J., 1996. Deformation of the western Mediterranean Ridge: Importance of Messinian evaporitic formations. *Tectonophysics* 263(1-4), 163-190.
- Chemia, Z., Koyi, H., 2008. The control of salt supply on entrainment of an anhydrite layer within a salt diapir. *Journal of Structural Geology* 30(9), 1192-1200.
- Chin, H.P., Rogers, J.D., 1987. Creep Parameters of Rocks on an Engineering Scale. *Rock Mechanics and Rock Engineering* 20(2), 137-146.
- Cloos, M., Shreve, R.L., 1988. Subduction-channel model of prism accretion, melange formation, sediment subduction, and subduction erosion at convergent plate margins .1. Background and description. *Pure and Applied Geophysics* 128(3-4), 455-500.
- Cobbold, P.R., Durand, S., Mourgues, R., 2001. Sandbox modelling of thrust wedges with fluid-assisted detachments. *Tectonophysics* 334(3-4), 245-258.
- Collop, A.C., Sewell, A.J., Thom, N.H., 2004. Laboratory assessment of the resistance to crack propagation in high-stiffness asphaltic materials. *Proceedings of the Institution of Mechanical Engineers Part L-Journal of Materials-Design and Applications* 218(L1), 55-66.
- Costa, E., Camerlenghi, A., Polonia, A., Cooper, C., Fabretti, P., Mosconi, A., Murelli, P., Romanelli, M., Sormani, L., Wardell, N., 2004. Modeling deformation and salt tectonics in the eastern Mediterranean Ridge accretionary wedge. *Geological Society of America Bulletin* 116(7-8), 880-894.
- Costa, E., Vendeville, B.C., 2002. Experimental insights on the geometry and kinematics of fold-and-thrust belts above weak, viscous evaporitic décollement. *Journal of Structural Geology* 24(11), 1729-1739.
- Cotton, J.T., Koyi, H.A., 2000. Modeling of thrust fronts above ductile and frictional detachments: application to structures in the Salt Range and Potwar Plateau, Pakistan. *Geological Society of America Bulletin* 112(3), 351-363.
- Coulomb, C. A., 1776, Essai sur une application des regles des maximis et minimis a quelques problemes de statique relatifs, a la architecture. *Mem. Acad. Roy. Div. Sav.* 7, 343-387.
- Couzens-Schultz, B.A., Vendeville, B.C., Wiltshko, D.V., 2003. Duplex style and triangle zone formation: insights from physical modeling. *Journal of Structural Geology* 25(10), 1623-1644.
- Cruz, L., Malinski, J., Wilson, A., Take, W.A., Hilley, G., 2010. Erosional control of the

- kinematics and geometry of fold-and-thrust belts imaged in a physical and numerical sandbox. *Journal of Geophysical Research* 115, B09404.
- Cundall, P.A., 1987. Distinct Element Models of Rock and Soil Structure, in: Brown, E.T. (Ed.), *Analytical and Computational Methods in engineering Rock Mechanics*. Allen and Unwin, London.
- Cundall, P.A., Strack, O.D.L., 1978. *BALL - A program to model granular media using the distinct element method*, Technical Note. Advanced Technology Group, Dames and Moore, London.
- Cundall, P.A., Strack, O.D.L., 1979. A discrete numerical model for granular assemblies. *Géotechnique* 29(1), 47-65.
- Cundall, P.A., Strack, O.D.L., 1983. Modeling of microscopic mechanisms in granular material, in: Jenkins, J.T., Satake, M. (Ed.), *Mechanics of Granular Materials: New Models and Constitutive Relations*. Elsevier Science Publishers B.V., Amsterdam.
- Dahlen, F.A., 1984. Noncohesive critical coulomb wedges: an exact solution. *Journal of Geophysical Research* 89(B12), 10125-10133.
- Dahlen, F.A., 1990. Critical taper model of fold-and-thrust belts and accretionary wedges. *Annu. Rev. Earth Planet. Sci.* 18, 55-99.
- Dahlen, F.A., Suppe, J., Davis, D., 1984. Mechanics of fold-and-thrust belts and accretionary wedges: cohesive coulomb theory. *Journal of Geophysical Research* 89(B12), 10087-10101.
- Dahlen, F.A., Suppe, J., 1988. Mechanics, growth, and erosion of mountain belts. Geological Society of America-Special Paper 218, 161-178.
- Davis, D., Suppe, J., Dahlen, F.A., 1983. Mechanics of fold-and-thrust belts and accretionary wedges. *Journal of Geophysical Research* 88(B12), 1153-1172.
- Davis, D.M., Engelder, T., 1985. The role of salt in fold-and-thrust belts. *Tectonophysics* 119(1-4), 67-88.
- Davis, D.M., Lillie, R.J., 1994. Changing Mechanical Response during Continental Collision - Active Examples from the Foreland Thrust Belts of Pakistan. *Journal of Structural Geology* 16(1), 21-34.
- DeMets, C, Gordon, R.G., Argus, D.F., Stein, S., 1990. *Current plate motions*. *Geophysical Journal International*, 101:425-478.
- Detournay, E., Peirce, A., Bungler, A.P., 2007. Viscosity-dominated hydraulic fractures. *Rock Mechanics: Meeting Society's Challenges and Demands*, 1(2), 1649-1656.
- de Voogd, B., Truffert, C., Chamotrooke, N., Huchon, P., Lallemand, S., Lepichon, X., 1992. 2-Ship Deep Seismic-Soundings in the Basins of the Eastern Mediterranean-Sea (Pasiphae Cruise). *Geophysical Journal International* 109(3), 536-552.
- Donelick, R.A., O'Sullivan, P.B., Ketcham, R.A., 2005. Apatite Fission-Track Analysis. *Reviews in Mineralogy & Geochemistry* 58, 49-94.
- Dooley, T.P., Jackson, M.P.A., Hudec, M.R., 2007. Initiation and growth of salt-based thrust belts on passive margins: results from physical models. *Basin Research* 19(1), 165-177.
- Dusseault, M.B., Fordham, C.J., 1993. Time Dependent Behaviour of Rocks, in: Hudson, J.D. (Ed.), *Comprehensive Rock Engineering: Principles, Practice and Projects*. Pergamon Press, Oxford, England, pp. 119-149.
- Elliot, D., 1976. The motion of thrust sheets. *Journal of Geophysical Research* 81,949-963.
- Ellis, S., Schreurs, G., Panien, M., 2004. Comparisons between analog and numerical models of thrust wedge development. *Journal of Structural Geology* 26(9), 1659-1675.
- Fillon, C., Huismans, R.S., van der Beek, P., 2013. Syntectonic sedimentation effects on the growth of fold-and-thrust belts. *Geology* 41(1), 83-86.
- Finetti, I., 1976. Mediterranean Ridge: A young submerged chain associated with the Hellenic Arc. *Boll. Geofis. Teor. Appl.* 19, 31-65.
- Frisch, W., Meschede, M., 2007. *Plattentektonik, Kontinentalverschiebung und Gebirgsbildung*, Wissenschaftliche Buchgesellschaft, Darmstadt, pp. 1-196.
- Fruehn, J., White, R.S., Minshull, T.A., 1997. Internal deformation and compaction of the Makran accretionary wedge. *Terra Nova* 9(3), 101-104.
- Gallagher, K., Brown, R., Johnson, C., 1998. Fission track analysis and its applications to geological problems. *Annual Review of Earth and Planetary Sciences* 26, 519-572.
- Geiser, P.A., 1988. Mechanisms of thrust propagation - some examples and implications for the analysis of overthrust terranes. *Journal of Structural Geology* 10(8), 829-845.
- Giardini, D., Woodhouse, J.H., 1984. Deep seismicity and modes of deformation in Tonga subduction zone. *Nature* 307, 505-509
- Gleadow, A.J.W., Duddy, I.R., 1981. A natural long-term track annealing experiment for apatite. *Nuclear Tracks* 5(1/2), 169-174.
- Gleadow, A.J.W., Fitzgerald, P.G., 1987. Uplift history and structure of the Transantarctic Mountains: new evidence from fission track dating of basement apatites in the Dry Valleys area, southern Victoria Land. *Earth and Planetary Science Letters* 82(1), 1-14.
- Glodny, J., Lohrmann, J., Echtler, H., Gräfe, K., Seifert, W., Collao, S., Figueroa, O., 2005. Internal dynamics of a paleoaccretionary wedge: insights from combined isotope tectonochronology and sandbox modelling of

- the South-Central Chilean forearc. *Earth and Planetary Science Letters* 231(1-2), 23-39.
- Graveleau, F., Malavieille, J., Dominguez, S., 2012. Experimental modelling of orogenic wedges: A review. *Tectonophysics* (538-540), 1-66.
- Gutscher, M.A., Klaeschen, D., Flueh, E., Malavieille, J., 2001. Non-Coulomb wedges, wrong-way thrusting, and natural hazards in Cascadia. *Geology* 29(5), 379-382.
- Gutscher, M.A., Kukowski, N., Malavieille, J., Lallemand, S., 1996. Cyclical behavior of thrust wedges: Insights from high basal friction sandbox experiments. *Geology* 24(2), 135-138.
- Gutscher, M.A., Kukowski, N., Malavieille, J., Lallemand, S., 1998a. Episodic imbricate thrusting and underthrusting: analog experiments and mechanical analysis applied to the Alaskan accretionary wedge. *Journal of Geophysical Research* 103(B5), 10161-10176.
- Gutscher, M.A., Kukowski, N., Malavieille, J., Lallemand, S., 1998b. Material transfer in accretionary wedges from analysis of a systematic series of analog experiments. *Journal of Structural Geology* 20(4), 407-416.
- Hafner, W., 1951. Stress distributions and faulting. *Bulletin of the American Geological Society of America* 62(4), 373-398.
- Hardy, S., Duncan, C., Masek, J., Brown, D., 1998. Minimum work, fault activity and the growth of critical wedges in fold and thrust belts. *Basin Research* 10(3), 365-373.
- Hardy, S., McClay, K., Munoz, J.A., 2009. Deformation and fault activity in space and time in high-resolution numerical models of doubly vergent thrust wedges. *Marine and Petroleum Geology* 26(2), 232-248.
- Hoth, S., Adam, J., Kukowski, N., Oncken, O., 2006. Influence of erosion on the kinematics of bivergent orogens: Results from scaled sandbox simulations. *Tectonics, Climate, and Landscape Evolution* 398, 201-225.
- Hsü, K.J., Cita, M.B., W.B.F., R., 1973. The origin of the Mediterranean evaporites, in: Hsü, K.J., Ryan, W.B.F. (Eds.), *Initial reports of the Deep Sea Drilling Projekt*. Government Printing Office, Washington D.C., pp. 1203-1231.
- Hubbert, M. K., 1951. Mechanical basis for certain geological structures. *Geological Society America Bulletin* 62, 355-372.
- Huhn, K., Kock, I., Kopf, A.J., 2006. Comparative numerical and analog shear box experiments and their implications for the mechanics along the failure plane of landslides. *Norwegian Journal of Geology* 86(3), 209-220.
- Huiqi, L., McClay, K.R., Powell, D., 1992. Physical models of thrust wedges, in: McClay, K.R. (Ed.), *Thrust Tectonics*. Chapman and Hall, New York, pp. 71-81.
- Hung, J.H., Wu, J.C., 2012. In-situ stress and fault reactivation associated with LNG injection in the Tiechanshan gas field, fold-thrust belt of Western Taiwan. *Journal of Petroleum Science and Engineering* 96-97, 37-48.
- Hurford, A., 1986. Cooling and uplift patterns in the Lepontine Alps South Central Switzerland and an age of vertical movement on the Insubric fault line. *Contributions to Mineralogy and Petrology* 92(4), 413-427.
- Itasca Consulting Group, Inc., 2004. *PFC2D – Particle Flow Code in 2 Dimensions*, Ver. 3.1 User's Guide. Minneapolis: Itasca.
- Jaeger, J.C., Cook, N.G.W., Zimmerman, R.W., 2007. *Fundamentals of Rock Mechanics*, Blackwell Publishing, pp. 1-475.
- Jeramic, M.L. (1994). *Rock mechanics in Salt Mining*, Rotterdam: A.A. Balkema.
- Jensen, R.P., Bosscher, P.J., Plesha, M.E., Edil, T.B., 1999. DEM simulation of granular media-structure interface: Effects of surface roughness and particle shape. *International Journal for Numerical and Analytical Methods in Geomechanics* 23(6), 531-547.
- Jolivet, L., Faccenna, C., Goffé, B., Mattei, M., Rossetti, F., Brunet, C., Storti, F., Funicello, R., Cadet, J.P., d'Agostino, N., Parra, T., 1998. Midcrustal shear zones in postorogenic extension: Example from the northern Tyrrhenian Sea. *Journal of Geophysical Research* 103(B6), 12123-12160.
- Kastens, K.A., Breen, N.A., Cita, M.B., 1992. Progressive deformation of an evaporite-bearing accretionary complex: Seamarc I, Seabeam and piston-core observations from the Mediterranean Ridge. *Marine Geophysical Research* 14(4), 249-298.
- Ketcham, R.A., 2009. *HeFTy Version 1.6.7 - User manual*. Apatite to Zircon, Inc. and Richard A. Ketcham.
- Ketcham, R.A., 2005. Forward and inverse modeling of low-temperature thermochronometry data. *Reviews in Mineralogy and Geochemistry* 58(1), 275-314.
- Ketcham, R.A., Carter, A., Donelick, R.A., Barbarand, J., Hurford, A.J., 2007. Improved modeling of fission-track annealing in apatite. *American Mineralogist* 92, 799-810.
- Kim, H., Wagoner, M.P., Buttlar, W.G., 2009. Numerical fracture analysis on the specimen size dependency of asphalt concrete using a cohesive softening model. *Construction and Building Materials* 23(5), 2112-2120.
- Kock, I., Huhn, K., 2007. Influence of particle shape on the frictional strength of sediments - A numerical case study. *Sedimentary Geology* 196(1-4), 217-233.
- Konstantinovskaia, E., Malavieille, J., 2005. Erosion and exhumation in accretionary orogens: Experimental and geological

- approaches. *Geochemistry Geophysics Geosystems* 6(2), Q02006.
- Konstantinovskaya, E., Malavieille, J., 2011. Thrust wedges with decollement levels and syntectonic erosion: A view from analog models. *Tectonophysics* 502(3-4), 336-350.
- Koons, P.O., 1990. 2-sided orogen - collision and erosion from the sandbox to the Southern Alps, New-Zealand. *Geology* 18(8), 679-682.
- Kopp, H., Kukowski, N., 2003. Backstop geometry and accretionary mechanics of the Sunda margin. *Tectonics* 22(6), 1072.
- Koyi, H.A., Hessami, K., Teixell, A., 2000. Epicenter distribution and magnitude of earthquakes in fold-thrust belts: insights from sandbox models. *Geophysical Research Letters* 27(2), 273-276.
- Koyi, H.A., Vendeville, B.C., 2003. The effect of decollement dip on geometry and kinematics of model accretionary wedges. *Journal of Structural Geology* 25(9), 1445-1450.
- Kühni, A., Pfiffner, O.A., 2001. The relief of the Swiss Alps and adjacent areas and its relation to lithology and structure: topographic analysis from a 250-m DEM. *Geomorphology* 41(4), 285-307.
- Kuhlemann, J., 2007. Paleogeographic and paleotopographic evolution of the Swiss and Eastern Alps since the Oligocene. *Global and Planetary Change* 58, 224-236
- Kukowski, N., Lallemand, S.E., Malavieille, J., Gutscher, M.A., Reston, T.J., 2002. Mechanical decoupling and basal duplex formation observed in sandbox experiments with application to the Western Mediterranean Ridge accretionary complex. *Marine Geology* 186(1-2), 29-42.
- Kusky, T.M., Bradley, D.C., Haeussler, P.J., Karl, S., 1997. Controls on accretion of flysch and melange belts at convergent margins: Evidence from the Chugach Bay thrust and Iceworm melange, Chugach accretionary wedge, Alaska. *Tectonics* 16(6), 855-878.
- Lallemand, S.E., Schnurle, P., Malavieille, J., 1994. Coulomb theory applied to accretionary and nonaccretionary wedges - possible causes for tectonic erosion and or frontal accretion. *Journal of Geophysical Research* 99(B6), 12033-12055.
- Lama, R.D., Vutukuri, V.S., 1978. Handbook on mechanical properties of rocks - testing techniques and results. Trans Tech Publications, Germany, pp 1-515.
- Laubscher, H.P., 1972. Some overall aspects of Jura dynamics. *American Journal of Science* 272(4), 293-304.
- Laubscher, H.P., 1977. Fold development in Jura. *Tectonophysics* 37(4), 337-362.
- Le Comte, P. 1965. Creep in Rock Salt. *The Journal of Geology* 73(3): 469-484.
- Le Pichon, X., Lyberis, N., Angelier, J., Renard, V., 1982. Strain distribution over the East Mediterranean Ridge - a synthesis incorporating new sea-beam data. *Tectonophysics* 86(1-3), 243-255.
- Letouzey, J., B. Colletta, R. Vially, and J. C. Chermette, 1995. Evolution of salt-related structures in compressional settings, in: Jackson, M. P. A, Roberts D. G., Snelson, S. (Eds.) *Salt tectonics: a global perspective*. AAPG Memoir 65, p. 41-60.
- Liu, H., McClay, K.R., Powell, D., 1992. Physical models of thrust wedges, in: McClay, K.R. (Ed.), *Thrust Tectonics*. Chapman & Hall, London, pp. 71-81.
- Lisker, F., Ventura, B., Glasmacher, U.A., 2009. Apatite thermochronology in modern geology, in: Lisker, F., Ventura, B., Glasmacher, U.A. (Eds.) *Thermochronological Methods*. Geological Society Special Publications, London, 324, pp 1-23.
- Lohrmann., J, 2002. *Identification of parameters controlling the accretive and tectonically erosive mass-transfer mode at the South-Central and North Chilean forearc using scaled 2D sandbox experiments*. Scientific Technical Report STR02/10, GeoForschungs-Zentrum Potsdam.
- Lohrmann, J., Kukowski, N., Adam, J., Oncken, O., 2003. The impact of analog material properties on the geometry, kinematics, and dynamics of convergent sand wedges. *Journal of Structural Geology* 25(10), 1691-1711.
- Lucente, C.C, Pini, G.A., 2008. Basin-wide mass-wasting complexes as markers of the Oligo-Miocene foredeep-accretionary wedge evolution in the Northern Apennines, Italy. *Basin Research*, 20, 49-71.
- Lujan, M., Storti, F., Balanya, J.C., Crespo-Blanc, A., Rossetti, F., 2003. Role of decollement material with different rheological properties in the structure of the Aljibe thrust imbricate (Flysch Trough, Gibraltar Arc): an analog modelling approach. *Journal of Structural Geology* 25(6), 867-881.
- Macedo, J., Marshak, S., 1999. Controls on the geometry of fold-thrust belt salients. *Geological Society of America Bulletin* 111(12), 1808-1822.
- Malavieille, J., Konstantinovskaya, E., 2010. Impact of surface processes on the growth of orogenic wedges: Insights from analog models and case studies. *Geotectonics* 44(6), 541-558.
- Malkin, A.Y., Isayev, A.I. (2006). *Rheology: Concepts, Methods and Applications*, Chemtec Publishing, Toronto.
- Mandal, N., Chattopdhyay, A., Bose, S., 1997. Imbricate thrust spacing: experimental and theoretical analyses, in: Sengupta, S. (Ed.), *Evolution of Geologic Structures in Micro to*

- Macro-scale*. Chapman & Hall, London, pp. 143-165.
- Mandl, G., Shippam, G.K., 1981. Mechanical model of thrust sheet gliding and imbrication, in: McClay, K.R., Price, N.J. (Eds.), *Thrust and Nappe Tectonics*. Geological Society of London Special Publication, pp. 79–98.
- Mandl, G. 1988. *Mechanics of tectonic faulting: models and basic concepts*. Amsterdam: Elsevier.
- Marone, C, 1988. Laboratory-derived friction laws and their application to seismic faulting. *Ann. Rev. Earth Planet Science* 26, 643-696.
- Marshak, S., Wilkerson, M.S., 1992. Effect of overburden thickness on thrust-belt geometry and development. *Tectonics* 11(3), 560-566.
- Mascle, J., Chaumillon, E., 1997. Pre-collisional geodynamics of the Mediterranean Sea: the Mediterranean Ridge and the Tyrrhenian Sea. *Annali Di Geofisica* 40(3), 569-586.
- Mascle, J., Chaumillon, E., 1998. An overview of Mediterranean Ridge collisional accretionary complex as deduced from multichannel seismic data. *Geo-Marine Letters* 18(2), 81-89.
- Mascle, J., Chaumillon, E., Hoffmann, H.J., Rehault, J.P., 1994. Preliminary-results of the multichannel seismic-reflection cruise prised across the Lonian Mediterranean Ridge. *Comptes Rendus Del Academie Des Sciences Serie* 318(5), 651-657.
- Mezger, T.G. 2006. *The rheology handbook*. Hannover: Vincentz Network.
- Mindlin, R.D., Deresiewicz, H., 1953. Elastic Spheres in Contact under Varying Oblique Forces. *Journal of Applied Mechanics-Transactions of the Asme* 20(3), 327-344.
- Minelli, L., Faccenna, C., 2010. Evolution of the Calabrian accretionary wedge (central Mediterranean). *Tectonics* 29, TC4004 .
- Mitra, G., Boyer, S.E., 1986. Energy-balance and deformation mechanisms of duplexes. *Journal of Structural Geology* 8(3-4), 291-304.
- Miyakawa, A., Yamada, Y., Matsuoka, T., 2010. Effect of increased shear stress along a plate boundary fault on the formation of an out-of-sequence thrust and a break in surface slope within an accretionary wedge, based on numerical simulations. *Tectonophysics* 484(1-4), 127-138.
- Moore, J.C., 1989. Tectonics and hydrogeology of accretionary prisms: role of the décollement zone. *Journal of Structural Geology* 11(1-2), 95-106.
- Morgan, J.K., Boettcher, M.S., 1999. Numerical simulations of granular shear zones using the distinct element method 1. Shear zone kinematics and the micromechanics of localization *Journal of Geophysical Research* 104(B2), 2703-2719.
- Mourgues, R., Cobbold, P.R., 2006. Thrust wedges and fluid overpressures: Sandbox models involving pore fluids. *Journal of Geophysical Research* 111(B5), B05404.
- Mugnier, J.L., Baby, P., Colletta, B., Vinour, P., Bale, P., Leturmy, P., 1997. Thrust geometry controlled by erosion and sedimentation: a view from analog models. *Geology* 25(5), 427-430.
- Mukherjee, S., Talbot, C.J., Koyi, H.A., 2010. Viscosity estimates of salt in the Hormuz and Namakdan salt diapirs, Persian Gulf. *Geological Magazine* 147(4), 497-507.
- Müller, W.H., Schmid, S.M., Briegel, U., 1981. Deformation experiments on anhydrite rocks of different grain sizes - Rheology and Microfabric. *Tectonophysics* 78(1-4), 527-543.
- Mulugeta, G., 1988. Modelling the geometry of coulomb thrust wedges. *Journal of Structural Geology* 10(8), 847-859.
- Mulugeta, G., Koyi, H., 1987. 3-dimensional geometry and kinematics of experimental piggyback thrusting. *Geology* 15(11), 1052-1056.
- Nalpas, T., Brun, J.P., 1993. Salt flow and diapirism related to extension at crustal-scale. *Tectonophysics* 228(3-4), 349-362.
- Naylor, M., Sinclair, H.D., Willett, S., Cowie, P.A., 2005. A discrete element model for orogenesis and accretionary wedge growth. *Journal of Geophysical Research* 110(B12), B12403.
- Nieuwland, D.A., Leutscher, J.H., Gast, J., 2000. Wedge equilibrium in fold-and-thrust belts: prediction of out-of-sequence thrusting based on sandbox experiments and natural examples. *Geologie En Mijnbouw-Netherlands Journal of Geosciences* 79(1), 81-91.
- Nilfouroushan, F., Koyi, H.A., Swantesson, J.O.H., Talbot, C.J., 2008. Effect of basal friction on surface and volumetric strain in models of convergent settings measured by laser scanner. *Journal of Structural Geology* 30(3), 366-379.
- Nilfouroushan, F., Pysklywec, R., Cruden, A., 2012. Sensitivity analysis of numerical scaled models of fold-and-thrust belts to granular material cohesion variation and comparison with analog experiments. *Tectonophysics* 526196-206.
- Panian, J., Wiltschko, D., 2007. Ramp initiation and spacing in a homogeneous thrust wedge. *Journal of Geophysical Research* 112(B5), B05417.
- Panien, M., Schreurs, G., Pfiffner, A., 2006. Mechanical behaviour of granular materials used in analog modelling: insights from grain characterisation, ring-shear tests and analog experiments. *Journal of Structural Geology* 28, 1710-1724.
- Parisi, E., Erba, E., Cita, M.B., 1987. Stratigraphy and Sedimentation in the Anoxic Bannock

- Basin (Eastern Mediterranean). *Marine Geology* 75(1-4), 93-117.
- Persson, K.S., Sokoutis, D., 2002. Analog models of orogenic wedges controlled by erosion. *Tectonophysics* 356(4), 323-336.
- Philippe, Y., Colletta, B., Deville, E., Mascle, A., 1996. The Jura fold-and-thrust belt: a kinematic model based on map balancing, in: P.A., Ziegler, F., Horvath (Eds.), *Structure and prospects of Alpine basins and forelands*. Peri-Téthys Memoir 2, Mus. Nat. Hist. Nat., Paris, pp. 170: 235-261.
- Platt, J.P., 1989. The mechanics of frontal imbrication: A first-order analysis. *Geologische Rundschau* 77, 577-589.
- Platt, J.P., 1990. Thrust Mechanics in Highly Overpressured Accretionary Wedges. *Journal of Geophysical Research* 95(B6), 9025-9034.
- Platt, J.P., 2000. Calibrating the bulk rheology of active obliquely convergent thrust belts and forearc wedges from surface profiles and velocity distributions. *Tectonics* 19(3), 529-548.
- Polonia, A., Camerlenghi, A., Davey, F., Storti, F., 2002. Accretion, structural style and syn-contractational sedimentation in the Eastern Mediterranean Sea. *Marine Geology* 186(1-2), 127-144.
- Polonia, A., Torelli, L., Mussoni, P., Gasperini, L., Artoni, A., Klaeschen, D., 2011. The Calabrian Arc subduction complex in the Ionian Sea: Regional architecture, active deformation, and seismic hazard. *Tectonics* 30(5), TC5018.
- Reiners, P.W., Ehlers, T.A., Zeitler, P.K., 2005. Past, present, and future of thermochronology. *Low-Temperature Thermochronology: Techniques, Interpretations, and Applications* (58), 1-18.
- Reiter, K., Kukowski, N., Ratschbacher, L., 2011. The interaction of two indenters in analog experiments and implications for curved fold-and-thrust belts. *Earth and Planetary Science Letters* 302(1-2), 132-146.
- Reston, T.J., Fruehn, J., von Huene, R., Grp, I.W., 2002a. The structure and evolution of the western Mediterranean Ridge. *Marine Geology* 186(1-2), 83-110.
- Reston, T.J., von Huene, R., Dickmann, T., Klaeschen, D., Kopp, H., 2002b. Frontal accretion along the western Mediterranean Ridge: the effect of Messinian evaporites on wedge mechanics and structural style. *Marine Geology* 186(1-2), 59-82.
- Rossi, S., Sartori, R., 1981. A seismic-reflection study of the external Calabrian Arc in the northern Ionian Sea (Eastern Mediterranean). *Marine Geophysical Researches* 4(4), 403-426.
- Ryan, W.B.F., Hsü, K.J., et. al., 1973. *Initial Reports of the Deep Sea Drilling Project, Leg 13*. Government Printing Office, Washington D.C.
- Ryan, W.B.F., Kastens, K.A., Cita, M.B., 1982. Geological evidence concerning compressional tectonics in the Eastern Mediterranean. *Tectonophysics* 86(1-3), 213-242.
- Saltzer, S.D., Pollard, D.D., 1992. Distinct element modeling of structures formed in sedimentary overburden by extensional reactivation of basement normal faults. *Tectonics* 11(1), 165-174.
- Sample, J.C., Fisher, D.M., 1986. Duplex accretion and underplating in an ancient accretionary complex, Kodiak Islands, Alaska. *Geology* 14(2), 160-163.
- Sassi, W., Colletta, B., Bale, P., Paquereau, T., 1993. Modeling of structural complexity in sedimentary basins - the role of preexisting faults in thrust tectonics. *Tectonophysics* 226(1-4), 97-112.
- Schellart, W. P., 2000. Shear test results for cohesion and friction coefficients for different granular materials: scaling implications for their usage in analog modelling. *Tectonophysics* 324, 1 - 16.
- Schmid, S.M., Fügenschuh, B., Kissling, E., Schuster, R., 2004. TRANSMED Transects IV, V and VI: Three lithospheric transects across the Alps and their forelands, in: Cavazza, W., Roure, F., Spakman, W., Stampfli, G.M., Ziegler, P.A. (Eds.), *The TRANSMED Atlas: the Mediterranean Region from Crust to Mantle*. Springer Verlag.
- Schmid, S.M., Pfiffner, O.A., Froitzheim, N., Schönborn, G., Kissling, E., 1996. Geophysical-geological transect and tectonic evolution of the Swiss-Italian Alps. *Tectonics* 15(5), 1036-1064.
- Schöpfer, M.P.J., Childs, C., Walsh, J.J., 2006. Localisation of normal faults in multilayer sequences. *Journal of Structural Geology* 28(5), 816-833.
- Schreurs, G., Buitter, S.J.H., Boutelier, D., Corti, G., Costa, E., Cruden, A.R., Daniel, J.M., Hoth, S., Koyi, H.A., Kukowski, N., Lohrmann, J., Ravaglia, A., Schlische, R.W., Withjack, M.O., Yamada, Y., CavoZZi, C., Del Ventisette, C., Brady, J.A.E., Hoffmann-Rothe, A., Mengus, J.M., Montanari, D., Nilforoushan, F., 2006. Analog benchmarks of shortening and extension experiments, in: Buitter, S.J.H., Schreurs, G. (Eds.) *Analog and Numerical Modelling of Crustal-Scale Processes*. Geological Society of London Special Publication, 253, pp. 1-27.
- Selzer, C., Buitter, S.J.H., Pfiffner, O.A., 2007. Sensitivity of shear zones in orogenic wedges to surface processes and strain softening. *Tectonophysics* 437(1-4), 51-70.
- Shearman, D.J., 1983. Syndepositional and late diagenetic alteration of primary gypsum to anhydrite, in: Schreiber, B.C. (Ed.), *Sixth*

- International Symposium on Salt*. Salt Institute, Toronto, Canada, pp. 41–55.
- Shipboard Scientific Party DSDP Leg 13, 1973a. Cleft in Mediterranean Ridge, Ionian Sea-Site 126, in: Ryan, W.B.F., Hsu, K.J. (Eds.), *Init. Rep. DSDP*, pp. 219-241.
- Shipboard Scientific Party DSDP Leg 13, 1973b. Hellenic Trench-Sites 127 and 128, in: Ryan, W.B.F., Hsu, K.J. (Eds.), *Init. Rep. DSDP*, pp. 243-322.
- Shipboard Scientific Party DSDP Leg 13, 1973c. Mediterranean Ridge, Ionian Sea-Site 125, in: Ryan, W.B.F., Hsu, K.J. (Eds.), *Init. Rep. DSDP*, pp. 175-218.
- Simpson, G., 2011. Mechanics of non-critical fold-thrust belts based on finite element models. *Tectonophysics* 499(1-4), 142-155.
- Smit, J.H.W., Brun, J.P., Sokoutis, D., 2003. Deformation of brittle-ductile thrust wedges in experiments and nature. *Journal of Geophysical Research* 108(B10), 2480.
- Spiers, C.J., Schutjens, P.M.T.M., Brzesowsky, R.H., Peach, C.J., Liezenberg, J.L., Zwart, H.J., 1990. Experimental determination of constitutive parameters governing creep of rocksalt by pressure solution, in: Knipe, R.J., Rutter, E.H. (Eds.), *Deformation Mechanisms, Rheology and Tectonics*. Geological Society of London Special Publication, pp. 215-227.
- Stockmal, G.S., Beaumont, C., Nguyen, M., Lee, B., 2007. Mechanics of thin-skinned fold-and-thrust belts: Insights from numerical models, in: Sears, J.W., T.A., H., Evenchick, C.A. (Eds.), *Whence the Mountains? Inquiries into the Evolution of Orogenic Systems: A Volume in Honor of Raymond A. Price*. Geological Society America Special Paper, pp. 63-98.
- Storti, F., Salvini, F. and McClay, K., 2000. Synchronous and velocity-partitioned thrusting, and thrust polarity reversal in experimentally produced, doubly-vergent thrust wedges: Implications for natural orogens. *Tectonics*, 19, 378-396.
- Storti, F., Marin, R.S., Rossetti, F., Sainz, A.M.C., 2007. Evolution of experimental thrust wedges accreted from along-strike tapered, silicone-floored multilayers. *Journal of the Geological Society* (164), 73-85.
- Strayer, L.M., Hudleston, P.J., Lorig, L.J., 2001. A numerical model of deformation and fluid-flow in an evolving thrust wedge. *Tectonophysics* 335(1-2), 121-145.
- Suppe, J., 1981. Mechanics of mountain building and metamorphism in Taiwan. *Memoir of the Geological Society of China* (4), 67–89.
- Tappin, D. R. 2009 Mass transport events and their tsunami hazard, in: (Eds.) Mosher, D.C., Shipp, R.C., Moscardilli, L., Chaytor, J.D., Baxter, C.D.P., Lee, H.P., Urgeles, R., *Submarine mass movements and their consequences*, Springer Science and Business Media Berlin, Germany, pp. 667–684.
- Tay, P.L., Lonergan, L., Warner, M., Jones, K.A., Grp, I.W., 2002. Seismic investigation of thick evaporite deposits on the central and inner unit of the Mediterranean Ridge accretionary complex. *Marine Geology* 186(1-2), 167-194.
- Taymaz, T., Jackson, J., Westaway, R., 1990. Earthquake mechanisms in the Hellenic Trench near Crete. *Geophysical Journal International* 102(3), 695-731.
- Teixell, A., Koyi, H.A., 2003. Experimental and field study of the effects of lithological contrasts on thrust-related deformation. *Tectonics* 22(5), 1054.
- Terzaghi, C., 1925. Principles of Soil Mechanics. *Engineering News-Record*, 95(19-27).
- Ting, J.M., Corkum, B.T., Kauffman, C.R., Greco, C., 1989. Discrete numerical-model for soil mechanics. *Journal of Geotechnical Engineering-Asce* 115(3), 379-398.
- Turcotte, D.L., Schubert, G., 2002. *Geodynamics*. Cambridge University Press.
- Urai, J.L., Spiers, C.J., Zwart, H.J., Lister, G.S., 1986. Weakening of rock salt by water during long-term creep. *Nature* 324(6097), 554-557.
- van Keken, P.E., Spiers, C.J., Vandenberg, A.P., Muyzert, E.J., 1993. The effective viscosity of rocksalt: implementation of steady-state creep laws in numerical-models of salt diapirism. *Tectonophysics* 225(4), 457-476.
- Vendeville, B., Cobbold, P.R., 1988. How normal faulting and sedimentation interact to produce listric fault profiles and stratigraphic wedges. *Journal of Structural Geology* 10(7), 649-659.
- Von Eynatten, H., Schlunegger, F., Gaupp, R., Wijbrans, J.R., 1999. Exhumation of the Central Alps: evidence from ⁴⁰Ar/³⁹Ar laserprobe dating of detrital white micas from the Swiss Molasse Basin. *Terra Nova* 11(6), 284-289.
- Von Huene, R., Scholl, D.W., 1991. Observations at convergent margins concerning sediment subduction, subduction erosion, and the growth of continental crust. *Reviews of Geophysics* 29(3), 279-316.
- Wagner, G.A., Reimer, G.M., 1972. Fission Track Tectonics - Tectonic Interpretation of Fission Track Apatite Ages. *Earth and Planetary Science Letters* 14(2), 263-268.
- Wang, K.L., Hu, Y., 2006. Accretionary prisms in subduction earthquake cycles: The theory of dynamic Coulomb wedge. *Journal of Geophysical Research*, 111(B6), B06410.
- Weijermars, R., Jackson, M.P.A., Vendeville, B., 1993. Rheological and Tectonic Modeling of Salt Provinces. *Tectonophysics* 217(1-2), 143-174.
- Weijermars, R., Schmeling, H., 1986. Scaling of Newtonian and Non-Newtonian Fluid-

- Dynamics without Inertia for Quantitative Modeling of Rock Flow Due to Gravity (Including the Concept of Rheological Similarity). *Physics of the Earth and Planetary Interiors* 43(4), 316-330.
- Wenk, L., Huhn, K., 2013a. Mechanics in heterogeneous accretionary wedges – to test implemented rheologies, in: Zhu, H., Hart, R., Detournay, C., Nelson, M. (Eds.), *Continuum and Distinct Element Numerical Modeling in Geomechanics*. Proceedings of the 3rd International FLAC/DEM Symposium, Hangzhou, China.
- Wenk, L., Huhn, K., 2013b. The influence of an embedded viscoelastic-plastic layer on kinematics and mass transport pattern within accretionary wedges. *Tectonophysics*, <http://dx.doi.org/10.1016/j.tecto.2013.08.015>
- Westbrook, G.K., 1975. The structure of the crust and upper mantle in the region of Barbados and the Lesser Antilles. *Geophysical Journal of Royal Astronomical Society*, 43:201-242.
- White, R.S., 1977. Recent fold development in the Gulf of Oman. *Earth and Planetary Science Letters* 36, 85-91.
- Willett, S., 1992. Dynamic and kinematic growth and change of a Coulomb wedge, in: McClay, K.R. (Ed.), *Thrust tectonics*. Chapman and Hall, London, pp. 19-31.
- Willett, S., 1999. Orogeny and orography: The effects of erosion on the structure of mountain belts. *Journal of Geophysical Research-Solid Earth* 104(B12), 28957-28981.
- Willett, S., Beaumont, C., Fullsack, P., 1993. Mechanical model for the tectonics of doubly-vergent compressional orogens. *Geology*, 21, 371 -374.
- Yamada, Y., Baba, K., Matsuoka, T., 2006. Analog and numerical modelling of accretionary prisms with a décollement in sediments. In: S.J.H. Buiter and G. Schreurs (Eds.), *Analog and Numerical Modelling of Crustal-Scale Processes*. Geological Society of London Special Publication, 253: 169-183.
- Yamato, P., Kaus, B.J.P., Mouthereau, F., Castelltort, S., 2011. Dynamic constraints on the crustal-scale rheology of the Zagros fold belt, Iran. *Geology* 39(9), 815-818.
- Zhao, W.L., Davis, D.M., Dahlen, F.A., Suppe, J., 1986. Origin of convex accretionary wedges - evidence from barbados. *Journal of Geophysical Research* 91(B10), 246-258.

Danksagung

Das Verfassen dieser Dissertation in den vergangenen vier Jahren war eine spannende und lehrreiche Herausforderung für mich. Ich möchte mich auf diesem Wege bei allen bedanken, die mich dabei begleitet haben.

Insbesondere danke ich meiner Betreuerin Frau Professor Dr. Katrin Huhn für das interessante Thema, die Betreuung, die hilfreiche Unterstützung und für viele anregende Diskussionen, die mich immer wieder motiviert haben. Ihr Vertrauen in meine fachlichen Fähigkeiten und ihre wissenschaftliche Erfahrung haben mich während der gesamten Zeit begleitet und bestärkt.

Einen Einblick in neue Themenbereiche ermöglichte mir auch die Kooperation mit Frau Professor Dr. Cornelia Spiegel. Ich möchte ich nicht nur für die Übernahme des Gutachtens sondern auch für den hilfreichen Gedankenaustausch bei unseren Treffen und die konstruktive Kritik danken. In diesem Projekt gilt auch mein Dank Simon Elfert, mit dem ich in vielen Stunden daran gearbeitet habe zwei unterschiedliche Themen in spannender und verständlicher Art zu verbinden. Durch seine freundliche und hilfsbereite Art, hat mir die Zusammenarbeit mit ihm viel Freude bereitet, auch wenn manche Lösungsfindung kompliziert war.

Ich danke der gesamten Arbeitsgruppe (Lutz, Lina, Bryna, Arzu, Gerhard, Mella, Jannes, Sarah, Xin, Ella, Gesa, Franziska), in der ich mich sehr wohl gefühlt habe und die mich bei vielen Problemen unterstützt und mir mit Rat und Tat weitergeholfen hat.

Ich danke der „Hamburg Crew“ aus Miriam, Janna und Wisa als auch Agnes, die mich immer wieder aufgefangen, motiviert und in wissenschaftlichen Fragestellungen unterstützt haben aber auch immer ein Sofa zum Übernachten parat hatten. Darüber hinaus möchte ich auch meinen übrigen Freunden wie Jojo+Raffi, Nicole, Veronica, Vanessa und Belli danken, die viel Geduld mit mir hatte, wenn ich mal wieder absagen musste und mich immer bestärkt haben.

Ich danke meinem Mann Paul für seine unglaubliche Geduld, seine Aufmunterungen, seinen fachlichen Beistand, und dass er mich immer wieder zum Lachen gebracht hat.

Und nicht zuletzt danke ich meiner Mutter und meiner gesamten Familie, die in jeglicher Hinsicht die Grundsteine für meinen Weg gelegt haben und mich bei allem unterstützen was ich tue.

Appendix I: Combined DEM and AFT study

LINKING MECHANIC AND KINEMATIC PROPERTIES WITH UPPER CRUSTAL PROCESSES OF OROGENIC WEDGES I: COMBINING NUMERICAL SANDBOX MODELING AND APATITE FISSION TRACK THERMOCHRONOLOGY

Linda Wenk^{1*}, Simon Elfert², Cornelia Spiegel² and Katrin Huhn¹

¹ *MARUM – Center of Marine Environmental Science and Faculty of Geosciences, University of Bremen, Leobener Straße, 28359 Bremen, Germany*

² *Faculty of Geosciences, Klagenfurter Straße, University of Bremen 28359 Bremen, Germany*

Keywords:

Double-vergent wedge; numerical modeling; thermal modeling; model coupling; apatite fission track (AFT) analysis; thermochronology

Abstract

The study is focused on the relation between deep crustal and upper crustal processes. To bridge the scales in between, we present an approach in which numerical ‘sandbox’ modeling and apatite fission track analysis are combined. Three numerical Discrete Element experiments in which double-vergent wedges grow are developed. These wedges grow on top of a low or a high frictional décollement and with or without deep seated lower crustal fragment. Afterwards, synthetic apatite fission track ages are calculated from these experiments by a forward thermal history modeling of the time-temperature histories of selected particles. The combined analysis of the structural wedge evolution and the synthetic cooling age patterns revealed the effect of the different deep seated boundary conditions on the exhumation history of the upper crust. Within our experiments, high décollement strength results due to the basal accretion in a single U-shaped distribution of apatite fission track ages related to maximum uplift in the central part of the double-vergent

wedge. In contrast, low décollement strength with imbrication leads to stronger uplift at the wedge flanks and which results in a more W-shape distribution. Consequently, the apatite fission track analysis yielded an alternating series of young and old cooling ages. Additionally, the implementation of a non-deformable lower crustal fragment leads to a steeper flank in the cooling age pattern above of the structure, associated with the localization of thrusts and deformation. In contrast, the cooling age pattern evolves flatter with a non-localization of the thrust if the crustal fragment is missing.

1. Introduction

Fold-and-thrust belts, or accretionary wedges, are formed during continent-continent collisions or subduction along active continental margins as a result of the continuous deformation and compression of incoming rocks. The evolution and shape of orogens are influenced by different climatic, tectonic, and deep-seated mantle processes, as well as material properties and rheologies.

Fold-and-thrust belts which evolve due to an incoming indenter which has a similar vertical height than the incoming material are called double-vergent orogenic wedges (Byrne et al., 1988). In such scenarios, the uplifted material of the wedge distributes above the indenting material and can migrate bi-directionally along a frontal- and a retro-wedge flank. Natural examples of such structures are the Alps (e.g., Schmid et al., 1996; von Eynatten et al., 1999; Kühni and Pfiffner, 2001) or the Apennines (e.g., Jolivet et al., 1998). The evolution of these wedges is influenced by various factors such as the push from the rear (e.g., Chapple, 1978), the basal pull (e.g., Willett et al., 1993), the strength of the basal décollements (e.g., Hardy et al., 1998) or the backstop geometry (e.g., Koons, 1990). Many analog and numerical modeling studies investigate the mechanics and kinematics of double-vergent wedges (e.g., Beaumont et al., 1992; Willett et al., 1993; Storti et al., 2000; Persson and Sokoutis, 2002). Therein, it has been found that these wedges often grow episodically in association with the development of fore- and back-kinks, which are local, small-scale, fault-like structures (Fig. AI-1, see Sec. 1.1).

Yet, relationships between deep seated (lower crustal) and upper crustal processes are not fully understood, due to their different temporal and spatial scales. While analog and numerical sandbox approaches are used to study the mechanical aspects and mass transport patterns of double-vergent wedges on orogen scale, regional exhumation patterns and upper crustal to near surface processes are usually addressed by applying other methods such as low-temperature thermochronology. Analyzing time-temperature histories of rocks allows for inferences about denudation and about spatial distribution, timing and rate of exhumation (e.g., Wagner and Reimer, 1972; Hurford, 1986; Reiners et al., 2005; Lisker et al., 2009).

In this study, we combine numerical ‘sandbox’ modeling and AFT analysis to investigate the effect of deep seated processes and geometries on near surface processes as well as

mass transports patterns of orogenic wedges. In detail, this paper concentrates on the coupling approach itself and discusses the influence of décollement strength and deep seated fragments on the exhumation process. We present three numerical ‘sandbox’ experiments, which are utilized by the granular model approach based on the Discrete Element Method (DEM; Cundall and Strack, 1978). This technique was successfully used to simulate large scale deformation and complex tectonic processes, (Burbidge and Braun, 2002; Naylor et al., 2005; Miyakawa et al., 2010). Furthermore, a reference experiment (Sc1) with a high frictional décollement and a lower crustal fragment, two more experiments with modified initial conditions are presented. To test the influence of décollement strength, the friction coefficient of the décollement is reduced in a second experiment (Sc2). Omitting the lower crustal fragment in a third experiment (Sc3), allows for evaluating the effect of deep seated (lower crustal) fragments on the evolution of an orogen.

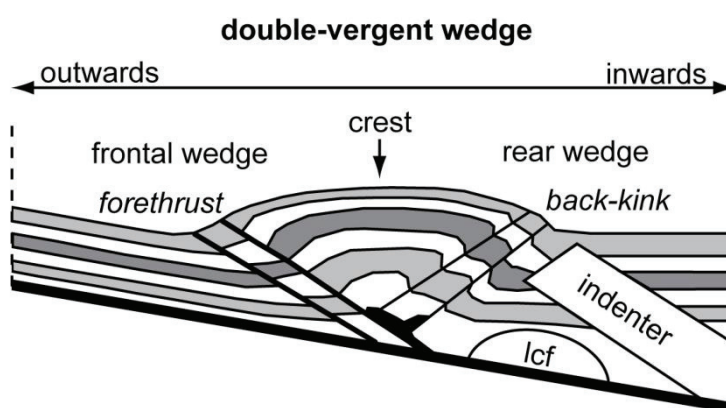


Fig. AI-1: Simplified schema of a double-vergent orogenic wedge; (lcf) lower crustal fragment (modified after Persson and Sokoutis, 2002).

Synthetic AFT ages are calculated for all experiments at specific moments during the model run and used to complement and improve the structural analysis of upper crustal dynamics. Furthermore, differences in the evolution and spatial distribution of the synthetic AFT ages between the experiments can be associated with the underlying deep seated conditions (Sc2 and Sc3) and, therefore, can be used to estimate their effect on near-surface processes.

Additionally, Elfert et al. (this volume) show that this approach can also be used to better understand observed cooling patterns. In the companion paper (“Linking mechanic and kinematic properties with upper crustal processes of orogenic wedges II: an example from

the European Central Alps”), they compare thermal histories and cooling patterns derived from observed AFT and (U-Th-Sm)/He data with synthetic AFT ages derived from a numerical sandbox experiment. Thus, on the one hand, synthetic AFT ages can be used as an additional tool to improve the analysis of numerical sandbox experiments and estimate the impact of deep seated on upper crustal processes. On the other hand, numerical sandbox experiments and synthetic AFT ages derived to evaluate hypotheses based on low-temperature thermochronology (Elfert et al., this volume).

1.1 Evolution of double-vergent wedges

Double-vergent wedges often grow episodically in association with the development of fore- and back-kinks, which are local, small-scaled, fault-like structures (Fig. AI-1). During the evolution of double-vergent wedges, at least two different stages are identified (Mandl, 1988; Willett et al., 1993; Storti et al., 2000). The first stage is characterized by high-velocity thrusting in the retro-wedge in concert with low displacement folding and thrusting in the pro-wedge (Fig. AI-1). During the subsequent second stage, the main deformation is located in the pro-wedge where low-frequency, high-displacement thrusting occurs, while low-velocity thrusting is active in the retro-wedge. The switch from stage 1 to stage 2 is triggered by the wedge uplift as soon as the crest of the wedge reaches a critical height whereas the inward wedge domain behaves similar to a backstop (Mandl, 1988; Willett et al., 1993).

Willett et al. (1993) describe a third stage in which the retro-wedge develops a break in slope. In this moment, the slope angles along the retro-wedge flank decrease due to the evolution of a new backthrust. Based on the different growing mechanisms, double-vergent wedges evolve asymmetrically with different shapes and internal geometries in the pro-wedge versus the retro-wedge. While material at the pro-wedge is frontally or basally accreted, material is thrust and added simultaneously at the retro-wedge (Willett et al., 1993). However, the structural evolution and the principle stresses within the double-vergent wedges are defined by the relation of the internal friction of the incoming material and the internal friction of the décollement on which the wedge grows (Koons, 1990; Smit et al., 2003). Above a low frictional detachment, a low tapered, frontally accreted wedge evolves (e.g., Davis and Engelder, 1985). There, material is slightly uplifted and accreted

along steep dipping forethrusts with lower offsets (Chapple, 1978; Davis and Engelder, 1985; Bonini, 2007). In the case of a high frictional detachment, the material is far underthrust under the deformation front (DF) towards the center of the wedge. This basal accretion is followed by strong vertical uplift (e.g., Davis et al., 1983).

2. Method

2.1 Discrete Element Method

The Discrete Element Method (DEM) is a numerical modeling technique based on a granular model approach. It allows for the investigation of the deformation behavior of rocks through the implementation of particle assemblages. For our study, we use the commercial code PFC2D (Cundall and Strack, 1978; ITASCA Manual, 2004). This software uses discretized rigid elements with a spherical shape that can be displaced in any direction. In response to applied boundary conditions, the particles interact and overlap with their neighboring elements (Cundall and Strack, 1978). These interactions cause contact forces, which are calculated through the magnitude of the overlap in combination with the physical particle parameters (e.g., the coefficient of friction (μ), shear and normal stiffness (k_s , k_n), and density (ρ)) via simple physical force-displacement laws (Mindlin and Deresiewicz, 1953; Cundall and Strack, 1979; Morgan and Boettcher, 1999). The code allows the user to obtain detailed information about particle position, granular texture, and forces, as well as information about the internal structure of the particle assembly at each time step. For a more detailed description of the code, please see e.g., Cundall and Strack (1978, 1979, 1983), Cundall (1987) or the PFC2D ITASCA Manual (2004).

Natural rocks often have an elasto-plastic material behavior. This is implemented in the numerical approach using the Hooke's law for the elastic deformation and a Mohr Coulomb (MC) rheology for the plastic deformation (Morgan and Boettcher, 1999). Both describe the elasto-plastic material behavior and, therewith, the brittle deformation behavior of the upper crust enabling the simulation of the deformation processes of accretionary wedges (Miyakawa et al., 2010).

2.2 Apatite fission track analysis

Thermochronology derives the time-temperature history of rocks by taking advantage of the temperature sensitivity of different radiometric dating methods. Cooling can be associated with the exhumation of rocks, where temperatures decrease from high values to surface values. Within the sensitivity of a given dating method, also renewed heating can be investigated. In this study, we apply apatite fission track (AFT) analysis (Gleadow and Duddy, 1981; Gallagher et al., 1998) and create a synthetic dataset of AFT cooling ages. Generally, AFT thermochronology is based on the spontaneous fission of ^{238}U , which causes defects ('fission tracks') of the crystal lattice. Until cooling below $\sim 110\text{ }^\circ\text{C}$, fission tracks anneal completely. Within the partial annealing zone between $110\text{ }^\circ\text{C}$ and $60\text{ }^\circ\text{C}$, fission tracks are shortened, but are not completely annealed (Wagner and Reimer, 1972; Gleadow and Dudy, 1981; Gallagher et al., 1998). Below $60\text{ }^\circ\text{C}$, fission track are largely stable with less than 10% shortening, and accumulate with time. An AFT age is derived from the elapsed time since the rock's temperature is between $110\text{ }^\circ\text{C}$ and $60\text{ }^\circ\text{C}$ (Fig. AI-2).

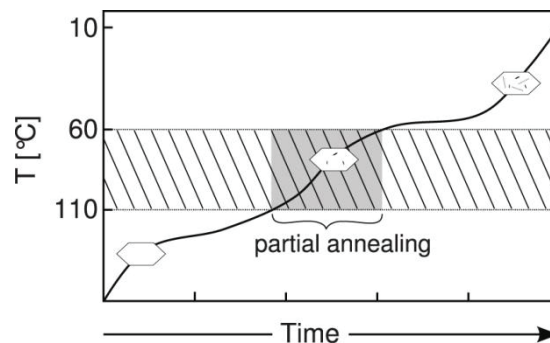


Fig. AI-2: Schematic cooling path of a rock through time. At temperatures between $110\text{ }^\circ\text{C}$ and $60\text{ }^\circ\text{C}$ fission tracks in apatite are preserved and only partially anneal. Below $60\text{ }^\circ\text{C}$ fission tracks in apatite retain almost without shortening.

The cooling rate of a rock within the zone of partial annealing (Gleadow and Duddy, 1981; Gleadow and Fitzgerald, 1987) impacts the AFT cooling age. The thermal history between $\sim 110\text{ }^\circ\text{C}$ and $60\text{ }^\circ\text{C}$ can be inferred from the distribution of fission track lengths. In case of burial for example, renewed heating above the temperature sensitivity of the thermochronologic system can result in partial or complete reset of cooling ages, depending on the maximum temperature and the time spend within the sensitive temperature range. In case of AFT thermochronology, reheating above $60\text{ }^\circ\text{C}$ causes renewed fission track annealing and shortening of formerly stable fission tracks.

Furthermore, AFT analysis depends on the kinetic properties of the analyzed crystals (Burtner et al., 1994; review of Donelick et al., 2005). Carlson et al. (1999) investigated ranges and relationships of kinetic properties in apatites and annealing rates.

AFT thermochronology is well suited for our approach due to its temperature sensitivity. Depicting the cooling of the upper crust (~1.8 to 3.3 km depth at a geothermal gradient of 30 °C km⁻¹), AFT cooling ages are sensitive to both, endogenic and exogenic dynamics.

2.3 Model setup

The numerical ‘sandbox’ consists of a fixed box bottom with a simulated length of 350 km that dips in a fixed angle of $\beta = 12^\circ$ inwards (direction of subduction, Fig. AI-3). The bottom is limited along the side by a fixed vertical 120 km high wall. Walls are composed of particles with a homogeneous radius of 600 m, and act together as stiff, undeformable boundaries. During all experimental runs the box bottom moves with a constant velocity in positive x-direction to simulate a down-going detachment of a subduction zone. The entire box is filled with 12,000 randomly distributed particles. Three particle sizes with diameters of 500, 600, 700 m are used to prevent symmetrical particle packing (Saltzer and Pollard, 1992). These particles are deposited under the force of gravity, on the box bottom ($g = 9.81 \text{ m s}^{-2}$) to create a triangular undeformed ‘sediment’ body. For the model setup and the general construction, a seismic profile of the western Alps (NFP-20 WEST, Schmid et al., 2004) has been used as a reference. To allow for continuous addition of particles to the numerical sandbox the detachment is extended beyond the outward (opposite to subduction direction) edge. On top of the extended detachment a 10 km thick layer is deposited. This region is not included in the figures. To investigate the influence of different geological conditions on the mass transport pattern and on the cooling paths of the particles, three different initial states (Sc1, Sc2, Sc3) are designed. After particles are deposited and equilibrium is achieved, a group of particles are fixed implemented in the shape of a crustal indenter within all experiments. This fixed part has a thickness of ~26 km at the top and ~35 km at the bottom. It dips with an angle of 45° inwards (Fig. AI-3). It simulates an obducted, lower crust in a subduction setting. Additionally, in two experiments (Sc1, Sc2) a second particle grouping in a semi-circular shape (radius 30 km) is fixed implemented directly on top of the detachment (between 100 and 160 km) to simulate a lower crustal fragment.

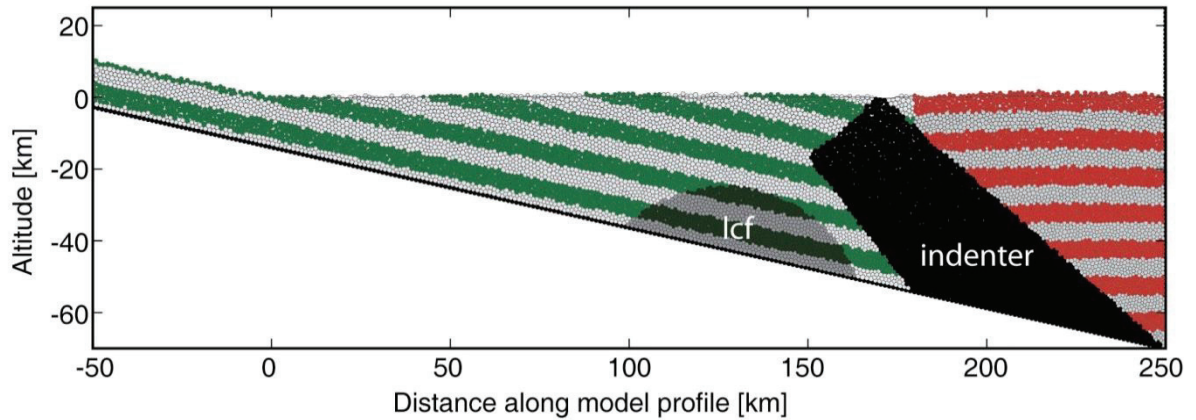


Fig. AI-3: Model setup. The lower crustal fragment (lcf) is only implemented in two of three experiments. Grey and green particles: upper crustal material. Black particles: fixed lower crustal material.

The material properties (e.g., μ_p , ρ , k_n , k_s) to simulate the brittle material are held constant through all experiments. The only parameter that is varied is the coefficient of friction value for the basal box bottom (i.e. the detachment). For experiments Sc1 and Sc3 the coefficient of particle friction of the detachment is $\mu_p = 0.2$ and in experiment Sc2, $\mu_p = 0.1$. All physical parameters are adopted from previous studies on numerical experiments simulating the evolution of orogenic wedges (Naylor et al., 2005; Wenk and Huhn, 2013a, b). The boundary particles of the fixed sidewalls are given properties similar to the brittle material layer (Table AI-1).

Summarizing, the difference between Sc1 and Sc2 is the friction along the décollement and the difference between Sc1 and Sc3 the missing lower crustal fragment in Sc3.

Table AI-1: Parameter properties.

<i>particles</i>	μ_p	ρ [kg/m ³]	k_n [N/m]	k_s [N/m]
model particles	0.6	2700	1×10^{13}	1×10^{13}
side-wall particles	0.6	2700	1×10^{13}	1×10^{13}
box bottom	0.1/0.2	2700	1×10^{13}	1×10^{13}

2.4 Model limitations

Some simplifications are necessary for the numerical experiment to obtain clearer results. As we are interested in large scale coherences, a fine stratification which leads to property variations within the strata, influence of fluids and cohesion are not accounted in the calculation. Such property variations would influence the strength of the internal or the basal material and, hence, the wedge mechanics. Furthermore, we use a numerical 2D model, though being aware of the spatial character of natural processes. Processes with a strong spatial character perpendicular to the profile axis are ignored. These limitations result in unreasonable fault angles that can be compared relatively, but only carefully with natural structures (Morgan and Boettcher, 1999). Real world AFT ages and erosion patterns can be affected by long-wavelength topography or small-scale tectonic structures. Neither of them can be resolved in this study. On the other hand, model runs are performed in a reasonable time frame due to the implemented particle size. This study firstly combines two established methods. For reasons of clarity and simplicity we implemented neither erosion nor isostasy (Chapter 2.5.2). Erosion, however, is calculated in the course of the generation of synthetic cooling ages.

2.5 Analysis and interpretation techniques

During the experimental-run, particle positions are saved every 0.05 % shortening (i.e. storage step of 200 m ‘subduction’) for each experiment. Thereby, a detailed picture of particle positions and relative displacements are recorded enabling the monitoring of internal deformation, e.g., fault zones. Horizontal layers are colored in accordance with analog sandbox experiments to visualize the internal structures by offsets or folding of the layers (Fig. AI-3).

The relative displacements of each particle in the x - and y -directions are extracted for each storage step and are used to calculate a normalized displacement between different storage steps. This reveals zones where particles exhibit large relative offsets. If two groups of particles move into opposing direction, it can be interpreted as a fault zone (Morgan and Boettcher, 1999). Based on our model configuration, whereupon the origin of our coordinate system is located on the lower left side (such that the wedges evolve in positive x -direction along the modeled profiles; Fig. AI-3), these faults can be interpreted as forethrusts or backthrusts. However, only thrusts that are active during the extracted time

periods can be observed. Thus, the tracking of older inactive faults is not possible. Therefore a combination of particle configuration images and relative displacement plots is essential.

In addition, the granular model approach enables to track single particles during the entire experiment to gain a deeper insight into the mass transport pathways and the resulting cooling paths. In this study, selected particles are tracked and saved on a calculated erosional surface (Chapter 2.6.4). These data allow for a detailed analysis of particle transport pathways, displacement rates, and movements in space and time. This approach provides an opportunity to get a first impression of the wedge kinematics and deformational domains on deep and shallow crustal level.

Deriving time-temperature histories

To couple numerical ‘sandbox’ experiments and low-temperature thermochronology, the tracked particle pathways of the DEM model have to be translated into time-temperature paths.

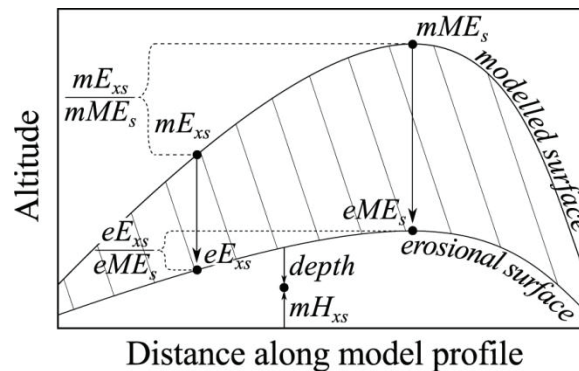


Fig. AI-4: Derivation of depth below the surface of a given point (mH_x) at a given time (s), assuming the ratio between the modeled maximum elevation (mME_s) and the modeled local elevation (mE_{xs}) equals the ratio of the erosional maximum elevation (eME_s) and the erosional local elevation (eE_{xs} ; eq. AI-3).

The first step in the transformation routine is to append temperature as an additional particle property. The temperature of a particle at a particular time is derived by assuming a geothermal gradient and multiplying it by the depth [km below the surface] of the particle. The depth of a particle would be assumed as its distance to the surface. However, since the numerical ‘sandbox experiment does not contain erosion, the uppermost particles cannot serve for estimating the actual surface. The erosional surface level at a given point along must be calculated for each storage step. One way to reconstruct the paleo-surface along the profile is to infer it from published estimates. However, we decided to derive the

erosional surface of each storage step from the model itself (see below for details, eq. AI-1 to AI-5 and Fig. AI-4). Thereby, we are taking account the modeled evolution, rather than risking to associate externally derived elevations with the wrong model time erroneously. The presented approach can be applied on multiple geological settings even if estimates for the surface evolution are lacking. Nonetheless, maximum elevations for different model times match roughly with estimates of paleo-elevations from the European Central Alps (Kuhlemann, 2007).

2.5.1 Modeling constraints

Model setup and the subsequent thermal coupling are arranged within an arbitrary time and space. We correlate the horizontal movement at the model detachment with the estimated convergence of the European and Adriatic plates (Schmid et al., 1996) to achieve realistic dimensions. In doing so, a particular model storage step could be associated with a particular geological time. A similar approach is followed for the boundary conditions of the model topography. Roughly based on the topography of the European Central Alps, the initial and final maximum elevations (eME_i – ‘erosional Maximum Elevation initial’, eME_n – ‘erosional Maximum Elevation after n storage steps’) are set to $eME_i = 500$ m and $eME_n = 3000$ m (Table AI-2).

2.5.2. Computing the erosional surface

Before the profile surface is calculated for any storage step, the maximum elevation (i.e. altitude of the highest lying particle) for each step is determined (Fig. AI-4). An index q is allocated to each storage step s , which indicates the relation between the modeled maximum elevation (mME) of the current storage step and the mME of the last storage step n (eq. AI-1).

$$q_s = \frac{(mME_s - mME_i)}{(mME_n - mME_i)} \quad (\text{eq. AI-1})$$

Afterwards, the mME of each storage step (i.e. still without erosion) is substituted by the erosional maximum elevation (eME , eq. AI-2) with respect to the q of each storage.

$$eME_s = eME_i + (q_s \cdot (eME_n - eME_i)) \quad (\text{eq. AI-2})$$

Maximum exhumation is assumed at the point of maximum uplift. The relation of the erosional elevation (i.e. surface altitude) at any point x along the profile at storage step s ($eE_{x,s}$) and the corresponding maximum elevation of the erosional surface (eME_s) should,

therefore, equal the relation of the modeled elevation (at that point and time: $mE_{x,s}$) and the corresponding mME_s . Given that assumption, the actual surface (i.e. with erosion) is determined for all points and times (eq. AI-3; Fig. AI-4). By this means, varying speed of uplift is translated into varying speed of exhumation. The erosional surface and is only calculated along the model profile and not for the outwards extended detachment (negative x-values) and its layer of additional particles.

$$eE_{x,s} = eME_s \cdot \left(\frac{mE_{x,s}}{mME_s} \right) \quad (\text{eq. AI-3})$$

Table AI-2: Abbreviations and setting of coupling parameters

Parameter	Indices	Meaning and units	Setting
Q	S	Topography index [] <i>storage step</i>	-
mME	s, i, n	modeled Maximum Elevation [km] <i>storage step, initial (0), no. of storage steps</i>	-
eME	s, i, n	erosional Maximum Elevation [km] <i>storage step, initial, no. of storage steps</i>	$eME_i=0.5$ $eME_e=3$
mE	x, s	modeled Elevation [km] <i>distance along profile, storage step</i>	-
rE	x, s	erosional Elevation [km] <i>distance along profile, storage step</i>	-
T	x, y, s <i>surf</i>	Temperature [°C] <i>distance along profile (x) and height (y), storage step</i> <i>surface</i>	$T_{surf}=10$
mH	x, s	modeled height of a particle (i.e. y value) [km] <i>distance along profile, storage step</i>	-
g_t		Geothermal gradient [°C km ⁻¹]	$g_t=30$

2.5.3 Computing temperatures and AFT cooling ages

Assuming a geothermal gradient (g_t) of 30 °C km⁻¹ and a surface temperature (T_{surf}) of 10 °C, the temperature at a given point (x, y) and at a particular storage step s ($T_{x,y,s}$) is derived based on the distance of the particle height $mH_{x,s}$ to $eE_{x,s}$ (eq. AI-4). Therein, the term $eE_{x,s} - mH_{x,s}$ can be interpreted as depth below surface.

$$T_{x,y,s} = \left((eE_{x,s} - mH_{x,s}) \cdot g_t \right) + T_{surf} \quad (\text{eq. AI-4})$$

The interpretation of a synthetic AFT age only makes sense if the corresponding particle is

positioned at the surface at the end of the simulation. Thus, we only consider particles, which intersect the erosional surface above their center point at the time of ‘sampling’ (see next paragraph). The distance between its center point and the erosional surface at the time of ‘sampling’ is added to the $mH_{x,n}$ of each of the previous storage steps (eq. AI-5). By this means, it is ensured that the particle's depth at the time of ‘sampling’ is zero. In other words, the time-temperature history of that part of the particle, which actually intersects the surface at the time of ‘sampling’, is calculated and saved.

$$T_{x,y,s} = \left(\left(eE_{x,s} - \left(mH_{x,s} + \left(eE_{x,n} - mH_{x,n} \right) \right) \right) \cdot g_t \right) + T_{surf} \quad (\text{eq. AI-5})$$

To analyze the influence of the different initial and boundary conditions of our experiments (Chapter 2.3), the thermal histories of the selected particles are calculated (eq. AI-5) and extracted. The HeFTy program (version 1.7.5; Ketcham, 2005) is used to predict synthetic AFT ages from the time-temperature paths of the selected particles. These are imported in HeFTy and forward modeled, using the annealing model of Ketcham et al. (2007). Default HeFTy values are adopted for the kinetic properties. These values account for the variations in natural occurring apatites in terms of annealing properties (Carlson et al., 1999; Ketcham, 2009).

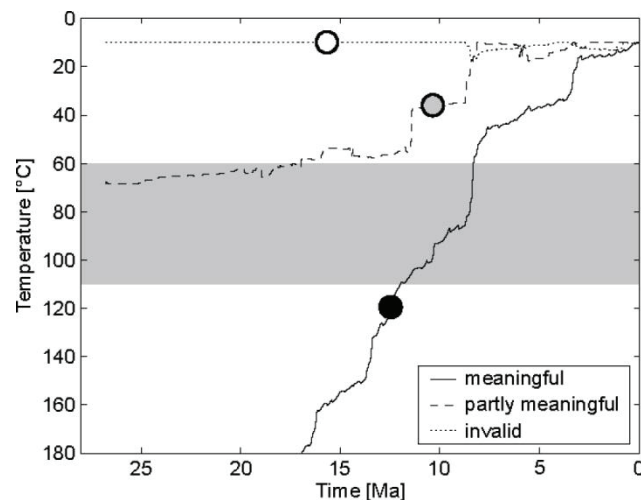


Fig. AI-5: The derived time-temperature paths are used for thermal history modeling and evaluated with respect to their information on the exhumation history. (Black balls/black line) meaningful tT-history, particle completely reset with respect to the AFT system. (Grey balls/dashed line) partly meaningful tT-history, no complete reset, but sufficient tT-information. (White balls/dotted line) invalid tT-history, mainly at or above the computed erosional surface.

Finally, all time-temperature histories are evaluated with respect to their significance (Fig. AI-5). In several cases, particles, which intersect the erosional surface at the end of

the simulation, are above the erosional surface (i.e. already 'completely eroded') during previous steps. Particles, which spent most of the time above the erosional surface are rated as invalid, while particles, which spent sufficient time below the erosional surface are rated as partly meaningful. Only those particles, which experience a complete reset of the AFT system during the model run are fully trusted.

Note that the particles of the numerical sandbox do not inherit time-temperature information prior to the simulated cycle of orogeny (in contrast to real samples, which are not reset during the current cycle of orogeny). Thus, the synthetic AFT ages may only slightly exceed the simulated model runtime at the most.

2.5.4 Sampling

At specific time intervals within each model run (each 20 km shortening), particles located at the current erosional surface are extracted. From these extracted particles the current AFT cooling ages are calculated to determine the evolution of AFT pattern through time.

3. Results

To investigate the temporal progress of wedge accretion, we present the respective development stages after 20 km, 40 km, 60 km, 80 km, 100 km and 119 km shortening. Referring to Schmid et al. (1996), the Alpine Belt experienced 119 km shortening in the last 32 Ma. Accordingly, the investigated development stages can be interpreted as snapshots after 5.4 Myr, 10.8 Myr, 16.1 Myr, 21.5 Myr, 26.9 Myr and 32 Myr of orogeny.

3.1 Experiment Sc1 (high friction detachment, indenter, lcf)

3.1.1 Mechanical and kinematic evolution

A double-vergent wedge evolves in the reference experiment Sc1 due to the movement of the basal box bottom (Fig. AI-6). After 20 km of shortening, a wedge with a steep frontal slope angle ($\alpha_1 \sim 21^\circ$) evolves associated with active forethrusts of $\sim 14^\circ$ dipping angle (Fig. AI-7). Along these flat thrusts underthrusting occurs and the incoming material is basally stacked. Due to this basal accretion the pro-wedge is continuously uplifted against the lower crustal fragment and the indenter. The slope angle of the retro-wedge flank is small ($\alpha_2 \sim 5^\circ$). The crest and the steepest particle paths are located at ~ 55 km modeled profile length (mkm).

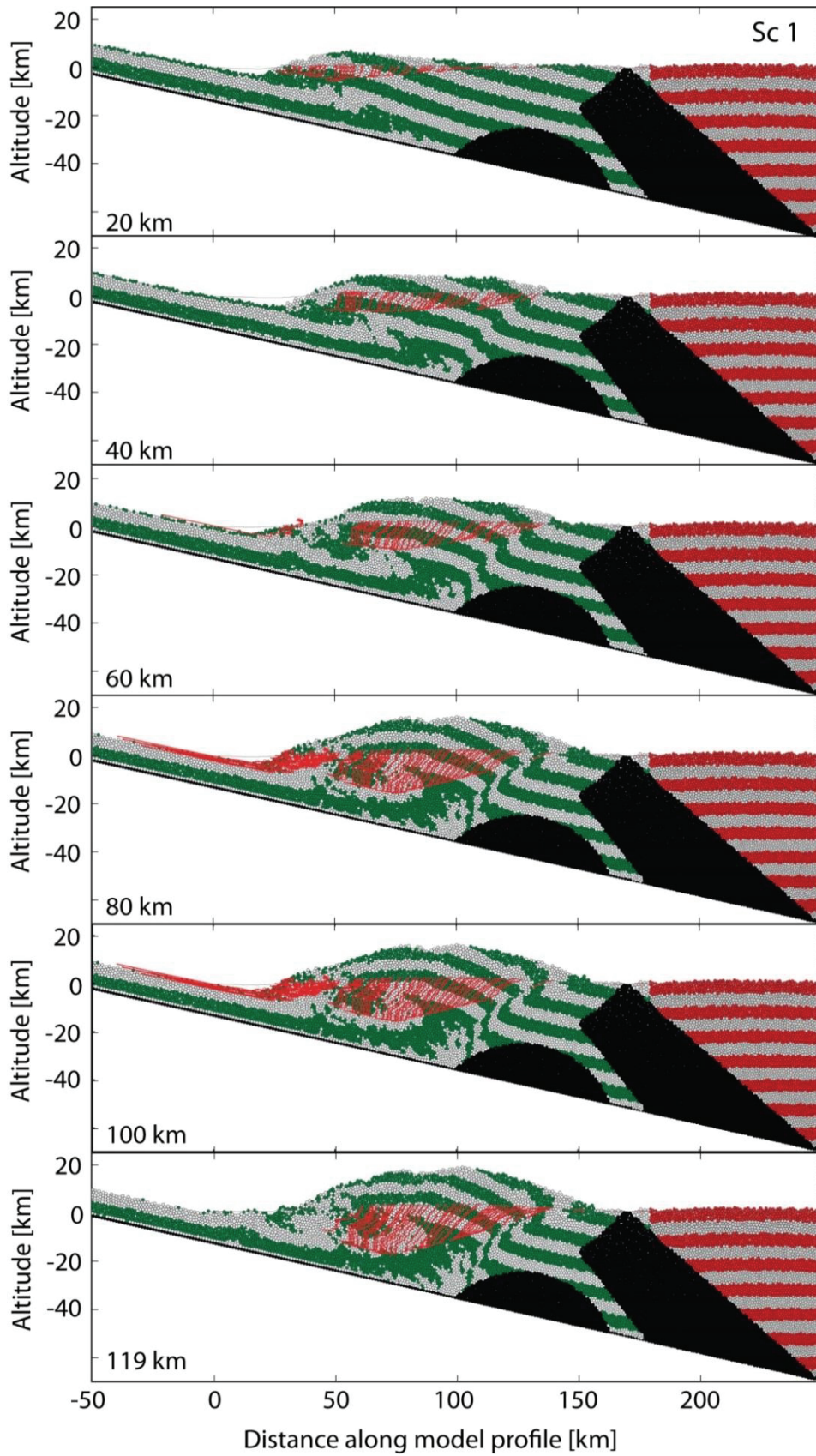


Fig AI-6: Particle setting of experiment Sc1 after 20 km, 40 km, 60 km, 80 km, 100 km and 119 km shortening corresponding to 5.4 Ma, 11 Ma, 16 Ma, 22 Ma, 27 Ma and 32 Ma orogeny. (Red lines) particle paths.

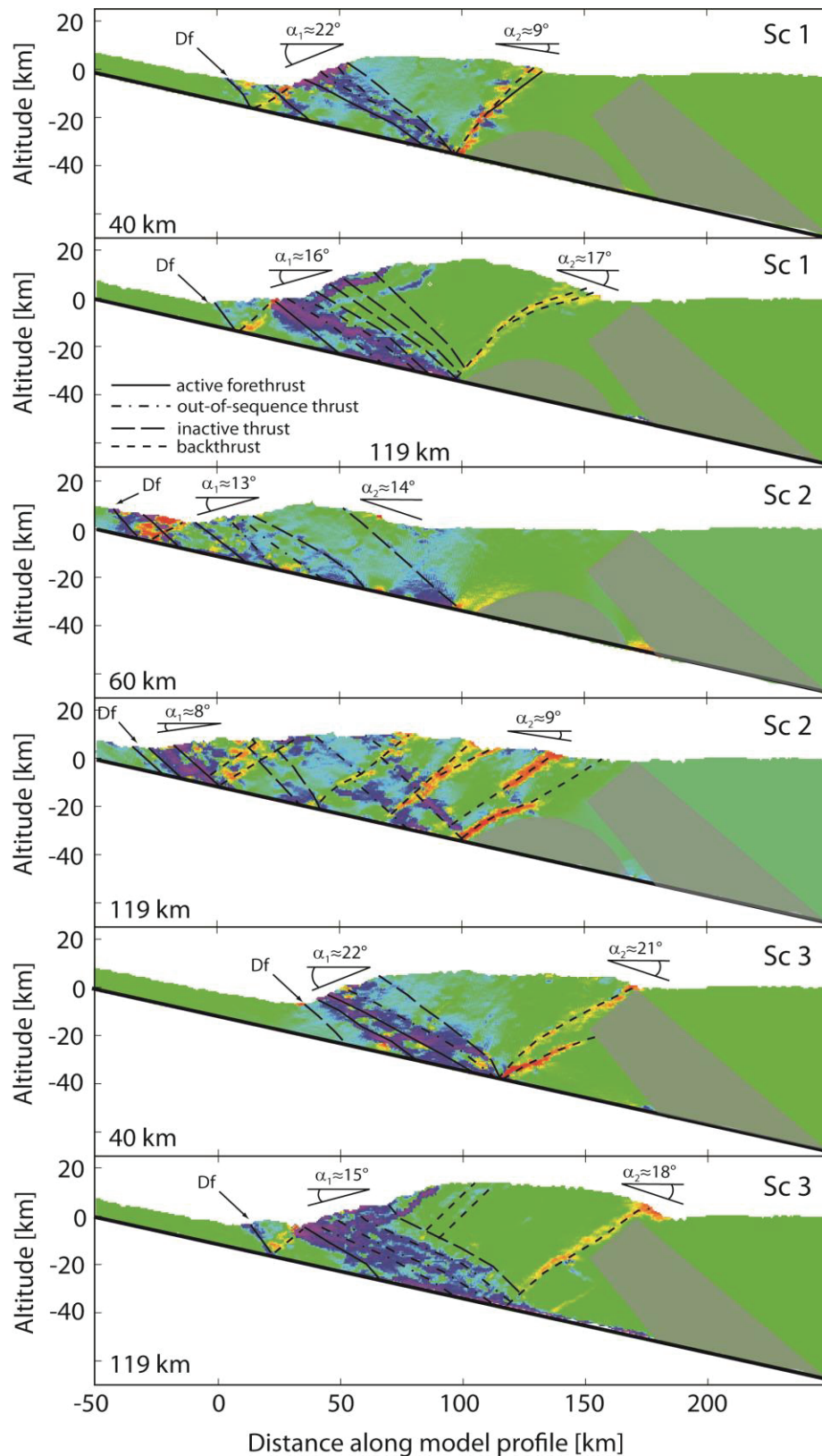


Fig. AI-7: Gradient of displacement plot after 119 km shortening corresponding to 32 Ma orogeny. From top to bottom: Sc1 (high frictional detachment, indenter and lower crustal fragment), Sc2 (low frictional detachment, indenter and lower crustal fragment) and Sc3 (high frictional detachment, indenter). (Df) deformation front. (α) slope angle at the pro-wedge flank (1) and retro-wedge flank (2).

With ongoing shortening (40 km) new flat forethrusts evolve along which incoming material is progressively underthrust. Further inwards, these forethrusts get reactivated as out-of-sequence thrusts with rising angles between 19° and 27° (Fig. AI-7-Sc1). Simultaneously, due to material stacking, backthrusts (dipping angle $\sim 57^\circ$) occur with distinct offsets and the crest with the highest particle uplift starts to migrate inwards to the position of 60-70 mkm. The resulting slope angles of the pro- and the retro-wedge flank increase to $\alpha_1 \sim 22^\circ$ and $\alpha_2 \sim 9^\circ$.

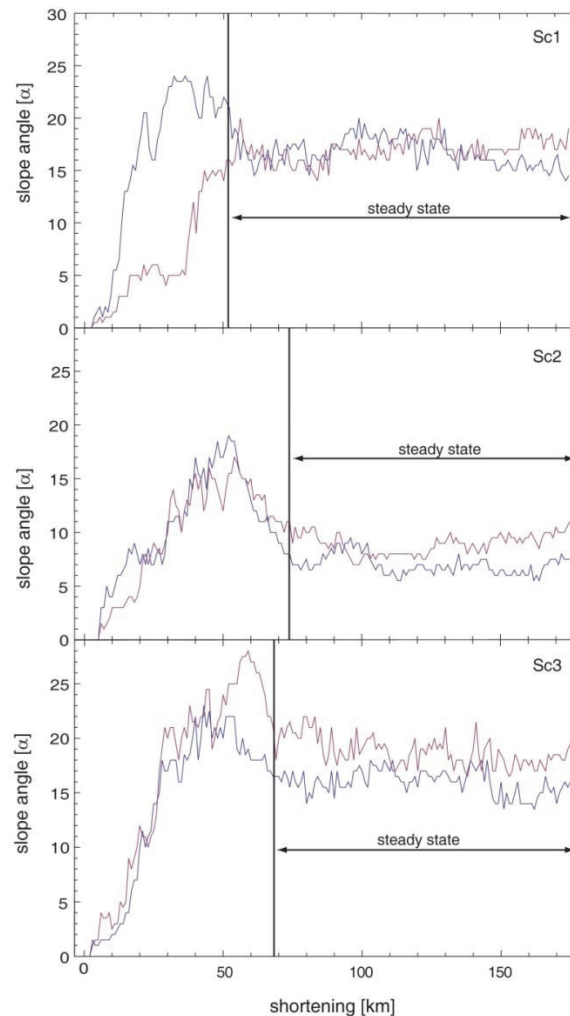


Fig. AI-8: Evolution of slope angles along the pro (blue lines) and retro-wedge flanks (red lines). From top to bottom: Sc1 (high frictional detachment, indenter and lower crustal fragment), Sc2 (low frictional detachment, indenter and lower crustal fragment) and Sc3 (high frictional detachment, indenter).

Contemporaneously with ongoing accretion, the crest propagates slightly inwards, similarly to the positions of the backthrusts. After ~ 52 km shortening, the frontal slope has an angle of $\alpha_1 \sim 16^\circ$ and the retro slope an angle of $\alpha_2 \sim 17^\circ$. From this time on, the slope

angle remains constant (Fig. AI-8 Sc1). After 60 km shortening, a new steeper forethrust of $\sim 22^\circ$ dipping angle occurs and the DF jumps outwards, in front of the main wedge structure. This forethrust gives rise to a small uplift structure, which is subsequently underthrust again. The crest is located at ~ 80 mkm, but slowly starts to move outwards again due to continuous underthrusting. After 100 km shortening, the uplifted structure is completely underthrust and a steep frontal flank ($\alpha_1 \sim 20^\circ$) evolves. In the last stage, after 119 km shortening, again a new steep forethrust (of $\sim 23^\circ$) rise from the detachment and leads to an outward movement of the DF (Fig. AI-6, AI-7 Sc1). The corresponding backthrusts rise steeper with 47° . Additionally, reactivated out-of-sequence thrusts evolve with increasing distance to the DF steeper (Fig. AI-7 Sc1) and rearrange the underthrust material. This results in a further uplift and steepening of the wedge crest ($\alpha_1 \sim 16^\circ$). This correspond with the particle paths which start rising shortly inwards of the DF with a gradient that increases proportionally with increasing distance to the DF (Fig. AI-7 Sc1). At the retro-wedge flank of this imbricated wedge, one main active backthrust is observed, which is regularly activated through the model run. This backthrust cuts through the surface with $\sim 51^\circ$ and runs in a slight curve upward but does not touch the implemented indenter nor the lower crustal fragment. The offset along the backthrust is relatively small, hence, it evolves as a back-kink. The retro-wedge flank develops slightly steeper with a slope angle $\alpha_2 \sim 17^\circ$.

3.1.2 Thermal history

After 20 km shortening (corresponding to 5.4 Myr of orogeny), synthetic AFT ages from experiment Sc1 vary from 2.4 Ma to 5.5 Ma and show a distinct U-shaped distribution between 40 mkm and 80 mkm. Beyond that, AFT ages are homogeneously distributed. Youngest ages are predicted in the center (at 50-60 mkm) and older ages towards the terminations of the profile (Fig. AI-11). Thus, the central parts seem to be rapidly exhumed during the first stage of orogeny, while the outer parts cooled more slowly, if at all. After 40 km shortening (corresponding to 10.8 Myr of orogeny), the section of young AFT ages shifts to 80-125 mkm (Fig. AI-11). AFT ages range from 3.4 Ma to 11 Ma, with youngest ages between 110 mkm and 120 mkm.

The cooling age distribution evolves more complex after 60 km shortening (corresponding to 16.1 Myr of orogeny), with young AFT ages, pointing to enhanced deformation, both in the center of the U-shaped distribution (5-6 Ma at 80-100 mkm) and along the pro-wedge

flank (6-9 Ma at ~30 mkm). In between these regions and along the retro-wedge flank, AFT ages increase gradually up to 16 Ma (Fig. AI-11). This pattern gets even clearer after 80 km and 100 km shortening (corresponding to 21.5 Myr and 26.9 Myr of orogeny, respectively). Thus, along the pro-wedge flank a second, smaller U-shaped pattern evolves, corresponding to the contemporaneous forward jump of the DF. Youngest cooling ages of the major pattern migrate from ~85 mkm (5.2 Ma) to ~80 mkm (5.5 Ma), while the section of young cooling ages along the pro-wedge flank broadens towards ~40 mkm (6.5 Ma) and ~45 mkm (6 Ma) (Fig. AI-11). AFT ages along the pro-wedge flank at ~30 mkm increase to 22 Ma at the same time.

At the last time slice (119 km shortening corresponding to 32 Myr of orogeny), both former sections of young cooling ages merge and a broad, shallow U-shaped distribution of AFT ages establishes between 40 mkm and 140 mkm. Meanwhile, cooling ages at the very beginning of the pro-wedge (~30 mkm) flank decrease again (10-12.5 Ma), indicating a new section of rapid cooling, which is in line with the anew observed forward jump of the DF.

3.2 Experiment Sc2 (low friction detachment, indenter, lcf)

3.2.1 Mechanical and kinematical evolution

The double-vergent wedge in Sc2 differs from those of Sc1 and Sc3. In this experiment, after 20 km shortening, active forethrusts rise at the DF in steep angles (~37°), and, simultaneously, corresponding backthrusts of ~57° occur next to the retro-wedge flank. Consequently, within this setup the wedge grows by frontal accretion between the imbricated units. The highest uplift is observed at ~25 mkm (Fig. AI-9). The pro-wedge flank and the retro-wedge flank evolve similarly with $\alpha_1 \sim 7.5^\circ$ and $\alpha_2 \sim 5^\circ$ (Fig. AI-7 Sc2). With ongoing shortening, the double-vergent wedge extends by slowly propagating bidirectionally. Hence, new steep forethrusts evolve outwards in front of the DF and new backthrusts are activated further inwards cropping out at the retro-wedge flank. The slope angles increase, simultaneously, to $\alpha_1 \sim 16.5^\circ$ and $\alpha_2 \sim 15^\circ$ after 40 km of shortening. Nevertheless, main deformation takes place at the retro-wedge flank.

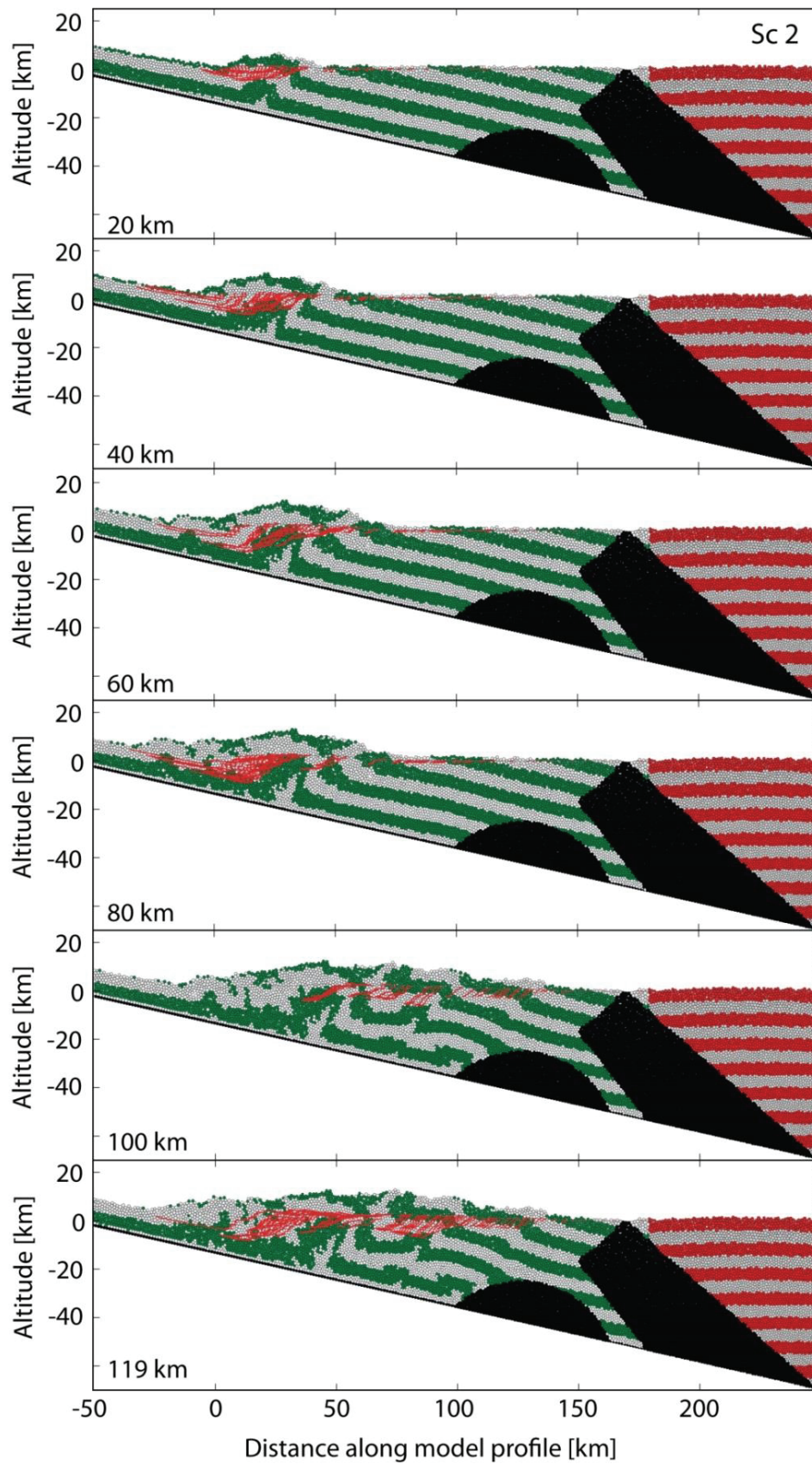


Fig. AI-9: Particle setting of experiment Sc2 after 20 km, 40 km, 60 km, 80 km, 100 km and 119 km shortening corresponding to 5.4 Ma, 11 Ma, 16 Ma, 22 Ma, 27 Ma and 32 Ma orogeny. (Red lines) particle paths.

After 60 km of shortening, the DF propagates further outwards due to the development of new steep forethrusts (rising angle $\sim 48^\circ$). Simultaneously, new backthrusts (dipping angle $\sim 55^\circ$) evolve further inwards as well as out-of-sequence thrusts, which are short-time reactivated (dipping angle $\sim 30^\circ$; Fig. AI-7 Sc2). The wedge continues to extend in both directions while the crest slowly propagates inwards to ~ 28 mkm. The continuous extension of the accreted wedge reduces the slope angles to $\alpha_1 \sim 13^\circ$ at the frontal flank and to $\alpha_2 \sim 14^\circ$ at the retro-wedge flank. Slope angles decrease until the wedge becomes stable after ~ 73 km shortening (Fig. AI-8).

After 80 km shortening, the crest position is located at ~ 30 mkm, while the thrust evolution and extension is more distinct at the pro-wedge than at the retro-wedge. Between 80 km and 100 km of shortening, the DF and the retro-wedge flank move far inwards due to the development of two backthrusts with distinct offsets. For the first time, the whole material between the DF and the lower crustal fragment is slightly uplifted, which is shown by the whole range of steep particles paths (Fig. AI-9). Consequently, the crest has moved far inwards while the main particle uplift still occurs at the DF. In the following (119 km shortening), the DF propagates again outward, whereas the retro-wedge remains stable. Forethrusts crop out at the surface with steep angles of $\sim 40^\circ$ and are reactivated slightly flatter ($\sim 31^\circ$) inwards (Fig. AI-7 Sc2). The pro-wedge has slightly flatten to $\alpha_1 \sim 8^\circ$. Additionally, particle paths rise flat and the highest uplift is observed at ~ 73 mkm (Fig. AI-9).

In contrast to experiment Sc1 and Sc3, this wedge evolves wide, extended. This is also true for the retro-wedge flank of the wedge, which evolves similar flat with an angle of $\alpha_2 \sim 9^\circ$. A group of backthrusts cut out at the retro-wedge flank which are frequently reactivated and evolve with small offsets as back-kinks. The most inward positioned backthrust migrates along the lower crustal fragment. At the highest point of this fragment, the latter backthrust is cut by a flat forethrust and runs further inwards, now parallel to the indenter, but in a distinct distance (Fig. AI-7-Sc2).

3.2.2 Thermal history

The distributions of synthetic AFT ages of experiment Sc2 (Fig. AI-12) are more complex in comparison to Sc1 and Sc3. After 20 km shortening, a U-shaped distribution of cooling ages is established, similarly to the evolution of the other experiments (Fig. AI-12).

Nonetheless, youngest cooling ages are found more outwards (15-30 mkm) compared to experiments Sc1 and Sc3, related to the observed back- and forethrusts in that region. Within the section of young cooling ages, two subregions can be distinguished with AFT ages clustering around 3 Ma (15-20 mkm) and 3.5 Ma (25-30 mkm). The youngest AFT age (2.4 Ma), however, is predicted at 33 mkm. The time-temperature history of the corresponding particle shows its affiliation to the grouping of particles further inwards with slow cooling until ~2 Ma (before the end of the simulation) and fast cooling afterwards. However, slow cooling of this particle occurs at temperatures between ~120 °C and 110 °C (i.e. within the partial annealing zone of the AFT system), while the adjacent particles are already positioned at ~60 °C at the beginning of the simulation (thus track annealing has only subordinate impact). Apart from the profile section with young AFT ages, AFT ages are distributed homogeneously (~5.5 Ma). Exhumation starts in the very beginning of the profile.

The two-step pattern in the section with young cooling ages is still roughly preserved after 40 km shortening (Fig. AI-12). However, while AFT ages in the center of this section (23-30 mkm) cluster around 6 Ma and thus grow older with respect to the previous time-slice, youngest ages shift outwards (3.1 Ma at 13 mkm) and indicate constant and fast cooling (i.e. strong deformation) along the pro-wedge flank. Contemporaneously, the U-shaped distribution is also extended inwards until 42 mkm, with another though less distinct region with younger cooling ages at 40 mkm.

Shortening of 60 km and 80 km establishes this bimodal distribution of AFT ages with the frontal region of younger AFT ages shifting back and forth to 22 mkm (5.9 Ma) and 18 mkm (9 Ma), while the outwards region of younger AFT ages slowly migrates inwards to 48 mkm (4.6 Ma) and 50 mkm (8.3 Ma), (Fig. AI-12). The last two time-slices (100 km and 119 km shortening, corresponding to 26.9 Myr and 32 Myr of orogeny, respectively) depict the same AFT patterns as before, with a bimodal cooling age distribution in the beginning of the profile, albeit it is shifted by some 15 mkm in inward direction and the frontal part is only ill constrained until 60 mkm. Additionally, two more regions of very young AFT ages develop from 75 mkm to 130 mkm (Fig. AI-12). Cooling ages of this outward positioned section mainly cluster around 3-4 Ma and 7-8 Ma after 100 km and 119 km shortening, respectively. Still they are not homogeneously distributed, but rather in a further bimodal curving, culminating in the center at ~110 mkm. Thus, after 119 km shortening, the synthetic AFT ages indicate an uneven cooling style along the profile, alternating between

regions of fast and slow cooling.

3.3 Experiment Sc3 (high friction detachment and indenter)

3.3.1 Mechanical and kinematic evolution

In order to investigate the effect of deep seated geometry in the model setup, the lower crustal fragment is not integrated into experiment Sc3 (Fig. AI-10). The thrust system evolves similarly to that in Sc1 due to the high frictional basal detachment. In this case, after 20 km shortening the double-vergent wedge evolves between a dominant back-kink ($\sim 55^\circ$ dipping angle) and a flat forethrusts ($\sim 19^\circ$ dipping angle) with a second corresponding smaller back-kink ($\sim 59^\circ$ dipping angle). The dominant back-kink runs parallel to the indenter, uplifting the retro-wedge (Fig AI-7 Sc3). Consequently, the retro flank evolves steeper ($\alpha_2 \sim 12^\circ$) than the frontal flank ($\alpha_1 \sim 10^\circ$) where underthrusting along the flat forethrusts occurs. This imbalance in uplift is reflected by the particle paths showing a steeper curve next to the indenter. The crest of the wedge is located at ~ 140 mkm. With ongoing shortening (40 km), a back-kink of $\sim 45^\circ$ dipping angle evolves between the two previous structures and the offset along the forethrust increases while more material is underthrust.

Migrating inwards, these steep forethrusts are rotated to flat rising forethrusts ($\sim 15^\circ$) along which the incoming material is underthrust and basally accreted. Later they are reactivated as out-of-sequence thrusts (Fig. AI-7 Sc3). While uplift along the retro-wedge flank stagnates, uplift along the pro-wedge becomes more pronounced. This goes along with a slope angle increase to $\alpha_1 \sim 22^\circ$ and to $\alpha_2 \sim 21.5^\circ$ and an outward shift of the crest to ~ 90 mkm. Corresponding, the particle paths become steeper in the pro-wedge part.

With ongoing accretion, the frontal part is uplifted by underthrusting, but, simultaneously, also the retro-wedge flank is uplifted, associated with steep particle paths. In this phase the slope angles are steep with $\alpha_1 \sim 23^\circ$ at the frontal slope and $\alpha_2 \sim 25^\circ$ at the retro-wedge flank. The crest is located at ~ 100 mkm. After 60 km shortening, a steep forethrust (of around $\sim 30^\circ$) leads to the evolution of a small rise in front of the DF and the slope angle declines (Fig. AI-10). The slope angles reach values of $\alpha_1 \sim 16.5^\circ$ at the pro-wedge and $\alpha_2 \sim 18.5^\circ$ at the retro-wedge flank. Afterwards, slope angle variations are smaller, but no adjustment occurs in contrast to the previous experiments.

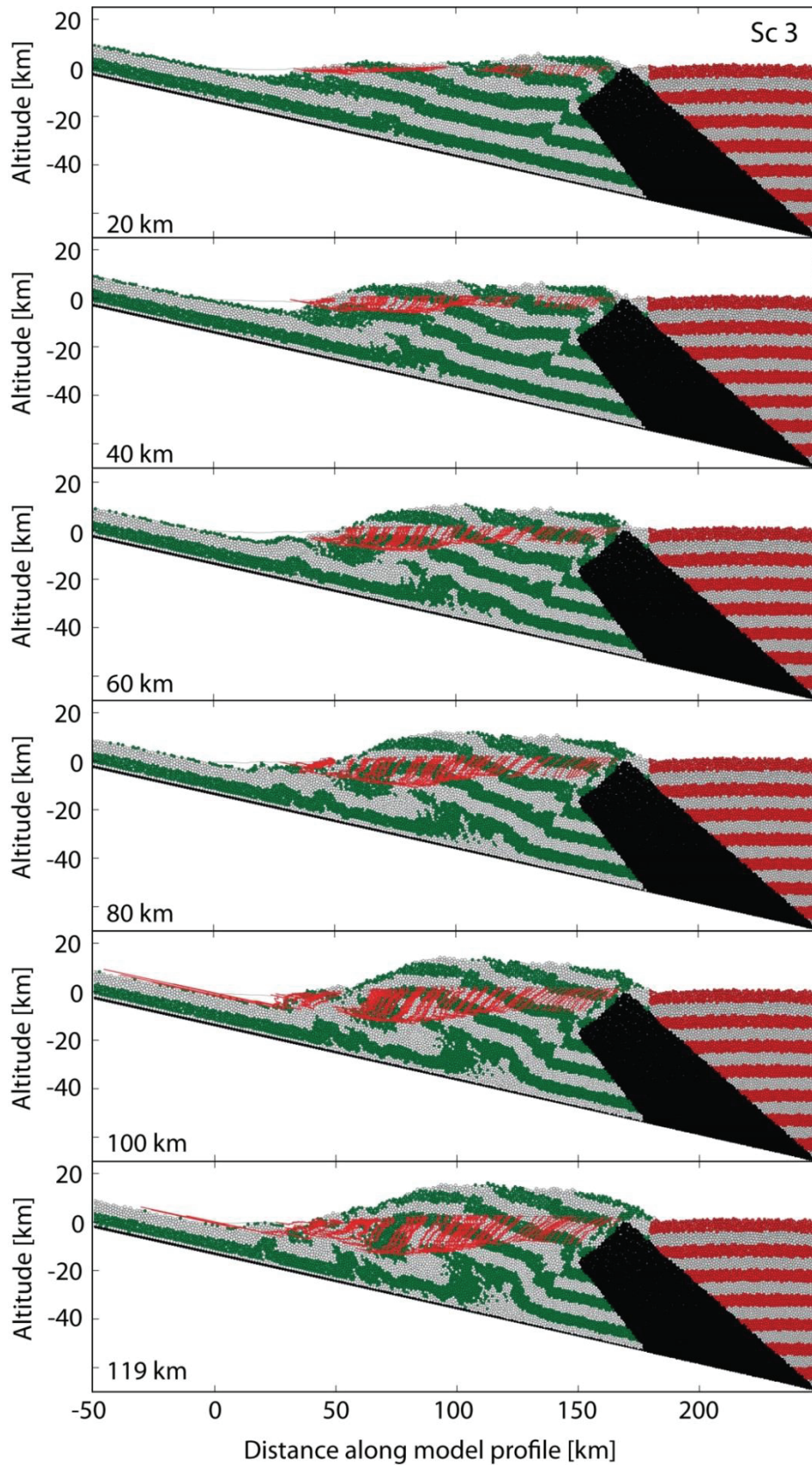


Fig. AI-10: Particle setting of experiment Sc3 after 20 km, 40 km, 60 km, 80 km, 100 km and 119 km shortening corresponding to 5.4 Ma, 11 Ma, 16 Ma, 22 Ma, 27 Ma and 32 Ma orogeny. (Red lines) particle paths.

Main deformation takes place at the pro-wedge, where new flat forethrusts occur at the DF. These are underthrust afterwards, which goes along with an alternation of de- and increasing slope angles. Slope angle at the frontal wedge decrease after 80 km shortening ($\alpha_1 \sim 14^\circ$), whereas a steepening occurs at the retro-wedge flank ($\alpha_2 \sim 18^\circ$) after 100 km shortening. During this evolution, the crest stays at the same position. After 119 km shortening, again a steep, new forethrust of $\sim 35^\circ$ dipping angle develops and the DF propagates outwards (Fig. AI-10). Simultaneously, structures at the retro-wedge behave stably. Comparing the results with those of experiment Sc1, the wedge has much more space to evolve which results in a wider extended wedge structure.

The double-vergent wedge is strongly compressed with largest uplift occurring at ~ 111 mkm and steep rising particle paths (Fig. AI-10). Due to the missing crustal fragment and the associated space on hand, the slope angle of the pro-wedge evolves slightly flatter ($\alpha_1 \sim 15^\circ$) than in the reference experiment. Similar to Sc1, one main backthrust is observed which crops out at the retro-wedge flank. This frequently reactivated thrust runs parallel and in a small distance to the indenter and shows a larger offset than the corresponding thrusts in Sc1. Thus, the retro-wedge flank develops steeper ($\alpha_2 \sim 18^\circ$, Fig. AI-7 Sc3).

3.3.2 Thermal history

Youngest AFT ages range between 2 Ma and 3 Ma in experiment Sc3 after 20 km shortening (Fig. AI-13). In contrast to the previous experiments, the section with young cooling ages is far more inwards (127-157 mkm) and dichotomously arranged between 127-130 mkm and 146-157 mkm. In between and towards both terminations of the profile, cooling ages increase up to 4.7 Ma and 5.5 Ma, respectively.

This first major pattern is mostly preserved after 40 km shortening with young AFT ages (~ 8.4 Ma) at 125 mkm and a well-defined U-shaped distribution of AFT ages between 140 mkm and 161 mkm with AFT ages down to 6.8 Ma. An even more pronounced region with AFT ages as young as 4.1 Ma evolves between 57 mkm and 100 mkm as a second major region (Fig. AI-13). On the basis of the structural analysis (Chapter 3.1.3) this second region can be related to frontal wedge deformation associated with underthrusting along flat forethrusts.

After 60 km shortening (corresponding to 16.1 Myr of orogeny), both major regions begin to merge into a large and rather flat two-step distribution of AFT ages with young cooling

ages (10-12 Ma) between 130 mkm and 164 mkm and even younger ages (6-7 Ma) between 68 mkm and 121 mkm (Fig. AI-13). A minimum age of 6.2 Ma is predicted at 85 mkm. From 80 km on to 119 km shortening (corresponding to 21.5 Myr to 32 Myr of orogeny), one major pattern dominates the AFT age distribution: Between 65 mkm and 164 mkm, cooling ages form a U-shape with youngest ages in the center and older ages towards the terminations of the modeled profile length (Fig. AI-13). After 80 km, 100 km and 119 km shortening, youngest cooling ages are predicted at 102 mkm (7 Ma), 103 mkm (6 Ma) and both at 82 mkm and 102 mkm (7.4 Ma), respectively. Besides, young AFT ages (~6 Ma, 6-10 Ma and 11-16 Ma) are also calculated for the very beginning of the pro-wedge flank (35-50 mkm) for these time slices, partially being even younger than in the center of the profile.

4. Discussion

In all three experiments Sc1, Sc2 and Sc3 double-vergent wedges evolve with a pro- and a retro-wedge flank due to the movement of the basal box bottom. The different stage occurrences, the structural evolution, the wedge topography, and the mass moving patterns of these wedges are affected by the simulated indenter and the lower crustal fragment as well as the basal friction value. This will be discussed in detail also in comparison with previous wedge studies (e.g., Willett et al., 1993; Storti et al., 2000). The patterns of the synthetic AFT cooling ages reinforce the wedge evolution according to the stage allocation (Mandl, 1988; Willett et al., 1993; Storti et al., 2000), which we refer to in this study. In general, AFT ages are notably younger after 20 km shortening, compared to the later storages, what is expected as a methodological weakness. Synthetic cooling ages cannot exceed the range of the modeled time, while corresponding real samples, probably would have yielded older cooling ages. Instead of overinterpreting the range of ages, we rather concentrate on the shape of their distribution. Since all AFT cooling ages are computed from particles on the erosional surface, the relative difference between the ages are interpreted as differences in exhumation rates of the samples cropping adjacent to each other. Consequently, the youngest ages within one time slice suggest highest denudation rates and, therefore, locate the main deformation at the current amount of shortening.

4.1 Influence of detachment strength (coefficient of friction of lower crust)

Corresponding with the basal friction value of the detachment, the double-vergent wedge in Sc1 grows by underthrusting due to the high frictional décollement. In contrast, the wedge in Sc2 evolves as a result of the weak décollement by frontal accretion of imbricated units. This result is in agreement with a various amount of analog and numerical experiments dealing with the importance of the basal friction at the décollement (e.g Davis et al., 1983; Mulugeta, 1988; Moore, 1989; Mugnier et al., 1997; Hardy et al., 1998; Burbidge and Braun, 2002; Lohrmann et al., 2003; Ellis et al., 2004; Gutscher et al., 1998b).

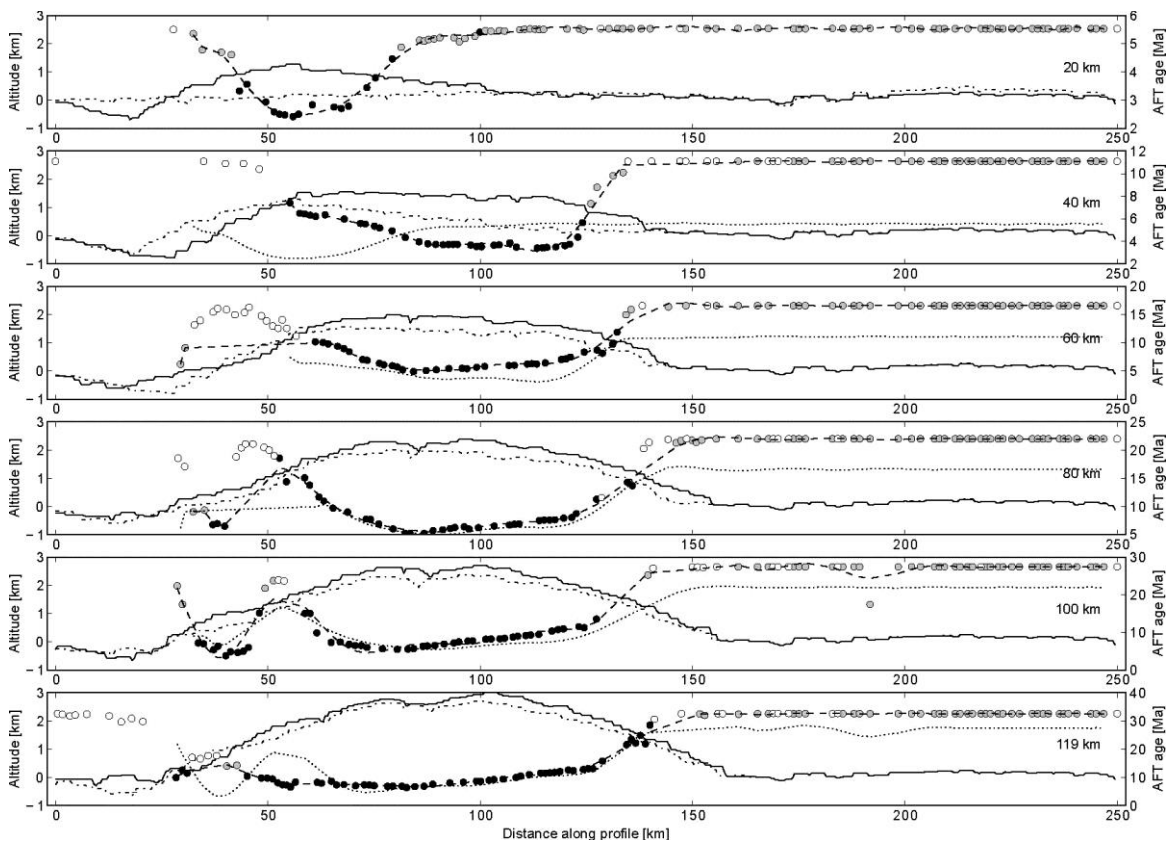


Fig. AI-11: Evolution of the computed erosional surface profile and the synthetic AFT cooling ages of Sc1 through time. From top to bottom: situation after 20 km, 40 km, 60 km, 80 km, 100 km and 119 km shortening, corresponding to 5.4 Ma, 11 Ma, 16 Ma, 22 Ma, 27 Ma and 32 Ma orogeny, respectively. Black line: erosional surface of current time slice. Dash-dotted line: erosional surface of the last time slice. Balls: AFT ages (signature see Fig. AI-5). Dashed line: Trendline of valid AFT ages of the current time slice. Dotted line: Trendline of valid AFT ages of the last time slice.

The analysis of the DEM model gives a detailed structural picture of the influence of the décollement strength. Dipping angles of fore- and backthrusts show that in Sc1 the accretionary wedge grows by underthrusting with basal accretion. Main deformation takes place at the pro-wedge flank, without backthrusting along the retro-wedge. If we follow the

description of Storti et al. (2000) in this case only a stage 2 is recorded. If a comparison with the synthetic AFT patterns is made, it can be inferred that the youngest cooling ages are at the same position where the main deformation takes place. Consequently, the AFT data support the observations which have been made within the structural analysis of the DEM model (Fig. AI-11). During the further model run, the main deformation along the pro-wedge flank continues, what indicates that until the end of the experiment stage 3 (Willet et al., 1993) is not reached. This also corresponds to AFT age patterns, which indicate a simple pattern with highest exhumation rates in the center of the wedge which are probably triggered by the continuous underthrusting.

Additionally, underthrusting of the latest uplifted structure is reported in the AFT pattern from the successive merging of regions with young cooling ages between 80 km and 119 km shortening. The inherent forward jump of the DF is observed between 100 km and 119 km shortening and is also accompanied by a strong decrease of the AFT cooling ages compared to the previous time slice along the pro-wedge flank which suggest a late exhumation impulse.

As already mentioned, in agreement with previous studies (e.g., Huiqi et al., 1992), the accretionary wedge in Sc2 grows by frontal accretion. At the beginning of this experiment, the main activity takes place at the retro-wedge flank due to the development of relatively steep fore- and backthrusts. These structures evolve symmetrically due to the reduced stress caused by the lower basal friction (Davis et al., 1983). As a result, the wedge rather grows in horizontal direction compared to Sc1 and the initial deformation occurs long way to the collisional zone. This phase can be allocated with stage 1 where dominant block uplift takes place. Similarly, as in experiment Sc1 the structural interpretation can be supported by the AFT patterns which approves the location of initial deformation and indicates high exhumation rates along both flanks of the wedge in accordance with the uplift regions. After 40 km shortening the wedge reaches stage 2 with active thrusting and at the DF and at the retro-flank. Consequently, the wedge evolves bi-directionally.

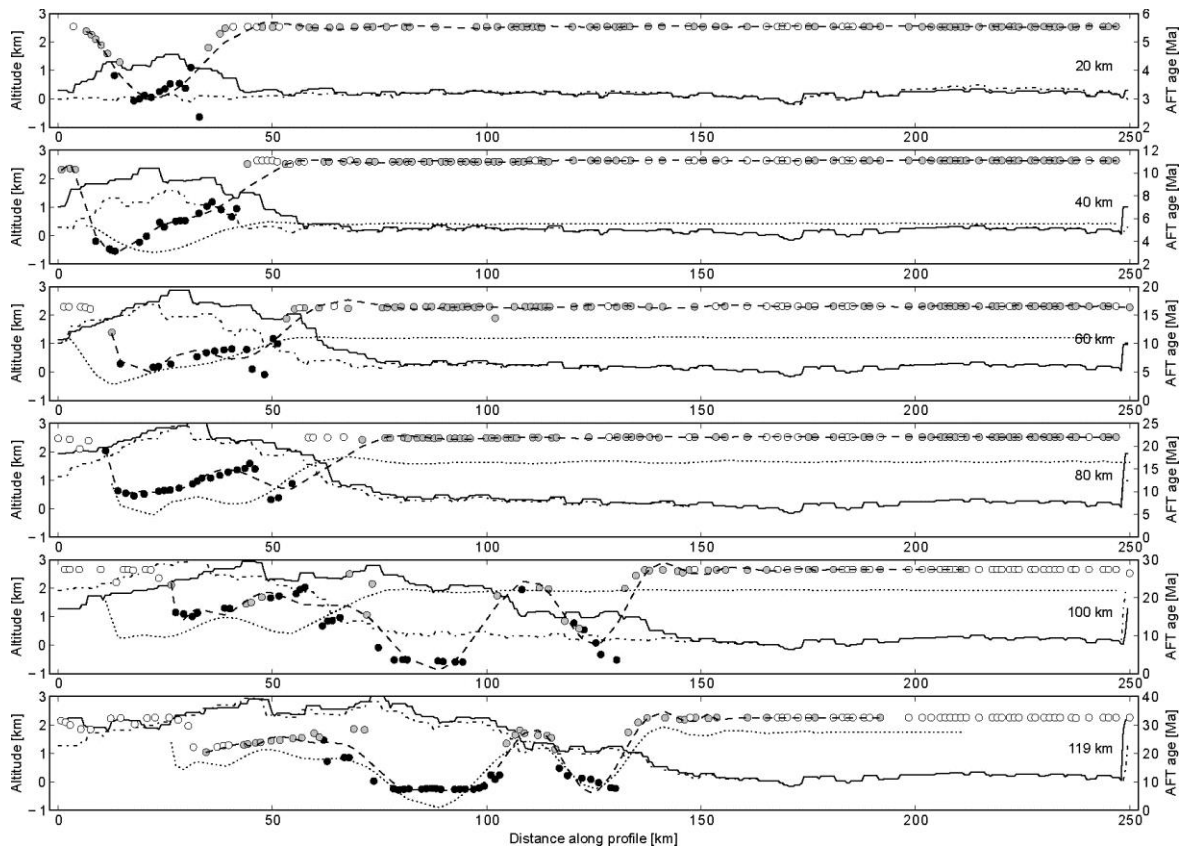


Fig. AI-12: Evolution of the computed erosional surface and the synthetic AFT cooling ages of Sc2 through time. (signatures see Fig. AI-11)

The AFT ages show an outward trend with rapid exhumation at the beginning of the modeled profile length (Fig. AI-12). Additionally, AFT analyses are not only sensitive to the appearance of deformation within an orogenic wedge, but also to the rate of it. This is also true for the synthetic AFT ages, which do not migrate far outward until 80 km shortening, but suggest high exhumation rates along the retro-wedge with young cooling ages along the retro flank. Though both flanks are deformed simultaneously, the amount of uplift and the associated exhumation distinctly exceeds the frontal counterpart (especially between 40 km and 60 km shortening). This attitude of the structural wedge system indicates that the stage 3 is reached, where a new kink at the retro-wedge flank develops. Hence, the reduced basal friction in Sc2 allows that the wedge develops all three stages (Willett et al., 1993; Storti et al., 2000). In contrast, in case of a high basal friction the material is more compressed and pressed against the lower crustal fragment and the indenter. This prevents the evolution of stage 1 and 3 where deformation occurs at the retro-wedge.

Additionally, the approach to use both methods helps to get an impression to what degree

a change in décollement strength impacts AFT analysis. High basal friction results in far underthrusting of the material and leads to a well-marked U-shaped AFT pattern with most rapid cooling in the central region of the wedge (Fig. AI-11). Only, if the DF jumps outwards in case of new forethrusts, a W-shape pattern occurs due to the 'young' uplifted region. In contrast, under low frictional conditions, lower uplift occurs and the AFT ages are either W-shaped distributed or as a series of U-shaped patterns over the whole accretion phases. This results out of a continuous frontal action where material is uplifted along steeper forethrusts and rearranged within the wedge. Additionally, also the retro-wedge flank is uplifted due to the slight compression induced by the box bottom. In later stages the central part of the wedge is no longer uplifted. Deformation and uplift is limited to the wedge flanks.

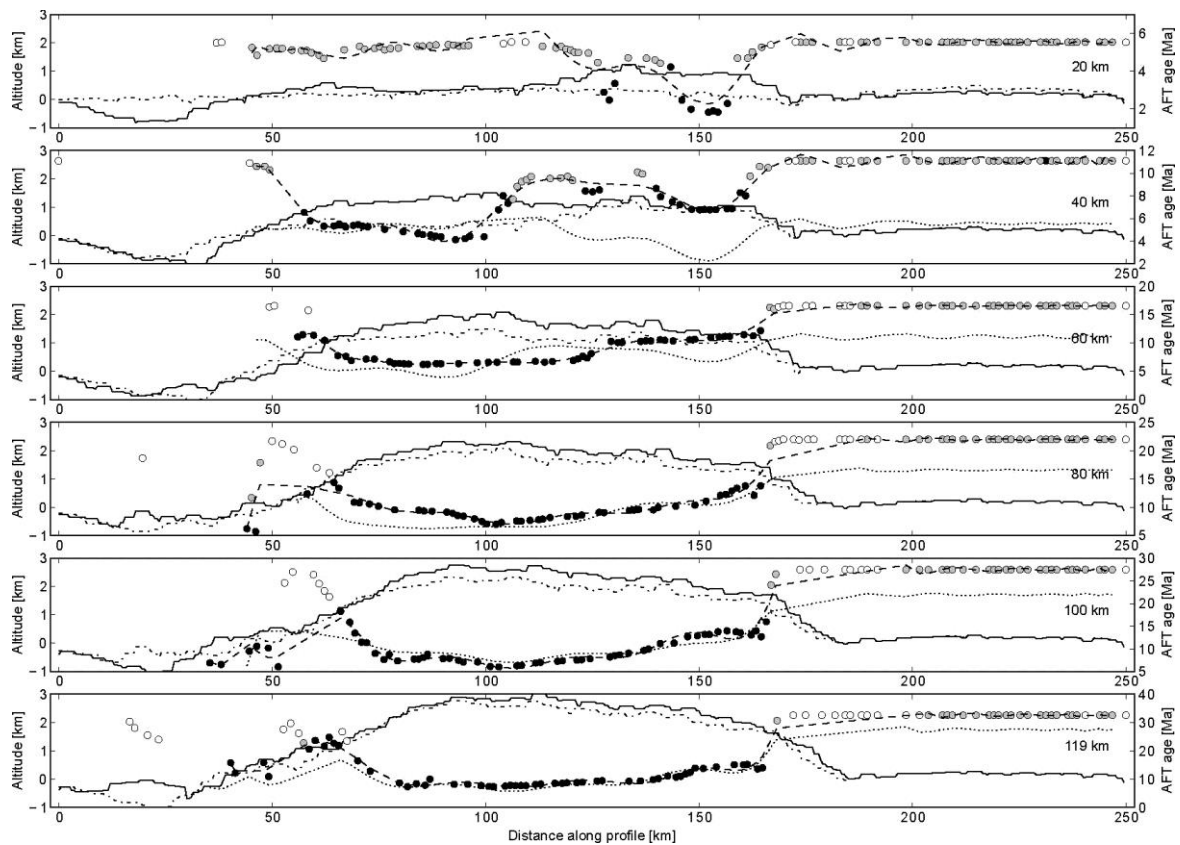


Fig. AI-13: Evolution of the computed erosional surface and the synthetic AFT cooling ages of Sc3 through time. (signatures see Fig. AI-11)

An example of such a W-shape pattern is shown in Fig. AI-14. Comparing the stress gradients within the wedge after 80 km and 100 km shortening, the alternating younger and older ages between 80 mkm and 130 mkm (Fig. AI-12 and second frame from top in Fig. AI-14) can be associated with the development of backthrusts along the retro-wedge

flank (Fig. AI-14 bottommost frame).

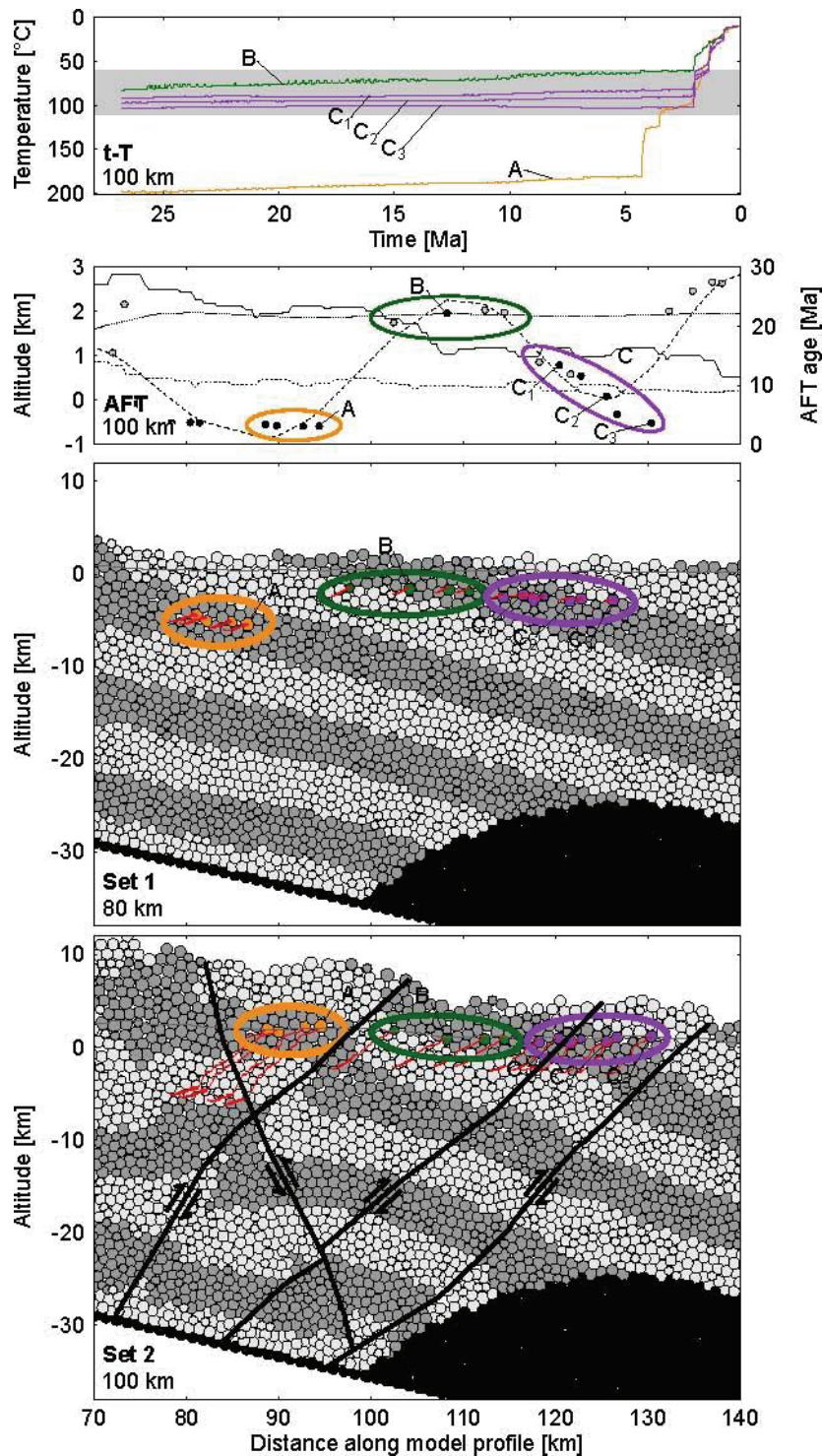


Fig. AI-14: Synthetic AFT cooling ages reveal mode and rate of modeled fault systems. From top to bottom: t-T: Time-temperature paths of different particle groupings after 100 km shortening; AFT: clipping from Fig. AI-11 (signatures see Fig. AI-11) with adjacent AFT ages simultaneously indicating three different modes of exhumation; Set1: particle setting after 80 km shortening, observed particle groupings are marked; Set2: particle setting after 100 km shortening, observed particle groupings are marked, faults are observed from structural analyses.

Section A in Fig. AI-14 comprises particles, which are rapidly exhumed along a major backthrust (f1 in Fig. AI-14) between 80 km and 100 km shortening. In contrast, particles of section B, being located in the footwall of the first mentioned fault, are hardly exhumed, at all. The third grouping of particles (section C in Fig. AI-14) shows decreasing cooling ages with increasing proximity to the most inward located major fault in the clipping (f3 in Fig. AI-14), indicating their hanging wall position. However, the intermediate fault in the clipping of Fig. AI-14 (f2), located in the middle of the two major faults, intersects section C, but does not affect the cooling ages of the grouping. The amount of vertical offset (negligible at the central fault), therefore, crucially impacts the rate of exhumation and thus, the synthetic AFT age.

As a result, synthetic AFT analyses give a very detailed picture about the amount and locations of uplifted regions and uplift rates. Consequently, patterns of synthetic AFT ages can support the analysis of a wedge growing within a DEM model. Does the wedge grow on top of a high frictional décollement with one central, high uplift region or does it grow on top of a low frictional décollement with various, moderate uplifted regions? Which accretion mode (frontal or basal accretion) is active while the wedge grows? Additionally, we are able to reveal the timing and rate of structural evolution by the derivation of synthetic AFT cooling ages, and thus, to get a more detailed understanding for the structural evolution of processes. Nevertheless, besides the AFT data, for such kind of analyses also the morphology and the erosion rates are important factors which have to be considered.

4.2 Influence of deep seated geometries

The wedges in experiment Sc1 and Sc3 grow under identical conditions, regarding the parameterization. The crucial difference between the experiments is the absence of the lower crustal fragment in Sc3 in the model setup.

Similarly to Sc2, the wedge in Sc3 grows in an inward direction after 20 km of shortening, what can be interpreted as stage 1 (Storti et al., 2000). Youngest AFT ages after 20 km shortening are computed at the collisional zone near the implemented indenter, and thus, reinforce the suggestion that the main deformation is located at the retro-wedge flank. After 40 km shortening stage 2 is reached in Sc3 with underthrusting of incoming material along flat forethrusts at the pro-wedge flank – similar to the observations in Sc1 (Fig. AI-7).

Accordingly, the synthetic cooling age pattern reflects the evolution with youngest AFT ages further outwards. Nevertheless, also the first deformed region near the indenter preserves the early cooling history with local minimum ages at 125 mkm and 151 mkm after 40 km shortening. The wedge extends through to the indenter, and consequently, has no further space to spread inwards. As result, a double-vergent wedge evolves with highest uplift in the center. That is also conveyed by the synthetic cooling ages. From 60 km on unimodal U-shaped patterns are observed in the AFT ages along the modeled profile length indicating highest exhumation rates in the center. Comparable to the evolution in Sc1, the fixed indenter is able to prevent that the wedge reaches the last stage, due to the restricted space. Consequently, in Sc3 stage 1 is established due to the missing crustal fragment.

Since synthetic AFT ages support the mechanical analysis of the DEM model, they also change in dependence of the geometry of the initial numerical model. In this case the missing of the lower crustal fragment lead to a flatter evolution of the AFT pattern in Sc3 compared to Sc1. Furthermore, a stepwise uplift can be inferred in Sc3. Hence, uplift slowly decreases with decreasing distance to the lower crustal fragment. The strongly uplifted region in Sc1 has much steeper flanks than in Sc3, where uplift impacts a much wider region as a result of the missing lower crustal fragment. As a result, the geometrical changes of the deep crustal conditions in the numerical experiment had an important influence on the AFT age pattern. The more compression occurs from the back side (in our case a composition of the indenter and the lower crustal fragment), the steeper the AFT age patterns evolve, whereas an oblique back-side allows a further spreading of the wedge with a more balanced uplift and AFT age patterns. This also has an influence on the evolutionary stages as more compression prevents the evolution of those stages where deformation of the retro-flank occurs. Consequently, the AFT age patterns can help to get a first impression about the geometrical initial conditions of the backstops within the deep mantel. Nevertheless, additional information and more numerical tests are necessary to get an overall picture on which deep crustal effects and parameters have which effect on the particle paths and exhumation patterns.

5. Conclusions

The advantage of the approach to couple numerical sandbox modeling and AFT thermochronology is the ability not only to investigate large-scale structures within a

growing orogenic wedge, but rather to focus on their effect regarding near-surface processes in high temporal and selectable resolution.

The granular model approach allows getting information about particle position and movements. This enables a comprehensive qualitative structural analysis. Moreover, we developed an approach to calculate erosion and append temperature as a parameter to the particles of the numerical ‘sandbox’, thereby combining the granular model approach and apatite fission track thermochronology. After deriving synthetic AFT cooling ages from the time-temperature histories of particles, the spatial distribution of these ages allows for a quantitative description and evaluation of the influence of deep seated (i.e. lower crustal) structures on near-surface (i.e. upper crustal) processes in addition to the qualitative insights into the structural evolution of the modeled wedge, revealed by the granular model approach.

Three numerical simulations with different deep crustal initial conditions are undertaken, in which either the décollement strength or the geometry is varied. Depending on the friction values the wedge grows either by frontal accretion or by basal accretion. In coherence with the stress induced from the presence or absence of the crustal splinter, the double-vergent wedges within the implemented experiments have reduced or dilated space to spread, as expected with regard to previous studies. Synthetic cooling ages reflect exactly the structural evolution, as they allow for gaining a detailed picture where and when uplift occurs within the models. AFT ages are sensitive to the current deformation stage, exhumation rate and reflect the initial state of the deep seated conditions. Furthermore, former structural evolution is preserved in the AFT patterns, thus, both, the current stage and the evolution hitherto is depicted from the synthetic thermochronologic data.

Summing up:

1. Calculating erosion in a numerical sandbox setting, results in a computed erosional surface, which can be used to derive temperature values for any particle at any position at any time in the model run. The time-temperature history of selected and tracked particles can be reconstructed, which in turn can be used for forward thermal history modeling, resulting in synthetic cooling ages.
2. Synthetic AFT-patterns support the structural analysis and interpretation of a structural DEM model.
3. We are able to detect and quantify the effects of deep seated structural geometries and rheologies on upper crustal structures during the evolution of a double-vergent

orogenic wedge. Therein, we show that high compression or pressure results in steep AFT patterns, whereas low compression results in a moderate trend. Additionally, the AFT patterns give a first impression about uplifted regions and, therewith, on the accretion mechanism, from with characteristic properties of the décollement can be derived.

ACKNOWLEDGEMENTS

This study is part of the EUROCORES TOPO-EUROPE project from the European Science Foundation and was funded by the German Science Foundation (DfG). We would like to thank Lisa-Carmen Eckhart, Sebastian Trüttner and Leonard Rossmann (University of Bremen) for support during data processing.

Erklärung

Datum: 04.11.2013
Name: Linda Marie Wenk
Adresse: Bayerwaldstrasse 27, 93059 Regensburg

Hiermit versichere ich, dass ich

1. die Arbeit ohne unerlaubte fremde Hilfe angefertigt habe,
2. keine anderen als die von mir angegebenen Quellen und Hilfsmittel benutzt habe und
3. die den benutzten Werken wörtlich oder inhaltlich entnommenen Stellen als solche kenntlich gemacht habe.



Linda Wenk
4.11. 2013
Universität Bremen